UNIVERSITÀ DEGLI STUDI DI MILANO

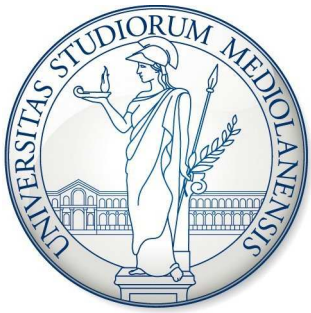

Facoltà di Scienze MM.FF.NN.

Dipartimento di Chimica Fisica ed Elettrochimica

Corso di Dottorato di Ricerca in SCIENZE CHIMICHE - CHIM/02

IMPROVING THE PHOTOCATALYTIC ACTIVITY OF TiO_2 FOR ENVIRONMENTAL APPLICATIONS: EFFECTS OF DOPING AND OF SURFACE MODIFICATION

Tutor: Prof. Elena SELLI

Coordinatore: Prof. Silvia ARDIZZONE

Tesi di Dottorato di Ricerca di:

Maria Vittoria DOZZI

Matricola R08321

Anno Accademico 2010-2011

葛飾北斎 - Katsushika Hokusai (1760-1849)

‘Then Comes the Sun’ …

艱難辛苦を乗り越える …

Table of Contents

Chapter 1

Abstract

In the field of energy and environmental application of heterogeneous photocatalysis TiO_2 appears as the most active and most suitable semiconductor.[1,2] In fact, TiO_2 has a high oxidation ability, its photogenerated holes being at E^0 = 2.9 V *vs.* NHE at pH 0; moreover, it is biologically and chemically inert, photostable and cheap.

In nature, TiO_2 can crystallize in the three polymorphs anatase, rutile and brookite. Anatase is thermodynamically less stable than rutile. It exhibits a shorter wavelength absorption edge and is largely recognized to be more active than rutile in oxidative detoxification reactions. Mixtures of these two polymorphs may produce intriguing effects on charge carrier transfer processes in photocatalytic applications.[3,4]

However, the following major factors limit both photocatalytic efficiency and activity of TiO_2:

a) The band gap of anatase TiO_2 is 3.2 eV, *i.e.* it absorbs light in the UV region, so that only a small portion (5%) of sunlight can be used for photocatalytic processes.
b) As in all semiconductors, photogenerated electron-hole couples undergo fast recombination in competition with charge transfer to adsorbed species.
c) The use of slurries could limit the industrial applications of photocatalysis, the separation of semiconductor powders after liquid phase reactions being troublesome and expensive.

In this context, during this PhD project different routes have been explored for solving the first two limiting aspects of TiO_2 use in photocatalytic processes.

At first the effects of TiO_2 surface modification were investigated, aiming at mitigating the high rate of photogenerated electron/hole pairs recombination. The attention was first focused on the consequences produced by the deposition of noble metal nanoparticles on TiO_2. In noble metal-modified photocatalysts, photopromoted electrons can be 'captured' by the noble metal nanoparticles, which have a Fermi level lower in energy than the conduction band potential. This facilitates electron transfer to adsorbed reducible species and favours electron–hole separation, with a consequent increase of the semiconductor photocatalytic activity. Whereas noble metal co-catalysts are known to be beneficial in the photocatalytic production of hydrogen from water solutions,[5-7] their effective role in photocatalytic oxidative reactions may appear rather controversial, especially in the case of gold-modified TiO_2,[8–10] the properties of such

metal-oxide composites depending on the conditions of gold deposition, on gold loading, particle size and shape, and also on storage conditions.[11-14]

A systematic study was thus undertaken on the photocatalytic performance of commercial TiO_2 (Degussa P25) bearing gold nanoparticles deposited by deposition-precipitation (DP), with particular attention on the method, either thermal or chemical, employed to reduce the Au(III) precursor into metallic gold. Two organic substrates, *i.e.* the azo dye Acid Red 1 (AR1) and formic acid (FA), were employed as substrates in photocatalytic oxidative degradation kinetic tests. Hydrogen peroxide evolution was also monitored during the runs in order to have a better insight into the role played by gold nanoparticles on both oxidative and reductive primary photocatalytic processes (Chapter 5).[15]

Other Au/TiO_2 photocatalysts were then prepared by employing the photodeposition technique, based on the irradiation of aqueous suspensions containing P25 TiO_2 and chloroauric acid under anoxic conditions. Gold loading in the 0.1-1.0 wt.% range was obtained by this way.[16]

The role played by photodeposited gold nanoparticles on the primary photocatalytic processes involving photopromoted conduction band electrons and valence band holes was also tested in both an oxidation and a reduction reaction, *i.e.* in the photocatalytic mineralization of formic acid (FA) and in the photoreduction of pollutant Cr(VI) in aqueous suspensions at pH 3.7, under UV-visible light irradiation. Some combined reactions were also performed in the presence of both FA and Cr(VI) substrates (Chapter 6). Commercial TiO_2 samples with different phase composition and surface area were then tested as photocatalysts in the photoinduced reduction of Cr(VI). This reaction was also coupled with the simultaneous photocatalytic oxidation of the pollutant azo dye Acid Orange 8 (AO8) or of formic acid, acting as hole scavengers. In general the co-presence of oxidizable and reducible species ensured better separation of photogenerated charge carriers, resulting in a higher rate of organics oxidation and Cr(VI) reduction, especially in the case of high surface area anatase TiO_2, having the strongest affinity for Cr(VI) and AO8, as demonstrated by competitive adsorption tests.[17]

The central part of this PhD work was devoted to the exploration of different routes to minimize the major drawback of TiO_2 as a photocatalytic material, *i.e.* its high-

energy band gap (3.2 eV). The fact that TiO_2 is able to absorb only a small portion of sunlight represents a great limitation in its use as photocatalyst, particularly for the conversion of solar into chemical energy.

Anion doping with *p*-block elements was successfully pursued in recent years to sensitize TiO_2 towards visible light,[18,19] either by introducing newly created mid-gap energy states, or by narrowing the band gap itself. However, the nature of doping titanium dioxide with main group elements, such as N,[18,20,21] C,[19,22,23] B,[24] S,[23,25] P,[26] I,[27] and F,[28-30] is still not completely understood. The insertion of dopant impurities in the oxide structure may induce light absorption in the visible region, but also increase the rate of the undesired recombination of photogenerated charge carriers, an effect becoming relatively lower, the higher is the crystallinity of the oxide structure.

In this PhD thesis, the attention was focused on sulphur, fluorine and boron as dopants of TiO_2, the effects of N or C doping on the photocatalytic efficiency of TiO_2 having been widely investigated in the last decade.[18-23] The sol-gel method, which is very flexible and suitable for systematic structure *vs.* photoactivity studies, was adopted to incorporate the anion dopants in the TiO_2 structure. Two series of TiO_2-based doped samples were first prepared by the sol-gel method in the presence of different amounts of dopant source (thiourea and NH_4F for S-doped and F-doped samples, respectively), followed by calcination at different temperature (500, 600 or 700°C). Reference undoped materials were prepared by following the same synthetic procedure apart from the addition of the dopant precursor. All samples were characterized by BET, UV-vis absorption, XPS, HRTEM, XRD and EPR analyses. The effects of the dopant amount and of the calcination temperature on the structural features of the doped materials were systematically investigated in relation to their photocatalytic activity.

The photocatalytic degradation of formic acid (FA) in aqueous suspension was employed first as test reaction. This substrate was chosen mainly because it does not absorb in the visible region, thus allowing a straightforward evaluation of the photocatalysts' visible light activity, and undergoes direct photomineralization without forming any stable intermediate species, which simplifies the interpretation of kinetic results (Chapter 7).[31]

The photocatalytic behaviour of an extended series of NH_4F-doped TiO_2 photocatalysts was further explored in two other reactions, *i.e.* the decomposition of acetic acid in aqueous suspension and the gas phase mineralization of acetaldehyde.

In the photooxidation of both these organic substrates, neither of which absorbs visible light, the good photooxidation ability of the NH_4F-doped materials (D-TiO_2 series) was further confirmed. Furthermore, the photooxidation of acetic acid was also investigated systematically as a function of the irradiation wavelength, by collecting so-called action spectra. This type of analysis, representing the most powerful photocatalytic characterization tool to determine the effective wavelength-dependent response and activity of a photocatalyst,[32,33] was carried out in the laboratories of the Catalysis Research Center, Hokkaido University in Sapporo (Japan), under the supervision of Prof. Bunsho Ohtani (Chapter 8). The comparison between the shapes of the absorption and the action spectra allowed to distinguish between absorption features which are active or inactive in photocatalysis.[34]

XPS and EPR analysis of NH_4F-doped materials, even if calcined at 700°C, revealed the presence of residual nitrogen-containing species, that might be responsible for the spectral features and/or photoactivity of NH_4F-doped TiO_2. Indeed, the conflicting results reported in the literature on the effects of fluorine as TiO_2 dopant[28-30] are most likely due not only to the different routes employed to prepare the doped materials, but also to difficulties in the interpretation of results obtained with photocatalysts containing more than one dopant element, because of possible synergistic effects.[29,30]

In order to better clarify the role of fluorine and/or nitrogen dopants of TiO_2, another series of doped photocatalysts was prepared according to the same synthetic procedure employing HF instead of NH_4F as dopant source, thus avoiding the co-presence of nitrogen impurities in the material. At the same time, aiming at elucidating the effects of F-doping and co-doping of TiO_2, an investigation was started on the effects of the co-presence of *p*-block elements boron and fluorine in titania. The photocatalytic activity of these new doped systems, prepared by using the sol-gel method in the presence of different amounts of dopant source and calcined at different temperatures, was investigated in the oxidative decomposition of formic and acetic acid in aqueous suspension. Moreover, in order to better compare the photoactivity of these photocatalytic systems with that of samples prepared in presence of the NH_4F dopant source (D-TiO_2 series), the photooxidation of the transparent acetic acid substrate was systematically investigated as a function of irradiation wavelength for the three main new series of doped samples. All photocatalysts were characterized by BET, XRD, UV-vis absorption analyses, so as to enlighten the effects of dopant concentration and

calcination temperature on the structural features of the doped materials, in relation to their photocatalytic activity (Chapter 9).

Finally in the last part of the PhD thesis the effect of noble metal (Pt and Au) nanoparticles photodeposition on the activity of the best performing series of NH_4F-doped TiO_2 photocatalysts calcined at 700°C was investigated in both energetically down-hill and up-hill reactions, *i.e.* in formic acid and acetic acid degradation in aqueous suspensions and in hydrogen production from methanol/water vapour mixtures, a reaction which has been thoroughly investigated in our research group.[35,36] Intriguing synergistic effects of TiO_2 doping and of noble metal nanoparticles deposition have been observed in both types of reaction (Chapter 10).

References

1. X. Chen and S. S. Mao, Chem. Rev., **2007**, 107, 2891.
2. A. Fujishima, X. Zhang and D. A. Tryk, Surf. Sci. Rep., **2008**, 63, 515.
3. J. Yu, J.C. Yu, M.K.-P. Leung, W. Ho, B. Cheng, X. Zhao and J. Zhao, J. Catal., **2003**, 217, 69.
4. C. Bernardini, G. Cappelletti, M. V. Dozzi and E. Selli, J. Photochem. Photobiol., A: Chem., **2010**, 211, 185.
5. C. M. Wang, A. Heller and H. Gerischer, J. Am. Chem. Soc., **1992**, 114, 5230.
6. R. Baba, S. Nakabayashi, A. Fujishima and K. Honda, J. Phys. Chem., **1985**, 89, 1902.
7. G. L. Chiarello, E. Selli and L. Forni, Appl. Catal. B, **2008**, 84, 332.
8. H. Li, Z. Bian, J. Zhu, Y. Huo, H. Li and Y. Lu, J. Am. Chem. Soc., **2007**, 129, 4538.
9. S. L. Lee, J. Scott, K. Chiang and R. Amal, J. Nanopart. Res., **2009**, 11, 209.
10. E. Kowalska, R. Abe and B. Ohtani, Chem. Commun., **2009**, 241.
11. R. Zanella, S. Giorgio, C. R. Henry and C. Louis, J. Phys. Chem. B, **2002**, 106, 7634.
12. Y. Wu, K. Q. Sun, J. Yu and B. Q. Xu, Phys. Chem. Chem. Phys., **2008**, 10, 6399.
13. G. M. Veith, A. R. Lupini and N. J. Dudney, J. Phys. Chem. C, **2009**, 113, 269.
14. M. Mrowetz, A. Villa, L. Prati and E. Selli, Gold Bulletin, **2007**, 40, 154.
15. M. V. Dozzi, L. Prati, P. Canton and E. Selli, Phys. Chem. Chem. Phys., **2009**, 11, 7171.

16. M. V. Dozzi, G.L. Chiarello and E. Selli, J. Adv. Oxid. Technol., **2010**, 13, 305.
17. M. V. Dozzi, A. Saccomanni and E. Selli, J. Hazard. Mater, **2011**, in press, doi: 10.1016/j.jhazmat.2011.09.038;.
18. R. Asahi, T. Morikawa, T. Ohwaki, K. Aoki and Y. Taga, Science, **2001**, 293, 269.
19. S. U. M. Khan, M. Al-Shahry and W. B. Ingler, Jr., Science, **2002**, 297, 2243.
20. S. Sakthivel, M. Janczarek and H. Kisch, J. Phys. Chem. B, **2004**, 108, 19384.
21. M. Mrowetz, W. Balcerski, A. J. Colussi and M. R. Hoffmann, J. Phys. Chem. B, **2004**, 108, 17269.
22. S. Sakthivel and H. Kisch, Angew. Chem., Int. Ed., **2003**, 42, 4908.
23. T. Tachikawa, S. Tojo, K. Kawai, M. Endo, M. Fujitsuka, T. Ohno, K. Nishijima, Z. Miyamoto and T. Majima, J. Phys. Chem. B, **2004**, 108, 19299.
24. W. Zhao, W. Ma, C. Chen, J. Zhao and Z. Shuai, J. Am. Chem. Soc., **2004**, 126, 4782.
25. T. Ohno, M. Akiyoshi, T. Umebayashi, K. Asai, T. Mitsui and M. Matsumura, Appl. Catal. A, **2004**, 265, 115.
26. J. C. Yu, L. Zhang, Z. Zheng and J. Zhao, Chem. Mater., **2003**, 15, 2280.
27. G. Liu, Z. Chen, C. Dong, Y. Zhao, F. Li, G. Q. Lu and H.-M. Cheng, J. Phys. Chem. B, **2006**, 110, 20823.
28. J. C. Yu, J. Yu, W. Ho, Z. Jiang and L. Zhang, Chem. Mater., **2002**, 14, 3808.
29. D. Li, N. Ohashi, S. Hishita, T. Kolodiazhnyi and H. Haneda, J. Solid State Chem., **2005**, 178, 3293.
30. S. Livraghi, K. Elghniji, A. M. Czoska, M. C. Paganini, E. Giamello and M. Ksibi, J. Photochem. Photobiol., A, **2009**, 205, 93.
31. M. V. Dozzi, S. Livraghi, E. Giamello and E. Selli, Photochem. Photobiol. Sci., **2011**, 10, 343.
32. B. Ohtani, Chem. Lett., **2008**, 37, 217.
33. E. Kowalska, O. O. Prieto-Mahaney, R. Abe and B. Ohtani, Phys. Chem. Chem. Phys., **2010**, 12, 2344.
34. M. V. Dozzi, B. Ohtani and E. Selli, Phys. Chem. Chem. Phys., **2011**, 13, 18217.
35. G. L. Chiarello, M. H. Aguirre and E. Selli, J. Catal., **2010**, 273, 182.
36. G. L. Chiarello, D. Ferri and E. Selli, J. Catal., **2011**, 280, 168.

Chapter 2

Background

2.1 Introduction

Environmental pollution, such as contaminated water or polluted air, has become a global issue threatening the health of mankind. Typical polluting sources are toxic organic molecules or exhausted gas compounds which are released from household waste, livestock waste and local industries. Science is thus involved in searching for new alternatives and ecologically sustainable methods for cleaning up environmental contamination. Different solutions for depollution have already been proposed: air scrubbing, adsorption, activated carbon, etc., but some of them only remove the pollutant from one phase to another one and then require additional processes to eliminate toxic compounds.

Heterogeneous photocatalysis is a potential solution that has been the object of intense research efforts since the early 1970s, when Fujishima and Honda discovered the photocatalytic splitting of water on TiO_2 electrodes.[1] This technique can be envisaged as one of the most promising Advanced Oxidation Process (AOPs) because of its specific advantages, such as bland reaction conditions, the possibility of using molecular oxygen as oxidant species, the total mineralization of pollutants into substances innocuous to the environment.

Heterogeneous photocatalysis is based on the interaction between semiconductor materials and light. By considering that we can get 'free' light from the sun, the idea of using solar light energy as resource to clean up the environment is an ideal and extremely promising approach.

Sun light, with wavelengths ranging from 10^{-5} to 10^{5} nm, is a clean and renewable energy source that is readily available. Before reaching the Earth's surface, a part of the solar energy is absorbed by the stratosphere, ozonosphere and other atmospheric layers. Of the solar radiation reaching the Earth, 5% is UV light, 50% is visible light and the remaining part is composed of infrared and longer wavelengths radiation (Fig. 2.1). Approximately a 40% of the total amount of radiation arriving to Earth, mainly composed of visible, infrared, and radio energies, is constantly arriving to its surface. In particular Ultraviolet light (UV-light), generally divided into three regions, A (315 – 400 nm), B (280 – 315 nm) and C (100 – 280 nm), is responsible for most of the photochemical processes occurring in the atmosphere. While the UV-C region is mostly filtered by Earth's ozone layer, UV-A and UV-B radiations still pass and have

the potential to generate photochemical processes such as the synthesis of vitamin D in our body or the tanned skin colour we get after having been exposed to sunlight.

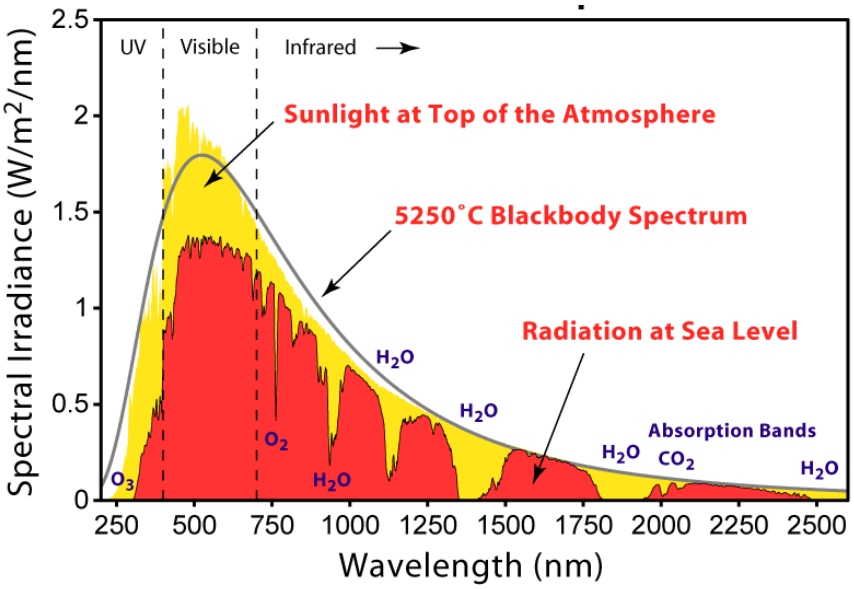

Figure 2.1 Earth's light environment (solar spectrum).

The development of photocatalytic technology with its different kinds of application (see Table 2.1) has especially promoted, in its early age, a revolutionary idea of cleanliness, as suggested by the Japanese 'fathers' of this field. Whereas in the past 'light cleaning' meant a cursory job – a quick wipe-up or dusting – in the future it will come to mean 'cleaning with light', as depicted in Fig. 2.2.

Figure 2.2 Representation of a city governed by urban photocatalysis, proposed by Italcementi group.

Table 2.1 Overview of different photocatalysis applications.

Property	***Category***	***Application***
Self-cleaning	Material for residential and office buildings	Exterior tiles, kitchen and bathroom components, interior furnishings, plastic surfaces, building stones
	Indoor and outdoor lamps and related systems	Translucent paper for indoor lamp covers, coatings on fluorescent lamps and highway tunnel lamp cover glass
	Materials for roads	Tunnel wall, soundproofed wall, traffic signs and reflectors
	Others	Tent material, clothes for hospital garments and uniforms and spray coating for cars
Air-cleaning	Indoor air cleaners	Room air cleaner, photocatalyst-equipped air conditioners and interior air cleaner for factories
	Outdoor air purifiers	Concrete for highways, roadways and footpaths, tunnel walls, soundproofed walls and building
Water puification	Drinking water	River water, groundwater, lakes and water storage tanks
	Others	Fish feeding tanks, drainage water and industrial wastewater
Antitumor activity	Cancer therapy	Endoscopic-like instruments
Self-sterilizing	Hospital	Tiles to cover the floor and walls of operating rooms, silicone rubber for medical catheters and hospital garments and uniforms
	Others	Public rest rooms, bathrooms

2.2 Principles of semiconductor photocatalysis

Photocatalysis is generally defined as the change in the rate of a chemical reaction or its initiation under the action of ultraviolet, visible or infrared radiation in the presence of a substance – the photocatalyst – that absorbs light and is involved in the chemical transformation of the reaction partners. Moreover, when a solid material is used as the photocatalyst the definition of heterogeneous photocatalysis is preferred.[2] The most commonly used photocatalysts are semiconductor materials (most of them metal oxides) which, unlike metals, possess a void energy region (band-energy structure), where no energy levels are available (Fig. 2.3). The void region which extends from the top of the filled valence band to the bottom of the vacant conduction band is called band gap, E_g.

Activation of a semiconductor photocatalyst is achieved through the absorption of a photon of ultra-band gap energy, which results in the promotion of an electron from the valence band into the conduction band, e^-_{CB}, and in the concomitant generation of a hole in the valence band, h^+_{VB}. The reaction of either the photopromoted electron with a

reducible adsorbed substrate (usually oxygen in aerated system) and/or the hole with an oxidizable adsorbed species can subsequently occur.

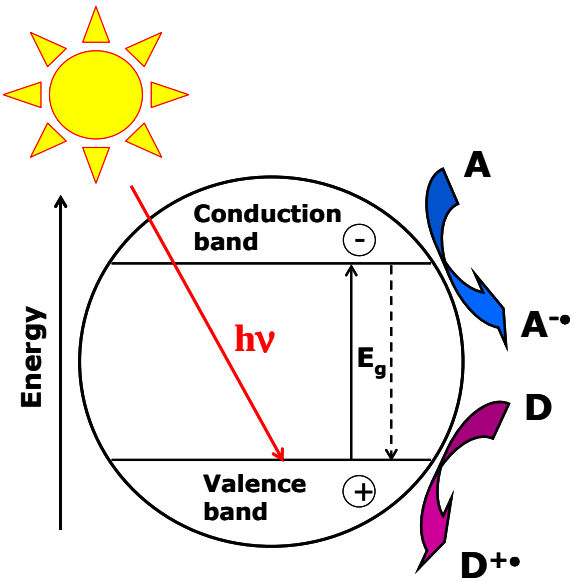

Figure 2.3 Simplified scheme of semiconductor activation.

The probability and the rate of such charge transfer processes depend on the position of the conduction and valence band edges and on the redox potentials of the adsorbed species. For example, when a semiconductor is used as a photocatalyst in the environmental remediation, usually involving the photodecomposition or complete mineralization of organic pollutants, it should be capable to generate a valence band hole with a redox potential that is positive enough to oxidise the organic pollutant. At the same time the photogenerated electron in the conduction band should be negative enough to reduce adsorbed O_2 to superoxide radical anion.[3]

Figure 2.4 shows the band gap values of different semiconductors and their position on the electrochemical scale. A substrate can successfully interact only with some semiconductors: it is necessary that the electrochemical potential value of the electron acceptor is more positive (down in the graph) than the semiconductor conduction band potential, and that the electron donor potential is more negative (up in the graph) than that of the semiconductor valence band. A photocatalytic reaction can take place only under such conditions.

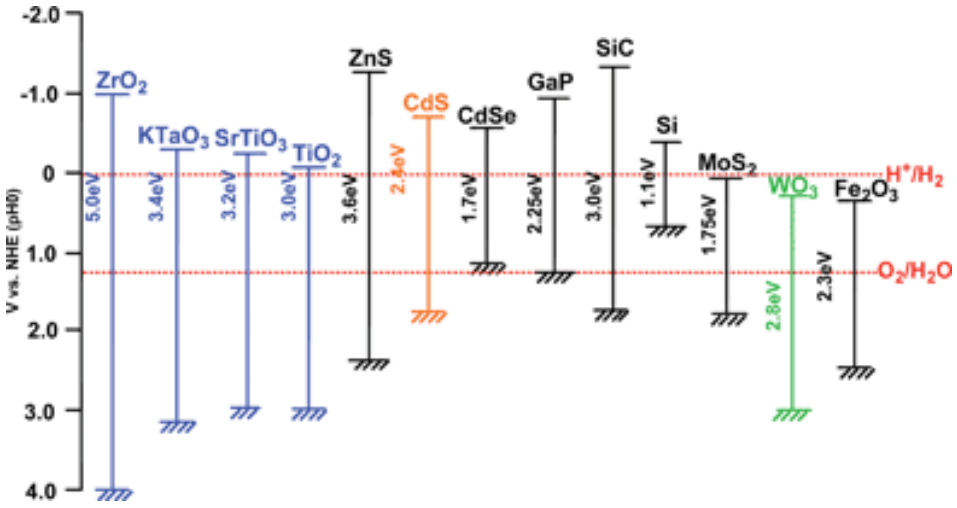

Figure 2.4 Relationship between the band structure of some selected metal oxide and non-oxide semiconductors and the redox potentials of water splitting.[4]

Recombination of electron-hole pairs can occur, in competition with charge transfer to adsorbed species, in the volume of the semiconductor particle or in its surface with the release of heat. This phenomenon represents the major deactivation path which could significantly decrease the overall photocatalytic efficiency.

The detrimental process of back-donation to the semiconductor after charge transfer to the adsorbed species can also occur. Thus, by considering TiO_2 as an example of semiconductor with photocatalytic properties, the main reaction scheme of a photocatalytic process can be mainly summarized in the following equations and depicted in Fig. 2.5.

a) Charge separation

$$TiO_2 + h\nu \rightarrow e^-_{CB} + h^+_{VB} \quad (2.1)$$

b) Bulk/surface recombination

$$e^-_{CB} + h^+_{VB} \rightarrow \text{heat} \quad (2.2)$$

c) Surface trapping

$$h^+_{VB} + \equiv Ti\text{-}OH \rightarrow \equiv Ti\text{-}O^{\bullet} + H^+ \quad (2.3)$$

$$e^-_{CB} + \equiv Ti\text{-}OH \rightarrow \equiv Ti^{\bullet} + OH^- \quad (2.4)$$

d) Surface recombination

$$e_{CB}^{-} + \equiv Ti\text{-}O^{\bullet} + H^{+} \rightarrow \equiv Ti\text{-}OH \quad (2.5)$$

$$h_{VB}^{+} + \equiv Ti^{\bullet} + OH^{-} \rightarrow \equiv Ti\text{-}OH \quad (2.6)$$

e) Interfacial charge transfer

$$Red_1 + \equiv Ti\text{-}O^{\bullet} \rightarrow Ox_1 + \equiv Ti\text{-}OH \quad (2.7)$$

$$Ox_2 + H_2O + \equiv Ti^{\bullet} \rightarrow Red_2 + \equiv Ti\text{-}OH \quad (2.8)$$

f) Back reaction

$$Red_2 + \equiv Ti\text{-}O^{\bullet} \rightarrow Ox_2 + \equiv Ti\text{-}OH \quad (2.9)$$

$$Ox_1 + \equiv Ti^{\bullet} \rightarrow Red_1 + \equiv Ti\text{-}OH \quad (2.10)$$

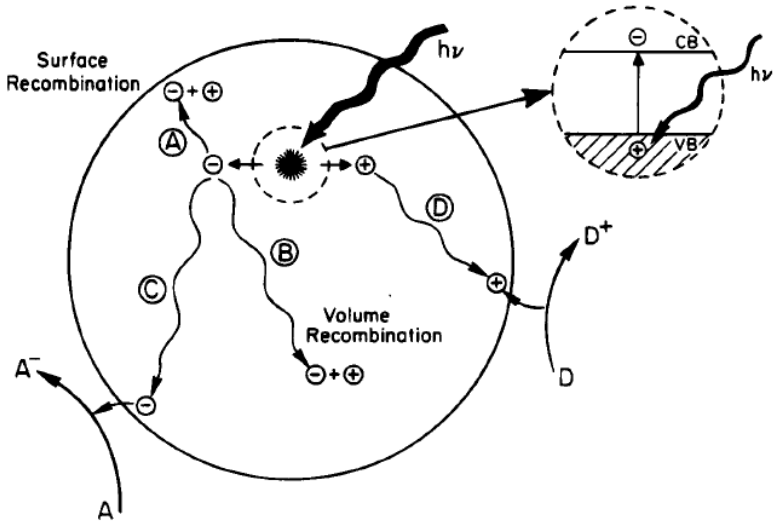

Figure 2.5 Schematic representation of a nanosized photocatalyst particle where the de-excitation process (following the initial irradiation) can occur in four general ways: (A) surface recombination, (B) volume recombination, (C) reduction with electron acceptors, and (D) oxidation with electron donors.[5]

It's worth to remember that a semiconductor free of impurities is defined *intrinsic*. A semiconductor doped with impurities is called *extrinsic*.

Doping involves the addition of a different element into the semiconductor. The simplest example of this involves the introduction of a group V element (*e.g.*, P) or a group III element (*e.g.*, Al) into a group IV element (*e.g.*, Si). The addition of P into Si

introduces occupied energy levels into the band gap close to the lower edge of the conduction band, thereby allowing facile promotion of electrons into the conduction band (Fig. 2.6b). The addition of Al introduces vacant energy levels into the band gap close to the upper edge of the valence band, which allows facile promotion of electrons from the valence band (Fig. 2.6c). This leads to the formation of holes in the valence band.

Doped semiconductors in which the dominant or majority charge carriers are electrons are referred to as *n-type* semiconductors, whereas those in which holes are the majority charge carriers are referred to as *p-type* semiconductors.

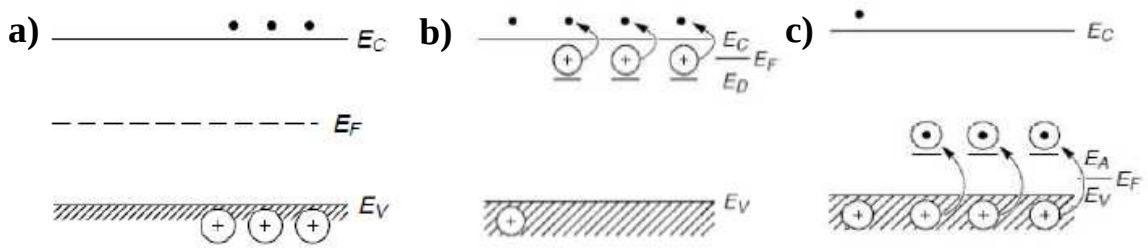

Figure 2.6 Schematic diagram of the energy levels of an a) intrinsic, b) n-type and c) p-type semiconductor.

Another important concept in discussion of solid state materials is the Fermi level. This is defined as the energy level at which the probability of occupation by an electron is ½ at absolute zero temperature; for example, for an *intrinsic* semiconductor the Fermi level lies at the mid-point of the band gap (Fig. 2.6a).

Doping changes the distribution of electrons within the solid, and hence changes the Fermi level. For a *n-type* semiconductor, the Fermi level lies just below the conduction band (Fig. 2.6b), whereas for a *p-type* semiconductor it lies just above the valence band (Fig. 2.6c). In addition, as with metals, the Fermi level of a semiconductor varies with the applied potential; for example, moving to more negative potentials will raise the Fermi level.[6]

The contact between a semiconductor and another phase (liquid, gaseous or metallic) generally causes a charge redistribution. In order for the two phases to be in equilibrium, their electrochemical potential must be the same. The electrochemical potential of the solution is determined by the redox potential of the electrolyte solution, and the redox potential of the semiconductor is determined by the Fermi level.

If the redox potential of the solution and the Fermi level do not lie at the same energy, a movement of charge between the semiconductor and the solution is required in order to equilibrate the two phases. The excess charge that is now located on the semiconductor does not lie at the surface but extends for a significant distance (100 - 10000 Å). This region is referred to as the *space charge region*, and has an associated electrical field. Hence, there are two double layers to consider: the *interfacial* (semiconductor/solution) *double layer*, and the *space charge double layer*. For an *n-type* semiconductor the Fermi level is typically higher than the redox potential of the solution, and hence electrons will be transferred from the semiconductor into the solution. Therefore, there is a positive charge associated with the *space charge region*, and this is reflected in an upward bending of the band edges. Since the majority charge carrier of the semiconductor has been removed from this region, this region is also referred to as a *depletion layer* (Fig. 2.7).

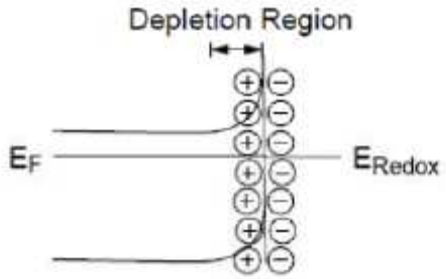

Figure 2.7 Band bending for an n-type semiconductor in equilibrium with a solution.

As for metals, changing the applied potential shifts the Fermi level. The band edges in the interior of the semiconductor (*i.e.*, away from the depletion region) also vary with the applied potential in the same way as the Fermi level. However, the energies of the band edges at the interface are not affected by changes in the applied potential. Therefore, the change in the energies of the band edges on going from the interior of the semiconductor to the interface, and hence the magnitude and direction of band bending, varies with the applied potential. There are three different situations to be considered:

- at a certain potential, the Fermi level lies at the same energy as the solution redox potential (Fig. 2.8b). There is no net transfer of charge, and hence there is no band bending. This potential is referred to as *flatband potential*, E_{fb}.

- depletion regions arise at potentials positive of the *flatband potential*, $E > E_{fb}$, for an n-type semiconductor (Fig. 2.8a).
- at potentials negative of the *flatband potential* ($E < E_{fb}$) for an n-type semiconductor, there is now an excess of the majority charge carrier (electrons) in this *space charge region*, which is referred to as an *accumulation layer* (Fig. 2.8c).[6]

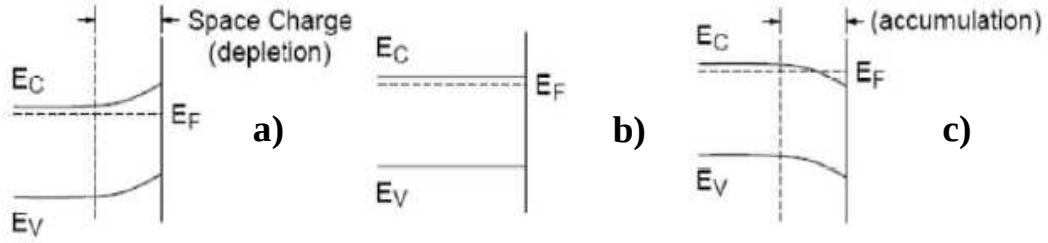

Figure 2.8 Effect of varying the applied potential (E) on the band edges in the interior of an n-type semiconductor. a) $E > E_{fb}$, b) $E = E_{fb}$, c) $E < E_{fb}$.

2.3 TiO_2 as photocatalyst

As for any common catalytic material, which is not consumed during the course of a chemical reaction, a photocatalyst must be stable and not prone to decompose due to long exposure to light. In addition, for some processes in which water suspensions are used, stability in water at various pH is essential.

As a general rule, a good photocatalyst must be:[7]

- photoactive
- able to absorb visible and/or near UV light
- biologically and chemically inert
- photostable (*i.e.* not liable to photoanodic corrosion)
- inexpensive
- non-toxic

In many cases, the semiconductor risks to incur in oxidative decomposition by the photogenerated holes. Generally, only *n-type* semiconductor oxides are stable towards photoanodic corrosion, although such oxides usually have large band gap, so that the semiconductor absorb only UV light. CdS is an example of a highly active semiconductor which can be activated using visible light (thus, sunlight could be used), but, as usually occurs for visible light absorbing semiconductors, it is subject to

photoanodic corrosion and this feature makes it unacceptable as a photocatalyst for water purification.

Among different semiconductor photocatalysts, TiO_2 appears as the most active and most suitable one for a wide variety of energy and environmental applications. In fact, TiO_2 has a high oxidation ability, its photogenerated holes being at $E^0 = 2.9$ V *vs.* NHE at pH 0; moreover, it is biologically and chemically inert, photostable and cheap. Finally the location of the bottom of conduction band (Fig. 2.4) is suitable for using this material for the photocatalytic production of hydrogen from water, which has received extensive attention in the last decade for its potential application in the field of solar energy harvesting, conversion and storage.[4,8-10]

Even after choosing TiO_2 as semiconductor in photocatalytic experiments, the choice of its crystalline form is important as well. The crystalline forms of TiO_2 are anatase, rutile and brookite.

Brookite is a natural phase, which is quite difficult to synthesize in a laboratory. It is also rare in nature and structurally more complex than the other two polymorphs. It is constituted by an elementary cell containing 8 formula units with an orthorhombic symmetry. The Ti surrounding coordination polyhedron is an octahedron and there is a high oxygen atom packing. It forms very flat small tubular crystals with a variable color, from yellow to brown reddish. This polymorph is metastable: out of a restricted pressure and temperature interval it is converted into the two other phases (Fig. 2.9).

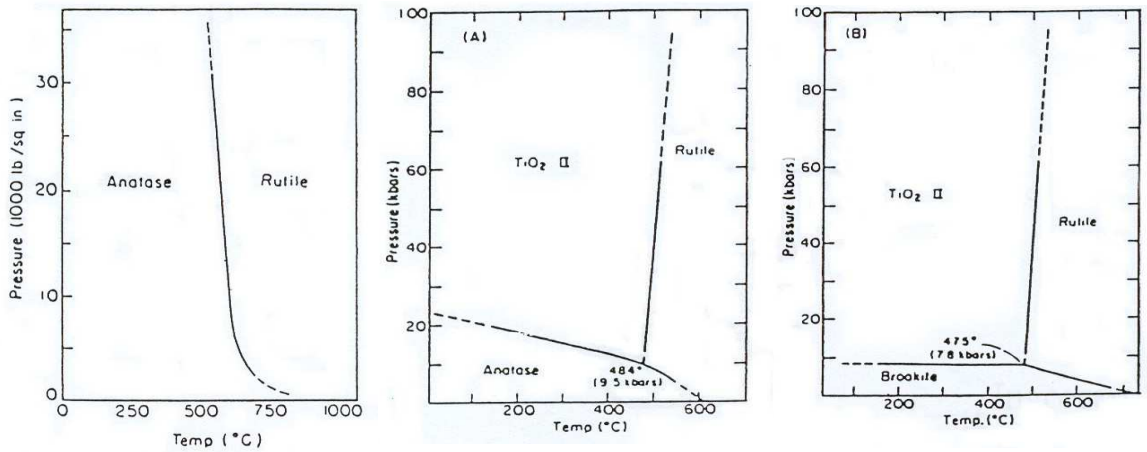

Figure 2.9 Phase diagrams of TiO_2 at low and high pressures.

The rutile and anatase phases are the most used in photocatalytic studies (Fig. 2.10). Rutile is the most common mineral form of TiO_2 in nature. The rutile structure is not compact. Its unit cell is tetragonal: one axis is 30% shorter of than the other two (a = 4.593 Å, c = 2.959 Å). The structure is constituted by very distorted octahedral TiO_6, with oxygen ions shared with other adjacent Ti ions. Every Ti ion is a octahedral surrounded by six O ions, and every O ion is surrounded by 3 Ti ions at the edges of an equilateral triangle. It can be envisaged as a central body cubic lattice of Ti ions that is considerably distorted. The crystallites can be present in nature as black or reddish and also transparent when completely without impurities. The color can also be orange if the mineral is in very thin needle form.

Anatase, also improperly called octahedrite, presents a tetragonal bipyramidal symmetry, with a form similar to an elongated octahedron (a = 3.785 Å, c = 9.514 Å). The structure is based on a polyhedral chain of TiO_6. The difference with rutile is that anatase presents a more distorted structure, where every polyhedron shares 4 edges with the adjacent one. In particular, the tetragonal elementary cell contains 4 units, instead of 2, and the cell sides are a = 3.785 Å and c = 9.514 Å. The anatase crystals are really small, the natural color ranges from blue sapphire to yellow-brown.

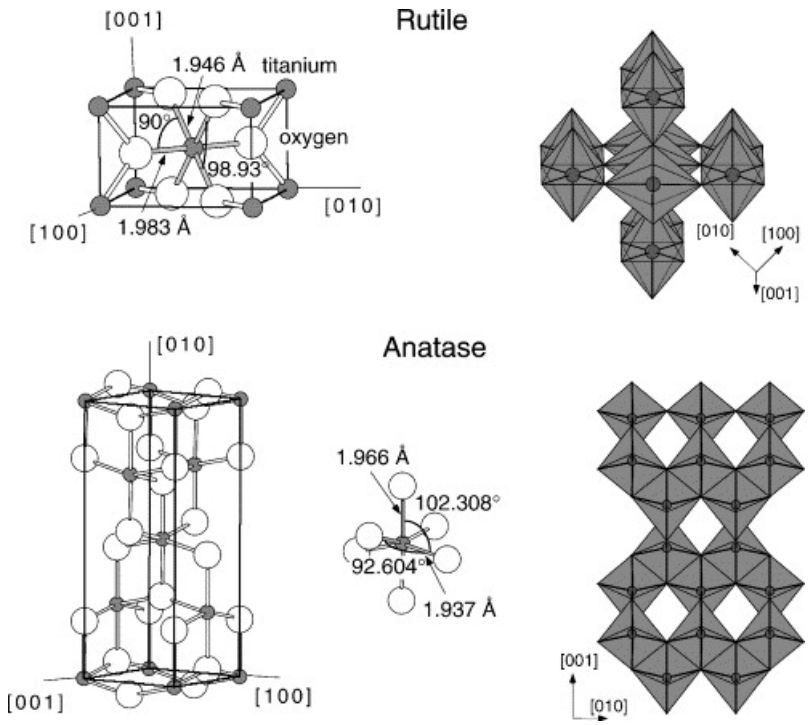

Figure 2.10 Bulk crystal structure of rutile and anatase.[11]

These differences in lattice structures cause different mass densities and electronic band structures for the two main TiO_2 polymorphs. In particular titanium dioxide is characterized by an allowed and indirect band gap, which is equal to 3.2 and 3.0 eV, respectively, for the anatase and rutile phase. The band gap occupied states (valence band, VB) are mostly O 2p atomic orbitals-derived, while the conduction band (CB) is mostly Ti 3d-derived (Fig. 2.11).[12]

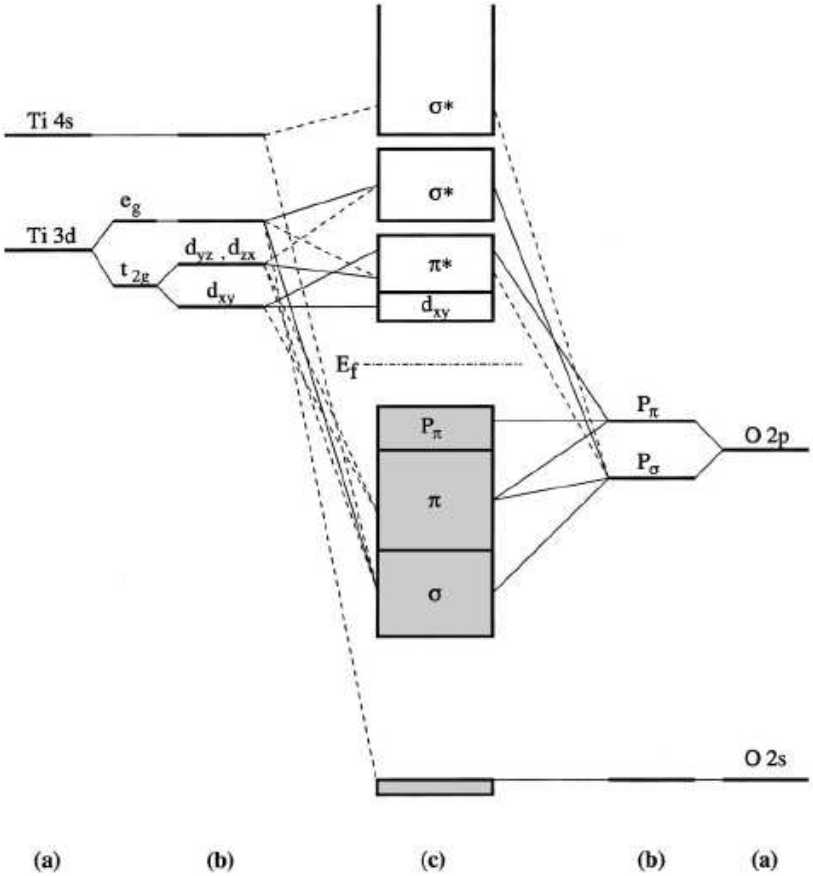

Figure 2.11 Molecular orbital structure of anatase: a) atomic levels, b) crystal – field split levels, c) final interaction states.[12]

Moreover TiO_2, like other oxides and chalcogenides, is thermodynamically stable as a non-stoichiometric compound, with anion deficiencies. Therefore, a more correct denotation would be TiO_{2-x}. Generally the material defects, such as vacancies, can introduce localized ionized states. In the case of TiO_2 oxygen vacancies are formally compensated by the adoption of the +3 oxidation state by an equivalent number of titanium atoms. These Ti^{3+} ions operate as electron donors, introducing localized levels next to the conduction band. This is due to the *n-type* semiconductor character of TiO_2.

The anatase phase is one of titania's most studied cristalline phases because it is commonly considered as the most photoactive polymorph, especially for the decomposition of water and organic compounds.

As previously mentioned, after photoexcitation of titania, electron-hole pairs are transferred to surface-adsorbed reactants in competition with mutual recombination. Since recombination is expected to occur on grain boundaries and crystal defects, the use of single-crystal particles with a low density of defects is one of the possible strategies to be pursued. Indeed, single-crystal anatase particles exhibited a high level of photocatalytic activity when they had a large specific surface area.[13]

In general, well developed anatase single crystals exhibit a octahedral shape, *i.e.*, tetragonal bipyramids, dominated by {101} facets, which are the thermodynamically most stable surface.[14-16] Interest has thus been shown in octahedral shape with {101} facets.[17-20] On the other hand, the preparation of single-crystal anatase particles with a largely-truncated octahedral shape with two square {001} facets, *e.g.*, a decahedral shape, has also been reported.[21,22]

Since the {001} surface is more reactive for dissociative adsorption of reactant molecules compared with {101} facets,[23-27] high photocatalytic efficiency is expected for particles with {001} facets,[28] though present information about their photocatalytic activity is still scarce. In agreement with natural minerals, a truncated octahedral bipyramid, exposing eight {101} facets as well as two {001} facets, has been shown to be the most thermodynamically stable shape of anatase crystallites based on Wulff construction.[15,30] In spite of the important applications of anatase TiO_2, experimental studies on the photoactive property of a single crystal surface have been limited by the difficulty in obtaining high-quality (and purity) anatase samples.[31] A few studies have suggested a significant role of facets of TiO_2 polyhedral particles for photocatalytic reactions.[32,33] Recently developed hydrothermal reaction methods have enabled the preparation of anatase crystalline particles with well-developed {001} facets in a relatively high yield. In particular Yang *et al*. have synthesized uniform anatase TiO_2 single crystals with a high percentage (around 47%) of {001} facets using hydrofluoric acid as a morphology controlling agent.[21]

The same research group has also reported a new solvothermal method using 2-propanol as a synergistic capping agent and reaction medium, together with HF to synthesize high-quality anatase TiO_2 single-crystal nanosheets (SCNSs) with 64% of

{001} facets.[34] The efficiency of these TiO_2 SCNSs materials in heterogeneous photocatalytic reactions was investigated by measuring the formation of active hydroxyl radicals ($^{\bullet}OH$) upon irradiation, which are considered as one of the most important oxidative species in photocatalysis reactions.[35] Terephthalic acid (TA) was used as a fluorescence probe because it can react with $^{\bullet}OH$ in basic solution to generate 2-hydroxy terephthalic acid (TAOH), which emits a unique fluorescence signal peaking around 426 nm.[36] The normalized (calculated per unit surface area) concentration of $^{\bullet}OH$ radicals generated from SCNSs clean surfaces was found to be more than 5 times higher than that on standard Degussa P25 TiO_2. It's important to note that in order to compare the photocatalytic activity of well-defined anatase single crystal particles with that of commercial TiO_2 photocatalytic powders, the crystalline size should be at least of submicrometric scale, in order to have a surface area comparable to that of commercial powders. Ohtani *et al*. succeed in this goal; decahedral-shaped anatase titania particles (DAPs) have been prepared by controlled gas-phase reaction of titanium(IV) chloride and oxygen at 1473K (Fig. 2.12).[37,38]

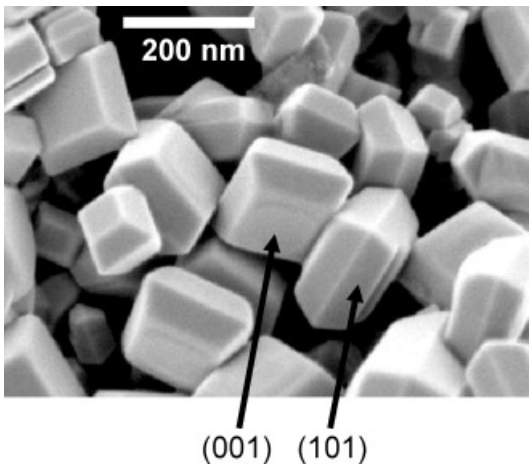

Figure 2.12 A representative SEM image of decahedral anatase-titania particles prepared by controlled gas-phase reaction of titanium(IV) chloride and oxygen at 1473 K. Most particles expose two square (001) facets and eight trapezoidal (101) facets.[37]

In this case the photocatalytic activity of DAPs was reported to be much higher than the photocatalytic activities of commercial titania particles, *e.g.*, Degussa (Evonik) P25, presumably due to relatively large specific surface area able to adsorb a large amount of substrate(s) and due to high crystallinity, *i.e*. less crystal defects to reduce e^{-}–h^{+} recombination. Aiming at investigating the intrinsic effect of decahedral shape on

photocatalytic activity, Ohtani's group compared results obtained with DAPs with those described in their recent study, in which the photocatalytic activities and the physical and structural properties of 35 commercial titania powders were statistically analyzed to find the predominant properties determining the activity in a given reaction system.[39] Standardized photocatalytic activities for five kinds of reactions were fairly well reproduced by a linear combination of six kinds of physical and structural properties of photocatalysts, *i.e.*, specific surface area, density of crystal defects, primary particle size, secondary particle size and existence of anatase and rutile phases. It was suggested that high levels of photocatalytic activity of DAPs could not be reproduced by the correlation equations derived in the above-mentioned multivariable analysis,[40] *i.e.*, another property, such as "shape" may affect the photocatalytic activities. A more detailed study on this shape effect still needs further investigation.

The rigorous statistical approach of Ohtani's research group[39] merits to be appreciated, because for the first time they tried to prove, in a strict scientific sense, the common understanding or myth in the photocatalysis field that anatase is more active than rutile.

2.4 Modifications of TiO_2 photocatalysts

Even if TiO_2 still remains as the most active and most suitable semiconductor photocatalyst for a wide variety of energy and environmental applications, the following major factors limit its photocatalytic efficiency and activity:

1. The band gap of TiO_2 (anatase phase) is 3.2 eV, *i.e.* it absorbs light in the UV region, so that only a small portion (5%) of the sunlight can be used for photocatalytic processes.
2. As in all semiconductors, photogenerated electron-hole couples undergo fast recombination in competition with charge transfer to adsorbed species.
3. The use of slurries could limit the industrial applications of photocatalysis, the separation of semiconductor powders after liquid phase reactions being troublesome and expensive.

Concerning the third point, several practical problems arise from the use of TiO_2 powders in photocatalytic processes: (a) difficult separation of the insoluble catalyst from the liquid, (b) aggregation of the suspended particles, especially at high concentration and (c) difficulties in a possible scale-up to continuous flow systems. In

this regard the use of photocatalysts in thin film form would not only avoid the drawbacks encountered with powder suspensions, but could also have photoinduced surface hydrophilicity applications.[41]

Among the different methods applied to obtain TiO_2 films,[42-47] the so called 'doctor blade' method appears as a fast and no-energy consuming procedure for the production of thin porous films with good uniformity, high adhesion and reproducible properties, which are expected to have very good photocatalytic activity. Several other techniques have been developed to produce tailored photocatalysts films, such as CVD (chemical vapour deposition), magnetron sputtering, drop casting or electrochemical anodisation.

However, in this PhD work the attention was focused on the exploration of different routes for the solution of the first two previously listed limiting aspects of TiO_2 use in photocatalytic processes. In order to extend the spectral breadth and efficiency of TiO_2 photoresponse, a lot of scientific efforts have been done in the last decade.

In this regard we can identify the following four main generations of TiO_2 photocatalysts.[48]

i) the first generation involved pure TiO_2 materials.

ii) the second generation consists of TiO_2 materials doped with metals, such as Cr, V, W, Mo, Ru, Os, Re, Rh, Co, Al, Sn and Fe.[48-50] The charged carrier recombination rates and interfacial electron-transfer rates can be significantly altered due to doping with metal ions. The photoreactivity of doped TiO_2 is influenced by several parameters such as the dopant concentration, the energy levels of dopants differently located within the TiO_2 lattice, their *d* electronic configurations and the light intensity.[49,50] Therefore the photocatalytic performance of doped materials varies case by case. For example Cao *et al*. noticed that Sn^{4+}-doped TiO_2 film, prepared by plasma enhanced CVD method, exhibits more surface defects and a consequent enhanced photocatalytic activity for the degradation of phenol under both UV and visible light.[51]

Wang *et al.* found that in Fe^{3+}-doped TiO_2 synthesized by oxidative pyrolysis the formation of rutile was strongly promoted by iron doping.[52] Choi *et al.*, in turn, found that doping TiO_2 with metal ions (Fe^{3+}, Mo^{5+}, V^{4+}) by sol–gel method significantly increased the photoreactivity as the dopant concentration increased.[50] Karvinen *et al.* theoretically investigated the role of transition metal dopants (V^{3+}, Cr^{3+}, Mn^{3+}, Fe^{3+}) in both anatase and rutile TiO_2 models and observed significant

bang gap narrowing caused by those metals only in the anatase system.[53] However Herrmann *et al.* reported that metal ion dopants like Cr^{3+}, for example, can increase electron–hole recombination.[54] Much additional work have been done on metal doping of TiO_2, but a detailed understanding from a surface science viewpoint has not yet been achieved.

Among the second generation of photocatalysts, structural and/or surface modification of TiO_2 by noble metal (Pd, Pt, Au) deposition represents an emerging research field which has attracted wide attention. In particular there are two main approaches to the noble metal modification of TiO_2. Firstly, the high rate of photogenerated electron/hole pairs recombination can be limited by loading noble metal nanoparticles only on the surface of TiO_2. In these systems, photopromoted electrons can thus be 'captured' by the noble metal nanoparticles, which have a Fermi level lower in energy than the conduction band potential of the semiconductor (Fig. 2.13 and 2.14), with a consequent increase of the overall photocatalytic efficiency, especially under UV light.[55]

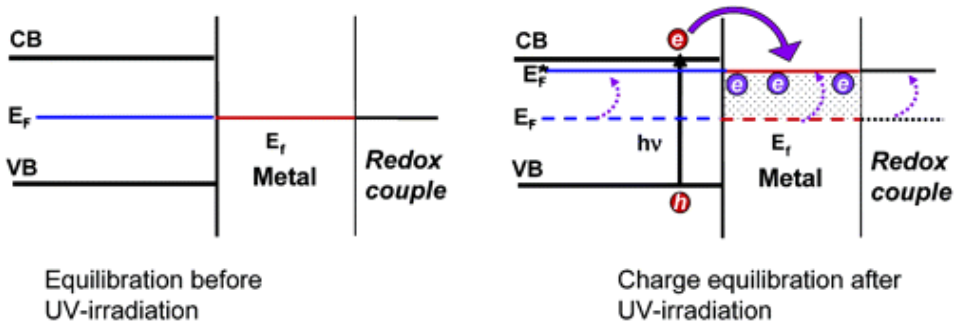

Figure 2.13 Equilibration of semiconductor-metal nanocomposites with the redox couple before and after UV irradiation.[55]

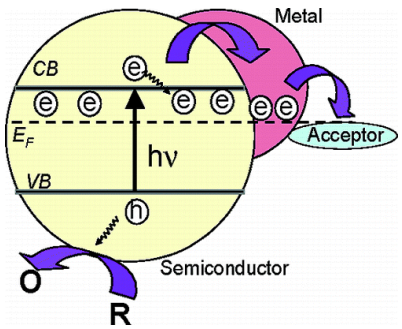

Figure 2.14 Schematic representation of the catalysis mechanism of gold nanoparticles deposited on TiO_2 surface. [55]

It's important to take into account that the gold nanoparticles deposited on the TiO_2 surface are known to induce strong localized surface plasmon resonance

(LSPR) responsible for light absorption around 550 nm, which was recently found to produce the photoinduced oxidation of 2-propanol over Au/TiO_2.[56] The presence in these reaction systems of a semiconducting material for electron transfer and of oxygen as an electron acceptor was found to be necessary. In particular the mechanism of visible-light-induced oxidation of organic compounds on gold–titania, proposed by Kowalska *et al.*, is schematically shown in Fig. 2.15.

First, incident photons are absorbed by gold particles through their LSPR excitation. Electrons may be then injected from Au particles into the CB of titania and reduce molecular oxygen adsorbed on the surface of titania. The resultant electron-deficient gold can oxidize organic compounds, such as 2-propanol and acetic acid, to be recovered to its original metallic state. Therefore, the photocatalytic action of gold particles was confirmed, for the first time, by observing a resemblance of action and absorption spectra (Fig. 2.16), with a turnover number exceeding unity.

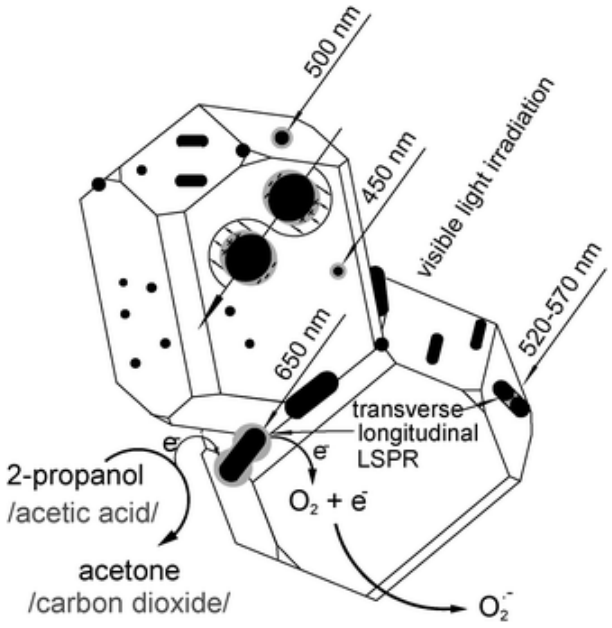

Figure 2.15 Schematic representation of the mechanism of organic compounds oxidation by Au/TiO_2 under vis irradiation.[56]

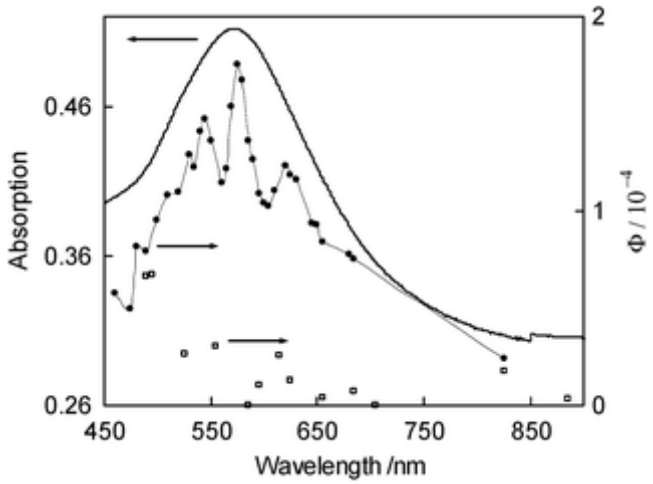

Figure 2.16 Action spectrum of 2-propanol oxidation on TiO_2 (ST41): ● Au-modified, □ bare, and ▬ absorption spectrum of Au/TiO_2 (ST41) measured with barium sulfate as a reference.[56]

A second way to modify TiO_2 by noble metals consists in the insertion of metal ions (due to a doping process) into the semiconductor crystal structure, with a consequent decrease of the titania band gap extension. Details of photon absorption for gold ions doped in TiO_2, reported by Li *et al.*, are depicted in Fig. 2.17.[57]

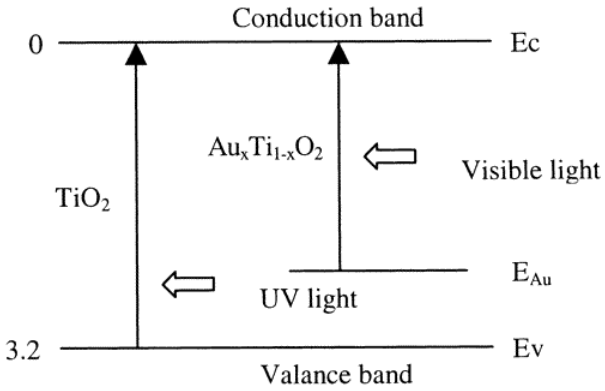

Fig 2.17 Proposed $Au_xTi_{1-x}O_2$ energy level and photoinduced electron excitation.[57]

Furthermore, the transfer of conduction-band electrons from TiO_2 to another semiconductor might also be a feasible way to decrease charge recombination in photoexcited TiO_2.[58-63] On this basis, titanium dioxide has been combined with several semiconductor oxides, such as ZrO_2, SnO_2, WO_3 and $ZnFe_2O_4$. Increased surface acidity, as well as textural/structural modifications especially in the surface layers, have been invoked to explain the higher photocatalytic activity of coupled oxides.[64]

Moreover, in the last years these kind of coupled systems have found important environmental applications. For example, electron storage in the presence of O_2 was successfully realized in a hybrid WO_3/TiO_2 material. In particular, this system could be charged under UV irradiation, holding the electrons in the presence of O_2 for a long term, and can be discharged by a suitable reduction process which could be represented by the reduction treatment of poisonous heavy metal ions.[65]

Furthermore it was shown that the introduction of CeO_2 into the TiO_2 framework not only improve the thermal stability of the ordered mesoporous structure, but also effectively extend the photo-response of TiO_2 to the visible-light region.[66]

iii) the third generation of materials mainly consists of TiO_2 doped with non-metal elements, in order to shift the absorption threshold of TiO_2 into the visible light range. In particular, after the first report about visible-light-sensitive N-doped TiO_2 photocatalysts in 2001,[67] the attention has been mainly switched to the preparation, characterization and testing of different types of TiO_2 doped with *p*-block elements, such as S, C, B, P and I.[68-72] Such materials exhibit a red shift of the light absorption edge, the origin of which has arisen a lively debate. The main point of discussion concerns the eventual narrowing of the semiconductor band gap as a consequence of doping or the creation of intra band gap states. Also, the chemical nature and the location in the solid of the dopant species responsible for visible light activity is still controversial, together with the role of oxygen vacancies, stabilized by the presence of dopants as a result of charge compensation.[73-75]

iv) the fourth generation of materials is based on the surface deposition of dye sensitizer molecules on the TiO_2 semiconductor. Surface sensitization of the photocatalyst *via* chemisorbed or physisorbed dyes can increase the efficiency of the photoexcitation process and expand the excitation wavelengths range of the photocatalyst through excitation of the sensitizer followed by charge transfer to the semiconductor. The mechanism of the process is briefly outlined by reactions (2.11) and (2.12). Organic and/or inorganic dyes, such as erythrosin B, thionine and analogs of $Ru(bpy)_3$, are commonly used as sensitizers.[76,77]

$$Dye + hv \rightarrow Dye^* \quad (2.11)$$

$$Dye^* + TiO_2 \rightarrow Dye^{*\bullet} + TiO_2\,(e^-) \quad (2.12)$$

These systems can find application especially for the photocatalytic evolution of H_2 and/or photocurrent production, even when the energy of light is lower than the band gap of pure TiO_2 (Fig. 2.18).

The interaction of the sensitizer with light plays an important role in determining the efficiency of sensitized TiO_2. However, a careful design is required in order to avoid some drawbacks such as thermal instability of the dye and a high recombination of the charged carriers.[78]

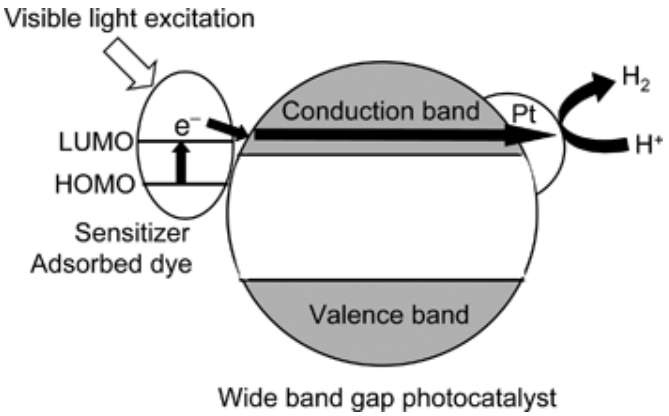

Fig 2.18 Scheme of sensitized-type photocatalyst.[4]

It's worth to underline that in most cases the emergence of visible light response in doped materials sacrifices the UV light activity of TiO_2, mainly because doping generates impurity and/or vacancy levels in the bulk acting as recombination centres. Furthermore, the oxidation power and mobility of photogenerated holes in localized narrow bands are less than in the TiO_2 valence band.[79-81]

As an alternative, the visible light activation of TiO_2 has been recently achieved by surface modification with oxides of transition metals including Fe,[82-84] Cu [85] and Cr.[86] This approach is attractive in that visible light response can be induced in such hybrid materials without the introduction of impurity/vacancy levels into the bulk of TiO_2.

In the Cu(II) grafted system,[85] visible light was first assumed to initiate interfacial charge transfer (IFCT), so that electrons in the valence band of TiO_2 are directly transferred to Cu(II) and form Cu(I), as well as holes in the TiO_2 valence band, which are able to decompose organic substances. In contrast, Cu(I) produced by electron transfer reduces adsorbed O_2 through multielectron reduction, with the consequent consumption of photoexcited electrons (Fig. 2.19).

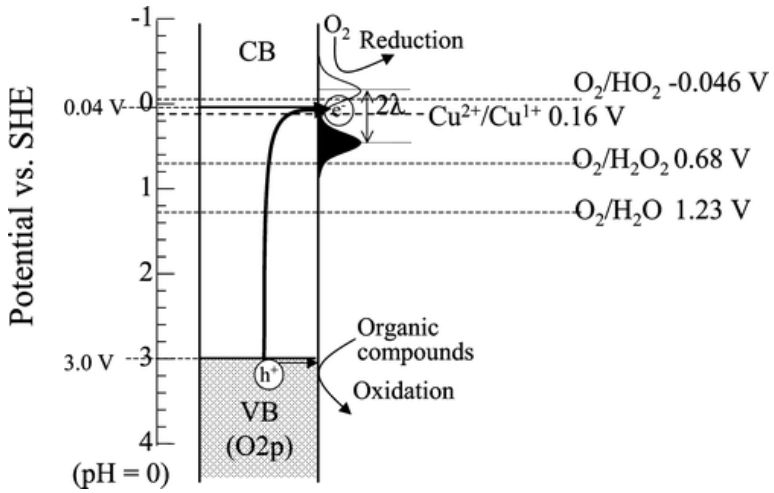

Figure 2.19 Proposed mechanism for the generation of photocatalytic activity under visible light for Cu(II)-grafted TiO_2 systems. Visible light irradiation induces interfacial charge transfer (IFCT) from the valence band of TiO_2 to Cu(II) ions.[85]

The mechanism proposed in the case of grafted Cr(III) ions is slightly different, because the Cr(IV)/Cr(III) redox potential is slightly above that of the TiO_2 valence band. In this system a charge transfer process would occur from the grafted atomic metal ions into the conduction band of TiO_2.[86] The photoproduced Cr(IV) species may oxidize organic molecules and return back to the original Cr(III) state, while the electrons in the TiO_2 conduction band are consumed in the reduction of adsorbed oxygen molecules (Fig. 2.20).

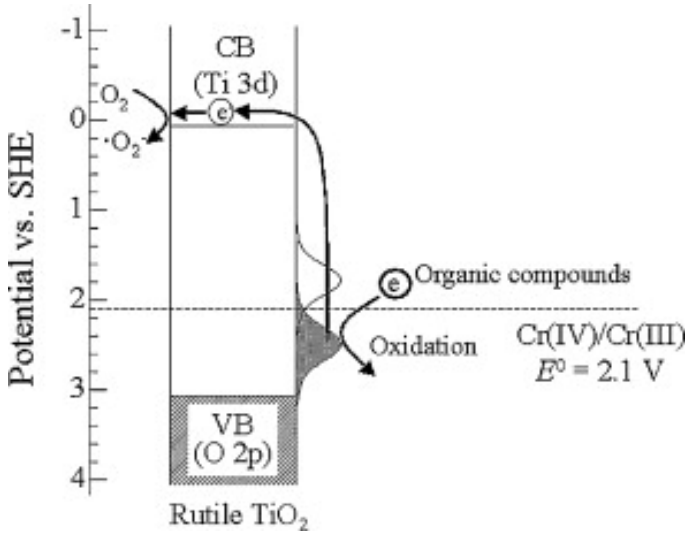

Figure 2.20 Proposed mechanism for the generation of photocatalytic activity under visible light. Visible light irradiation induces a metal charge transfer process (MMCT) from the grafted Cr(III) metal ions to the conduction band (CB) of TiO_2, mainly consisting of Ti(3d) orbitals.[86]

The visible light induced activity of such hybrid materials is noticeable in the case of rutile TiO_2; however, the effect is small for anatase TiO_2. A key point in this kind of surface modification is the dispersion state of the metal oxide on the TiO_2 surface.

Very promising results have been recently obtained by means of the chemisorption-calcination cycle (CCC) technique, in which metal complexes are adsorbed by chemical bonds on the TiO_2 surface.[87,88] The organic ligands are then oxidized by post-heating to prepare metal oxide clusters and ultrathin films at a molecular scale.

The choice of the semiconductor could strongly affect the photoefficiency of these novel and promising grafted systems. In this regard it was found that Cu(II)/WO_3 showed a higher quantum efficiency respect to Cu(II)/TiO_2 during the decomposition of 2-propanol under visible light irradiation.[89] This fact could be ascribed both to the higher visible light absorption capability of the first system respect to the second one and to the intrinsic higher oxidation power of the holes photogenerated in the VB of WO_3 respect to those obtained in TiO_2 materials.

These preliminary results described in the literature suggest metal ions grafting of TiO_2 as a simple and effective method for the design of novel and efficient photocatalysts which respond to visible light irradiation, even better than well-known and commercially available doped materials (N-doped TiO_2, HP-NO8, Showa Denko, which is already used for indoor application).

2.5 References

1. A. Fujishima and K. Honda, Nature, **1972**, 238, 37.
2. M. Schiavello, Heterogeneous photocatalysis - Vol. 3. John Wiley & Sons, 1st Edition, **1997**.
3. M. R. Hoffmann, S. T. Martin, W. Choi and D. W. Bahnemann, Chem. Rev, **1995**, 95, 69.
4. A. Kudo and Y. Miseki, Chem. Soc. Rev., **2009**, 38, 253.
5. A. L. Linsebigler, G. Lu and J. T. Yates, Chem. Rev., **1995**, 95, 735.
6. A. W. Bott, Current Separ., **1998**, 17, 87.
7. D. S. Bhatkhande, V. G. Pangarkar and A. ACM Beenackers, J. Chem. Technol. Biotechnol., **2001**, 77, 102.
8. R. Abe, J. Photochem. Photobiol. C: Photochem. Rev., **2010**, 11, 4, 179.
9. G. L. Chiarello and E. Selli, Recent Pat. Eng., **2010**, 4, 155.
10. M. Kitano and M. Hara, J. Mater. Chem., **2010**, 20, 627.
11. U. Diebold, Surf. Sci. Rep., **2003**, 48, 53.
12. R. Asahi, Y. T Aga, W. Mannstadt and A. J. Freeman, Phys. Rev. B, **2000**, 7459.
13. H. Kominami, J. I. Kato, M. Kohno, Y. Kera and B. Ohtani, Chem. Lett., **1996**, 12, 1051.
14. R. L. Penn and J. F. Banfield, Geochim. Cosmochim. Acta, **1999**, 63, 1549.
15. M. Lazzeri, A. Vittadini and A. Selloni, Phys. Rev. B, **2001**, 63, 155409.
16. A. S. Barnard and P. Zapol, Phys. Rev. B, **2004**, 70, 235403.
17. M. Miyauchi, J. Mater. Chem., **2008**, 18, 1858.
18. D. H. Wang, J. Liu, Q.S. Huo, Z. M. Nie, W. G. Lu, R. E. Williford and Y. B. Jiang, J. Am. Chem. Soc., **2006**, 128, 13670.
19. E. Hosono, S. Fujihara, H. Lmai, I. Honma, I. Masaki and H. S. Zhou, ACS Nano, **2007**, 1, 273.
20. F. Amano, T. Yasumoto, O. O. Prieto-Mahaney, S. Uchida, T. Shibayama and B. Ohtani, Chem. Commun., **2009**, 2311.
21. H. G. Yang, C. H. Sun, S. Z. Qiao, J. Zou, G. Liu, S. C. Smith, H. M. Cheng and G. Q. Lu, Nature, **2008**, 453, 638-UA.
22. P. P. Ahonen, A. Moisala, U. Tapper, D. P. Brown, J. K. Jokiniemi and E. I. Kauppinen, J. Nanoparticle Res., **2002**, 4, 43.

23. A. Vittadini, A. Selloni F. P. Rotzinger and M. Grätzel, Phys. Rev. Lett., **1998**, 81, 2954.
24. G. S. Herman, Z. Dohnalek, N. Ruzycki and U. Diebold, J. Phys. Chem. B, **2003**, 107, 2788.
25. A. Tilocca and A. Selloni, J. Phys. Chem. B, **2004**, 108, 19314.
26. X. Q. Gong and A. Selloni, J. Phys. Chem. B, **2005**, 109, 19560.
27. C. Arrouvel, M. Digne, M. Breysse, H. Toulhoat and P. Raybaud, J. Catal., **2004**, 222, 152.
28. A. Selloni, Nature, **2008**, 7, 613.
29. A. Fujishima, K. Hashimoto and T. Watanabe, Photocatalysis: fundamentals and applications; BKC, Tokyo, **1999**.
30. U. Diebold, N. Ruzycki, G. S. Herman and A. Selloni, Catal. Today, **2003**, 85, 93.
31. L. Kavan, M. Grätzel, S. E. Gilbert, C. Klemenz and H. J. Scheel, J. Am. Chem. Soc., **1996**, 118, 6716.
32. T. Ohno, K. Sarakawa and M. Matsumura, New J. Chem., **2002**, 26, 1167.
33. T. Taguchi, Y. Saito, K. Sarukawa, T. Ohno and M. Matsumura, New J. Chem., **2003**, 27, 1304.
34. H. G. Yang, G. Liu, S. Z. Qiao, C. H. Sun, Y. G. Jin, S. C. Smith, J. Zou, H. M. Cheng and G Q. M. Lu, J. Am. Chem. Soc., **2009**, 131, 4078.
35. H. Hsutomu and Y. Nosaka, Langmuir, **2002**, 18, 3247.
36. J. C. Yu, J. Yu, W. Ho, Z. Jiang and L. Zhang, Chem. Mater., **2002**, 14, 3808.
37. F. Amano, O. O. Prieto-Mahaney, Y. Terada, T. Yasumoto, T. Shibayama and B. Ohtani, Chem. Mater., **2009**, 21, 2601.
38. B. Ohtani, F. Amano, T. Yasumoto, O. O. Prieto-Mahaney, S. Uchida, T. Shibayama and Y. Terada, Top. Catal., **2010**, 53, 455.
39. O. O. Prieto-Mahaney, N. Murakami, R. Abe and B. Ohtani, Chem. Lett., **2009**, 38, 238.
40. B. Ohtani, O. O. Prieto-Mahaney, F. Amano, N. Murakami and R. Abe, J. Adv. Oxid. Technol., **2010**, 13, 247.
41. A. Fujishima, T. N. Rao and D. A. Tryk, J. Photochem. Photobiol. C, **2000**, 1.
42. I. Moriguchi, H. Maeda, Y. Teraoka and S. Kagawa, Chem. Mater., **1997**, 9, 1050.
43. H. Hidaka, K. Ajisaka, S. Horikoshi, T. Oyamab, K. Takeuchi, J. Zhaoc and N. Serpone, J. Photochem. Photobiol. A: Chem., **2001**, 138, 1852.

44. I. M. Arabatzis, S. Antonaraki, T. Stergiopoulos, A. Hiskia, E. Papaconstantinou, M. C. Bernard and P. Falaras, J. Photochem. Photobiol. A: Chem, **2002**, 149, 237.
45. S. C. Leen, J. H. Lee, T. S. Oh and Y. H. Kim, Sol. Energy Mater. Sol. Cells, **2003**, 75, 481.
46. A. I. Kontos, I. M. Arabatzis, D. S. Tsoukleris, A. G. Kontos, M. C. Bernard, D. E. Petrakis and P. Falaras, Catal. Today, **2005**, 101, 275.
47. J. O. Carneiro, V. Teixeira, A. Portinha, A. Magalhaes, P. Coutinho, C. J. Tavares and R. Newton, Mater. Sci. Eng. B, **2007**, 138, 144.
48. X Chen and S. S. MaO, Chem. Rev., **2007**, 107, 2891.
49. W. Y. Choi, A. Termin and M. R. Hoffman, Angew. Chem. Int. Ed., **1994**, 33, 1091.
50. W. Y. Choi, A. Termin and M. R. Hoffman, J. Phys. Chem., **1994**, 98, 13669.
51. Y. Cao, W. Yang, W. Zhang, G. Liu and P. Yue, New J. Chem., **2004**, 28, 218.
52. X. H. Wang, J. G. Li, H. Kamiyama, M. Katada, N. Ohashi, Y. Moriyoshi and T. Ishigaki, J. Am. Chem. Soc., **2005**, 127, 10982.
53. S. Karvinen, P. Hirva and T. A. Pakkanen, J. Mol. Struct.-Theochem, **2003**, 626, 271.
54. J. M. Herrmann, J. Disdier and P. Pichat, Chem. Phys. Lett., **1984**, 6, 618.
55. V. Subramanian, E. E. Wolf and P. V. Kamat, J. Am. Chem. Soc., **2004**, 126, 4943.
56. E. Kowalska, O. O. Prieto-Mahaney, R. Abe and B. Ohtani, Phys. Chem. Chem. Phys., **2010**, 12, 2344.
57. X. Z. Li and F. B. Li., Environ. Sci. Technol., **2001**, 35, 2381.
58. Z. Yuan and L. Zhangb, J. Mater. Chem., **2001**, 11, 1265.
59. S. Hotchandani and H. V. Kamat, J. Phys. Chem., **1992**, 96, 6834.
60. P. Cheng, W. Li, T. Zhou, Y. Jin and M. Gu, J. Photochem. Photobiol. A: Chem., **2004**, 168, 97.
61. S. Sakthivel , S. U. Geissen , D. W. Bahnemann, V. Murugesan and A. Vogelpohl, J. Photochem. Photobiol. A: Chem., **2002**, 148, 283.
62. J. Zhu, D. Yang, J. Geng, D. Chen and Z. Jiang, J. Nanopart. Res., **2008**, 10, 729.
63. Y. Bessekhouad, N. Chaoui, M. Trzpit, N. Ghazzal, D. Robert and J. V. Weber, J. Photochem. Photobiol. A: Chem., **2006**, 183, 218.
64. A. G. Agrios and P. Pichat, J. Appl. Electrochem., **2005**, 35, 655.
65. D. Zhao, C. Chen, C. Yu, W. Ma and J. Zhao, J. Phys. Chem. C, **2009**, 113, 13160.

66. G. Li, D. Zhang and J. C. Yu, Phys. Chem. Chem. Phys., **2009**, 11, 3775.
67. R. Asahi, T. Morikawa, T. Ohwaki, K. Aoki and Y. Taga, Science, **2001**, 293, 269.
68. H. Irie, Y. Watanabe and K. Hashimoto, J. Phys. Chem. B, **2003**, 107, 5483.
69. T. Umebayashi, T. Yamaki, H. Itoh and K. Asai, Appl. Phys. Lett., **2002**, 81, 454.
70. T. Ohno, T. Mitsui and M. Matsumura, Chem. Lett., **2003**, 32, 364.
71. H. Irie, Y. Watanabe and K. Hashimoto, Chem. Lett., **2003**, 32, 772.
72. Y. Zhao, X. Qiu and C. Burda, Chem. Mater., **2008**, 20, 2629.
73. V. N. Kuznetsov and N. Serpone, J. Phys. Chem. B, **2006**, 110, 25203.
74. C. Di Valentin, E. Finazzi, G. Pacchioni, A. Selloni, S. Livraghi, M. C. Paganini and E. Giamello, Chem. Phys., **2007**, 339, 44.
75. J. Graciani, L. J. Alvarez, J. A. Rodriguez and J. F. Sanz, J. Phys. Chem. C, **2008**, 112, 2624.
76. M. Gratzel, Nature, **2001**, 414, 338-344.
77. A. Hagfeldt and M. Gratzel, Chem. Rev., **1995**, 95, 49.
78. C. J. Meyer, Inorg. Chem., **2005**, 44, 6852.
79. Q. Wang, C. Chen, W. Ma, H. Zhu and J. Zhao, Chem Eur. J., **2009**, 15, 4765.
80. R. Nakamura, T. Tanaka and Y. Nakato, J. Phys. Chem. B, **2004**, 108, 10617.
81. M. Mrowetz, W. Balcerski, A. J. Colussi and M. R. Hoffmann, J. Phys. Chem. B, **2004**, 108, 17269.
82. N. Murakami, T. Chiyoya, T. Tsubota and T. Ohno, Appl. Catal. A, **2008**, 348, 148.
83. N. Murakami, A. Ono, M. Nakamura, T. Tsubota and T. Ohno, Appl. Catal. B, **2010**, 97, 115.
84. H. Yu, H. Irie, Y. Shimodaira, Y. Hosogi, Y. Kuroda, M. Miyauchi and K. Hashimoto, J. Phys. Chem. C, **2010**, 114, 16481.
85. H. Irie, K. Kamiya, T. Shibanuma, S. Miura, D. A. Tryk, T. Yokoyama and K. Hashimoto, J. Phys. Chem. C, **2009**, 113, 10761.
86. H. Irie, T. Shibanuma, K. Kamiya, S. Miura, T. Yokoyama and K. Hashimoto, Appl. Catal. B, **2010**, 96, 142.
87. H. Tada, Q. Jin, H. Nishijima, H. Yamamoto, M. Fujishima, S. Okuoka, T. Hattori, Y. Sumida and H. Kobayashi, Angew. Chem. Int. Ed., **2011**, 50, 3501.
88. Q. Jin, M. Fujishima and H. Tada, J. Phys. Chem. C, **2011**, 115, 6478.
89. H. Irie, S. Miura, R. Nakamura and K. Hashimoto, Chem. Lett., **2008**, 37, 252.

Chapter 3

Sol-gel synthesis and characterisation techniques

Different strategies such as sol-gel, micelle and inverse micelle, hydrothermal, solvothermal, direct oxidation, chemical vapour deposition, flame spray pyrolysis electrodeposition, sonochemical and microwave methods have been proposed to synthesise TiO_2 materials for photocatalytic applications.[1]

Among all these techniques, the sol-gel method is the most commonly used due to its relatively low cost and great flexibility. This technique has been chosen for the preparation of home-made doped TiO_2 samples, which have been investigated during this PhD thesis (Chapters 7-10).

3.1 Sol-gel process

Sol and gels are two forms of matter in colloidal state, which are either available in nature (milk, serum) or prepared by chemical synthesis. The activity for synthesizing inorganic materials by sol – gel processes began in 1846 with Ebelman's discovery of SiO_2 formation upon hydrolysis of tetraethylorthosilicate (TEOS) under acidic conditions.[2] In 1864, studies on the structure of inorganic gels confirmed that a gel consisted of a solid network with continuous porosity (three dimensional molecular network). In the mid-1970s the interest in sol – gel process increased significantly when monoliths were produced by carefully drying the gel.[3]

Nowadays, the sol – gel process is used to prepare various types of materials, which are implemented into a variety of technologies, such as nonlinear optical devices, luminescent solar concentrators and chemical sensors.

The sol - gel method is based on inorganic polymerization reactions, involving four basic steps: *hydrolysis, polycondensation, drying and thermal decomposition of precursors*. These are, usually, inorganic metal salts or metal organic compounds such as metal alkoxides $M(OR)_n$ or oxoalkoxides $MO(RN)_n$, where R is associated with saturated or unsaturated aryl or alkyl groups, in some cases with β-diketonates (RCOCHCOR') or metal carboxylates $M(O_2CR)_n$.[4] When specifically preparing TiO_2-based materials by sol-gel method, titanium alkoxide (*e.g.* titanium tetraisopropoxide) is often used as a precursor.

The general mechanisms in the metal-organic route are based on the growth of metal oxo-polymers in a solvent. The main reactions at work can be divided into two steps:

1. first step: hydroxylation upon the hydrolysis of alkoxy groups

   $M\text{-}OR + H_2O \rightarrow M\text{-}OH + R\text{-}OH$ (3.1)

2. second step: polycondensation due to water (a) and/or alcohol (b) condensation

   $M\text{-}OH + HO\text{-}M \rightarrow M\text{-}O\text{-}M + H_2O$ (3.2)

   $M\text{-}OH + RO\text{-}M \rightarrow M\text{-}O\text{-}M + ROH$ (3.3)

Generally speaking, the hydrolysis reaction, through the addition of water replaces alkoxide groups (OR) with hydroxyl groups (OH). Subsequent condensation reactions involving the M-OH groups produce M-O-M bonds plus the by-products water or alcohol. Additionally, because water and alkoxides are immiscible, the use of a mutual solvent such as an alcohol is necessary. With the presence of this homogenizing agent, *i.e.* the alcohol, hydrolysis is facilitated due to the miscibility of the alkoxide and water.[5]

Several parameters, such as type of precursor, type of solvent, water content, pH, concentration of precursor and temperature, can influence the structure of the initial gel, and, in turn, the properties of the resulting materials, including the crystal structure, particle size, shape and crystallinity.[6-19]

In particular hydrolysis and polycondensation reactions, which are the main paths during the sol-gel reaction, may be strongly promoted by either acid or alkaline pH. Examples will be reported below with reference to the formation of SiO_2, but the invoked mechanisms are general and can be apply to any other oxide.

Under <u>acid conditions</u>, *e.g.* with mineral acids, the hydrolysis reaction is speeded up more efficiently than the condensation reaction:[5,20-22]

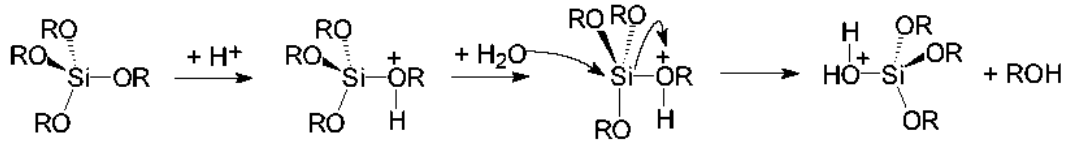

protonation of the alkoxo group, making alcohol a better leaving group

Condensation involves the attack of silicon atoms carrying protonated silanol species by neutral ≡Si-OH nucleophiles.

→ acid conditions promote the formation of protonated silanol species, but inhibit some nucleophiles;

→ the most basic silanol species (expected to be protonated) are those contained in monomers or weakly branched oligomers: so a bushy network of weakly branched polymers is obtained.

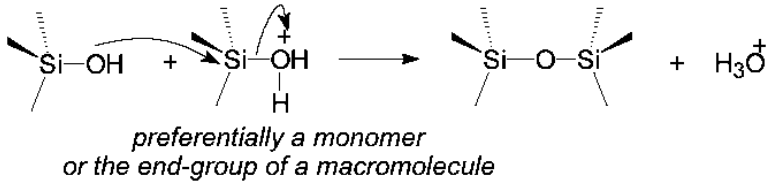

Under basic conditions, *e.g.* with ammonia, hydroxyl anions (OH^-) and deprotonated silanol (≡Si-O^-) are better nucleophiles than water and silanol species; a fast attack at the silicon atom and both hydrolysis and condensation reactions occur simultaneously. The condensation involves the attack of a deprotonated silanol (≡Si-O^-) on a neutral siloxane species; the acidity of silanol increases when -OH or -OR groups are replaced with -O-Si≡ groups because of the reduced electron density on the Si atom:[5,20-22]

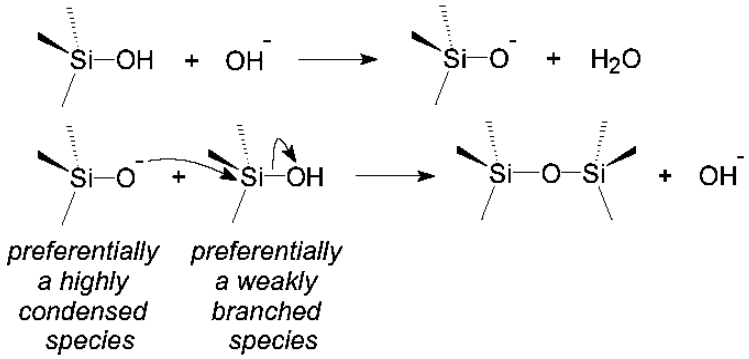

The result of basic catalysis is an aggregation (monomer-cluster) that leads to more compact highly branched silica networks, that are not interpenetrable before drying and thus behave as discrete species.

The gel, which is a solid matrix containing the solvent, needs to be dried in order to remove the solvent. The period between the formation of the gel and its drying is known as ageing, during which the gel may keep undergoing the hydrolysis or the condensation. The ageing step is crucial to obtain an increase of the strength of the gel without changing the pore structure and an increase of the pore size while reducing the surface area through dissolution and riprecipitation of the particles.

Drying is the following step in the sol–gel process, which is necessary in order to remove the solvent from the gel-network. The methods adopted for the elimination of the residual solvent are influenced by the specific use of the dried material. The choice of how to perform the solvent removal is not trivial especially in the case of an oxide

where the surface state is ruling the reactivity. Further, the solvent elimination route might affect not only the surface features, but also the bulk and the morphological characteristics of the powders.[23-27] In particular there are three main procedures. The gels can be dried: 1) by heating in oven (xerogels); 2) by freeze drying (cryogels); 3) by reaching supercritical solvent conditions in autoclave (aerogels).

Finally a calcination step (thermal treatment), in a different temperature range, is necessary in order to convert the dried gel to a crystalline material. During this procedure the following reactions can occur:

- desorption of physically adsorbed solvent and water molecules from the walls of micropores (100-200 °C);
- decomposition of residual organic groups into CO_2 (300-500 °C);
- collapse of small pores (400-500 °C);
- collapse of larger pores (700-900 °C);
- persistent polycondensation (100-700 °C).

Sintering and densification phenomena also take place, *via* typical sintering mechanisms, such as evaporation condensation, surface diffusion, grain boundary and bulk diffusion. The small particle size of the powders leads to high reactivities and enhanced sintering and/or coarsening rates.

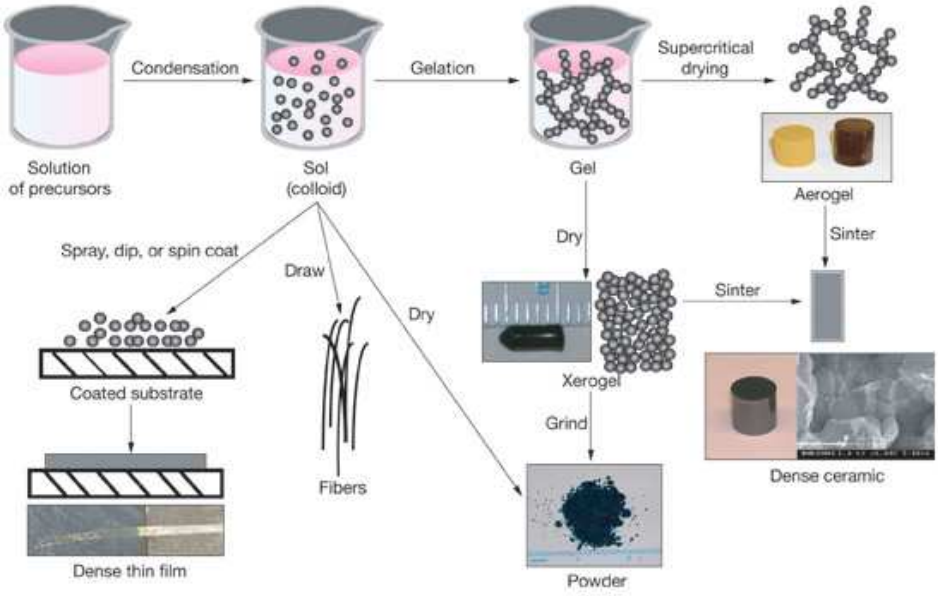

Figure 3.1 Schematic overview of the sol-gel process.[4]

The sol-gel approach has numerous advantages. For instance, it allows tailoring of both the bulk properties (such as phase composition) and the surface characteristics (such as the surface area, the total pore volume distribution, etc) of a material on a nanometer scale from the earliest stages of processing.

Moreover this technique permits:

- the production of new hybrid organic–inorganic materials, which do not exist in nature;
- the synthesis of high purity products (submicron powders, nuclear fuels, electronic and ionic conductors, magnetic materials) because organometallic alkoxy precursors can be purified by distillation or recrystallisation;
- the use of low temperature in the first step of the process, so that thermally labile compounds can be entrapped in the sol–gel matrix;
- the production of different physical forms (fibers, monoliths, coatings, powder) by modifying few experimental parameters (Fig. 3.2).

The main drawbacks consist in the possible high cost for the majority of alkoxide precursors and in the long processing steps.

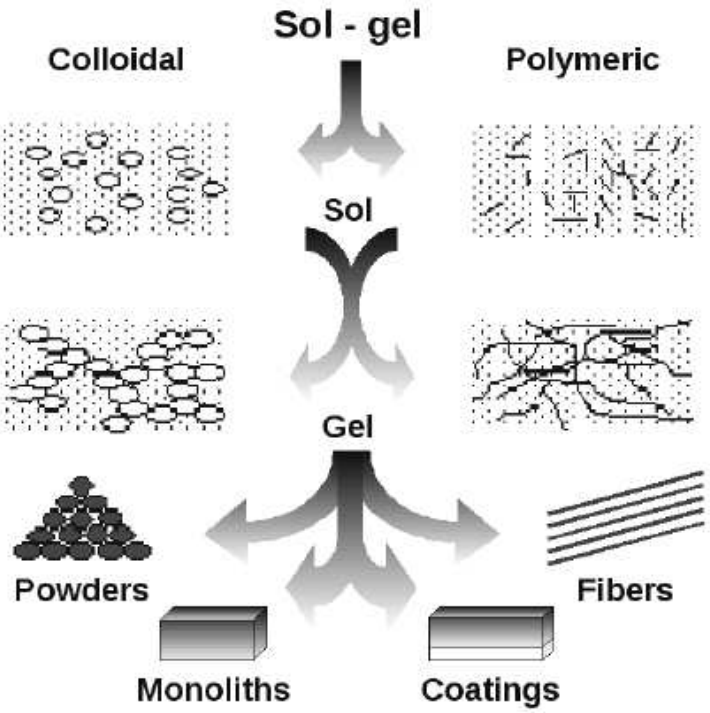

Figure 3.2 Schematic view of the different physical forms obtained by sol–gel synthesis.

3.2 X-ray Powder Diffraction (XRPD)

X-ray powder diffraction (XRPD) is a non-destructive analytical technique widely applied for the characterization of crystalline materials.[28-31] This method has been traditionally used for phase identification, quantitative analysis and the determination of structure imperfections of powdered solid samples.

Powder diffraction is commonly used to identify unknown substances, by comparing diffraction data with those in the international data base. In fact each crystalline solid produces distinctive diffraction patterns. The technique may be also useful to characterize heterogeneous solid mixtures, to determine relative abundance of crystalline compounds and, if coupled with one of the refinement techniques (*e.g.* the Rietveld refinement), can provide quantitative structural information.

When a monochromatic X-ray beam passes through a crystalline sample, it interacts with the electrons in the atoms, resulting in scattering of the radiation. If the matter is crystalline, *i.e.* the atoms are organized in planes and the distances between the atoms are of the same magnitude as the X-rays wavelength, constructive and destructive interference will occur. The process of diffraction is described in terms of incident and reflected (or diffracted) rays, each forming an angle, θ, with a fixed crystal plane.

In particular, when the interaction of the incident rays with the sample produces constructive interference (Fig. 3.3), the diffraction phenomena satisfy the so-called Bragg law:[32]

$$n\lambda = 2\,d\,\mathrm{sen}\theta \qquad (3.4)$$

where:

λ = incident light wavelength.

n = integer positive number (0,1,2,3, etc.).

d = interplane spacing.

θ = angle between the incident radiation and the planes (h k l).

The incident angle is chosen by rotating the crystal relative to the beam, the wavelength is fixed and thus the interplanar spacing d is obtained. The conclusion is that any set of planes in a crystal will reflect an X-ray beam if the set of planes is at right angle to the incident beam. But there arises another question, whether the planes will reflect the beam strongly or not.

The intensity of the reflected beam is proportional to the product of the intensity of the incident beam and the concentration of electrons in the reflecting plane. Thus if the

unit cell dimensions are known and, subsequently, the atomic number of each of the atoms, it is possible to calculate the concentration of electrons and hence the intensity of the reflected beam.

Now considering the reverse situation, if the size of the unit cell and the intensities of the reflections are known, the positions of atoms and also the relative number of electrons per atom are found. It is obvious that all compounds with different formula or unit cells have different collections of d-spacings and different intensities of reflections. The observed patterns of spacings and intensities can thus be used to identify an unknown compound in a specific crystalline phase.

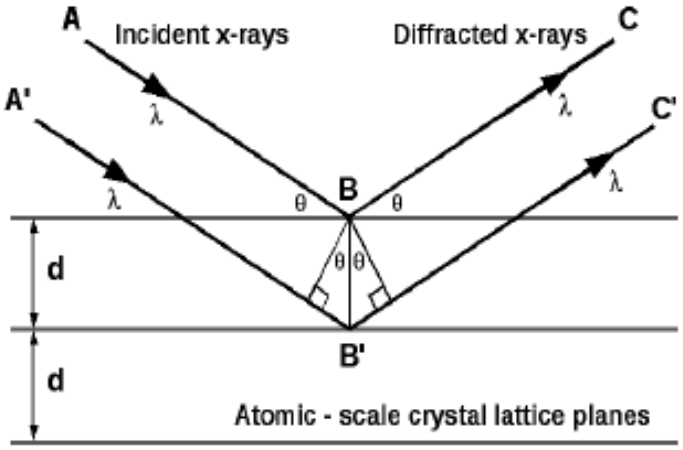

Figure 3.3 Bragg's Law for X-ray diffraction. The diffracted X-rays exhibit constructive interference when the distance between paths ABC and A'B'C' differs by an integer number of wavelengths (λ).[32]

In powder diffraction it's important to have samples with a smooth plane surface, with the crystallites randomly distributed.

The powder sample is filled in a small disc and placed in the analysis equipment. The monochromatic X-ray source is placed on a rotating arm, in order to light the sample with a variable angle θ. The reflected radiation is collected by the detector, even fixed on a rotating arm, placed at twice this angle. As 2θ is the angle measured between the detector and the incident beam, as shown in Fig. 3.4, the diffracted radiation is collected by the detector at the very same incident angle θ.

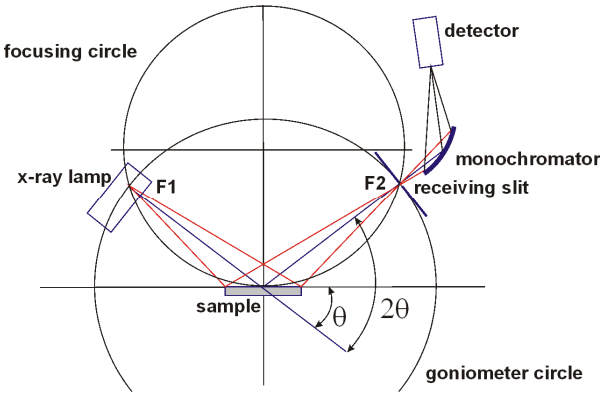

Figure 3.4 Schematic diagram of an X-ray diffractometer.

A typical diffraction pattern consists of a plot of reflected intensities versus the detecting angle 2θ. Comparing the results with the data base of organic and inorganic spectra leads to the determination of the analyzed species.

In particular in this work XRPD patterns of all investigated photocatalysts were collected using a Philips PW3020 powder diffractometer, operating at 40 kV and 40 mA, employing filtered Cu Kα radiation (λ = 1.54056 Å) as X-ray source. The diffractograms were recorded by continuous scanning between 15.025° and 99.975° (2θ) angles, with a step of 0.05°. Quantitative phase analysis was made by the Rietveld refinement method,[33-35] using the ‘‘Quanto” software.[36]

Moreover from XRPD patterns, crystallite sizes can be calculated. Generally as the size of the crystallite decreases, the angular spread of the reflection increases. In this thesis the value of the FWHM (full width at half maximum) of the most intensive line of each phase was used in order to measure the mean particle (crystallite) size, by applying the Scherrer formula:

$$d_{hkl} = \frac{0.9\lambda}{\beta \cos\theta} \qquad (3.5)$$

where:

$d_{(hkl)}$ = size (nm) of particles in the direction vertical to the corresponding lattice plane.

λ = X-ray incident wavelength.

β = line broadening at half maximum intensity (FWHM) expressed in rad.

θ = incident angle.

This formula is quite satisfactory for studies comparing the crystallite sizes of a number of samples belonging to a related series, but it should be used with caution when sizes of best absolute accuracy are needed. In this regard the Sherrer equation shows two main limitations:

1. the numerical value of the shape factor K for spheres has been approximated to 0.9.[37]
2. the pure diffraction width of the sample, β, does not directly correspond to that of the observed peak, because of instrumental aberrations (broadening due to the optical path in the diffract-meter). In order to solve this problem Warren proposed the following equation:[38,39]

   $$B^2 = \beta^2 + b^2 \qquad (3.6)$$

   according to which the squared breadth of the observed peak (B^2) equals the sum of the squares of breadths of the pure diffraction profile (β^2) and the profile of the instrumental broadening (b^2). The instrumental broadening is usually evaluated by means of the spectrum of a standard Si powder.

   Equation (3.6) yields a most convenient and sufficiently reliable means for correcting observed line breadths for instrumental broadening, when the primary purpose is the comparison of crystallite sizes and not the evaluation of absolute dimensions. The Sherrer equation is limited to nano-scale particles. It is not used for grains larger that 0.1 μm because in that situation pure diffraction breadth becomes negligibly small in comparison with the breadth due to the experimental arrangement.

   Furthermore broadening of FWHM of XRPD peaks is also induced by distortion of the crystalline lattice. The Williamson–Hall equation includes this, as well as the effect of particle size.[40] In other words, Scherrer's equation neglects the effect of crystal lattice distortion. So, for samples that are expected to have a large degree of distortion, analyses using the Williamson–Hall equation should be carried out. Anyway it's strongly recommended to compare the particles size results calculated from XRPD data with those obtained by using other techniques, such as transmission or scanning electron microscopy.

Finally a few critical aspects related to the use of XRPD analysis in photocatalysis field of research merit to be outlined. One of the limitation of XRPD analyses is that

only crystalline phases can be detected, while the amorphous component, if present in samples, exhibits no diffraction peaks. Actually there are no reports showing a quantitative determination of the amorphous content. Thus, the amorphous content should be determined as a remaining of the crystalline part and therefore an accurate determination of the crystalline content is necessary. In principle, XRPD peak intensity is proportional to the content of the corresponding crystallites, but a problem is how to get global standard samples of each crystalline phase, because smaller crystallites may exhibit lower peak intensity.[41] In this regard an accurate analysis of crystalline content (including amorphous component determination) can be guaranteed when pure crystalline particles included in a sample are chemically extracted (from the original sample) and used for making an XRPD calibration curve[42,43] based on the assumption that crystallites and amorphous particles are separated, *i.e.* not in the form of, for example, a core–shell structure (Fig. 3.5). In fact, if a sample particle is made by a core–shell structure, a precise determination of the crystalline content may be very difficult.

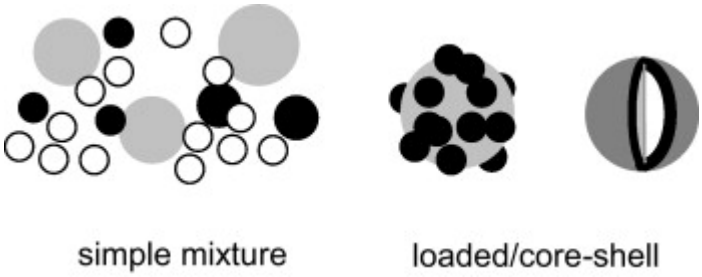

Figure 3.5 Representative patterns of mixture of crystallites (white and gray particles) and amorphous parts (black).[46]

Confusion regarding the term “crystallinity” arises because the term is discussed on the basis of sharpness of an XRPD peak, *e.g.* “Sharpness of the peak indicates higher crystallinity of a photocatalyst.” Since the width of an XRPD peak reflects the size of a particle, as previously described for the Sherrer equation, peak sharpness shows the size of crystallites. In this sense, “crystallinity” is used to show how crystallites grow to be larger sized particles.

Another use of the term “crystallinity” is to show perfectness of crystals, *i.e.* higher crystallinity means lower density of crystalline defects. Assuming that larger crystallites are expected to contain a lower density of crystalline defects, the sharpness

of XRPD peaks can also be a relative/indirect measure of this second meaning of "crystallinity".

3.3 X-ray Photoelectron Spectroscopy (XPS)

X-ray Photoelectron Spectroscopy is a surface chemical analysis technique based on monitoring the energy of electrons emitted by a system under stimulation of X-rays.[44] Traditionally, when the technique has been used for surface studies it has been subdivided according to the source of exciting radiation into:

- X-ray Photoelectron Spectroscopy (XPS) using soft X-ray (200-2000 eV) radiation to examine core levels;
- Ultraviolet Photoelectron Spectroscopy (UPS) using vacuum UV (10-45 eV) radiation to examine valence levels;
- The development of synchrotron radiation sources has enabled high resolution studies to be carried out with radiation spanning a much wider and more complete energy range (5-5000 eV), but such type of analysis is, and will remain, a minority of all photoelectron studies due to the expense, complexity and limited availability of such sources.

Photoelectron spectroscopy is based upon a single photon in/electron out process. The energy of a photon is given by the Einstein relation:

$$E = h\nu \tag{3.7}$$

where h is the Planck constant ($6.62 \cdot 10^{-34}$ J·s), and ν is the frequency (Hz) of the radiation.

Photoelectron spectroscopy uses monochromatic sources of radiation (*i.e.* photons of fixed energy). In XPS the photon is absorbed by an atom in a molecule or solid, leading to ionization and the emission of a core (inner shell) electron. By contrast, in UPS the photon interacts with valence levels of the molecule or solid, leading to ionisation by removal of one of these valence electrons. The kinetic energy distribution of the emitted photoelectrons (*i.e.* the number of emitted photoelectrons as a function of their kinetic energy) can be measured using any appropriate electron energy analyser and a photoelectron spectrum can thus be recorded.

Knowing the kinetic energy of the emitted electrons (KE), the electron binding energy (BE) of each of the emitted electrons can be determined as a difference between the energy of the primary photon (hν) and the kinetic energy of the photoelectron:

$$KE = h\nu - BE \quad (3.8a)$$

The positions of the peaks in the XPS spectrum plotted as emission intensity *vs.* the electron binding energy gives the information about the atomic composition of the sample surface. Furthermore, the intensity of the peaks is related to the concentration of the element within the sampled region. Thus, the technique provides a quantitative analysis of the surface composition and is sometimes known by the alternative acronym, ESCA (Electron Spectroscopy for Chemical Analysis).

The most commonly employed X-ray sources are those giving rise to:

Mg K_α radiation: hν = 1253.6 eV

Al K_α radiation: hν= 1486.6 eV

The emitted photoelectrons will therefore have kinetic energies in the range of *ca*. 0-1250 eV or 0-1480 eV .

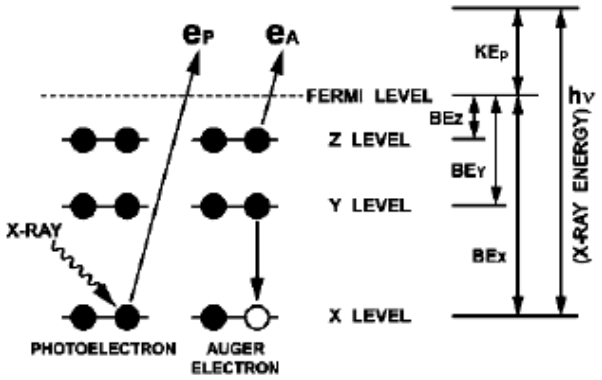

Figure 3.6 Photoelectron (e_P) and Auger electron (e_A) emission processes induced by X–rays.[44]

It's worth to note that, as schematically depicted in Fig. 3.6, the binding energies (BE) of energy levels in solids are conventionally measured with respect to the Fermi level of the solid, rather than the vacuum level. This involves a necessary correction to the equation given above in order to account for the work function (Φ) of the solid, as described by the following relation:

$$KE = h\nu - BE - \Phi \quad (3.8b)$$

The exact binding energy of an electron depends not only upon the level from which photoemission is occurring, but also upon:

1. the formal oxidation state of the atom;
2. the local chemical and physical environment.

Changes in either (1) or (2) give rise to small shifts in the peak positions in the spectrum, so-called *chemical shifts*. Such shifts are readily observable and interpretable in XPS spectra because the technique:

- is of high intrinsic resolution (as core levels are discrete and generally of a well-defined energy);
- is a one electron process (thus simplifying the interpretation).

Atoms of a higher positive oxidation state exhibit a higher binding energy due to the extra coulombic interaction between the photo-emitted electron and the ion core. This ability to discriminate between different oxidation states and chemical environments is one of the major strengths of XPS technique.

In practice, the ability to resolve between atoms exhibiting slightly different chemical shifts is limited by the peak widths which are governed by a combination of factors, in particular:

- the intrinsic width of the initial level and the lifetime of the final state;
- the line-width of the incident radiation - which for traditional X-ray sources can only be improved by using X-ray monochromators;
- the resolving power of the electron-energy analyser.

Finally the basic requirements for a photoemission experiment (XPS or UPS) are:

1. a source of fixed-energy radiation (an X-ray source for XPS or, typically, a He discharge lamp for UPS);
2. an electron energy analyser (which can disperse the emitted electrons according to their kinetic energy, and thereby measure the flux of emitted electrons of a particular energy);
3. a high vacuum environment (to enable the emitted photoelectrons to be analysed without interference from gas phase collisions).

Such a system is illustrated schematically in Fig. 3.7. There are many different designs of electron energy analyser but the preferred option for photoemission experiments is a concentric hemispherical analyser (CHA), which uses an electric field

between two hemispherical surfaces to disperse the electrons according to their kinetic energy.

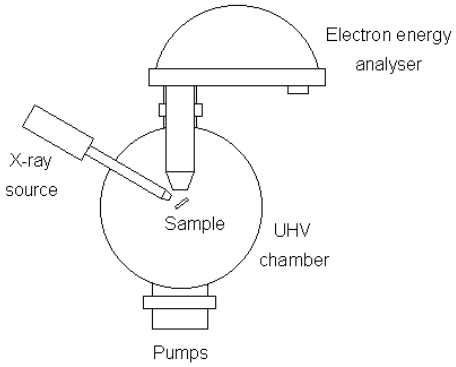

Figure 3.7 Basic scheme of XPS instrumentation.

3.4 UV-vis Diffuse Reflectance Spectroscopy (DRS UV-vis)

Diffuse Reflectance Spectroscopy is based on the interaction between a UV or visible beam and a powdered sample, from which the beam can be reflected in all directions. Only the fraction of beam which is scattered within a sample and returned to the surface is considered to be a diffuse reflection. All the reflected radiation can thus be collected within an integrating sphere, enhancing the signal-to noise ratio. The internal walls of the sphere are usually covered with barium sulfide, a compound that ensures a reflectivity greater than 0.98 in the UV-vis light region. Moreover the reflectance spectrum of a reference standard ($BaSO_4$) should always be recorded prior to that of any other sample.

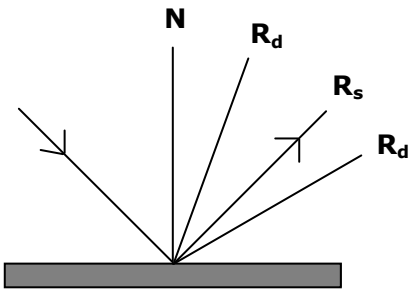

Figure 3.8 Schematic representation of the radiation interaction with the sample; R_s stands for the specular reflected beam, R_d for the diffuse reflected beam.

It's clear that the raw diffuse reflectance spectrum is different from its equivalent absorption due to the multiple surface reflections of the powder grain. At the same time

photoabsorption is one of the most significant steps in photocatalysis and the estimation of the number (or flux) of absorbed photons is an important fundamental experiment, considering the first law of photochemistry,[45] *i.e.* light must be absorbed by a chemical substance in order to promote a photochemical reaction. However, it's still rather difficult to get accurate expressions of photoabsorption spectra of solid materials.

In the literature on photocatalysis, a photoabsorption spectrum, *i.e.* a plot of the absorption extent as a function of wavelength, is usually reported in terms of absorbance units or Kubelka–Munk function. The former, *i.e.* absorbance, is traditionally defined as $\log(I_0/I)$, where I_0 and I are the intensities of incident and transmitted light, respectively. Otherwise when photoabsorption is measured in a reflection mode, I can be considered the reflection intensity, while I_0 represents the reflection of a 'standard material', such as $BaSO_4$, which can reflect all the incident light, *i.e.* 100% reflection. In this regard the Kubelka-Munk (KM) function, usually employed for samples diluted with a medium of less photoabsorption, is otherwise defined as follows:

$$F(R_\infty) = \frac{(1-R_\infty)^2}{2R_\infty} = \frac{\alpha}{s} \tag{3.9}$$

where R_∞, α and s are the diffuse reflectance (I/I_0), the absorption coefficient in cm^{-1} units and the scattering factor, respectively.

The use of absorbance units for measurements performed in reflectance mode is not correct, since absorbance can be defined for the case where extinction of light intensity is assumed to be induced only by photoabsorption and not by scattering.

Moreover, as pointed out by Ohtani in a recent review,[46] both these kinds of absorption expressions are not appropriate as a measure of absorbed light intensity. Absorbance and K-M units are mainly proportional to the concentration of a given material dispersed in a homogeneous medium (liquid or solid matrix), but not to the number of photons absorbed by a solid sample. This is easily understood by the fact that absorbance values equal to 1 and 2 correspond to 90 and 99% absorption of incident light. In order to calculate the extent of photoabsorption of a solid sample, it's thus strongly recommended to measure absorption which can be calculated as (1-R), where R represents the diffuse reflectance value.

In photocatalysis, especially when dealing with doped materials, extremely important is to estimate the optical absorption edge energy of a semiconductor material. The optical absorption edge energy is the minimum photon energy required to promote electrons from the highest occupied molecular orbital (HOMO) to the lowest unoccupied molecular orbital (LUMO). Two basic types of electronic transitions are distinguished, *i.e.* direct and indirect.[47] Direct transitions demand only the excitation of electrons by photons, while indirect transitions require additionally concerted vibrations and energy from the crystal lattice (phonons). The electron energy near the absorption edge in the case of semiconductors is given by:[48]

$$\alpha = \frac{(h\nu - E_g)^{\eta}}{h\nu} \tag{3.10}$$

where α is the absorption coefficient, h*ν* is the energy of the incident photon and E_g is the optical absorption edge energy. The variable η depends on the type of the optical transition caused by photon absorption. In crystalline semiconductors η can assume the following values:

- 1/2 when the transition is direct-allowed
- 3/2 when the transition is direct-forbidden
- 2 when the transition is indirect-allowed
- 3 when the transition is indirect-forbidden

In the case of amorphous, homogeneous semiconductors η is 2 independently of the type of transition.[49] In case of TiO_2, η = 2 is usually considered.

Experimental diffuse reflectance data cannot be used directly to measure absorption coefficients (α) because of scattering contributions to the reflectance spectra. Scattering coefficient s, however, depends weakly on energy and $F(R_\infty)$ can be considered to be proportional to the absorption coefficient within the narrow range of energy containing the absorption edge features. In such way, the determination of the absorption edge energy can be estimated from the $(F(R_\infty)\cdot h\nu)^{1/\eta}$ versus h*ν* plot. In particular the experimental band gap value can be obtained from the x-intercept of the straight tangent line to this plot.

Figure 3.9 shows an example of the above-mentioned analysis for a well-crystallized rutile titania.[46] In this case the linearity of $(F(R_\infty)\cdot h\nu)^{1/\eta}$ versus h*ν* plots has been checked for both allowed direct or indirect modes of transition.

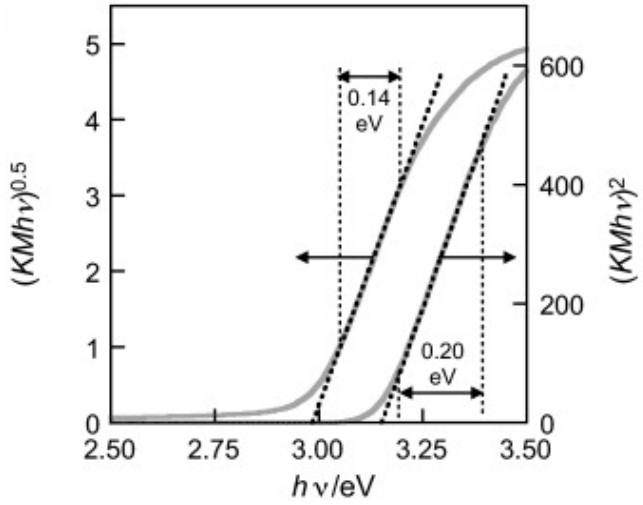

Figure 3.9 Two kinds of plot for the determination of band gap energy (E_g) of rutile titania. Assumptions of indirect (left) and direct (right) allowed transitions give band gaps of 3.00 and 3.14 eV, respectively.[46]

We can note that these plots show a quite similar extent of linearity, that is 0.14 eV and 0.20 eV for indirect and direct transition, respectively. Moreover their x-intercepts, 3.00 and 3.14 eV, are expression of the corresponding optical band gap.

In this regard the real difficulty that this approach encounters in the calculation of experimental band gap values has been recently recognized.[46] In fact, the range of the linear part of the plots (Fig. 3.9) seems to be arbitrarily chosen and there seem to be no absolute ways/rules to discriminate the effective transition mode and to find reasonable data on semiconductor band gap energy. Moreover the absorption spectra, especially of doped materials, can be strongly affected by the presence of impurities or surface states. Therefore, discrimination of real narrowing of the semiconductor band gap from absorption originated by bulk or surface modification is rather difficult.

3.5 Surface area and pore structure evaluation by gas adsorption

Surface area and porosity are important parameters in powdered materials. The most widely used techniques for estimating surface area are based on physical adsorption of gas molecules on a solid surface.

Generally gas adsorption on solid surfaces and in the pore spaces is a complex phenomenon involving mass and energy interaction and phase changes. Depending upon the strength of the interaction, all adsorption processes can be divided into the two

categories of chemical or physical adsorption. The former, also called irreversible or chemisorption, is characterized mainly by large interaction potentials, which lead to high heats of adsorption often approaching the values of chemical bonds. This fact, coupled with other spectroscopic, electron spin resonance, and magnetic susceptibility measurements, confirms that chemisorption involves true chemical bonding of the gas or vapour with the surface. Because chemisorption occurs through chemical bonding, it is often found to occur at temperatures above the adsorbates' critical temperature. Strong bonding to the surface is necessary, in the presence of higher thermal energies, if adsorption has to occur at all. Also, as it is true for most chemical reactions, chemisorption is usually associated with an activation energy. In addition, chemisorption is necessarily restricted to, at most, a single layer of chemically bound adsorbate at the surface.

Another important factor relating to chemisorption is that the adsorbed molecules are localized on the surface. Because of the formation of a chemical bond between an adsorbate molecule and a specific site on the surface, the adsorbate is not free to migrate along the surface. This fact often enables the number of active sites on catalysts to be determined by simply measuring the quantity of chemisorbed gas.

The second category, reversible or physical adsorption, exhibits characteristics that makes it most suitable for surface area determinations as indicated by the following:

- Physical adsorption is accompanied by low heats of adsorption with no violent or disruptive structural changes occurring on the surface during the adsorption measurements.
- Unlike chemisorption, physical adsorption may lead to surface coverage by more than one layer of adsorbate. Thus, pores can be filled by the adsorbate for pore volume measurements.
- At elevate temperatures physical adsorption does not occur or is sufficiently slight that relatively clean surfaces can be prepared on which to make accurate surface area measurements.
- Physical adsorption equilibrium is achieved rapidly since no activation energy is required as in chemisorption. An exception here is adsorption in small pores, where diffusion can limit the adsorption rate.

- Physical adsorption is fully reversible, enabling both the adsorption and desorption processes to be studied.
- Physical adsorbed molecules are not restrained to specific sites and are free to cover the entire surface. For this reason surface areas, rather than the number of sites, can be calculated.

The kinetics and thermodynamics of adsorption have been extensively studied, but, when surface area and pore structure are the subject of interest, it's essential to establish the meaning of an adsorption (desorption) isotherm. This is a measure of the molar quantity of gas n (or standard volume V_α, or general quantity q) taken up, or released, at a constant temperature T by an initially clean solid surface as a function of gas pressure P. In order to increase the amount of physisorbed molecules (usually nitrogen) most frequently the test is conducted at a cryogenic temperature, usually that of liquid nitrogen (LN_2) at its boiling point (77.35 K at 1 atm pressure). Convention has established that the quantity of gas adsorbed is expressed as its volume at standard temperature and pressure conditions (0°C and 760 torr and denoted by STP), while the pressure is expressed as a relative pressure, which is the actual gas pressure P divided by the vapor pressure P_0 of the adsorbing gas at the temperature of the test. Plots of V_α as the ordinate against P/P_0 as the abscissa reveal much about the structure of the adsorbing material (called the adsorbent) simply from their shape.

The theory mainly used in order to get essential information (such as surface area and pore distribution) from experimental adsorption isotherm is known as BET theory from the surnames of its creators, Brunauer, Emmett and Teller.[50] This is an extension to multilayer adsorption of the Langmuir model (related to monolayer molecular adsorption) and the resulting BET equation is expressed as follows:

$$V_\alpha = \frac{V_m C P}{(P_0 - P)\left[1 + (C-1)\frac{P}{P_0}\right]} \tag{3.11}$$

where:

V_α = volume of adsorbed gas at pressure P.

V_m = monolayer volume.

P = gas pressure.

P_0 = saturation gas pressure.

The value of parameter C, fairly constant for a given class of materials, *e.g.* oxides and metals, in simplest terms is given by the following equation:

$$C \propto \exp\left(\frac{q_1 - q_L}{RT}\right) \tag{3.12}$$

where:

q_1 = heat of adsorption of the first layer.

q_L = heat of liquefaction of the adsorptive.

R = gas constant.

T = absolute temperature.

Small values of the C parameter stand for a higher affinity between molecules than between the molecules and the adsorbing species, resulting in lower wettability. On the contrary, high C values describe the typical isotherm, characterized, firstly, by a monolayer adsorption and then by the multilayer one, layer by layer (Fig. 3.10).

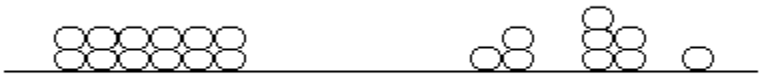

Figure 3.10 Examples of high (on the left) and low (on the right) wettability of a solid surface.

Equation (3.11) can also be written in the linear form:

$$\frac{P}{V_\alpha(P_0 - P)} = \frac{1}{V_m C} + \frac{C-1}{V_m C}\left(\frac{P}{P_0}\right) \tag{3.13}$$

Isotherm data for most solids when using nitrogen as the adsorptive and plotting them in according to equation (3.12) yield a straight line within the range $0.05 < P/P_0 < 0.35$.

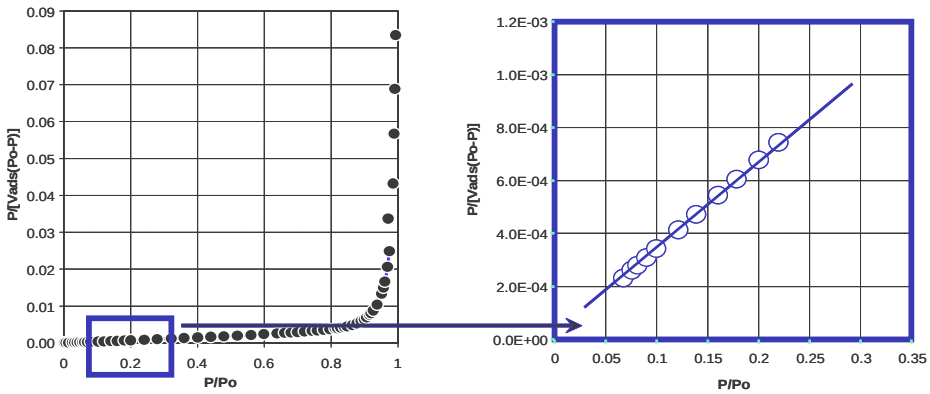

Figure 3.11 BET transform plot with a regression line through the linear region.

From the slope and intercept values of the BET linear plot it is possible to calculate both the amount of adsorbate corresponding to the first monolayer, V_m, and the C parameter can be calculated. Assuming that the surface occupied by a N_2 molecule is $16.2 \cdot 10^{-20}$ m^2, once calculated V_m, it's easy to obtain the Specific Surface Area (SSA) of the adsorbing material, by the following equation:

$$SSA = \frac{V_m N_A S_{N2}}{22.414 g} \tag{3.14}$$

where:

N_A = Avogadro number ($6.023 \cdot 10^{23}$ molecules mol^{-1}).

S_{N2} = surface occupied by a N_2 molecule adsorbed on the monolayer.

22.414 = volume (dm^3) occupied by 1 mole of gas under standard conditions.

g = sample quantity (g).

Moreover, the C value is most frequently between 50 and 300, when using nitrogen at 77 K. A high or negative C value is indicative of micropores and their measurement cannot be analysed by this BET model without further modification.

3.6 Impedance analysis

Electrochemical techniques imply the application of an electric perturbation (current, potential) to an electric circuit, causing the appearance of a response. Electrochemical Impedance Spectroscopy (EIS) studies the system response to the application of a periodic small amplitude AC signal. These measurements are carried out at different AC (alternative current) frequencies and, thus, the name impedance spectroscopy has been adopted.[51] This technique leads to highly accurate results as the system, being at the steady state, can be investigated for a long time and over a large range of potentials. The analysis of the system response contains information about the interface, its structure and the reactions taking place there.

Considering the application of an arbitrary (but known) potential E(t), the resistance (R) measures how strongly a circuit opposes to current flow, i(t), in direct current (DC) conditions:

DC conditions: $R = E(t)\ i(t)$ (3.15)

On the contrary, impedance (Z) measures how strongly a circuit opposes to current flow in alternating current (AC) conditions:

AC conditions: $E(t) = Z\, i(t)$ (3.16)

Both resistance and impedance are measured in Ohm (Ω).

The applied potential and the current intensity have typical sine wave flow:

$E(t) = E_0 \sin(\omega t)$ (3.17)

$i(t) = i_0 \sin(\omega t + \varphi)$ (3.18)

where ω stands for the frequency and φ for the phase angle.

According to the Euler relationship applied to complex numbers, both previous equations may be described by:

$E = E_0 \exp(j\omega t)$ (3.19)

$i = i_0 \exp[j(\omega t+\varphi)]$ (3.20)

As shown in relation 3.16, Z is the ratio between the applied potential and the current intensity; applying the complex number property, it can be described as:

$Z(\omega) = E_0 \exp(j\omega t) / i_0 \exp[j(\omega t+\varphi)] = |Z| \exp(j\varphi) = |Z| (\cos \varphi + j\sin \varphi)$ (3.21)

$|Z| \cos \varphi + |Z| j\sin \varphi = Z' - jZ'' = \mathrm{Re}(Z) - \mathrm{Im}(Z)$ (3.22)

Thus, impedance is defined as the transfer function (TF) between E(t) and i(t) at any frequencies ω and is a complex number containing phase information as well as magnitude.

EIS is based on the transfer function principle: the system is perturbed by a sine wave input signal and the output response, produced by the system, is recorded. When the input is the current intensity and the output is a potential, the TF is simply the impedance Z. Although EIS may be applied in a large number of electrochemical fields, its application is not so popular because it's a very sensitive technique and it must be used with great care. Besides, it is not yet well understood because of complex data analysis for quantification.

3.6.1 Mott-Schottky theory applied to impedance analysis

Photocatalyst particles can be considered as individual micro-electrodes kept under open circuit potential, inside which charge carriers (electrons and holes) can be generated upon band gap excitation. These charge carriers then migrate to the surface, eventually participating in a chemical reaction with a surface-adsorbed species.

The *Mott-Schottky* theory applied on impedance analysis gives information about the donor density and the flat band potential. The *donor density* represents the charge carriers density but can also be associated to the ability of the semiconductor in releasing electrons, available for the photoinduced process. The *flat band* potential is a measure of the reducing power of n-type semiconductor materials such as TiO_2. It is related to the electron affinity of the semiconductor and the charge density at its surface.

E_{fb} is also defined as the potential at which the Fermi energy lies at the same energy as the solution redox potential; hence there is no net transfer of charge and no band bending. As doping changes the distribution of electrons within the solid and hence changes the Fermi level, also the flat band potential is influenced by the characteristics of the material.[52]

From the flat band potential and the band gap values, the valence and conduction band can be localized and an evaluation of the relationship between the semiconductor bands and the pollutant redox potentials can be made, as well as an approximate prediction of the photocatalytic activity of semiconductors.

In particular flat band potentials and donor densities of TiO_2 thin films at the semiconductor/electrolyte junction can be obtained from Mott-Schottky plots using the following equation:

$$\frac{1}{C_{sc}^2} = \left(\frac{2}{\varepsilon_{TiO_2} \varepsilon_0 e_0 N_D} \right) \left(E - E_{FB} - \frac{kT}{e_0} \right) \tag{3.23}$$

where:

ε_0 = permittivity of free space.

ε_{TiO2} = permittivity of the semiconductor electrode.

e_0 = elementary charge.

N_D = donor density.

E = applied potential.

E_{FB} = flat band potential.

k = Boltzmann's constant.

T = temperature of operation.

C_{sc} = space charge capacitance.

The $1/C^2$ vs. E plot should thus yield a straight line, intersecting the potential axis at E_{FB} value. The donor density N_D value can be calculated from the slope of this line.

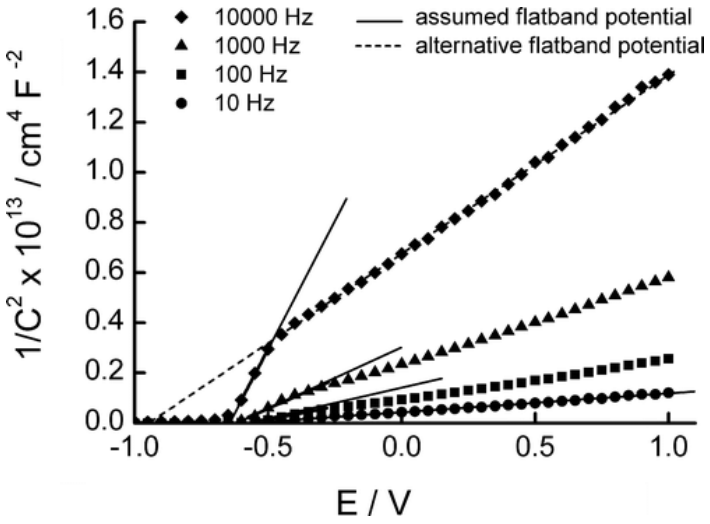

Figure 3.12 Mott-Schottky plot obtained at different frequencies for TiO_2 thin film electrodes.[53]

The commonly most employed frequency is 1000 Hz.[54,55]

3.7 Electron microscopy

Since its invention, the electron microscope has been a valuable tool in the development of scientific theory and it contributed greatly to biology, medicine and material sciences. This wide spread use of electron microscopes is based on the fact that they permit the observation and characterization of materials on a nanometer (nm) to micrometer (μm) scale. The basic theory for electron microscopy are here shortly presented, focusing on the two basic types of Ems; SEM (Scanning Electron Microscope) and TEM (Transmission Electron Microscope). In particular the main attention will be paid to the latter one, which has been employed in this PhD thesis.

Electron Microscopes are scientific instruments that use a beam of highly energetic electrons to examine objects on a very fine scale. This examination can yield information about the topography (surface features of an object), morphology (shape and size of the particles making up the object), composition (the elements and compounds that the object is composed of and the relative amounts of them) and crystallographic information (how the atoms are arranged in the object).

Electron Microscopes were developed due to the limitations of Light Microscopes which are limited by the physics of light to 500x or 1000x magnification with a

resolution of 0.2 μm. In the early 1930's this theoretical limit had been reached and there was a scientific desire to see the fine details of the interior structures of organic cells (nucleus, mitochondria...etc.). This required 10.000x plus magnification which was just not possible using Light Microscopes.

The Transmission Electron Microscope (TEM) was the first type of Electron Microscope to be developed and is patterned exactly on the Light Transmission Microscope except that a focused beam of electrons is used instead of light to "see through" the specimen. It was developed by Max Knoll and Ernst Ruska in Germany in 1931. The first Scanning Electron Microscope (SEM) debuted in 1942, with the first commercial instruments around 1965. Its late development was due to the electronics involved in "scanning" the beam of electrons across the sample.

Electron Microscopes (EMs) function exactly as their optical counterparts except that they use a focused beam of electrons instead of light to "image" the specimen and gain information as to its structure and composition.

3.7.1 Electron-matter interactions

When an electron beam interacts with the atoms in a sample, individual incident electrons undergo two types of scattering - elastic and inelastic. In the former, only the trajectory changes and the kinetic energy and velocity remain constant. In the case of inelastic scattering, some incident electrons will actually collide with and displace different kind of electrons from the specimen, thus loosing their kinetic energy. Figure 3.13 summarizes the main secondary signals (with different relative intensity) that can be produced due to electron–matter interactions.[56]

By considering the large amount of information obtained by this kind of interaction it’s essential try to amplify each single signal by using different kinds of instrumentation. In this regard the first main difference between SEM and TEM, mainly concerning the sample location in the microscope, can be outlined.

In particular SEM studies the information related to secondary and backscattered electrons, detected on the same side with respect to the incident electrons beam. In this case the sample holder is located at the end of microscope’s column (Fig. 3.14a). On the contrary TEM deals with transmitted, elastically or inelastically scattered electrons, detected on the opposite side with respect to the incident electrons beam. In this case the sample holder is located in the middle of the microscope’s column (Fig. 3.14b).

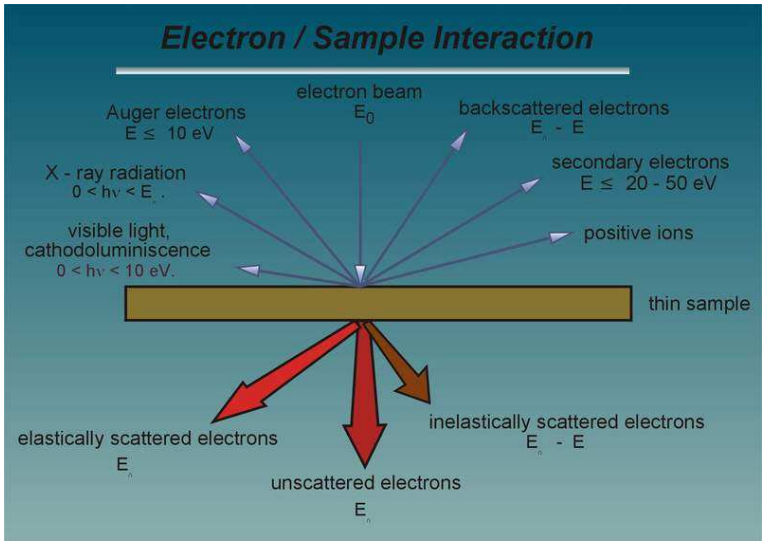

Figure 3.13 Signals generated when a high-energy beam of electrons interacts with a thin specimen. Most of these signals can be detected in different types of electron microscopes. The directions shown for each signal do not always represent the physical direction of the signal but indicate, in a relative manner, where the signal is strongest or where it is detected.

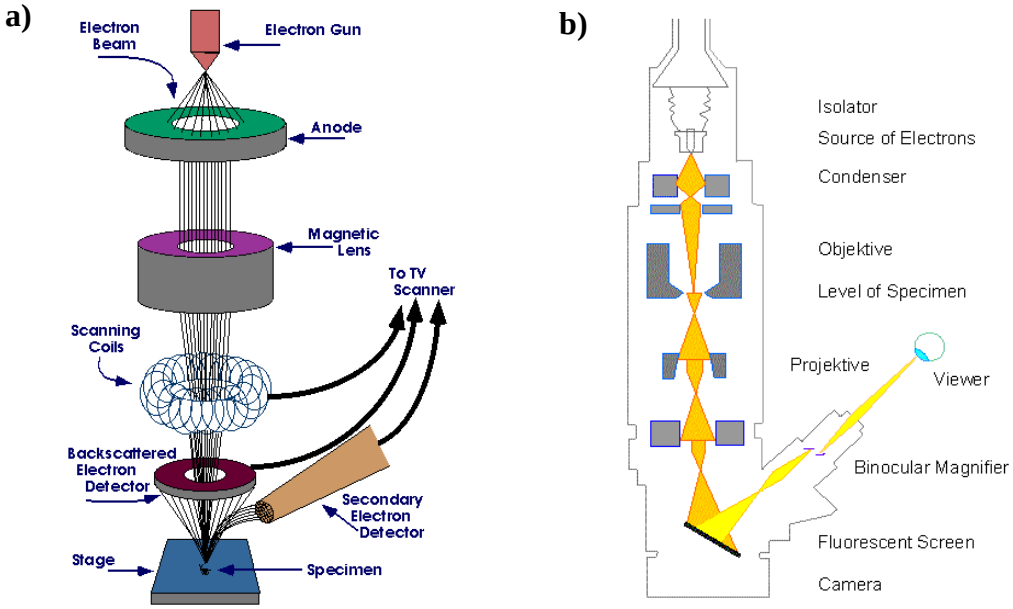

Figure 3.14 General scheme of a) SEM and b) TEM instrumentations.

Both SEM and TEM instruments must work under ultra high vacuum conditions (10^{-7}-10^{-8} Pa) in order to avoid any kind of collision between the electrons beam and atoms, which are not those contained in the investigated sample.

Moreover there are essential instrumental components which are common to SEM and TEM systems: electron guns, which can be divided into thermoionic and field-emission types, and metal apertures and magnetic lenses necessary to confine and focus the electron beam toward the specimen (thanks to the application of a proper potential).

3.7.2 Electrons exploited in Trasmission Electron Microscopy (TEM)

TEM exploits three different interactions of electron beam-specimen: unscattered electrons (transmitted beam), elastically scattered electrons (diffracted beam) and inelastically scattered electrons.

When incident electrons are transmitted through the thin specimen without any interaction occurring inside the specimen, then the beam of these electrons is called transmitted. The transmission of unscattered electrons is inversely proportional to the specimen thickness. Areas of the specimen that are thicker will have fewer transmitted unscattered electrons and so will appear darker; conversely the thinner areas will have more transmitted and thus will appear lighter.

Another part of the incident electrons, are scattered (deflected from their original path) by atoms in the specimen in an elastic fashion (without loss of energy). These diffracted electrons according to Bragg's law are then transmitted through the remaining portions of the specimen. In this case a diffraction pattern and the related information about orientation, atomic arrangements and phases present in the examined area can be obtained.

There are essentially three different imaging modes in TEM, which can be selected by changing proper apertures of the back focal plane (after the objective lens) (Fig. 3.15):

1. *Bright field mode*: the aperture selects only transmitted electrons. In this case, factors such as mass and thickness of the sample influence the formation of the image.
2. *Dark field mode:* in this case only diffracted electrons, which gave strong interaction with the sample, are selected. The image obtained can give information about the presence of defects or different phases of the specimen.
3. *High resolution (HR-TEM)*: in this case both transmitted and diffracted electrons are selected. Using proper corrections for spherical aberration, special high resolution TEMs can generate images with a resolution below 0.1 nm; it's thus

possible observe reticular planes and get crystallographic information of the examined sample. By considering that for TEM analysis the analyzed electrons have to pass through the sample, the specimens have to be rather thin, less than 100 nm.

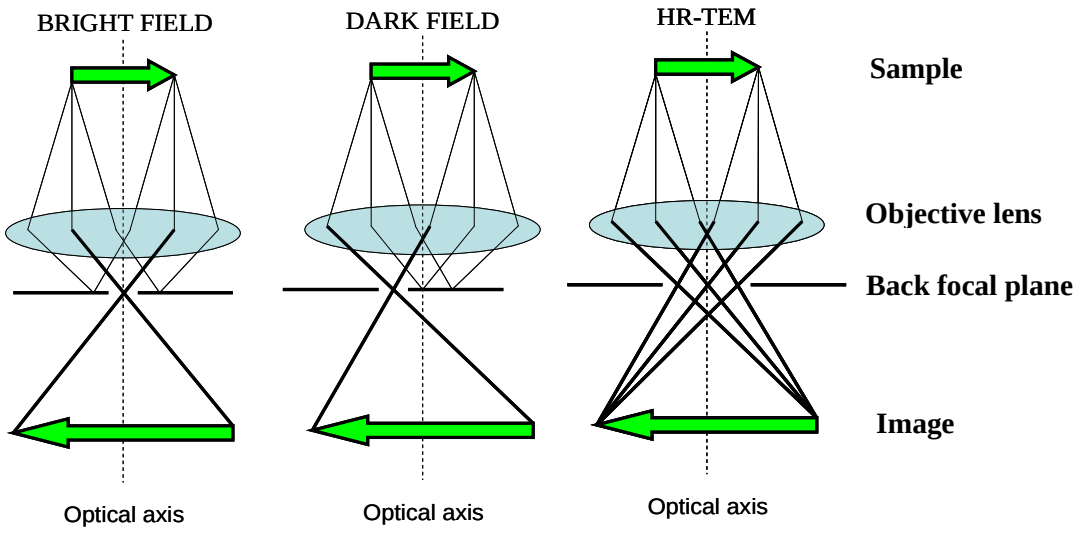

Fig. 3.15 Generalized description of the three main imaging modes in TEM.

HR-TEM measurements in the present study were performed by Prof. Patrizia Canton at Università degli Studi di Venezia.

3.8 Extended X-ray absorption fine structure (EXAFS)

EXAFS spectroscopy provides structural information about a sample by way of the analysis of its X-ray absorption spectrum. It allows determining the chemical environment of a single element in terms of the number and type of its neighbours, inter-atomic distances and structural disorders. This determination is confined to a distance given by the mean free path of the photoelectron in the condensed matter, which is between 5 and 10 Å radius from the element.[57-59]

These characteristics make EXAFS a powerful structural local probe, which does not require a long-range order. It is an important technique in several fields of natural sciences, from earth sciences to biochemistry.

Since EXAFS is a technique selective for a particular element and sensible only for a short-range order, it is one of the most appropriate spectroscopies to be applied in the following cases:

- amorphous solids, *e.g.* ceramics,
- liquids, *e.g.* solutions of ionic compounds or gels which cannot be studied by X-ray diffraction,
- biomolecules, *e.g.* solutions of metalloproteins,
- homogeneous and heterogeneous catalysts.

Furthermore, EXAFS does not require any particular experimental conditions, such as vacuum (at least in principle). There are several types of sample-holders that allow collecting experimental data under varying temperature and pressure, or while the sample is undergoing a chemical reaction (in-situ studies). Measures taken under working conditions are of critical importance in the case of heterogeneous catalysts in order to understand their behavior during catalysis, and in studying temperature and pressure induced changes.

On the other hand, there are some problems associated with this spectroscopy. First, the necessity of synchrotron light as a source, which is expensive and not easily available. Second, the use of simulation and best-fit procedures to obtain structural parameters; these methods are time consuming and they sometimes give ambiguous or unreliable results. However, if the system under study is properly chosen, EXAFS is able to supply useful and even essential information.

3.8.1 Origin of the EXAFS signal

The X-ray absorption coefficient for an atom, indicated as μx, is directly proportional to the probability of absorption of one photon and is a monotone decreasing function of energy. It shows several discontinuities known as absorption edges: they occur when the energy of the incident photons equals the binding energy of one electron of the atom and are classified with capital letters (K, L, M...) according to the principal quantum number of the electron in the ground state (n = 1, 2, 3...). There are many tables describing the energy position of all existing absorption edges for all types of atoms. The X-ray absorption coefficient μx can also be defined according to Lambert-Beer law as follow:

$$\ln \frac{I_0}{I} = \mu x \tag{3.24}$$

where I_0 e I represent the incident and the transmitted intensity of X-rays, respectively. Figure 3.16 shows this behaviour for Rh atoms: it is possible to recognize four edges due to K and L (LI, LII and LIII) electrons in the diagram of the absorption coefficient of atomic rhodium.

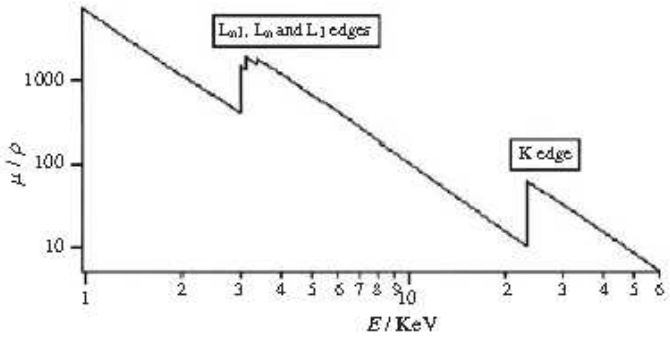

Figure 3.16 X-ray absorption spectrum for Rh atoms.

The edge energy is characteristic of each atom. In the case of an isolated atom (monatomic gas), the absorption coefficient decreases monotonously with energy between two subsequent edges. In all other situations, the spectrum also shows oscillations that start at the edge and finish a thousand eV above; *e.g.* Figure 3.17 shows the absorption spectrum of metallic Rh at edge K.

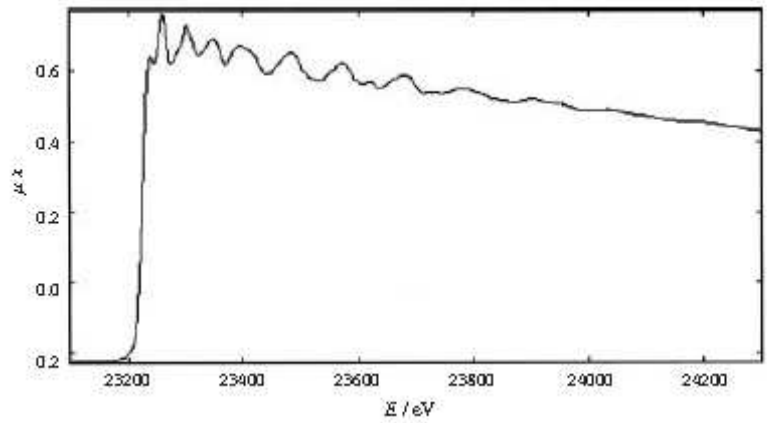

Figure 3.17 Absorption spectrum for metallic Rh (K edge) showing EXAFS signal.

Generally X-ray absorption spectrum can be divided into two main regions:

- XANES (X-ray Absorption Near Edge Structure): this is the portion of the X-ray absorption spectrum that extends from below the absorption edge to about 60-100 eV above the same edge.
- EXAFS (Extended X-ray Absorption Fine Structure): this is the portion of the absorption spectrum which starts about 60-100 eV above the absorption edge.

An incident photon is able to extract a core electron if its energy is equal to or greater than the edge energy. The ejected electron is called photoelectron and it has the characteristics of both a particle and a wave. Its kinetic energy is given by:

$$E = E_x - E_0 \tag{3.25}$$

where E_x is the energy of the X-ray photon and E_0 the energy of the edge. Its wave vector modulus is given by:

$$|k| = \frac{2\pi}{\lambda} = \sqrt{\frac{8\pi^2 m}{h^2}(E_x - E_0)} = \sqrt{0.2624 \cdot E} \tag{3.26}$$

If the absorbing atom is isolated, the photoelectron propagates as an unperturbed isotropic wave (Figure 3.18a), but in most cases there are many other atoms around the absorber. These become scattering centers of the photoelectron wave (Figure 3.18b).

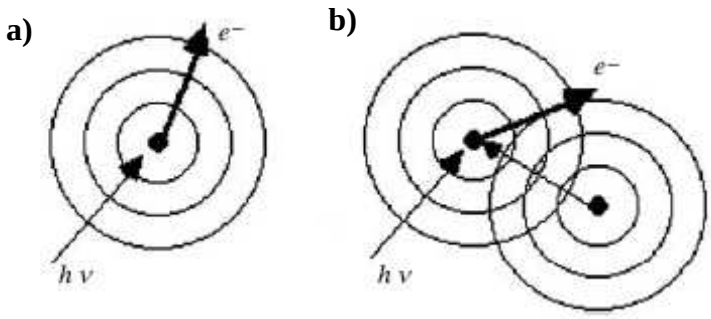

Figure 3.18 Schemes of scattering processes.

The final state of the photoelectron can be described by the sum of the original and scattered waves. This leads to an interference phenomenon that modifies the interaction probability between core electrons and incident photons. Constructive interference increases while destructive interference decreases the absorption coefficient of the atom (Fig. 3.19).

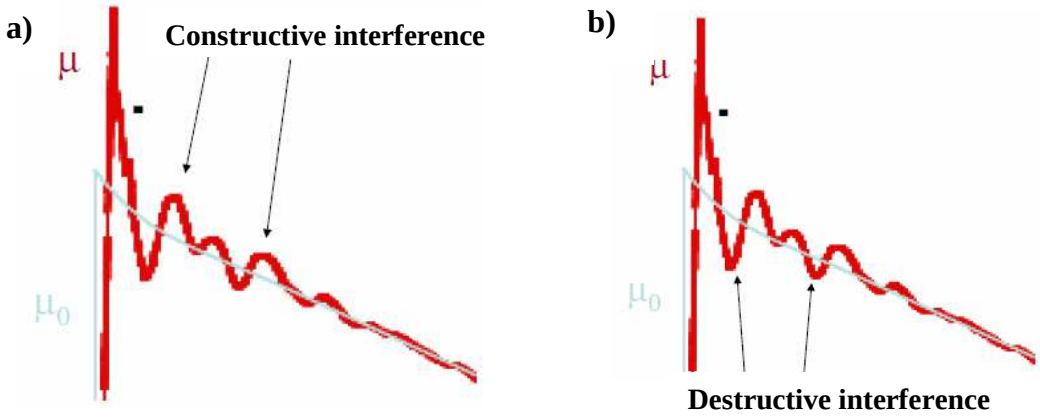

Figure 3.19 Example of effects produced on EXAFS spectrum due to a) constructive or b) destructive interference.

This interference phenomenon, for a given energy of the photoelectron, depends on the distance between emitting and scattering atoms, and their atomic numbers.
The EXAFS signal $\chi(k)$ is defined as a function of the wave vector k. It is mathematically defined as:

$$\chi(k) = \frac{\mu x - \mu_1 x}{\mu_1 x} = \frac{\mu x}{\mu_1 x} - 1 \qquad (3.27)$$

where μx is the experimental absorption coefficient and $\mu_1 x$ is the intrinsic atomic absorption coefficient.

By applying proper analytical expressions (whose detailed explanation goes beyond the scope of this thesis), EXAFS analysis allows obtaining coordination numbers, interatomic distances and an estimate of the disorder around the central atom. In particular EXAFS spectroscopy allows estimating structural parameters with a precision highly dependent on the data and analysis quality. Errors are usually about 0.01–0.02 Å for interatomic distances, and 5–15 % for coordination numbers.

Finally, since EXAFS spectroscopy requires an intense polychromatic X-ray source, the most suitable light source is a synchrotron storage ring. The most common EXAFS beam-line works in transmission (Fig. 3.20). It collects data measuring how the beam intensity decreases as it passes through the sample while scanning energy using a crystal monochromator. Experimental spectra are usually recorded by scanning energy

from about 200 eV below the explored edge to 1000 eV above it. Energy steps can be of 0.1–2.0 eV, depending on the energy interval and the experimental setup. The incident and transmitted X-ray fluxes are usually monitored by using ionization chambers.

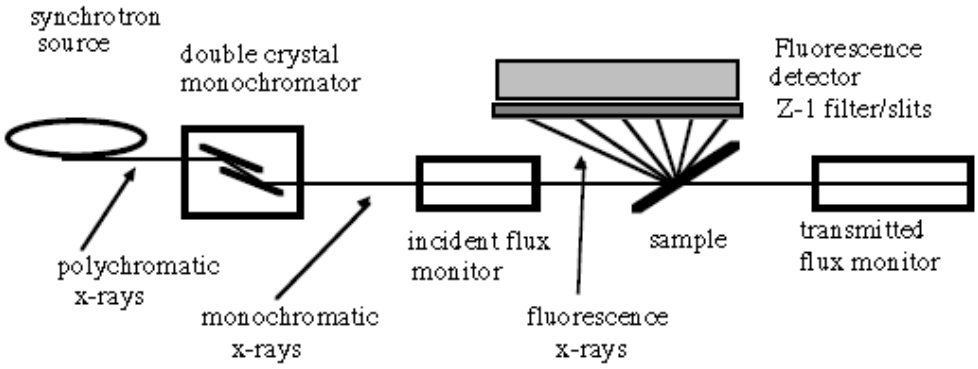

Figure 3.20 General scheme of experimental set-up adopted in EXAFS analysis.

3.9 References

1. X. Chen and S. S. Mao, Chem. Rev., **2007**, 107, 2891.
2. J. Ebelmen, Annales de Chimie et de Physique, Series 3, **1846**, 57, 311.
3. D. C. Bradley, R. C. Mehrotra and D. P. Gaur, Metal Alkoxides, **1978**, Academic Press: New York.
4. C. J. Brinker and G. W. Scherer, Sol–gel science: the physics and chemistry of sol – gel processing, Academic Press: United Kingdom, **1990**.
5. C. J. Brinker and G. W. Scherer, J. Non-Cryst. Solids, **1985**, 70, 301.
6. B. L. Wang and L. L. Hu, Mater. Chem. Phys., **2005**, 89, 417.
7. S. Biswas, A. Majumder, M. F. Hossain, T. Takahashi, Y. Kubota and A. Fujishima, J. Vac. Sci. Technol. A, **2008**, 26, 678.
8. Z. J. Chen, G. L. Zhao, H. Li, G. R. Han and B. Song, J. Am. Ceram. Soc., **2009**, 92, 1024.
9. Y. Djaoued, S. Badilescu, P. V. Ashrit, D. Bersani, P. P. Lottici and R. Bruning, J. Sol-Gel Sci. Techn., **2002**, 24, 247.
10. J. W. Gao, H. Yang and Q. H. Shen, Rare Metal Mat. Eng., **2008**, 37, 95.
11. G. Goutailler, C. Guillard, S. Daniele and L. G. Hubert-Pfalzgraf, J. Mater. Chem., **2003**, 13, 342.
12. Z. S. Guan, X. T. Zhang, Y. Ma, Y. A. Cao and J. N. Yao, J. Mater. Res., **2001**, 16, 907.
13. J. N. Hart, L. Bourgeois, R. Cervini, Y. B. Cheng, G. P. Simon and L. Spiccia, J. Sol-Gel Sci. Techn., **2007**, 42, 107.
14. M. F. Hossain, S. Biswas, M. Shahjahan, A. Majumder and T. Takahashi, J. Vac. Sci. Technol. A, **2009**, 27, 1042.
15. D. J. Kim, S. H. Hahn, S. H. Oh and E. J. Kim, Mater. Lett., **2002**, 57, 355.
16. J. Marugan, P. Christensen, T. Egerton and H. Purnama, Int. J. Photoenergy, **2008**.
17. M. Sun, W. X. Que and X. Hu, J. Vac. Sci. Technol., **2009**, 50, 415.
18. Y. L. Wang, H. Y. Du, J. Han and L. Cui, J. Rare Earths, **2005**, 23, 306.
19. Z. C. Wang, U. Helmersson and P. O. Kall, Thin Solid Films, **2002**, 405, 50.
20. E. Duguet, Introduction to Hybrid Organic-Inorganic Materials, Bordeaux, **2000**
21. B. J. J. Zelinski and D. R. Uhlmann, J. Phys. Chem. Solids, **1984**, 45, 1069.
22. J. Livage, Encyclopedia of Inorganic Chemistry, Wiley edition, New-York, **1994**, 3836.

23. S. Ardizzone, C. L. Bianchi and C. Galassi, J. Electroanal. Chem., **2000**, 490, 48.
24. S. Melada, M. Signoretto, S. Ardizzone and C. L. Bianchi, Catal. Lett., **2001**, 75, 199.
25. S. Ardizzone, L. Binaghi, G. Cappelletti, P. Fermo and S. Gilardoni, Phys. Chem. Chem. Phys., **2002**, 4, 5683.
26. R. Ricceri, S. Ardizzone, G. Baldi and P. Matteazzi, J. Europ. Ceram. Soc. **2002**, 22, 629.
27. G. Cappelletti, C. Ricci, S. Ardizzone, C. Parola and A. Anedda, J. Phys. Chem. B, **2005**, 109, 4448.
28. W. I. F. David, K. Shankland, L. B. Mc Cusker and C. Baerlocher, Structure Determination from Powder Diffraction Data, Oxford Science Publications, **1992**.
29. D. L. Bish, J. E. Post and J. E. Modern, Powder Diffraction published by The Mineralogical Society of America, **1989**.
30. L. V. Azaroff and M. J. Buerger, The Powder Method in X-ray Crystallography, McGraw Hill Book Company, Inc, **1975**.
31. M. J. Buerger, X-ray Crystallography, J. Wiley, New York, **1942**, 20.
32. L. Smart and E. A. Moore, Solid State Chemistry: an introduction, CRC Press: United States of America, **2005**.
33. H. M. Rietveld, J. Appl. Cryst., **1969**, 2, 65.
34. L. B. McCusker, R. B. Von Dreele, D. E. Cox, D. Louer and P. Scardi, J. Appl. Cryst., **1999**, 32, 36.
35. R. J. Hill and C. J. Howard, J. Appl. Cryst., **1987**, 20, 4.
36. A. Altomare, M. C. Burla, C. Giacovazzo, A. Guagliardi, A. G. G. Moliterni, G. Polidori and R. Rizzi, J. Appl. Cryst., **2001**, 34, 392.
37. H. P. Klug and L. E. Alexander, X-ray Diffraction Procedures for Polycrystalline and Amorphous Materials, 2nd ed., Wiley, New York, **1974**, 687.
38. B. E. Warren and J. Biscoe, J. Am. Ceram. Soc., **1938**, 21, 49.
39. B. E. Warren, J. Appl. Phys., **1941**, 12, 375.
40. G. K. Williamson and W. H. Hall, Acta Metall., **1953**, 1, 22.
41. B. Ohtani, Y. Ogawa and S. I. Nishimoto, J. Phys. Chem. B, **1997**, 101, 3746.
42. B. Ohtani, Y. Azuma, D. Li, T. Ihara and R. Abe, Trans. Mater. Res. Soc. Jpn., **2007**, 32, 401.

43. B. Ohtani, O. O. Prieto-Mahaney, D. Li and R. Abe, J. Photochem. Photobiol. A: Chem., **2010**, 216, 179.
44. H. Seyama, M. Soma and B.K.G. Theng, X-ray Photoelectron Spectroscopy, Handbook of Clay Science, Elsevier: Amsterdam, **2006**.
45. J. G. Calvert and J. N. Pitts Jr, Photochemistry, Wiley, New York, **1966**, 19.
46. B. Ohtani, J. Photochem. Photobiol C: Photochem. Rev., **2010**, 11, 4, 157.
47. R. A. Smith, Semiconductors, 2nd edition, Cambridge University Press: Cambridge (U.K), **1978**.
48. D. G. Barton, M. Sthein, R. D. Wilson, S. L. Soled and E. Iglesia, J. Phys. Chem. B, **1999**, 103, 630.
49. J. Tauc, Amorphous and Liquid Semiconductors, J. Tauc Ed, Plenum Press: London (U.K.), **1974**, 159.
50. S. Brunauer, P. H. Emmet and E. Teller, J. Am. Chem. Soc., **1938**, 60, 309.
51. A. Lasia, Electrochemical Impedance Spectroscopy and its Applications, Modern Aspects of Electrochemistry, B.E. Conway, J. Bockris, R.E. White, Eds., Kluwer Academic/Plenum Publishers, New York, **1999**, 32, 143.
52. A.W. Bott, Current Separ., **1998**, 17, 87.
53. C. Baumanis and D. W. Bahnemann, J. Phys. Chem. C, **2008**, 112 19097.
54. O. R. Camara, C. P. De Pauli, M. E. Vaschetto, B. Retamal, M.J. Aquirre, J. H. Zagal and S. R. Biaggio, J. Appl. Electrochem., **1995**, 25, 247.
55. S. Kumari, Y. S. Chaudhary, S. A. Agnihotry, C. Tripathi, A. Verma, D. Chauhan, R. Shrivastav, S. Dass and V. R. Satsangi, Int. J. Hydrogen Energy, **2007**, 32, 1299.
56. D. B. Williams and C. B. Carter, Transmission Electron Microscopy, Vol. 1, Springer, New York, **1996**.
57. B. K. Teo, EXAFS: Basic Principles and Data Analysis, Inorganic Chemistry Concepts, Vol. 9, Springer-Verlag, Berlin, **1986**.
58. D. C. Koningsberger and R. Prins, X-Ray Absorption: Principles, Applications, Techniques of EXAFS, SEXAFS and XANES; Chemical Analysis, Vol. 92, John Wiley and Sons, New York, **1988**.
59. P. Fornasini, Introduction to X-ray absorption spectroscopy, in: S. Mobilio and G. Vlaic (Eds.) Synchrotron Radiation: Fundamentals, Methodologies and Applications, Conference Proceedings, Vol. 82, SIF, Bologna, **2003**, 129.

Chapter 4

Photocatalytic set-ups and testing procedures

In this chapter the main experimental details of the set up used to investigate the photocatalytic activity of differently modified TiO_2 materials will be briefly presented. The set up employed in the laboratory of Prof. Elena Selli's group at the Università degli Studi di Milano (Dipartimento di Chimica Fisica ed Elettrochimica) will be described first, followed by an illustration of the different types of set up used during my staying at the laboratory of Professor Bunsho Ohtani at the Catalysis Research Center, Hokkaido University, Sapporo, Japan.

4.1 Set-up in Milano

In Milano the same photocatalysis set-up was employed to obtain the results discussed in Chapters 5-7 and 9. In particular, all photocatalytic degradation runs were performed under atmospheric conditions in a magnetically stirred cylindrical quartz reactor, inserted in a home-made housing consisting in a black box mounted on optical bench.

The irradiation source was an Osram, model Powerstar HCI-T, 150 W/NDL lamp, mounted on a Twin Beam T 150 R reflector, emitting at $\lambda_{em} > 340$ nm, with an average full emission intensity on the reactor of $2.53 \cdot 10^{-7}$ Einstein s^{-1} cm^{-2}, as periodically checked by ferrioxalate actinometry.[1,2] A 285 nm cut off filter was usually mounted at the black box entrance. Eventually 400 and 455 nm cut off filters were employed in some runs in order to perform experiments under visible light only. The lamp and the reactor were separated by a fixed distance of 10 cm. The whole set up was maintained at ambient temperature by a continuous stream of air.

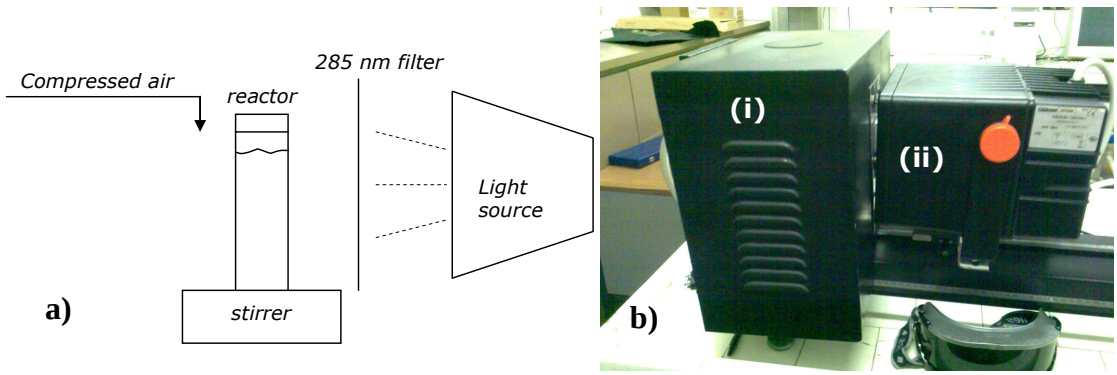

Figure 4.1 (a) Schematic representation of the set up used for testing the phototocatalytic activity of TiO_2-based materials in Milano. (b) Photograph of the light source (ii) and of the black box (i), equipped with a 285 nm cut off filter, mounted on the fixed optical bench.

All irradiated aqueous suspensions were always prepared using water purified by a Milli-Q water system (Millipore) and usually contained 0.1 g L^{-1} of photocatalyst. They were preliminarily sonicated in a Eurosonic, Model 22, apparatus for 30 min. After substrate addition, they were always magnetically stirred in the dark for 15 min to attain the adsorption equilibrium of the substrate on the photocatalyst surface, before starting irradiation. Stirring was continued during the runs. The lamp was always switched on at least 30 min before the beginning of irradiation. At different time intervals during the run, 2 mL-samples of the suspension were withdrawn from the reactor, centrifuged employing a EBA-20 Hettich centrifuge and the surnatant was analysed for residual organic substrate content.

All kinetic runs were repeated at least twice, to check their reproducibility. Formic acid concentration was usually monitored by ion chromatography with conductivity detection, employing a Metrohm 761 Compact IC instrument, after calibration for formate ion concentration in the 0-50 ppm range. A Perkin Elmer Lambda 16 spectrophotometer was always employed for all spectrophotometric analyses during the runs. An Amel, model 2335 pHmeter, was always employed for pH measurements.

The emission spectrum of the commercial metal halide lamp employed in this set up is depicted in Fig 4.2.

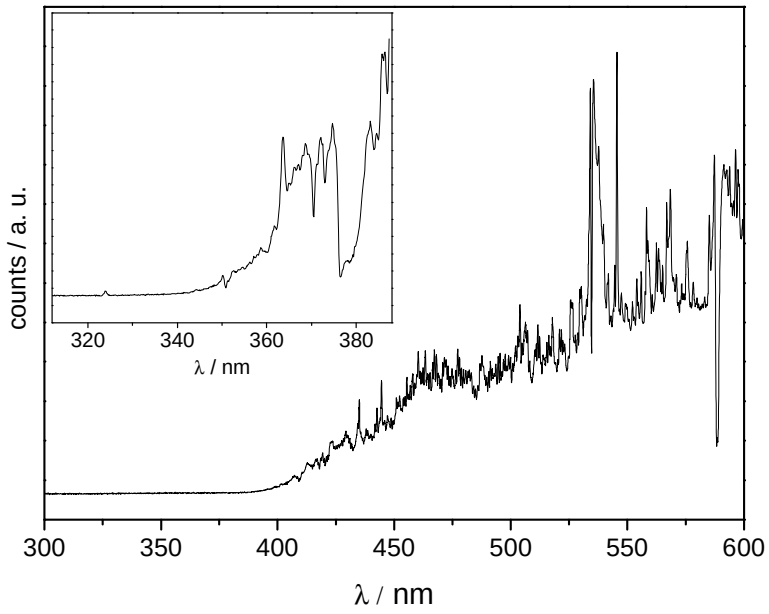

Figure 4.2 Emission spectrum of OSRAM 'Powerstar' lamp.

The photocatalytic conditions, chosen for each photocatalytic activity test reaction, including the preliminary adsorption time, the amount of photocatalyst and the concentration of the test molecule, the volume of the reaction suspension and its pH conditions will be detailed in each chapter. Water purified by a Milli-Q water system (Millipore) was used throughout.

4.2 Set-ups in Sapporo

In Sapporo different kinds of experimental set up were employed in order to deeply investigate the photocatalytic activity of non metal-doped TiO_2 materials, as detailed in Chapters 8-9.

4.2.1 Gas phase acetaldehyde decomposition under polychromatic irradiation

The investigation of acetaldehyde decomposition is considered to be important from a practical point of view because this organic substrate is known to be one of the principal odour-causing gases in indoor air, particularly in cigarette smoke.

The photocatalytic oxidative decomposition of gas-phase acetaldehyde in air was carried out in a closed cylindrical glass vessel, with a volume of 357 mL and an inner diameter of 5.37 cm. The photocatalyst powder (20 mg) was uniformly spread on a glass plate (1.0 cm × 1.0 cm), placed on the bottom of the photoreactor and pre-irradiated for 1 h in order to purify it from any adsorbed organic compound (Fig 4.3). Then gaseous acetaldehyde (0.36 mL, corresponding to *ca.* 0.014 mmol) was injected into the photoreactor, containing ambient air, thus attaining a 1000-ppm initial acetaldehyde concentration. This injection was performed through a rubber septum by using a lock-pressure syringe that allows organic substrate addition at the desired pressure, 1 atm in our case. In order to attain the adsorption equilibrium of the substrate on the photocatalyst surface, the system was then kept in the dark for 1 h. Irradiation ($\lambda > 290$ nm) was performed through a top window of the photoreactor using a 300-W xenon lamp (ILC Technology CERMAX-LX300F). Its emission spectrum is shown in Fig. 4.4. Acetaldehyde and CO_2 concentrations were automatically measured at fixed time intervals using an Agilent 3000 MicroGC.

The evolution of CO_2 was also monitored during irradiation to check whether acetaldehyde was effectively converted into CO_2 in the presence of the different photocatalysts, according to the reaction: $CH_3CHO + 5/2\ O_2 \rightarrow 2\ CO_2 + 2\ H_2O$.

Figure 4.3 Apparatus for gas-phase acetaldehyde photocatalytic degradation.

The graph below shows the emission spectrum of the used Xenon lamp.

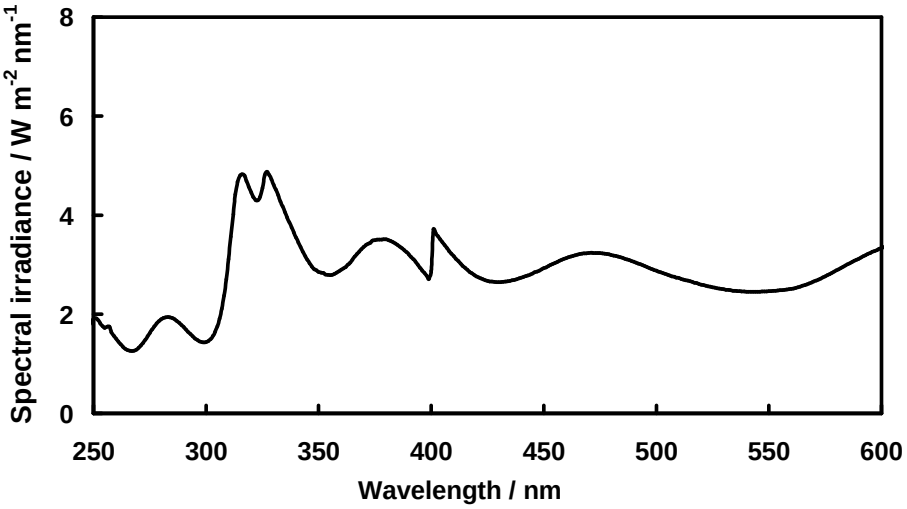

Figure 4.4 Emission spectrum of the 300-W Xenon lamp.

4.2.2 Acetic acid oxidative decomposition under polychromatic irradiation

The photocatalytic tests were performed in a glass tube (18 mm in inner diameter and 180 mm in length) with a volume of *ca.* 35 mL. Each photocatalyst powder (50 mg) was suspended in an aqueous solution (5.0 mL) containing 5.0 vol.% of acetic acid. This amount of photocatalyst powder in the suspension was large enough to ensure total light absorption. The glass tube was sealed with a double-capped rubber septum and Parafilm, to prevent leakage of gas and/or contamination during the runs (Fig. 4.5). The suspensions were irradiated using a 400-W high-pressure mercury lamp (Eikosha) under vigorous magnetic stirring (1000 rpm) (Fig. 4.5). The wavelength of light was > 290 nm, with an average emission intensity of 390 mW, which was checked daily using

a Molectron PM5200 laser power meter (Fig. 4.7). The reaction temperature was kept at 25 °C using a thermostated water bath. At regular time intervals during the runs, 0.2 mL samples of the gas in the tube were withdrawn with a gas-tight syringe and analysed using a Shimadzu GC-8A gas chromatograph with a TC detector, equipped with MS- 5A and Porapak-Q columns (Fig 4.7). The molar amount of carbon dioxide (CO_2) was calibrated considering the increase in pressure in the reaction tube consequent to the increased amount of gas-phase molecules. The kinetic runs were monitored for 80 min and repeated at least twice, in order to check their reproducibility.

a) **b)**

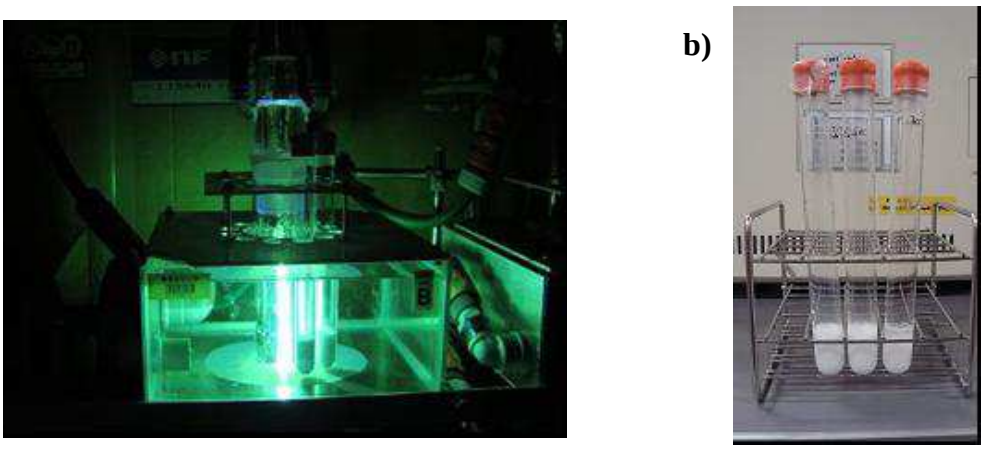

Figure 4.5 a) Apparatus employed for acetic acid photooxidation. This system allows the simultaneous analysis of more than one photocatalyst because the Hg lamp (400 Watt) is surrounded by 12 glass tube containers fixed at a specific distance from the irradiation source and immersed in the same thermostated water bath. b) Example of glass tubes adopted during the photocatalytic tests.

The graph below shows the emission spectrum of the used Hg lamp.

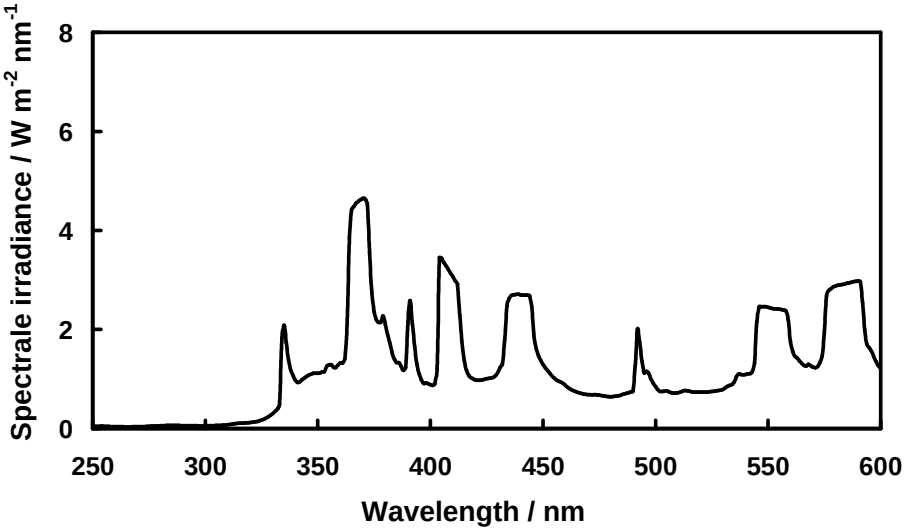

Figure 4.6 Emission spectrum of the 400-W high-pressure Hg lamp.

a)

b)

Figure 4.7 a) Shimadzu GC-8A gas chromatograph with a TC detector, equipped with Porapak-Q column, used for CO_2 gas phase analysis. b) Molectron PM5200 laser power meter used for daily checking the emission intensity of the Hg lamp.

4.2.3 Action spectra of acetic acid decomposition

In order to better elucidate the origin of the enhanced photoactivity of home-made doped materials and verify their possible activation in the visible region, the photooxidation of the transparent acetic acid substrate was systematically investigated as a function of the irradiation wavelength. Different series of action spectra, yielding the wavelength dependence of the apparent quantum efficiency, were thus performed.

As pointed out by recent review papers, action spectra analysis represents one of the most important and powerful photocatalytic characterization tools that enables one to discriminate the origin of real photoresponse by checking the wavelength dependence of photoactivity.[3,4] In particular, in order to show real visible-light induced activity of doped semiconductors it's strongly recommended to evidence resemblance between their absorption (diffuse reflectance) spectra and their action spectra.

In this regard Fig. 4.8 shows representative results proving visible-light response of sulfur-doped titania,[5] as a rare case among studies on visible light-sensitive photocatalysts, showing the resemblance of a diffuse-reflectance spectrum with an action spectrum for the photocatalytic oxidative decomposition of acetic acid in aerated

aqueous solution; in this case doping of (or at least modification with) sulfur induced photoabsorption and photocatalytic activity in the visible-light region.

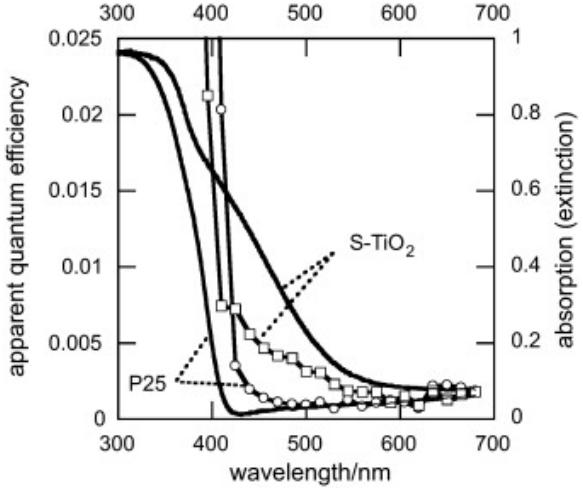

Figure 4.8 Diffuse reflectance (photoabsorption) and action spectra for acetic acid decomposition in aerated aqueous solutions of sulfur-doped titania (S-TiO_2) and Degussa (Evonik) P25.

Monochromatic light irradiation is required in order to record an action spectrum. In this thesis the photocatalytic decomposition of acetic acid in aerated liquid suspensions was investigated as a function of irradiation wavelength in quartz cells with a *ca*. 10.5 mL volume. Each photocatalyst powder (20 mg) was suspended in an aqueous solution (2.0 mL) containing 5.0 vol.% of acetic acid. The suspensions were stirred in the dark for 15 min, to attain the adsorption equilibrium of the substrate on the photocatalyst surface. A 300-W xenon lamp (Hamamatsu Photonics C2578-02) was employed as the irradiation source within a diffraction grating-type illuminator (Jasco CRM-FD), allowing selection of the irradiation wavelength in the 300–520 nm range, with a full width at half-maximum intensity (FWHM) of *ca*. 17 nm, irrespective of the selected irradiation wavelengths range, and a 20-nm step (Fig. 4.9).

The irradiation intensity, measured by a Hioki 3664 optical power meter (Fig. 4.9), was in the 15–20 mW range. All other conditions were similar to those of photocatalytic activity tests under high-pressure mercury lamp irradiation except for the use of Shimadzu GC-14B gas chromatograph with a FID detector, equipped with a Shimadzu MTN-1 kit for CO_2 methanation. The action spectra of selected photocatalysts were also measured in the 370–460 nm range with a 10-nm step and a narrower FWHM under otherwise identical experimental conditions.

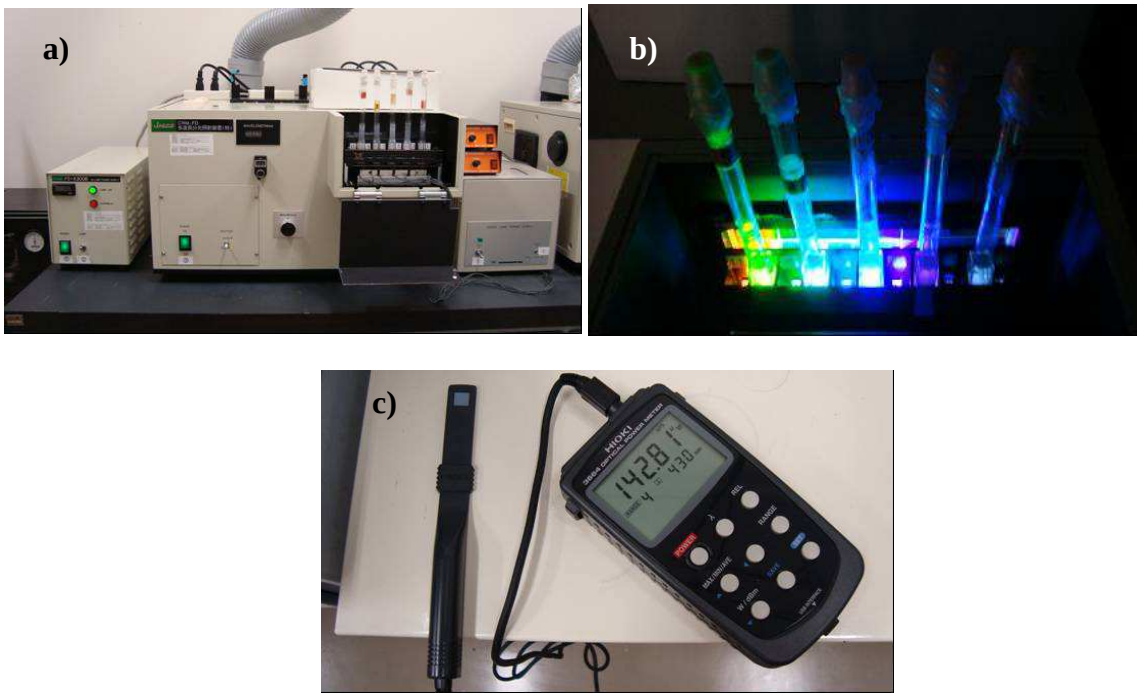

Figure 4.9 a-b) Apparatus employed for acetic acid photooxidation under monochromatic light irradiation. c) Hioki 3664 optical power meter used for checking the emission intensity at each selected wavelength.

The wavelength-dependent apparent quantum efficiency Φ_{app} was calculated as the ratio between the rate of photogenerated holes consumption and the flux of incident photons, by taking into account the fact that 8 electrons (holes) are required according to the stoichiometry of the reaction: $CH_3COOH + 2\ O_2 \rightarrow 2\ CO_2 + 2\ H_2O$. In particular the calculation of apparent quantum efficiency was performed by using the following formula:

$$\phi_{app} = \frac{v[mol \cdot h^{-1}] \cdot 4}{I[mJ \cdot s^{-1}] \cdot 10^{-3}[J \cdot mJ^{-1}] \cdot 3600[s \cdot h^{-1}] \cdot \frac{1}{\frac{h[J \cdot s] \cdot c[m \cdot s^{-1}]}{\lambda[nm] \cdot 10^{-9}[m \cdot nm^{-1}]} \cdot N_{AV}[mol^{-1}]}} \qquad (4.1)$$

where:

v = zero-order rate constant of CO_2 photocatalytic evolution obtained during acetic acid decomposition under a specific irradiation wavelength (λ).

I = incident light intensity on the quartz cell, measured at the investigated irradiation wavelength (λ).

h = Planck constant ($6.62 \cdot 10^{-34}$ J·s).

c = speed of light ($3.00 \cdot 10^{8}$ m·s^{-1}).

N_{AV} = Avogadro constant ($6.02 \cdot 10^{23}$ mol^{-1}).

Finally it's worth to recall that the calculation of apparent quantum efficiency of heterogeneous photocatalytic reactions is mainly based on the following assumptions:

- The number (*n*) of photogenerated electrons/holes necessary to obtain a molecule product of the photocatalytic reaction (in our case CO_2) are produced by the absorption of the same number (*n*) of photons.
- By considering the difficulty in determining the amount of photons really absorbed by the investigated suspension (mainly because of scattering limitations), one can just refer to the number of incident photons, thus referring to '*apparent*', and not real, quantum efficiency.

4.3 References

1. C. G. Hatchard and C. A. Parker, Proc. R. Soc. London, Ser. A, **1956**, 235, 518.
2. M. Mrowetz and E. Selli, J. Photochem. Photobiol. A: Chem., **2006**, 180, 15.
3. B. Ohtani, Chem. Lett., **2008**, 37, 3, 217.
4. H. Zhang, G. Chen and D. W. Bahnemann, J. Mater. Chem., **2009**, 19, 5089.
5. X. Yan, T. Ohno, K. Nishijima, R. Abe and B. Ohtani, Chem. Phys. Lett., **2006**, 429, 606.

Chapter 5

Effects of gold nanoparticles deposition on the photocatalytic activity of TiO_2 under visible light

5.1 Introduction

Heterogeneous photocatalysis with semiconductors is widely investigated as a useful technique not only for the degradation of contaminants in waste water and air, but also for solar energy harvesting.[1-5] Photocatalytic processes are initiated by semiconductor excitation with photons of energy higher than the band gap, yielding electron-hole pairs formation. Adsorbed organic compounds usually undergo oxidative decomposition, initiated either by the attack of hydroxyl radicals, produced by reaction of valence band holes with water or surface hydroxyl groups, or by direct interaction with photo-generated holes, leading to oxidised intermediates. At the same time, photo-promoted conduction band electrons may be scavenged by interaction with adsorbed reducible species, *i.e.* oxygen molecules if present, or H^+ in water to yield hydrogen molecules.

Two major factors presently limit extensive applications of photocatalytic processes. First of all, the most widely employed semiconductor photocatalysts, *i.e.* ZnO, WO_3 and in particular TiO_2 for its outstanding stability and electronic properties, can absorb only a minor portion of the solar energy, their bandgap being above 3 eV. Doping with non-metallic impurities[6,7] presently appears the most promising route to solve this problem.[4,5] The second limiting factor is that photogenerated electron/hole pairs undergo very fast recombination, releasing energy in the form of unproductive heat or photons. Conduction band electrons transfer to molecular oxygen has been recognised as the rate determining step in photocatalytic oxidation processes.[8] If O_2 is not reduced at a sufficiently high rate, electrons accumulate on the photocatalyst, with a consequent enhancement of electron-hole recombination.

Such highly undesired energy dissipation path may be reduced in the presence of noble metals on the semiconductor surface.[9,10] Owing to the formation of a Schottky junction at the metal-semiconductor interface, conduction band electrons can be efficiently captured by noble metals having a Fermi level lower in energy than the semiconductor conduction band potential. This would facilitate electron transfer to reducible species and increase electron-hole separation.

The deposition of noble metals, such as platinum,[11-14] gold,[12,15-23] silver[24,25] and palladium,[9,12,26] on semiconductor oxides has been reported to increase their photocatalytic activity, though controversial results have also been reported.[26-29] In fact, whereas the positive effect of noble metal co-catalysts on the photocatalytic production of hydrogen from water is well established since long time,[9,10,30-32] their effective role

in photocatalytic oxidative reactions is still under debate, especially in the case of gold-modified TiO_2.[33-36] Recent studies evidenced that the properties of such metal/oxide composites depend on the preparation method, in particular on the conditions of gold deposition, on gold loading, particles size and shape, and also on storage conditions.[37-39]

Deposition-precipitation (DP) is one of the most successful wet-chemical methods to deposit highly dispersed Au nanoparticles on metal oxides having an isoelectric point above 5, such as MgO, TiO_2, and Al_2O_3. The method has been widely employed in recent years to produce gold nanoparticles catalytically active, *e.g.* in the oxidation of CO at low temperature. The deposition of gold(III) species is usually followed by calcination to reduce the metal and obtain gold nanoparticles in metallic form.[40]

In the present study the photocatalytic performance under visible light of TiO_2 modified by gold nanoparticles deposition according to the DP procedure has been investigated, focusing on the effects induced by the deposition conditions and on the method, either thermal or chemical, employed for subsequent gold reduction. The photocatalytic oxidative degradation of two organic substrates, *i.e.* the azo dye Acid Red 1 (AR1) and formic acid (FA), was employed as test reaction. The main reductive path simultaneously occurring in the presence of air, *i.e.* hydrogen peroxide evolution initiated by O_2 combination with conduction band electrons, was also monitored during the runs, in order to have a better insight into the role played by gold nanoparticles on both primary photocatalytic processes.

5.2 Experimental section

5.2.1 Preparation and characterisation of Au/TiO_2 photocatalysts

Degussa P25 TiO_2 (50 m^2 g^{-1}, nanoporous, usually 80% anatase and 20% rutile, purity > 99.5%) was employed as starting material and used as received. Four series of Au/TiO_2 photocatalysts, labelled as DP x%, DPU x%, DPN x% and DPH x% , with "x" referring to the mass percent of gold, were prepared as follows.

The DP series was prepared following the original Haruta's method.[40] The TiO_2 support was dispersed in water (about 10 g L^{-1}) and the required amount of gold, in the form of $HAuCl_4$ solution (10 g L^{-1} Au), was added under vigorous stirring. Then the pH was adjusted to 10 by dropwise addition of a 1 M NaOH solution. The suspension was stirred for 3 h, filtered and repeatedly washed with distilled water to remove residual

Na^+ and Cl^- ions, as well as Au species not adsorbed on the semiconductor. Gold was then reduced by calcination in air at 450°C for 4 h.

The DPU samples were prepared according to a modified deposition method,[37] using urea as the precipitating agent. The required amount of TiO_2 was added to an aqueous solution containing $HAuCl_4$ (0.100 g L^{-1} Au) and urea (0.42 M). The suspension, thermostated at 80°C, was vigorously stirred for 4 h, until pH 7 was reached. The slurry was then filtered, washed thoroughly with water, dried at 80°C for 2 h and then calcined in air at 450°C for 4 h. This method allows a gradual and homogeneous addition of hydroxide ions throughout the suspension, thus minimising metal hydroxide precipitation in the aqueous phase and the consequent loss of precious metal.

DPN and DPH photocatalysts were prepared following the initial steps of the above-described DP procedure, but avoiding the final calcination step. DPN Au/TiO_2 was prepared by suspending the Au^{III}/TiO_2 powder in distilled water (about 10 g L^{-1}), followed by reduction due to addition, under stirring, of a 0.1 M freshly prepared solution of $NaBH_4$ ($NaBH_4$/Au = 5 mol/mol). After 10 min the slurry was filtered, thoroughly washed with distilled water and finally dried at 80°C for 2 h. Alternatively, the Au^{III}/TiO_2 powder was reduced in a hydrogen stream (10 mL min^{-1}) at 150°C for 2 h, yielding the DPH 1% sample.

The actual Au loadings on the TiO_2 powder were determined by ICP analysis on the filtrate. Au/TiO_2 photocatalysts with the following percent weight content of gold were prepared: 0.06%, 0.13%, 0.38% (DP), 0.5% and 2.5% (DP and DPU), 1.3% (DPN and DPH). A reference sample (0% Au) for each series was also prepared following the above described procedures, except for $HAuCl_4$ addition.

UV–vis diffuse reflectance (DR) spectra were recorded using a Lambda 19, Perkin-Elmer spectrophotometer equipped with an RSA-PE-20 integrating sphere assembly, using a calibrated SRS-99-010 Spectralon Reflectance Standard, produced by Labsphere, as a reference material.

HRTEM analysis was carried out with a JEM 3010 (JEOL) electron microscope operating at 300 kV, point to point resolution at Scherzer defocus of 0.17 nm. Specimens for HRTEM analysis were sonicated in 2-propanol and then transferred as a suspension to a copper grid covered with a holey carbon film.

XPS analyses were performed by a PHI-5500 – Physical Electronics spectrometer, equipped with a monochromatised source with aluminium anode (Kα = 1486.6 eV), operating at a 200 W of applied power, 5.85 eV pass energy and 0.05 eV energy step. XPS spectra were collected at takeoff angles of 45°. The analysis area was around 0.5 mm^2, the depth within 10 nm. The charging effect on the analysis was corrected considering the binding energy (BE) value of C 1s, due to adventitious carbon, at 284.8 (±0.3) eV. Quantification and spectral line decomposition were obtained using the PC-ACCESS software provided by Physical Electronics. These analyses were performed by Dr. Laura Meda at Eni Donegani, Novara.

X-ray diffraction analysis was performed employing a Philips PW 1820 powder diffractometer, operating at 40 kV and 40 mA, using filtered Cu K_α radiation (λ = 1.54056 Å). The BET surface area was measured by N_2 adsorption/desorption at 77 K on a Micromeritics ASAP 2010 apparatus.

5.2.2 Photocatalytic activity measurements

5.2.2.1 Materials

Acid Red 1 (AR1, an azo dye bearing two sulfonic groups), see Scheme 5.1, and formic acid (FA) were purchased from Aldrich. Peroxidase (type II, from horseradish) was purchased from Sigma. Tris(hydroxymethyl)aminomethane 99.7% was purchased from Baker Chemicals and *p*-hydroxyphenylacetic acid (POHPA), > 98% (fluorescence degree) was purchased from Fluka. All reagents were employed as received.

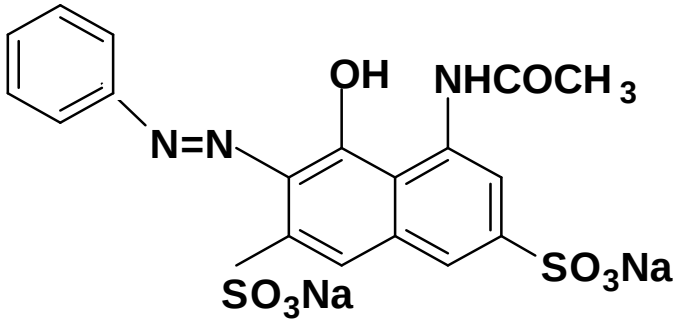

Scheme 5.1 Acid Red 1 (AR1).

5.2.2.2 Apparatus and procedure

All photocatalytic degradation runs were performed under atmospheric conditions in a magnetically stirred 60 mL cylindrical quartz reactor, inserted in a home made housing consisting in a black box mounted on optical bench, as described in Section 4.1. In particular the initial concentration of AR1 and FA in the aqueous suspensions containing 0.1 g L^{-1} of photocatalyst were 2.5×10^{-5} M and 1.0×10^{-3} M, respectively.

The cleavage of the AR1 azo bond, leading to its photobleaching, was monitored by spectrophotometric analysis at 531 nm [maximum AR1 absorption, $\varepsilon = (3.13 \pm 0.02) \times 10^4$ M^{-1} cm^{-1}]. FA mineralization was usually determined using a Total Organic Carbon (TOC) analyser (Shimadzu Instruments, TOC-5000A) in both the total carbon (TC) and inorganic carbon (IC) modes. TOC content was then calculated as the difference between TC and IC analyses. In some of the runs, FA concentration was monitored also by ion chromatography; results perfectly matching those of TOC analysis were obtained by this way.

All kinetic runs were performed at natural pH, up to *ca.* 70% substrate degradation, and repeated at least twice, to check their reproducibility. The pH of the suspension was measured before and after each degradation run. A decrease in pH was observed during AR1 photocatalytic degradation, from an initial value in the 6.5-5.5 range to a final value in the 4.5-3.8 range, as a consequence of the production of stable acids, due to the removal of the sulfonic groups and the oxidation of the azo double bond.[41] During FA degradation the pH increased, from initial values of 3.7 to *ca.* 4.8, as a consequence of the mineralization of the acid to CO_2 and H_2O.

Hydrogen peroxide concentration was monitored during the photodegradation runs by fluorimetric analysis (λ_{ex} = 316.5 nm, λ_{em} = 408.5 nm) of the fluorescent dimer formed in the horseradish peroxidase-catalysed reaction of hydrogen peroxide with *p*-hydroxyphenylacetic acid (POHPA),[42,43] using a 605-10S Perkin Elmer fluorescence spectrophotometer and an appropriate calibration curve, as already described.[44] In several experiments of FA photocatalytic degradation, H_2O_2 production was so high that successive dilutions of the surnatant solution were necessary to obtain fluorescence signals falling within the linear intensity *vs.* H_2O_2 concentration range, in order to avoid saturation of the fluorescence signal and auto-absorption phenomena.

5.3 Results and discussion

5.3.1 Photocatalysts design

As in most studies on gold-modified titanium dioxide photocatalysts,[12,19,21-23] the investigated Au/TiO_2 specimens were obtained by gold nanoparticles deposition on Degussa P25 TiO_2, which is widely employed as benchmark in photocatalysis owing to its high photocatalytic activity, though its properties may vary from batch to batch. This TiO_2 powder is manufactured by flame hydrolysis of titanium tetrachloride at high temperature and consists of intimately interconnected anatase (*ca.* 80%) and rutile particles. Recent studies of our research group evidenced that the photocatalytic performance under UV light of Au/TiO_2 photocatalysts prepared from P25 strongly depends on the procedure employed to deposit gold and on its amount on the TiO_2 surface.[45] During this thesis the attention was focused on the visible light activity of Au/TiO_2 photocatalysts and on the effects of gold nanoparticles deposition on the photocatalytic paths. All investigated Au/TiO_2 samples were prepared by deposition-precipitation, employing two different procedures to induce Au precipitation[37,40] (DP and DPU series) and different routes, either thermal (DP and DPU series) or chemical (DPN and DPH series), to reduce gold. Furthermore, aiming at discriminating the effects of gold nanoparticles on the oxide surface from those induced by TiO_2 modifications consequent to the deposition treatment,[39] for each series of Au/TiO_2 photocatalysts a blank sample was prepared following exactly the same procedure, apart from the addition of the gold precursor.

5.3.2 Photocatalysts characterisation

5.3.2.1 UV-vis DR spectra

The deposition of gold nanoparticles on TiO_2 was confirmed by the colour change of the modified oxide powder, turning from white into purple of different intensity, originated from the surface plasmon resonance of nanocrystalline Au^0 particles. As shown in Fig. 5.1, reporting the absorption properties of the DP Au/TiO_2 series in comparison to that of P25, all modified specimens, including the blank DP 0% sample, exhibited a red-shift of the absorption edge. A similar effect, whose origin is unclear, was reported in recent literature.[23] Gold containing samples also displayed the typical plasmon resonance absorption band, with a maximum around 550 nm. This absorption is observed when the wavelength of the incident light is much larger than the

nanoparticle size and is originated by light in resonance with the surface plasmon oscillation, causing the free electrons in the metal to oscillate in resonance with the light's frequency.[46] The intensity of the plasmon resonance band clearly increased with increasing the gold loading for the lower loading values in the DP series (Fig. 5.1), without any appreciable difference in the absorption maximum, indicating a progressive increase in particles density without marked variation of their dimensions. The absorption increase was much smaller when passing from 0.5% to 2.5% Au, with a sort of saturation behaviour.

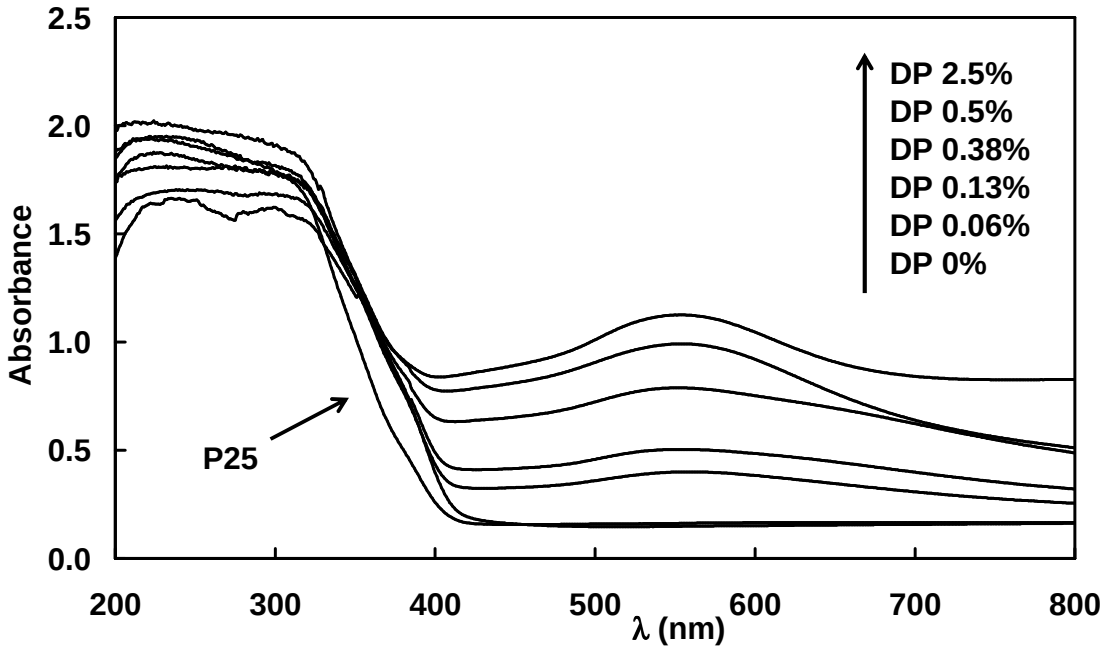

Figure 5.1 Absorption spectra of the DP Au/TiO_2 series with increasing Au loading.

By comparing the absorption bands of the DP series (Fig. 5.1) with those of the other Au/TiO_2 series (Fig. 5.2), some differences can be noticed, in relation to the gold nanoparticles properties[46] depending on the deposition method. In particular, DPU Au/TiO_2 exhibited a plasmon resonance band slightly shifted to longer wavelengths with respect to the DP series, indicating larger Au nanoparticles dimensions, whereas for the chemically reduced DPN and DPH photocatalysts the plasmon absorption band was blue-shifted and apparently less intense. This points to smaller gold nanoparticles[46] obtained by chemical reduction with respect to those obtained by the DP and DPU methods, both implying a calcination step.

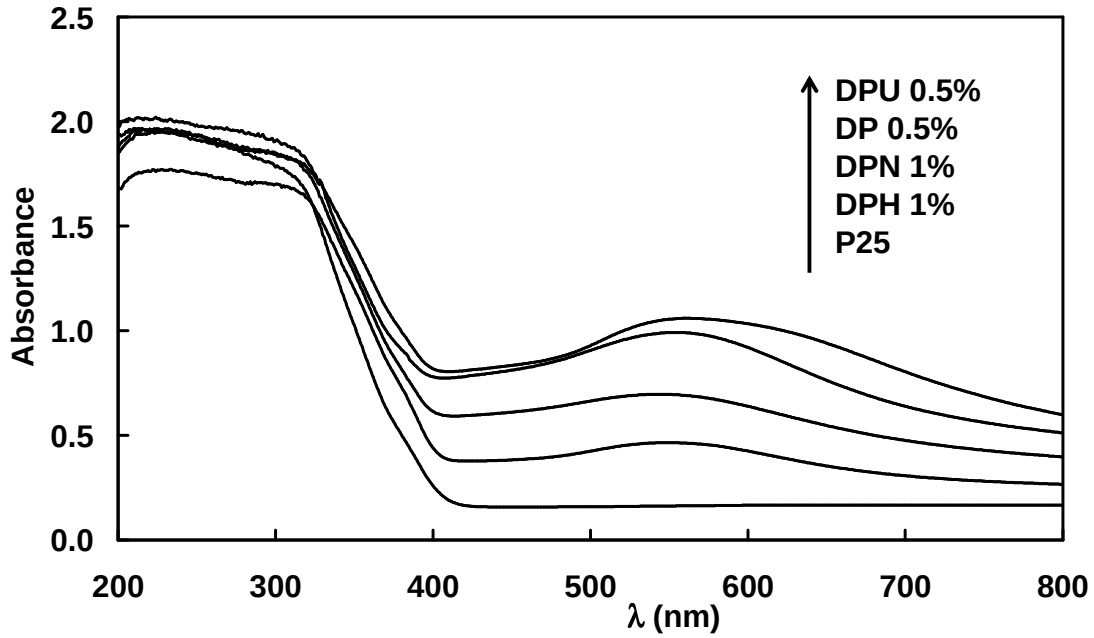

Figure 5.2 Absorption spectra of different Au/TiO_2 samples.

5.3.2.2 XPS analysis

The presence of gold nanoparticles was confirmed by XPS analysis. The XPS spectra of Au/TiO_2 photocatalysts exhibit two peaks at binding energies (BE) of *ca.* 84.0 eV and 87.7 eV, originated from Au $4f_{7/2}$ and $4f_{5/2}$ electrons of metallic gold.[39,47] Though exhibiting a light purple colour, the DP 0.13% and DPH 1% powders had a surface gold content below the XPS detection limit.

The surface chemical composition of representative Au/TiO_2 photocatalysts, as determined by XPS analysis, is reported in Table 5.1. All samples maintained a O/Ti atom ratio very close to 2, indicating no variation in the metal oxide composition,[39] and all of them, including the unmodified P25, exhibit a not negligible amount of adventitious surface carbon, with a percent amount of carbon slightly higher in the DP series. Trace amounts of Si 2p (*ca.* 1%), of Cl 2p (*ca.* 1%) and of N 1s (below 1%) were also detected, without any distinct dependence on the preparation conditions. In particular, no significant variation of chlorine atoms content was determined with respect to that of pristine P25, indicating the almost negligible persistence of Cl^- ions originated from the gold precursor.

In order to evidence possible variations of surface hydroxyl groups,[19,39,47] the oxygen 1s peak was fitted by two components, corresponding to oxygen in the oxide lattice (530.7 eV) and surface OH groups or undissociated water (531.8 eV). For all samples,

lattice oxygen constituted the majority of surface oxygen atoms,[39] being around 83% for unmodified P25 and also for the various specimens of the different Au/TiO_2 series.

Table 5.1 Surface composition of TiO_2 and Au/TiO_2 photocatalysts from XPS analysis.

	Atom %			
	C 1s	**O** 1s	**Ti** 2p	**Au** 4f
P25	14.1	55.9	28.0	---
DP 0%	12.8	55.5	28.0	---
DPU 0%	14.2	56.3	28.2	---
DPN 0%	12.5	55.7	28.5	---
DPH 0%	14.1	56.4	28.2	---
DP 0.13%	18.8	51.5	26.6	n.d.
DP 0.5%	18.6	52.4	25.7	0.46
DPU 0.5%	13.3	54.4	28.4	0.16
DPN 1%	15.5	53.8	27.6	0.19
DPH 1%	17.2	53.6	27.0	n.d.

n.d. = not determined

5.3.2.3 HRTEM analysis

Gold deposition on TiO_2 was also verified by HRTEM analysis, yielding valuable, direct information on the dimension and the distribution of Au nanoparticles on the TiO_2 surface. The mean diameter of gold nanoparticles obtained by chemical reduction varied between 2 and 4 nm, as shown in Fig. 5.3 (a,b) for DPN 1% and DPH 1%, respectively. Gold particles could hardly be distinguished in the HRTEM image of this latter (Fig. 5.3 b), because they are apparently embedded between oxide particles. On the contrary, deposited Au nanoparticles were clearly visible in the DP and DPU samples, with larger, rather variable dimensions, in the 4-10 nm range, as shown in Fig. 5.3 (c,d). This directly confirms the hypothesis drawn from the analysis of the plasmon resonance bands in DR analyses, *i.e.* the heat treatment at 450°C used for gold

reduction in the DP and DPU series implies the formation of larger particles of metallic gold, with respect to DPN and DPH photocatalysts.

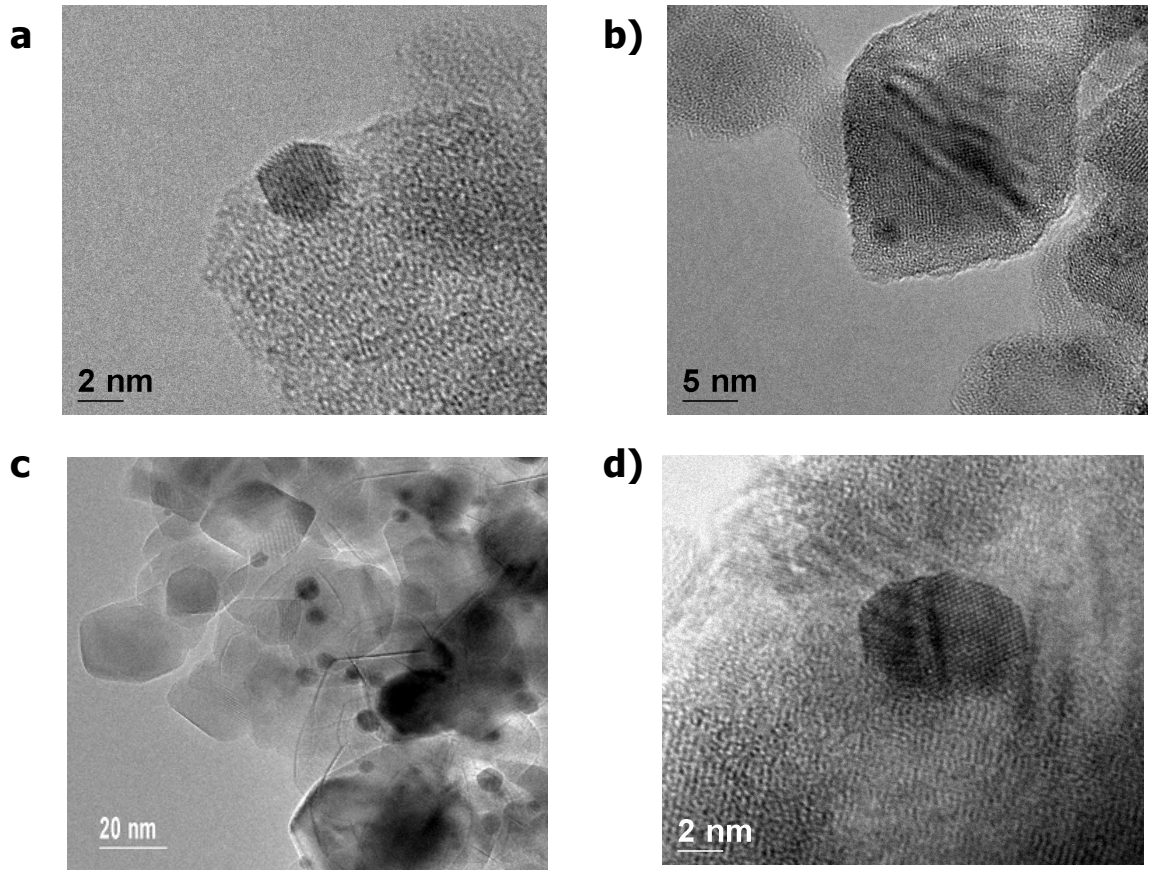

Figure 5.3 HRTEM images of Au/TiO_2: a) DPN 1%; b) DPH 1%; c) DP 0.5%; d) DPU 0.5%.

5.3.2.4 XRD and BET analyses

Practically identical XRD patterns were obtained with P25, DP 0%, DP 0.5%, DPU 0.5% and DPN 1% samples (not shown for the sake of brevity). Thus, gold deposition and calcination at 450°C apparently did not affect the original polymorph composition (anatase to rutile ratio ≈ 85/15 in the employed P25 batch), in agreement with recent reports.[23] Typical crystalline gold reflexes, expected at *ca.* $2\theta = 38.5$ and 44°, could not be detected in our XRD spectra, as in similar cases.[48]

Also the specific surface area of TiO_2, which has been recently reported to influence its photocatalytic activity more than its crystal structure,[49] did not vary upon gold nanoparticles deposition. In fact, BET analysis did not evidence any significant change in surface area for both blank and Au/TiO_2 samples with respect to unmodified P25, all

measured surface areas ranging between 50 and 53 m^2 g^{-1}, perfectly in line with analogous results obtained by other research groups.[12,19,25]

5.3.3 Photocatalytic activity

The photocatalytic activity of Au/TiO_2 samples was tested in aqueous suspensions, employing the azo dye AR1 or formic acid (FA) as degradation substrates. The stability of both substrates in aqueous solution was preliminarily verified under the adopted irradiation conditions. We also verified that they did not undergo any dark reaction catalysed by TiO_2 or by the deposited gold nanoparticles, which are known to catalyse low temperature CO oxidation. In particular, the stability of FA, even at 50°C, in a non-irradiated water suspension containing DPN 1% Au/TiO_2 was checked by highly sensitive ion chromatographic analysis.

5.3.3.1 AR1 photocatalytic degradation

The photocatalytic degradation of AR1 under visible light irradiation occurred at constant rate, *i.e.* according to a zero-order rate law, in the presence of both TiO_2 and Au/TiO_2 photocatalysts. The rate constant values k, obtained from the experimental AR1 concentration *vs.* time data, are collected in Fig 5.4, in the form of normalised values with respect to the rate constant value k_{P25} obtained with the benchmark P25 TiO_2 photocatalyst [$k_{P25} = (2.30 \pm 0.05) \times 10^{-9}$ M s^{-1}]. None of the Au/TiO_2 photocatalysts was more efficient than unmodified P25 and the effect of gold nanoparticles at first glance appeared small and not positive.

A more careful inspection of the rate data shown in Fig. 5.4 allows one to distinguish the effects induced by P25 TiO_2 modification consequent to the different Au deposition procedures from those induced by gold nanoparticles themselves. The degradation rate obtained with blank samples (0% Au content) was *ca.* 30% lower than that measured with unmodified P25 in the case of the DP and DPU series; the rate decrease was more limited for the chemically reduced DPN and DPH series. Thus, any modification of P25 implies a decrease of photocatalytic activity in AR1 degradation and this is more evident in the case of thermal treatments. However, the possible heat-induced conversion of the anatase phase into the usually less photoactive rutile phase should be excluded, on the basis of our XRD results. Furthermore, no significant variation in surface area of the photocatalysts with respect to P25 could be detected by BET

analysis. A reasonable explanation of the decreased photoactivity is that heat treatments reduce the amount of surface OH groups,[19,23] as verified by FTIR analysis.[47] This would lead to a decreased efficiency of hole trapping in the form of $TiO^{\bullet}$ and a lower availability of $^{\bullet}OH$ radical precursors.

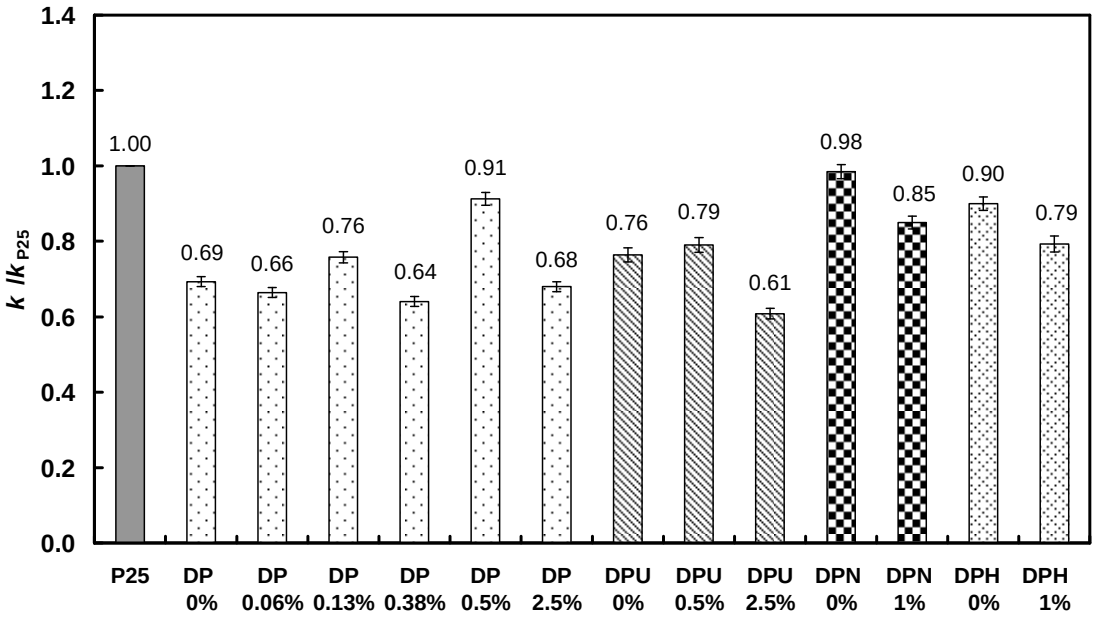

Figure 5.4 Photocatalytic degradation of AR1: ratio between the zero-order rate constant k measured with different Au/TiO_2 samples and that obtained with unmodified P25, k_{P25}.

The effects induced by the presence of gold nanoparticles on the TiO_2 surface can be evaluated by comparing the activities of Au/TiO_2 photocatalysts of each series to that of the corresponding blank specimens (0% Au loading). Whereas for the DP and DPU series small up and down effects can be seen (Fig. 5.4), with a clearly positive effect of Au nanoparticles only in the case of DP 0.5%, the presence of gold led to an activity decrease for the DPN and DPH photocatalysts, prepared by chemical reduction.

Kinetic results of hydrogen peroxide evolution during AR1 photodegradation complete this rather complex photoactivity picture. As already mentioned, H_2O_2 is produced through the main reduction path parallel to photocatalytic dye oxidation, *i.e.* O_2 reduction by conduction band electrons e_{CB}^-, according to reactions (5.1) and (5.2):

$$O_2 + e_{CB}^- \rightarrow O_2^{\bullet -} \quad (5.1)$$

$$O_2^{\bullet -} + e_{CB}^- + 2\,H^+ \rightarrow H_2O_2 \quad (5.2)$$

As shown in Fig. 5.5, hydrogen peroxide concentration in the aqueous phase continuously increased during all AR1 photodegradation runs, though with different slope for the different photocatalysts.

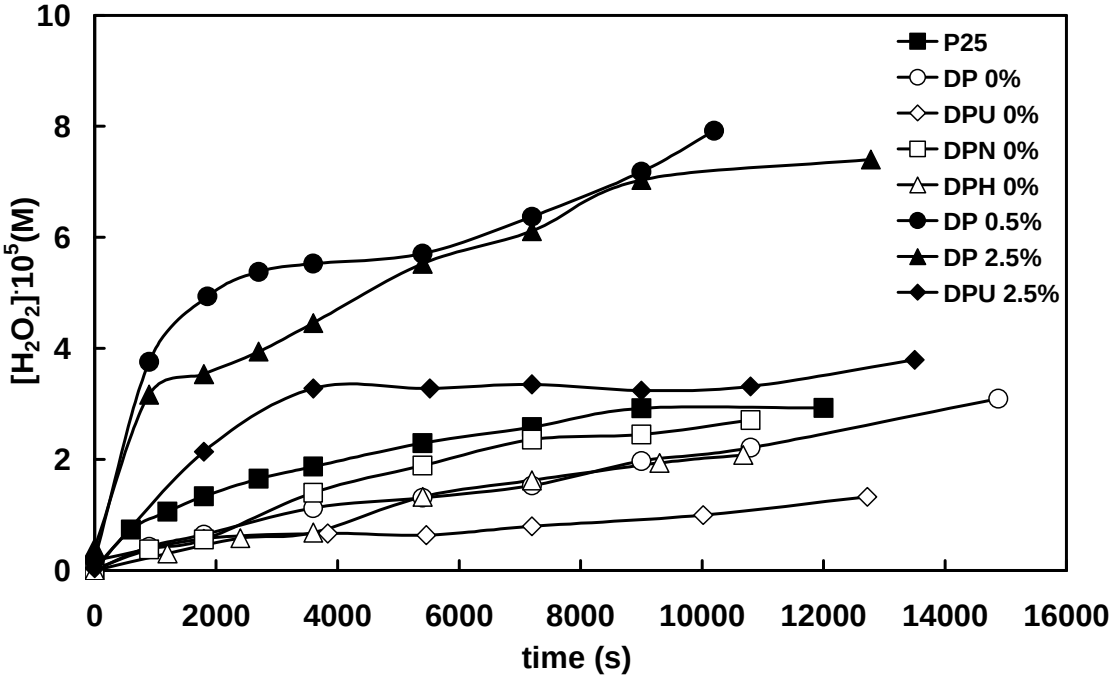

Figure 5.5 H_2O_2 evolution during AR1 photodegradation on different Au/TiO_2 samples, also including blank samples.

In the presence of all blank photocatalysts the rate of H_2O_2 accumulation was lower than with P25. A clearly parallel behaviour was thus observed between the oxidative and the reductive photocatalytic paths occurring on the bare TiO_2 surface: blank samples leading to lower AR1 photodegradation rate also led to lower H_2O_2 production rate, with almost identical photocatalytic activity scale for the two processes. This is in line with the identification of photogenerated charge carriers separation in semiconductors as the limiting step in both oxidative and reductive photocatalytic processes.

At difference with its effect in AR1 oxidative photodegradation, the presence of gold nanoparticles on the semiconductor led to an increase in H_2O_2 production rate within each photocatalyst series (see Fig. 5.5), with the maximum H_2O_2 amount produced with DP 0.5%, the photocatalyst exhibiting the higher photoactivity in AR1 degradation. The maximum hydrogen peroxide concentration attained during AR1 degradation with different Au/TiO_2 photocatalysts is reported in Table 5.2.

Table 5.2 Maximum H_2O_2 concentration attained during FA and AR1 photodegradation on P25 and on Au/TiO_2 samples.

	$10^5 \times [H_2O_2]_{max}$ (M)	
	AR1	**FA**
P25	2.9	0.07
DP 0.06%	3.2	0.52
DP 0.13%	3.6	1.1
DP 0.38%	4.1	21.7
DP 0.5%	7.9	27.9
DP 2.5%	7.4	24.4
DPU 0.5%	3.1	7.6
DPN 1%	3.3	25.4
DPH 1%	2.4	0.61

The effect of gold nanoparticles on TiO_2 thus appears controversial: they favour e_{CB}^- transfer to O_2 leading to H_2O_2 production, but the rate of AR1 photodegradation does not increase in parallel, probably resulting from several concurring effects. Of course, both adsorption equilibria and photoinduced electron transfer reactions can be affected by any surface modification of TiO_2.

The presence of gold nanoparticles may inhibit substrate adsorption on TiO_2. Preliminary tests performed with DP 1% Au/TiO_2 evidenced a substantial decrease of AR1 adsorption with respect to unmodified P25.[45] This is in line with the reported shift of the iso-electric point of Au/TiO_2 to lower pH values with respect to unmodified TiO_2,[16] which extends the pH region where the photocatalytic surface is negatively charged and the adsorption of negatively charged compounds, such as the bisulphonic azo dye AR1, is hindered.

Furthermore, as to mechanistic aspects, it is worth recalling that the azo dye AR1 itself absorbs a considerable portion of visible light under the adopted irradiation conditions. As shown in Fig. 5.6, its absorption spectrum largely overlaps the emission spectrum of the irradiation source employed in the present study. A self-sensitised mechanism is thus expected to be also at work: the dye molecule, excited by visible light, is able to transfer an electron into the conduction band of TiO_2, converting itself

into its radical cation,[50-52] which undergoes oxidation by interaction with O_2. The injected electron can then react with dioxygen adsorbed on the TiO_2 surface, to generate the superoxide radical anion and then other active oxygen species, such as H_2O_2, according to reactions (5.1) and (5.2).

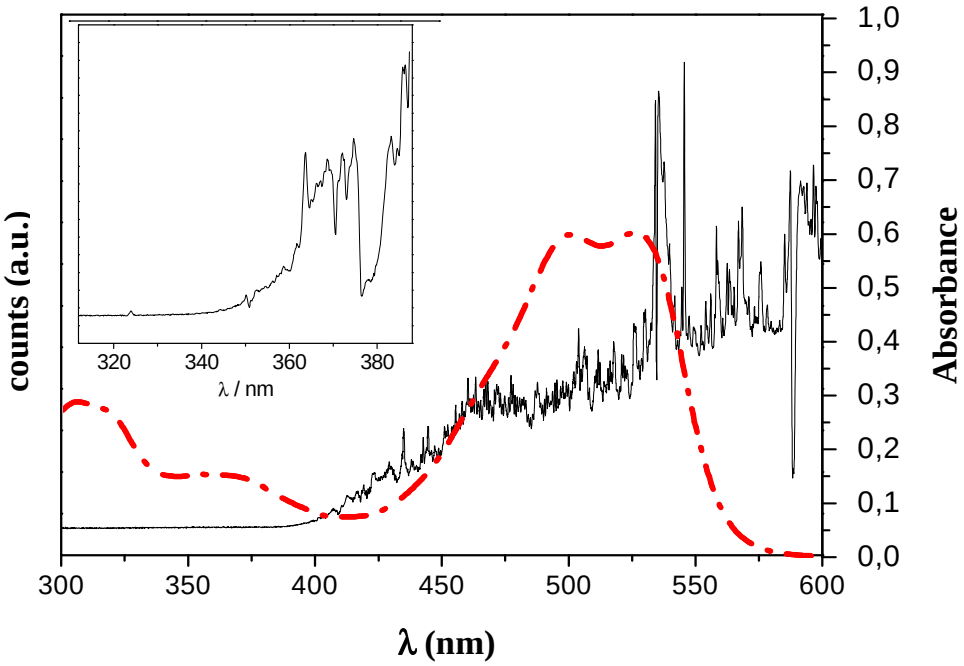

Figure 5.6 Emission spectrum of the Osram lamp and absorption spectrum of a 2.5 × 10^{-5} M aqueous solution of the dye AR1.

In order to verify the existence and extent of such mechanism, photocatalytic runs were carried out under conditions that exclude semiconductor band gap excitation. The high energy components of the emission spectrum of the lamp, which are absorbed by TiO_2, were eliminated by means of 400 or 455 nm cut off filters. Under such conditions AR1 degradation obviously occurred at lower rate. The rate constants obtained when employing P25 as photocatalyst were $k_{P25} = (2.0 \pm 0.1) \times 10^{-10}$ M s^{-1} ($\lambda_{irr} > 400$ nm) and $k_{P25} = (9.5 \pm 0.7) \times 10^{-11}$ M s^{-1} ($\lambda_{irr} > 455$ nm), *i.e.* the reaction rate was reduced to *ca.* 8.7% and 4.1% with respect to the rate measured with the full lamp emission. This demonstrates that a self-sensitised AR1 degradation mechanism was operative, parallel to that initiated by semiconductor band gap excitation, and its weight on the overall AR1 degradation under full lamp irradiation depended on the emission spectrum itself.

Gold nanoparticles on TiO_2 may affect the weight of this self-sensitised path. When employing the 455 nm cut off filter and DP 2.5% as photocatalyst, the rate constant of AR1 photodegradation was $k = (7.8 \pm 0.2) \times 10^{-11}$ M s^{-1}, to be compared with k = (1.40

$\pm 0.02) \times 10^{-9}$ M s^{-1} obtained with the full lamp emission. Thus, a residual reaction rate around 5.6% was maintained with $\lambda_{irr} > 455$ nm, *i.e.* slightly higher than the residual reaction rate obtained with P25 (*vide supra*), which does not exclude a possible role of gold nanoparticles in favouring the self-sensitised photodegradation of the dye.

Coming back to the photocatalytic activity results of Figs 5.4 and 5.5, a more in depth mechanistic analysis can be provided after discussing the results obtained in the photocatalytic degradation of formic acid (FA), whose interpretation is much more straightforward. In fact, FA does not absorb visible light, which excludes the existence of a self-sensitised path, and undergoes direct photocatalytic mineralization to CO_2 and H_2O, without the formation of any stable intermediate species, which may adsorb and react on the semiconductor surface, as in the case of AR1.

5.3.3.2 HCOOH photocatalytic mineralisation

FA photocatalytic degradation also occurred according to a zero-order rate law. The photocatalytic activity scale of the investigated TiO_2 and Au/TiO_2 samples can be appreciated in Fig. 5.7, reporting also in this case the ratio between the zero order rate constant of FA degradation obtained with each photocatalyst and that obtained in presence of unmodified P25 [$k_{P25} = (1.50 \pm 0.02) \times 10^{-7}$ M s^{-1}].

The decrease in activity consequent to the modification induced by Au deposition implying a thermal treatment was confirmed also in FA degradation: DP and DPU blank samples (0% Au) exhibited a lower photocatalytic activity with respect to unmodified P25. Chemical reduction by $NaBH_4$ also led to a decrease in photoactivity (DPN 0%), whereas the blank sample undergone hydrogen treatment (DPH 0%) was even more photoactive than P25 (Fig. 5.7). A comparison between the photoactivity of blank specimens in AR1 (Fig. 5.4) and FA (Fig. 5.7) degradation demonstrate that the effects induced by the deposition treatments influence the photocatalytic activity in different ways, which also depend on the adsorption and prevailing photodegradation mechanism of the organic substrate.

Fig. 5.7 also shows that for all the Au/TiO_2 photocatalyst series the presence of gold nanoparticles on TiO_2 was beneficial in the photocatalytic degradation of FA. As to the effect of Au loading, investigated within the DP series, the photocatalytic activity increased with increasing Au loading up to an optimal value (0.10 – 0.40%), and then

decreased. An optimal balance clearly exists between the beneficial role of gold nanoparticles in capturing e_{CB}^-, thus reducing the e_{CB}^- - h_{VB}^+ recombination rate, and the detrimental shielding effects of Au surface nanoparticles, decreasing the fraction of light absorbed by TiO_2. Similar trends and also similar values of optimal gold loading were recently reported in the degradation of different substrates.[12,19,23,33]

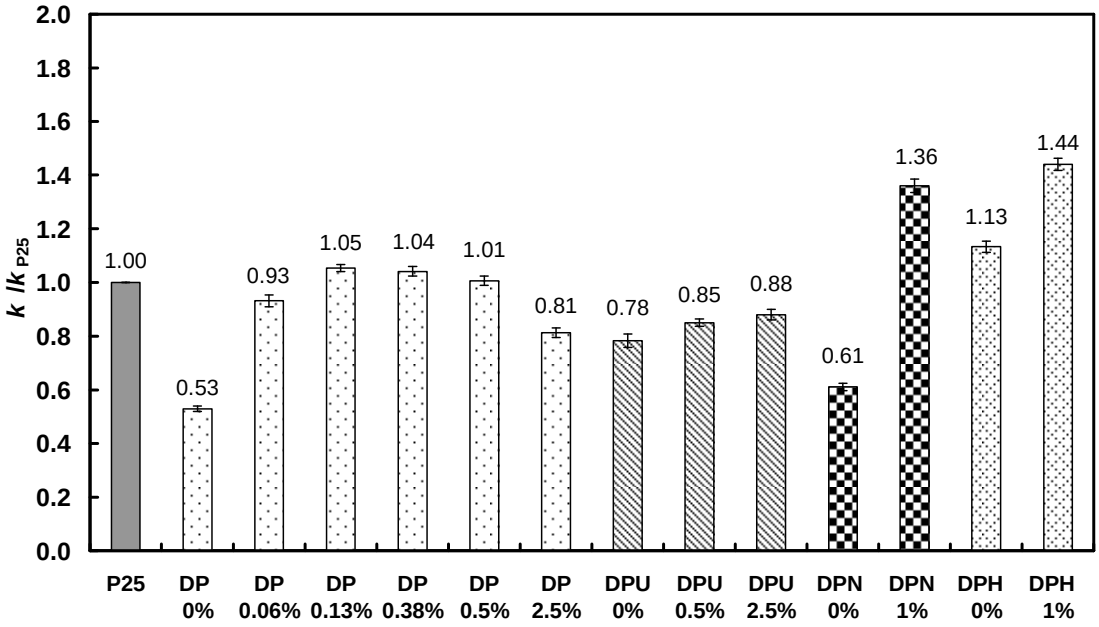

Figure 5.7 Photocatalytic degradation of formic acid: ratio between the zero-order rate constant k measured with different Au/TiO_2 samples and that obtained with unmodified P25, k_{P25}.

Au/TiO_2 photocatalysts prepared through chemical reduction (DPN 1% and DPH 1%) exhibited the best photocatalytic performance in FA photomineralization, with the highest rate increase attributable to the presence of Au nanoparticles being observed with DPN 1% (Fig. 5.7). Such photoactivity increase, higher than those observed for the DP and DPU series (Fig. 5.7), can be related to the lower Au nanoparticles size (2-3 nm) evidenced by HRTEM images. Very small Au particles were reported to be most active in CO oxidation[39,40] and to possess no more metallic, but semiconducting properties.[53] Their beneficial effect in photocatalytic processes might thus be ascribed to the creation of a semiconductor-semiconductor contact in Au/TiO_2, which could increase the separation of charge carriers photoproduced upon band gap excitation.[19]

With the FA substrate, unable to absorb visible light and undergo self-sensitised photocatalytic degradation, we also tried to evidence possible photoactivity initiated by excitation of the gold plasmon band, which has been first hypothesised by Ohtani's

group[36] in the case of gold deposited on large rutile particles. However, FA degradation rates measured with P25, DPN 0% and DPN 1% under irradiation with λ_{irr} > 400 nm were all *ca.* 5% of the corresponding rates measured under full lamp irradiation, indicating no rate increase consequent to gold nanoparticles excitation, in agreement with the results obtained also by Ohtani *et al*. when investigating the visible light-induced effects of gold deposition on P25.[36]

The H_2O_2 concentration profiles detected during FA photocatalytic degradation with the DP series photocatalysts are reported in Fig. 5.8. It is well established,[44,54,55] that H_2O_2 formation can hardly be detected during FA photomineralization on unmodified TiO_2, because of the high reactivity of the intermediate species produced on the oxide surface under irradiation.[54] The data shown in Fig. 5.8 confirm that practically no H_2O_2 could be detected during FA photomineralization on bare TiO_2 photocatalysts (P25 and DP 0%).

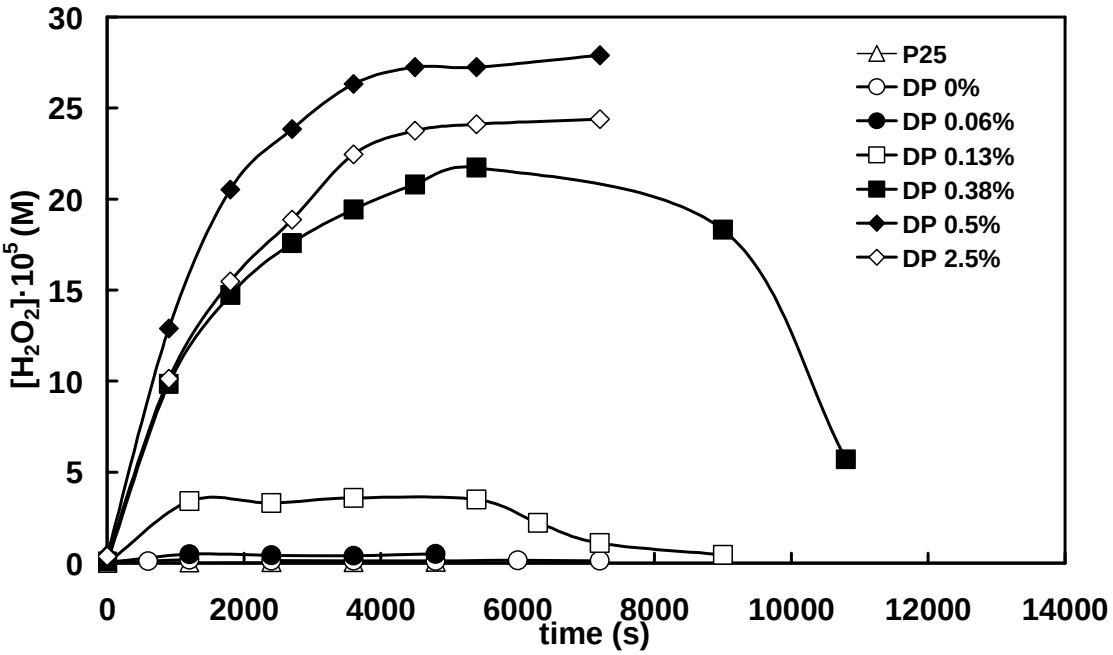

Figure 5.8 H_2O_2 evolution during FA photodegradation on P25 and on DP Au/TiO_2 samples with increasing Au loading.

By contrast, hydrogen peroxide was detected with gold-containing photocatalysts and its amount increased with increasing gold nanoparticles content up to DP 0.5%, and then slightly decreased with DP 2.5%. H_2O_2 concentration *vs.* irradiation time curves initially increased up to a maximum value and started to decline when total FA mineralization was attained. Maximum H_2O_2 concentration values recorded during FA

photodegradation on different Au/TiO_2 specimens, also reported in Table 5.2, were much higher than those attained during AR1 photocatalytic degradation, although the opposite occurred with the bare TiO_2 photocatalysts (see also Fig.s 5.5 and 5.8).

5.3.3.3 H_2O_2 photocatalytic degradation

A higher H_2O_2 accumulation during photocatalytic runs may result from either a higher production rate, or a lower H_2O_2 degradation rate, occurring through interaction with both conduction band electrons and valence band holes on the illuminated photocatalyst surface.[56]

Hydrogen peroxide photostability tests were performed with aqueous suspensions containing no organic substrate and initial H_2O_2 concentrations similar to those produced during the photocatalytic runs. The results shown in Fig. 5.9 demonstrate that P25 was the most active photocatalyst in hydrogen peroxide degradation under the irradiation conditions of the present work and any modification of its surface properties led to a decrease in photoactivity. In fact, H_2O_2 degradation was slower with DP 0%, though proceeding up to complete H_2O_2 disappearance. When a similar test was performed with gold-containing DP 0.5%, H_2O_2 concentration initially slightly decreased, but then tended to an almost constant value, indicating that the rate of H_2O_2 production (clearly occurring in this case also in the absence of organic species undergoing simultaneous oxidation) equaled its degradation rate under irradiation.

The lower photoactivity of DP 0% with respect to P25 demonstrates that the lower H_2O_2 amount detected during AR1 photodegradation with blank photocatalysts (Fig. 5.5) resulted from slower H_2O_2 formation, and not from faster H_2O_2 photodegradation on these latter, compared to P25. Furthermore, as to the effect of gold nanoparticles on the oxide surface, the higher H_2O_2 amounts detected with Au-containing photocatalysts in both AR1 and FA photocatalytic degradation (Fig.s 5.5 and 5.8 and Table 5.2) resulted from increased H_2O_2 formation rates, consequent to faster e_{CB}^- transfer to adsorbed dioxygen according to reaction (5.1), as discussed above. O_2 preferential adsorption on gold nanoparticles[57] was also invoked to contribute to the enhancement of e_{CB}^- transfer rate.

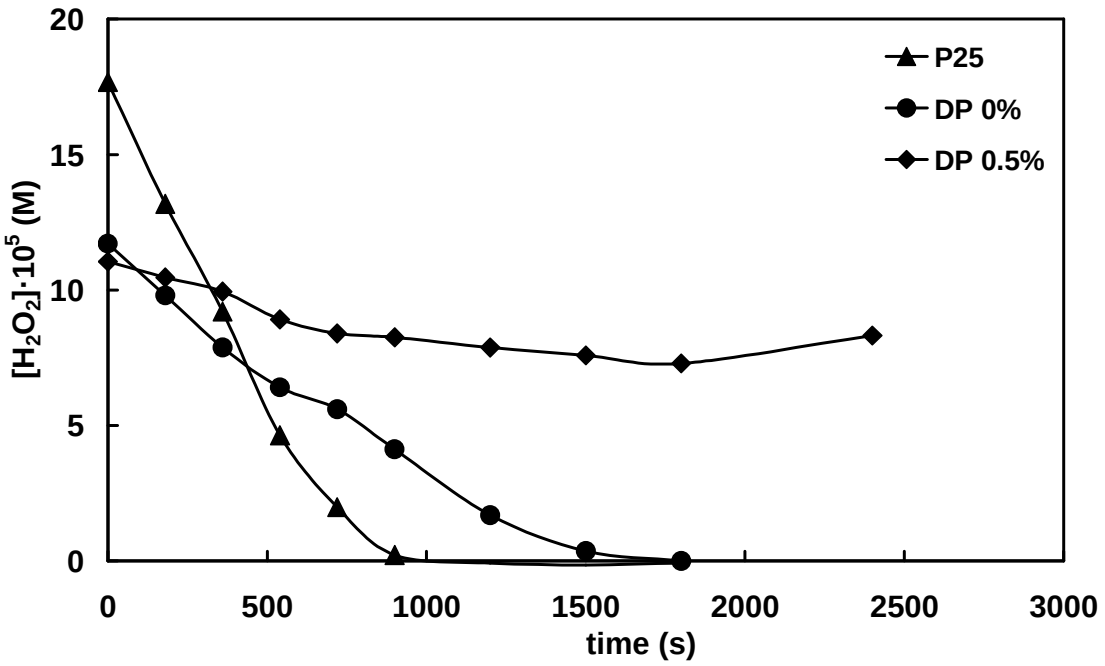

Figure 5.9 Hydrogen peroxide concentration profiles in aqueous suspensions containing 0.1 g L^{-1} of photocatalyst under irradiation in the absence of organic substrates.

5.3.3.4 Role of Au nanoparticles in FA photomineralization

Gold nanoparticles on TiO_2 clearly had a beneficial role in both the photocatalytic degradation of FA (Fig. 5.7) and the parallel reduction of adsorbed oxygen yielding hydrogen peroxide (Fig. 5.8). FA strongly adsorbs on the TiO_2 surface and undergoes rather fast photocatalytic oxidation preferentially initiated through direct electron transfer to valence band holes,[55,58,59] without the formation of any stable intermediate species. Upon one electron oxidation of FA, the highly unstable species $CO_2^{\bullet-}$, or $HCO_2^{\bullet}$ depending on pH, with a pK_a of 1.4, are formed:[55,60]

$$HCOO^- + h_{VB}^+ \rightarrow CO_2^{\bullet-} + H^+ \quad (5.3)$$

Because of the highly negative redox potential of the strongly reductant $CO_2^{-\bullet}$ radical anion, *i.e.* $E°(CO_2/CO_2^{\bullet-})$ = -1.8 V, this radical could either originate the so-called current doubling effect by injecting electrons into the semiconductor conduction band,[61] or mediate the reduction of a wide variety of molecules and, in particular, that of dissolved O_2, according to reaction (5.4).

$$CO_2^{\bullet-} + O_2 \rightarrow CO_2 + O_2^{\bullet-} \quad (5.4)$$

The so produced superoxide radical anion $O_2^{\bullet-}$ is a H_2O_2 precursor, according to reaction (5.2). Therefore, during FA photocatalytic degradation dioxygen reduction

proceeds on the photocatalyst surface through both the direct action of conduction band electrons, reaction (5.2), and that of adsorbed $CO_2^{\bullet-}$ radical anions. Gold nanoparticles on the oxide surface had a beneficial role in both these electron transfer processes, as demonstrated by the higher FA degradation rate and much higher H_2O_2 production rate in the presence of optimal Au amounts on the TiO_2 surface.

5.3.3.5 Role of gold on the photocatalytic oxidation of AR1

AR1 molecules mainly undergo photocatalytic oxidation according to a hydroxyl radical-mediated mechanism.[41,55,59,62] The low AR1 initial concentration, much smaller than the FA initial concentration, contributes in making this indirect oxidation path favoured with respect to direct interaction with photoproduced valence band holes. Fig. 5.4 shows that gold deposition on TiO_2, especially in the case of small nanoparticles (DPN and DPH series), was not beneficial in AR1 photocatalytic degradation, whereas the simultaneous H_2O_2 production did not change substantially (Table 5.2).

In order to understand these results, it is worth recalling that valence band holes (+2.5 V *vs.* NHE) and also photoproduced $^{\bullet}OH$ radicals (+1.9 V *vs.* NHE) could in principle be both able to oxidize metallic gold Au^0 in contact with the semiconductor surface into Au^I [$E°(Au^+/Au^0)$ = +1.68 V *vs.* NHE].[63,64] Gold in nanoparticle size domains is expected to be even more reactive than in the form of bulk metal. The Au^+ ions, so generated at the Au/TiO_2 interface, might be back reduced by photoexcited conduction band electrons. Consequently, the $^{\bullet}OH$ radicals consumed in gold oxidation are no more available to attack and oxidise AR1 molecules, whereas conduction band electrons involved in Au^I back reduction are not available for adsorbed O_2 reduction (see Scheme 5.2). Gold nanoparticles would definitely act as recombination centres of photoproduced active species in the case of organic substrates, such as AR1 in this study, unable of strong direct interaction with photoproduced valence band holes. Indeed, the maximum H_2O_2 concentration evolved on Au/TiO_2 during AR1 photodegradation runs was only doubled with respect to that produced on unmodified P25 (Table 5.2) and one order of magnitude lower than that measured during FA photodegradation on the same Au/TiO_2 photocatalysts.

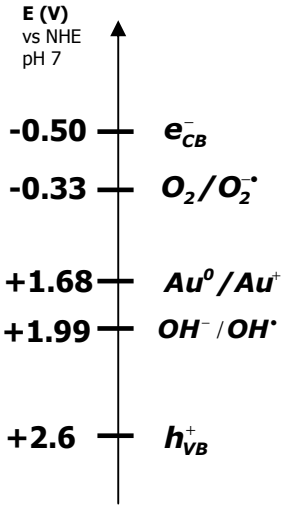

Scheme 5.2 Comparison of relevant homogeneous phase potentials in aqueous solution at pH 7.0.

By contrast, in the case of FA photocatalytic degradation, the formation of the strongly reductant $CO_2^{\bullet-}$ species on the photocatalyst surface may contribute in maintaining gold in the metallic form through reaction (5.5):

$$Au^+ + CO_2^{\bullet-} \rightarrow Au^0 + CO_2 \qquad (5.5)$$

This may be the principal origin of the rate increase in FA degradation observed upon gold nanoparticles deposition on TiO_2 and of the different efficiency of the investigated series of photocatalysts towards AR1 and FA photocatalytic degradation. AR1 photodegradation results appeared controversial, not only because also a parallel self-sensitised mechanism is at work, but mainly because in the mechanism initiated by band gap excitation AR1 oxidation does not occur through direct interaction with valence band holes, but through hydroxyl radicals attack. This would favour Au partial oxidation and gold acting as recombination centre of photoproduced charge carriers. Present results are in line with the recently reported enhanced photocatalytic oxidation induced by the presence of silver on the TiO_2 surface, observed only for organic compounds that are predominantly oxidised by holes.[25]

5.4 References

1. M. R. Hoffmann, S. T. Martin, W. Choi and D. W. Bahnemann, Chem. Rev., **1995**, 95, 69.
2. A. Fujishima, T. N. Rao and D. A. Tryk, J. Photochem. Photobiol. C: Photochem. Rev., **2000**, 1, 1.
3. D. W. Bahnemann, Solar Energy, **2004**, 77, 445.
4. X. Chen and S. S. Mao, Chem. Rev., **2007**, 107, 2891.
5. A. Fujishima, X. Zhang and D. A. Tryk, Surf. Sci. Rep., **2008**, 63, 515.
6. R. Ashai, T. Morikawa, T. Ohwaki, K. Aoki and Y. Taga, Science, **2001**, 293, 269.
7. S. U. M. Khan, M. Al-Shahry and W. B. Ingler Jr., Science, **2002**, 297, 2243.
8. H. Gerischer and A. Heller, J. Phys. Chem., **1991**, 95, 5261.
9. C. M. Wang, A. Heller and H. Gerischer, J. Am. Chem. Soc., **1992**, 114, 5230.
10. A. L. Linsebigler, G. Lu and J. T. Yates, Chem. Rev., **1995**, 95, 735.
11. A. Sclafani, L. Palmisano, G. Marcì and A. M. Venezia, Sol. Energy Mater. Sol. Cells, **1998**, 51, 203.
12. S. Sakthivel, M. V. Shankar, M. Palanichamy, B. Arabindoo, D. W. Bahnemann and V. Murugesan, Water Res., **2004**, 38, 3001.
13. J. Lee and W. Choi, J. Phys. Chem. B, **2005**, 109, 7399.
14. Z. Yu and S. S. C. Chuang, Appl. Catal. B: Environ., **2008**, 83, 277.
15. C. Wang, C. Liu, X. Zheng, J. Chen and T. Shen, Colloids Surf. A, **1998**, 131, 271.
16. X. Z. Li and F. B. Li, Environ. Sci. Technol., **2001**, 35, 2381.
17. A. Dobosz and A. Sobczyński, Monatsh. Chem., **2001**, 132, 1037.
18. M. Arabatzis, T. Stergiopoulos, D. Andreeva, S. Kitova, S. G. Neophytides and P. Falaras, J. Catal., **2003**, 220, 127.
19. A. Orlov, D. A. Jefferson, N. Macleod and R. M. Lambert, Catal. Letters, **2004**, 92, 41.
20. R. S. Sonatane and M. K. Dongare, J. Mol. Catal. A: Chem., **2006**, 243, 68.
21. V. Iliev, D. Tomova, R. Todorovska, D. Oliver, L. Petrov, D. Todorovsky and M. Uzunova-Bujova, Appl. Catal. A: General, **2006**, 313, 115.
22. A. Orlov, D. A. Jefferson, M. Tikhov and R. M. Lambert, Catal. Commun., **2007**, 8, 821.
23. B. Tian, J. Zhang, T. Tong and F. Chen, Appl. Catal. B: Environ., **2008**, 79, 394.

24. A. Sclafani and J. M. Hermann, J. Photochem. Photobiol. A: Chem., **1998**, 113, 181.
25. H. Tran, K. Chiang, J. Scott and R. Amal, Photochem. Photobiol. Sci., **2005**, 4, 565.
26. J. Chen, D. F. Ollis, W. H. Rulkens and H. Bruning, Water Res., **1999**, 33, 661.
27. M. Klare, J. Scheen, K. Vogelsang, H. Jacobs and J. A. C. Broekaert, Chemosphere, **2000**, 41, 353.
28. H. Einaga, S. Futamura and T. Ibusuki, Environ. Sci. Technol., **2001**, 35, 1880.
29. A. Sun, A. V. Vorontsov and P. G. Smirniotis, Langmuir, **2003**, 19, 3151.
30. J. Bard, J. Phys. Chem., **1982**, 86, 172.
31. R. Baba, S. Nakabayashi, A. Fujishima and K. Honda, J. Phys. Chem., **1985**, 89, 1902.
32. G. L. Chiarello, E. Selli and L. Forni, Appl. Catal. B: Environ., **2008**, 84 , 332.
33. H. Li, Z. Bian, J. Zhu, Y. Huo, H. Li and Y. Lu, J. Am. Chem. Soc., **2007**, 129, 4538.
34. S. L. Lee, J. Scott, K. Chiang and R. Amal, J. Nanopart. Res., **2009**, 11, 209.
35. K. Min, J. E. Heo, N. K. Youn, O. S. Joo, H. Lee, J. H. Kim and H. S. Kim, Catal. Commun., **2009**, 10, 712.
36. E. Kowalska, R. Abe and B. Ohtani, Chem. Commun., **2009**, 241.
37. R. Zanella, S. Giorgio, C. R. Henry and C. Louis, J. Phys. Chem. B, **2002**, 106, 7634.
38. Y. Wu, K. Q. Sun, J. Yu and B. Q. Xu, Phys. Chem. Chem. Phys., **2008**, 10, 6399.
39. G. M. Veith, A. R. Lupini and N. J. Dudney, J. Phys. Chem. C, **2009**, 113, 269.
40. M. Haruta, Catal. Today, **1997**, 36, 153.
41. J. M. Joseph, H. Destaillats, H. M. Hung and M. R. Hoffmann, J.Phys. Chem. A, **2000**, 104, 301.
42. G. G Guilbault, P. J. Brignac, Jr. and M. Juneau, Anal. Chem., **1968**, 40, 1256.
43. C. Kormann, D. W. Bahnemann and M. R. Hoffmann, Environ. Sci. Technol., **1988**, 22, 798.
44. M. Mrowetz and E. Selli, J. Photochem. Photobiol. A: Chem., **2006**, 180, 15.
45. M. Mrowetz, A. Villa, L. Prati and E. Selli, Gold Bull., **2007**, 40, 154.
46. S. Link and M. El-Sayed, J. Phys. Chem. B, **1999**, 103, 8410.
47. A. Zwijnenburg, A. Goossens, W. G. Sloof, M. W. J. Crajé, A. M. van der Kraan, L. Jos de Jongh, M. Makkee and J. A. Moulijn, J. Phys. Chem. B, **2002**, 106, 9853.

48. X. Z. Li, C. He, N. Graham and Y. Xiong, J. Appl. Electrochem., **2005**, 35, 741.
49. Y. Li, T. Sasaki, Y. Shimizu and N. Koshizaki, J. Am. Chem. Soc., **2008**, 130, 14755.
50. K. Vinodgopal, D. E. Wynkoop and P. V. Kamat, Environ. Sci. Technol., **1996**, 30, 1660.
51. T. Wu, G. Liu, J. Zhao, H. Hidaka and N. Serpone, J. Phys. Chem. B, **1998**, 102, 5845.
52. T. Wu, G. Liu, J. Zhao, H. Hidaka and N. Serpone, J. Phys. Chem. B, **1999**, 103, 4862.
53. M. Valden, X. Lai and D. W. Goodman, Science, **1998**, 281, 1647.
54. F. Shiraishi, T. Nakasako and Z. Hua, J. Phys. Chem. A, **2003**, 107, 11072.
55. M. Mrowetz and E. Selli, New J. Chem., **2006**, 30, 108.
56. J. Hoffman, E. R. Carraway and M. R. Hoffmann, Environ. Sci. Technol., **1994**, 28, 776.
57. N. Weiher, A. M. Beesley, N. Tsapatsaris, L. Delannoy, C. Louis, J. A. van Bokhoven and S. L. M. Schroeder, J. Am. Chem. Soc., **2007**, 129, 2240.
58. T. Lana Villarreal, R. Gómez, M. Neumann-Spallart, N. Alonso-Vante and P. Salvador, J. Phys. Chem. B, **2004**, 108, 15172.
59. H. Park and W. Choi, J. Phys. Chem. B, **2004**, 108, 4086.
60. L. L. Perissinotti, M. A. Brusa and M. A. Grela, Langmuir, **2001**, 17, 8422.
61. R. Carraway, A. J. Hoffman and M. R. Hoffmann, Environ. Sci. Technol., **1994**, 28, 786.
62. M. Mrowetz and E. Selli, Phys. Chem. Chem. Phys., **2005**, 7, 1100.
63. V. Subramanian, E. Wolf and P.V. Kamat, J. Phys. Chem. B, **2001**, 105, 11439.
64. V. Subramanian, E. E. Wolf and P.V. Kamat, Langmuir, **2003**, 19, 469.

Chapter 6

Cr(VI) photocatalytic reduction: effects of simultaneous organics oxidation and of gold nanoparticles photodeposition on TiO_2

6.1 Introduction

The mobility and toxicity of aqueous chromium, a notoriously toxic, mutagenic and carcinogenic,[1,2] common component of industrial wastes,[3] depend on its oxidation state. Cr(VI), usually present in the form of highly soluble and toxic chromate anions, can efficiently be converted into Cr(III), which exhibits lower toxicity and mobility in the environment,[4,5] by photocatalytic reduction on semiconductors.[6-11] When employing TiO_2, the most widely used semiconductor photocatalyst,[12-14] this process is possible on the grounds of the energy level of the TiO_2 conduction band and of the reduction potential of the Cr(VI)/Cr(III) couple and it is favored at low pH. In fact, due to the three electrons involved in Cr(VI) reduction to Cr(III), the potential of this couple shifts to more positive values with decreasing pH with a slope higher than that of the conduction band edge shift with pH.[11]

In order to investigate the influence of the surface and structural properties of this semiconductor on its photocatalytic activity, a series of commercial TiO_2 samples with different phase composition and surface area was tested in the photocatalytic reduction of Cr(VI) in aqueous suspensions at pH 3.7 under UV-visible light irradiation. This reaction was also coupled with the simultaneous photocatalytic oxidation of an organic pollutant, *i.e.* the azo dye Acid Orange 8 (AO8), see Scheme 6.1, and of formic acid (FA), also in this case chosen because it is a small organic molecule undergoing direct photocatalytic mineralization to CO_2 and water, without the formation of any stable intermediate species.

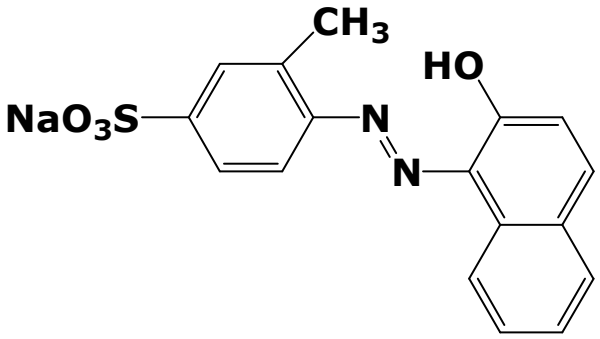

Scheme 6.1 Acid Orange 8 (AO8).

Investigation on the simultaneous reduction and oxidation processes occurring under irradiation on the photocatalyst surface in contact with water not only provides valuable information on the rate of the electron transfer paths at work in the reaction system, but

is of great importance in consideration of the fact that heavy metals, which can be photocatalytically reduced, and organic pollutants, which can be removed by photocatalytic oxidation, very often coexist in wastewaters. As outlined by Prairie *et al.* in their early study,[8] an efficient design of photocatalytic systems for wastewater treatment must take into account both oxidation and reduction processes.

The photocatalytic reduction of Cr(VI) was already investigated in the presence of organics frequently present in natural and waste waters, such as humic substances,[9] or pollutants, such as phenol and 4-chlorophenol,[15-17] dyes,[18-20] methyl *tert*-butyl ether,[21] or carboxylic acids.[17,22] An increase in the rate of Cr(VI) photocatalytic reduction was usually observed. Most of these studies were performed employing the P25 TiO_2 photocatalyst and were mainly focused on the effects of substrates concentration and of pH. This study is mainly focused on the effects of the TiO_2 phase composition and surface area on the rate of both Cr(VI) photocatalytic reduction and simultaneous oxidation of organic compounds, also in relation to their competitive adsorption on the photocatalyst surface.

Furthermore, the deposition of noble metals on semiconductor oxides is expected to enhance their photocatalytic activity by increasing the separation of photogenerated electron – hole pairs.[23] Indeed, the Fermi level of noble metals is usually lower in energy than the conduction band edge of TiO_2. Thus, photopromoted electrons can be captured by the noble metal, while photoproduced holes remain in the semiconductor valence band. However, whereas the positive effect of noble metal co-catalysts on the photocatalytic reduction processes, such as hydrogen production from water or O_2 reduction yielding hydrogen peroxide, is well established,[24-26] their effective role in photocatalytic oxidative reactions is still under debate, especially in the case of gold-modified TiO_2.[27,28]

Thus, the effect on Cr(VI) photocatalytic reduction of gold nanoparticles photodeposited on the TiO_2 surface was also investigated and compared to their effect in the photocatalytic mineralization of formic acid. A series of TiO_2–based photocatalysts with different Au loadings were prepared and tested. The modifications induced on the photocatalyst surface by the noble metal photodeposition treatment were also taken into account.

6.2 Experimental section

6.2.1 Photocatalysts preparation and characterisation

Most chemicals, *i.e.* $K_2Cr_2O_7$, formic acid (FA), purity 95-97%, and Acid Orange 8 (AO8), were purchased from Aldrich. They were all employed as received, apart from AO8, which was purified by repeated crystallization from methanol, as already mentioned.[29]

Mixed phase Degussa P25 titanium dioxide (*ca.* 80% anatase, 20% rutile, surface area 48 m^2 g^{-1}, according to our BET analysis),[30] and two pure anatase samples, purchased from Alfa Aesar, were employed as photocatalysts in powder form. These latter were labeled A118 and A235, with A standing for anatase, followed by a number indicating their surface area in m^2 g^{-1}.

The series of gold-modified photocatalysts (Au/TiO_2) was prepared starting from 6 vol.% methanol/water suspensions, containing 3 g L^{-1} of TiO_2 (Degussa P25) and the required amount of Au(III) acetate, as gold precursor, preliminary dissolved in an acidic aqueous medium. Au(III) photoreduction to metallic gold nanoparticles deposited on TiO_2 was achieved by irradiating the suspensions for 2 h under nitrogen atmosphere (see Scheme 6.2a). An immersion fluorescent, low pressure mercury arc lamp (Jelosil) was employed as the irradiation source, emitting in the 300–400 nm range, with a maximum emission peak at 360 nm (see Scheme 6.2b).

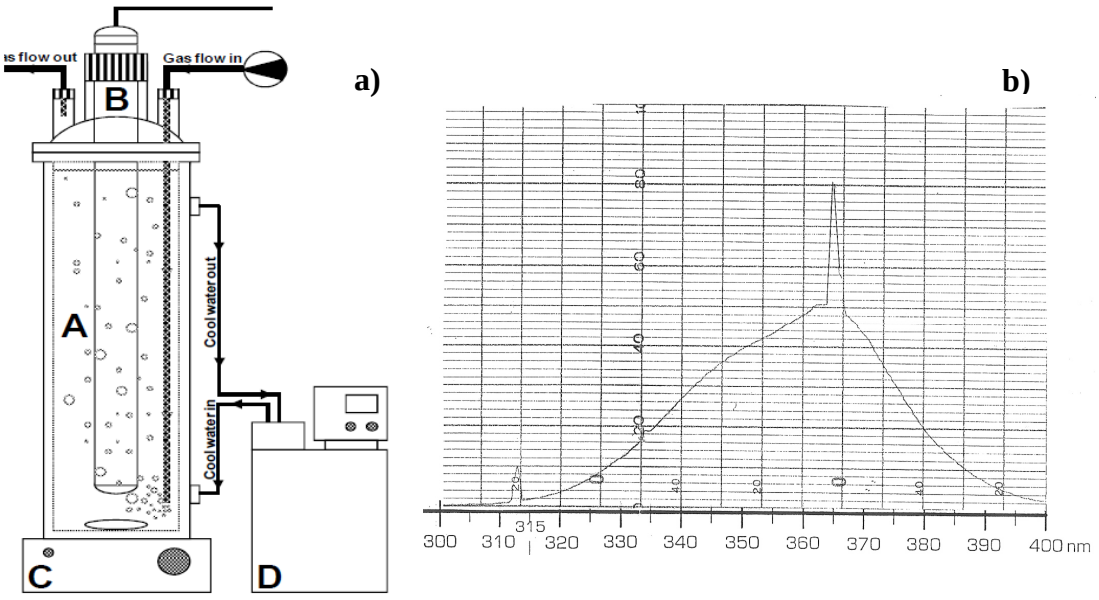

Scheme 6.2 a) Set up employed in order to perform gold nanoparticles photodeposition on TiO_2 samples; A: reactor, B: immersion UV lamp, C: stirrer, D: thermostat. b) Emission spectrum of the immersion fluorescent, low pressure mercury arc lamp (Jelosil).

Gold-modified TiO_2 powders were recovered after at least five centrifugation and washing cycles, up to the complete removal of residual ions and organic precursors. They were then dried at 70 °C for 1 day and stored in the absence of light and humidity. They were labeled with P, standing for "photodeposited", followed by their nominal gold content, in weight percent. A reference sample (P 0%) was prepared following exactly the same procedure, except for the addition of the gold precursor.

UV-Vis diffuse reflectance (DR) spectra were recorded with a Lambda 19, Perkin Elmer spectrophotometer equipped with an integrating sphere. HRTEM images were obtained with a JEM 3010 (JEOL) electron microscope operating at 300 kV. XPS analyses were performed by a PHI-5500-Physical Electronics spectrometer, equipped with a monochromatized source with aluminum anode (K_α = 1486.6 eV). These analyses were performed by Doctor Laura Meda at Eni Donegani group. XRD analysis was performed employing a Philips PW 1820 power diffractometer, using filtered Cu K_α radiation. The BET surface area was measured by nitrogen adsorption/desorption at 77 K employing a Micromeritics ASAP 2010 apparatus.

6.2.2 Photocatalytic and adsorption tests

All photocatalytic runs were performed in aqueous suspensions under atmospheric conditions, in a magnetically stirred 100 mL reactor, as described in Section 4.1. Appropriate volumes of stock solutions containing Cr(VI), Acid Orange 8 (AO8) or formic acid (FA) were added to pre-sonicated aqueous suspensions containing 0.1 g L^{-1} of photocatalyst. The initial concentration of the photocatalytic reaction substrates in the aqueous suspensions were fixed at the following values: 3.3×10^{-5} M for Cr(VI), from a solution obtained by dissolving $K_2Cr_2O_7$ in water, 1.0×10^{-3} M for FA, 2.8×10^{-5} M for AO8. At different time intervals during the runs, 3 mL-samples of the suspension were withdrawn from the reactor and centrifuged. The supernatant was analyzed colorimetrically for Cr(VI) residual content, using the 1,5-diphenylcarbazide method.[31] AO8 photobleaching was monitored during the runs by spectrophotometric analysis at the wavelength of maximum AO8 absorption, *i.e.* 490 nm. The molar extinction coefficient of the dye at this wavelength is $\varepsilon = (3.06 \pm 0.02) \times 10^4$ M^{-1} cm^{-1}, according to previous calibration.[29] FA content in the supernatant was determined by ion chromatography, as already described in Section 4.1.

All kinetic runs were performed up to *ca.* 70% Cr(VI) removal and repeated at least twice, to check their reproducibility. The initial pH of the suspensions was fixed at pH 3.7 by addition of the appropriate volume of a concentrated $HClO_4$ solution. No addition was necessary in the case of FA-containing suspensions, because 3.7 was the natural pH of the aqueous suspensions containing 1.0×10^{-3} M FA. No significant pH variation occurred during the runs.

Aiming at investigating the substrates affinity for the different photocatalysts, adsorption tests were performed at pH 3.7 under the same initial conditions of the photocatalytic runs, except for the amount of TiO_2, which was fixed at 1.0 g L^{-1}. The suspensions were kept under stirring in the dark and samples were withdrawn after 30 min, 1 h, 6 h and 24 h, centrifuged and analyzed for the Cr(VI) and/or AO8 amount in the supernatant. Adsorption equilibrium was attained in 30 min.

6.3 Results and discussion

6.3.1 Photocatalysts characterization

XRD analysis confirmed the mixed phase composition of Degussa P25, with a 78:22 anatase-to-rutile ratio, and mean diameter of the anatase and rutile crystallites of 25 ± 5 and 35 ± 8 nm, respectively.[30] Also the composition (pure anatase) of the A118 and A235 samples was confirmed by XRD analysis; the mean diameter of crystallites was 18 ± 3 and 9 ± 1 nm, respectively.

These TiO_2 samples exhibit quite similar absorption properties, with an absorption onset around 400 nm, according to UV-Vis DR measurements. In comparison to the pure anatase samples, P25 exhibits a slightly red-shifted absorption edge (see Fig. 6.1, inset), due to the presence of the rutile phase, characterized by a smaller band gap value (*i.e.* 3.0 eV *vs.* 3.2 eV for anatase).

As shown in Fig. 6.1, all Au/TiO_2 samples exhibited the typical plasmon resonance band of gold nanoparticles (< 20 nm), centered at 550 nm, *i.e.* red shifted compared to the pure gold plasmonic peak (520 nm), indicating interaction between gold and the titania support. The intensity of the plasmon resonance band regularly increased with increasing the gold loading without any appreciable difference in the absorption maximum (Fig. 6.1), indicating a progressive increase in gold nanoparticles density on the oxide surface without marked variation of their dimensions.

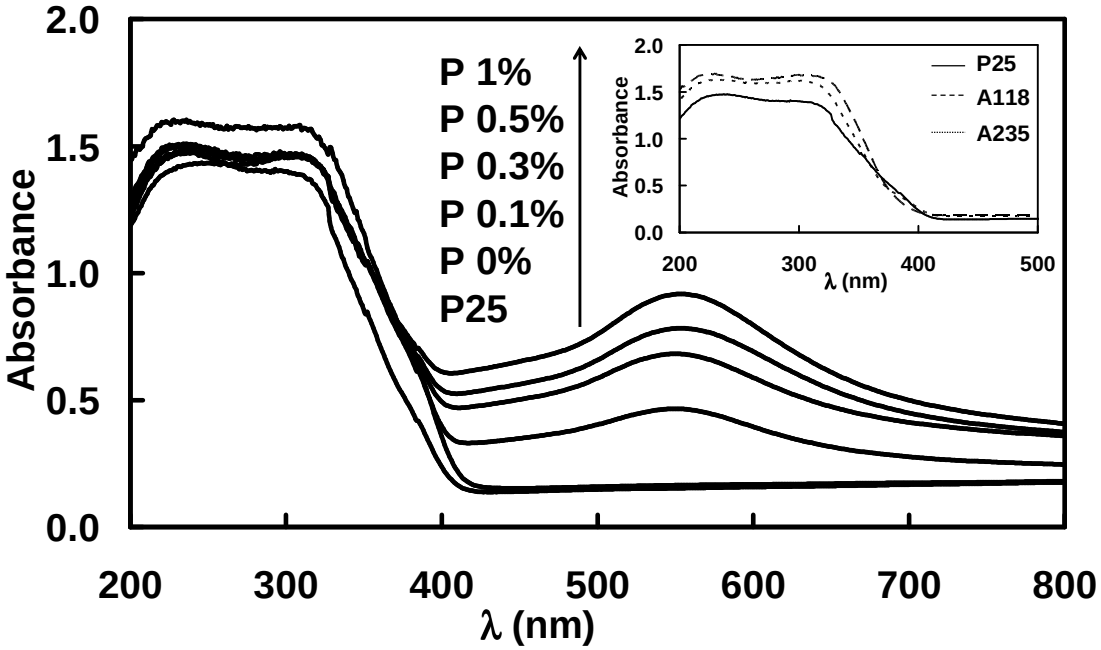

Figure 6.1 Absorption spectra of P25 TiO_2 and of the Au/TiO_2 photocatalysts series, with increasing Au loading, prepared by photodeposition. Inset: absorption spectra of P25, A118 and A235.

HRTEM analysis yielded direct information on the dimension and the distribution of Au nanoparticles. Examples of HRTEM images are reported in Fig. 6.2. The mean diameter of gold nanoparticles obtained by photoreduction varied between 5 and 20 nm. Compared to other gold deposition techniques (*e.g.* the deposition-precipitation method studied in Chapter 5), photodeposition was reported to produce larger and more spherical noble metal nanoparticles.[33]

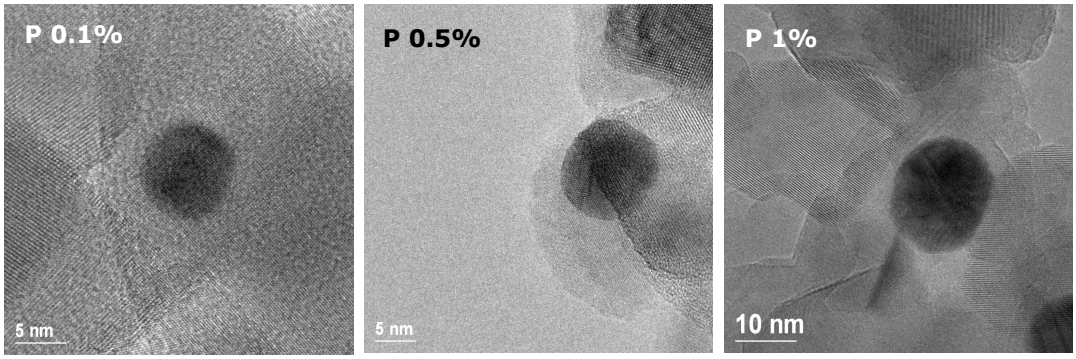

Figure 6.2 HRTEM images of selected Au/TiO_2 samples.

No variation in XRD patterns was expected after gold deposition by the adopted photodeposition procedure, not implying any heat treatment, as already verified in previous studies.[32,34] Also the specific surface area of P25 TiO_2 did not vary upon gold

nanoparticles deposition, in line with analogous results reported in Chapter 5 and also obtained by other research groups.[32,35-37]

The XPS analysis of the surface chemical composition, reported in Table 6.1, confirmed that all samples maintained a O/Ti atom ratio very close to 2, indicating no variation in the metal oxide surface composition, and confirmed the presence of gold nanoparticles deposited on the Au/TiO_2 photocatalysts. The gold percent surface amount detected by XPS analysis regularly increased with increasing the nominal gold loading of the samples prepared by photodeposition.

Table 6.1 Surface composition, from XPS analysis, of P25 TiO_2 and of Au/TiO_2 photocatalysts prepared by photodeposition of different percent amounts of gold nanoparticles on P25 TiO_2.

	Atom %				
	C 1s	**O** 1s	**Ti** 2p	**Cl** 2p	**Au** 4f
P25	14.1	55.9	28.0	0.8	---
P 0%	16.2	54.5	27.4	0.6	---
P 0.1%	15.6	54.8	27.7	0.6	0.06
P 0.3%	16.8	54.0	26.7	0.7	0.12
P 0.5%	15.8	54.2	27.4	0.8	0.16
P 1%	16.4	54.4	26.3	0.7	0.21

Furthermore, XPS analysis did not evidence any significant variation of chlorine content and of adventitious surface carbon content with respect to the values detected for pristine P25 TiO_2, indicating negligible persistence of Cl^- ions or of organic substances originating from the gold precursor.

6.3.2 Cr(VI) photocatalytic reduction tests on TiO_2

The photocatalytic reduction of Cr(VI) occurred according to a first order rate law in the presence of both TiO_2 and Au/TiO_2 photocatalysts. Determination coefficients R^2 obtained by treating the Cr(VI) concentration *vs.* time data according to a first order rate law were always greater than 0.98. The photoactivity of different photocatalyst powders was thus compared in terms of first order rate constants of Cr(VI) reduction obtained under identical irradiation conditions in the presence of an equal photocatalyst

amount (0.1 g L^{-1}). The effect of pH was preliminarily investigated employing P25 – containing suspensions, in order to attain optimal Cr(VI) photoreduction conditions. The rate constant of Cr(VI) photocatalytic reduction at the natural pH conditions of the dichromate suspension, *i.e.* pH *ca.* 6.5, was (8.2 ± 0.8) × 10^{-5} s^{-1}, whereas an almost doubled rate constant, *i.e.* (1.61 ± 0.05) × 10^{-4} s^{-1}, was determined employing a suspension at pH 3.7, obtained by $HClO_4$ addition. All subsequent runs were thus performed at this pH. This result is in agreement with previous findings of different laboratories and is expected from the already mentioned shift of potentials with decreasing pH.[8,11,12,38-40]

The photocatalytic activity of the different bare TiO_2 samples investigated in the present work can be compared in Fig. 6.3, in terms of first order rate constants of Cr(VI) reduction. Their uncertainties, obtained from repeated runs, are also shown in the figure. P25 TiO_2 was found to be the best performing photocatalyst, followed by A118 and by A235. The rate of Cr(VI) reduction thus appears totally independent of the photocatalyst surface area, but rather limited by the intrinsic efficiency in photoproduced charges separation of the employed photocatalyst powder. P25 TiO_2, manufactured by flame hydrolysis of titanium tetrachloride at high temperature, exhibits outstanding photocatalytic activity in several reactions, to be attributed to its peculiar nanostructured arrangement of interwoven anatase-rutile crystallites hindering charge recombination by charge separation across interfaces.[41,42]

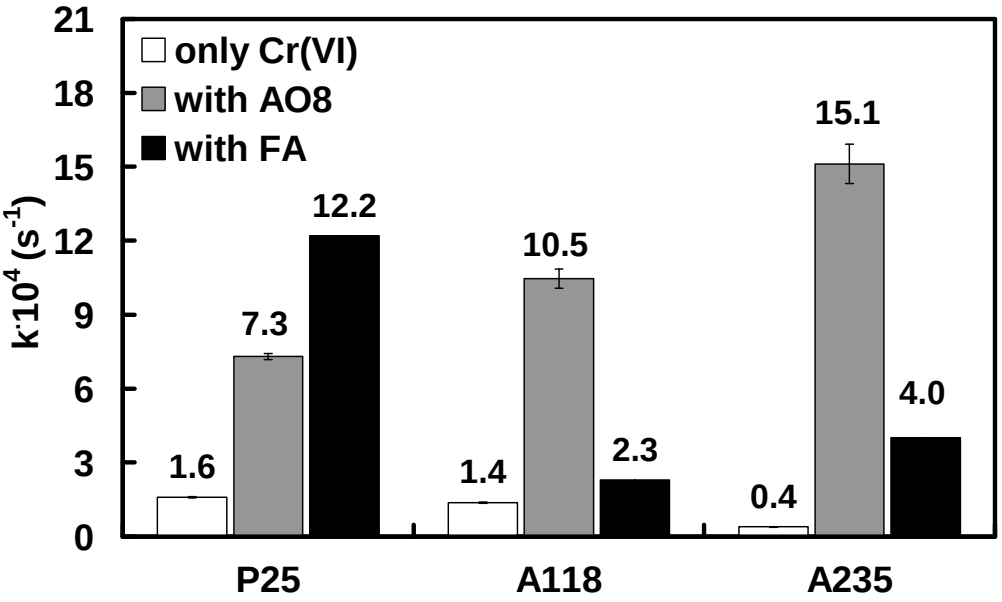

Figure 6.3 Rate constants of Cr(VI) photocatalytic reduction in the absence of organics and in the presence of the azo dye AO8 and of formic acid (FA).

6.3.3 Effect of AO8 on Cr(VI) adsorption and photocatalytic reduction on TiO_2

Preliminary tests of Cr(VI) and AO8 equilibrium adsorption on the investigated photocatalysts were performed at pH 3.7 under the same conditions employed in photocatalytic runs, except for a 10-fold higher amount of TiO_2.

The percent amount of Cr(VI) adsorbed on the photocatalysts, both in the presence and in the absence of AO8, is shown in Fig. 6.4. The adsorption of Cr(VI), present in the suspensions in the form of negatively charged $Cr_2O_7^{2-}$ ions, clearly increased with increasing the surface area of the TiO_2 photocatalysts. The extent of Cr(VI) adsorption on all photocatalysts was lower in the presence of the azo dye, indicating competitive adsorption. Indeed, at pH 3.7 both AO8 and Cr(VI) are in the anionic form, whereas the TiO_2 surface is positively charged, its point of zero charge being at pH higher than 3.7.

The extent of AO8 equilibrium adsorption on the photocatalysts was also measured, both in the presence and in the absence of Cr(VI). The results shown in Fig. 6.5 demonstrate that AO8 largely adsorbed on the TiO_2 photocatalysts, and that the adsorbed amount was also larger on higher surface area photocatalysts. The fact that AO8 adsorption occurred in competition with dichromate adsorption was confirmed by the lower AO8 adsorption extent attained in the presence of Cr(VI) (Fig. 6.5). The effects of competitive adsorption were more pronounced in the case of P25 photocatalyst, as expected, due to its lower specific surface area (Fig.s 6.4 and 6.5).

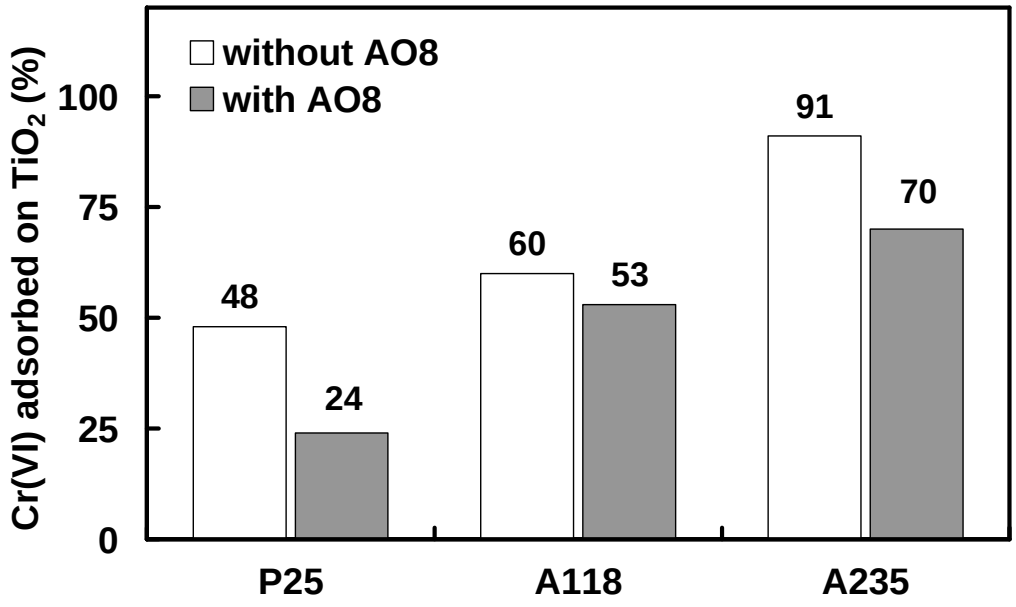

Figure 6.4 Percent amount of Cr(VI), in the form of dichromate anion, adsorbed at equilibrium on TiO_2 photocatalysts (1.0 g L^{-1}), in the absence and in the presence of the AO8 azo dye. Overall Cr(VI) concentration: 3.3 × 10^{-5} M; overall AO8 concentration: 2.8 × 10^{-5} M.

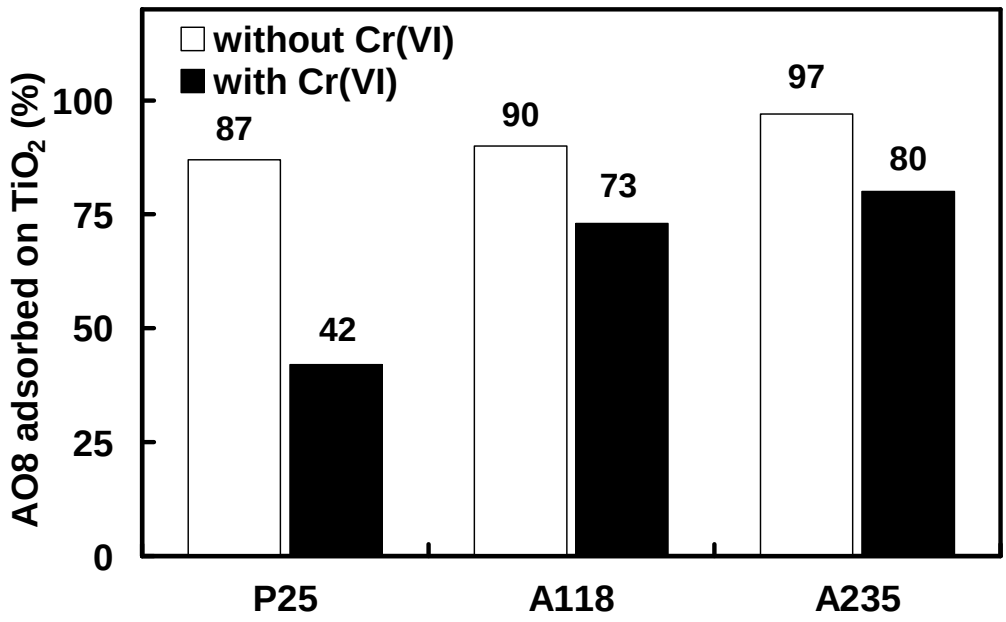

Figure 6.5 Percent amount of AO8 adsorbed at equilibrium on TiO_2 photocatalysts (1.0 g L^{-1}), in the absence and in the presence of Cr(VI) as dichromate anion. Overall AO8 concentration: 2.8 × 10^{-5} M; overall Cr(VI) concentration: 3.3 × 10^{-5} M.

The simultaneous presence of Cr(VI) and of the azo dye AO8, undergoing photocatalytic oxidation under irradiation, led to a marked enhancement of the rate of Cr(VI) photoreduction, which was clearly higher for photocatalysts with higher surface area (see Fig. 6.3). Similar results were obtained in the presence of other organics, *e.g.* methyl *tert*-butyl ether,[21] different dyes[18-20] or carboxylic acids.[17,22]

The dye itself was found to undergo photocatalytic oxidation according to a first order rate law, both in the presence and in the absence of Cr(VI). In both cases the photocatalytic bleaching of the dye increased with increasing the surface area of the photocatalyst, as shown in Fig. 6.6. Furthermore, AO8 photodegradation was markedly enhanced by the simultaneous presence of Cr(VI) and this effect was more remarkable for the two high surface area pure anatase photocatalysts (Fig. 6.6).

As already mentioned in Chapter 5, aromatic azo dyes undergo photocatalytic bleaching through an oxidation mechanism mainly involving hydroxyl radicals, which upon band gap excitation are photocatalytically generated on the oxide surface from the oxidation of surface –OH groups or water molecules. These radicals attack the diazo moiety, leading to loss of visible light absorption.[43-46] This occurs on the photocatalyst surface, the hydroxyl radicals being unable to leave it.[47] Consequently this oxidation path is largely favored by substrate adsorption on the photocatalyst surface. In fact,

both in the presence and in the absence of Cr(VI) the rate of AO8 photocatalytic oxidation increased with the surface area of the employed photocatalyst (Fig. 6.6), on which a larger percent amount of dye could adsorb (Fig. 6.5). The simultaneous photooxidation of the organic dye clearly had a synergistic effect in Cr(VI) reduction, and this effect was greater, the larger was the surface area of the photocatalyst (Fig. 6.3).

In fact, the photocatalytic activity in Cr(VI) reduction in the absence of AO8 did not increase with increasing the photocatalyst surface area, because it mainly depends on the intrinsic efficiency of electron-hole separation, as stated above. However, the simultaneous presence of Cr(VI) and AO8 led to an enhancement of the photocatalytic activity, which was clearly higher for photocatalysts with higher specific surface area, *i.e.* for photocatalysts on which AO8 underwent faster degradation. Indeed, photopromoted conduction band electrons became more readily available for Cr(VI) reduction in the presence of AO8, which indirectly consumed photoproduced valence band holes and thus inhibited electron-hole recombination. Therefore, the co-presence of oxidizable and reducible species ensured better separation of photogenerated charge carriers, especially in the case of high surface area anatase TiO_2, having the strongest affinity for both degradation substrates, as demonstrated by competitive adsorption tests.

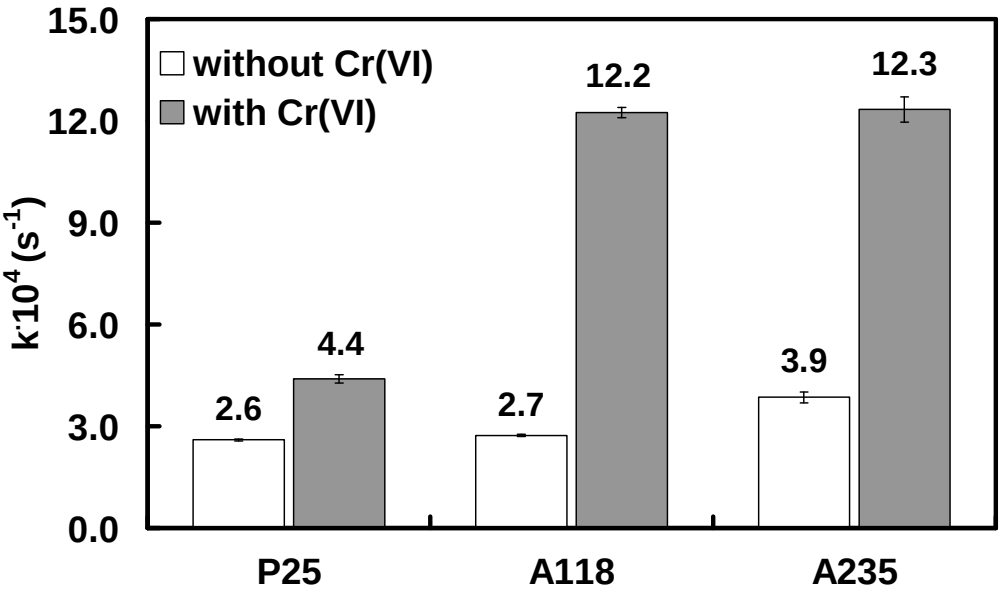

Figure 6.6 Rate constants of AO8 photocatalytic oxidation in the absence and in the presence of Cr(VI).

Concerning the mechanistic aspects of Cr(VI) photocatalytic reduction, the reaction was shown to occur through a sequence of one electron transfer steps and experimental evidence was obtained of the involvement of Cr(V) in the form of aquo and EDTA complex.[48,49] When the reaction was combined with the photocatalytic oxidation of an organic species able itself to absorb light, such as the azo dye AO8 in the present study, absorbing a considerable portion of visible light under the adopted irradiation conditions, a sensitized mechanism might be at work, in parallel to that initiated by semiconductor band gap absorption. In fact, as shown in Scheme 6.3, the electronically excited state of the dye, produced by visible light absorption, is able to transfer electrons into the conduction band of TiO_2 or to adsorbed Cr(VI), producing a dye radical cation, which easily undergoes oxidation by O_2 molecules. Such reaction path is responsible for the visible light-induced photocatalytic reduction of Cr(VI) in the presence of dyes[20] and is perfectly compatible with the surface area and adsorption dependence observed for the rate of both oxidation and reduction reactions simultaneously occurring on the photocatalyst surface.

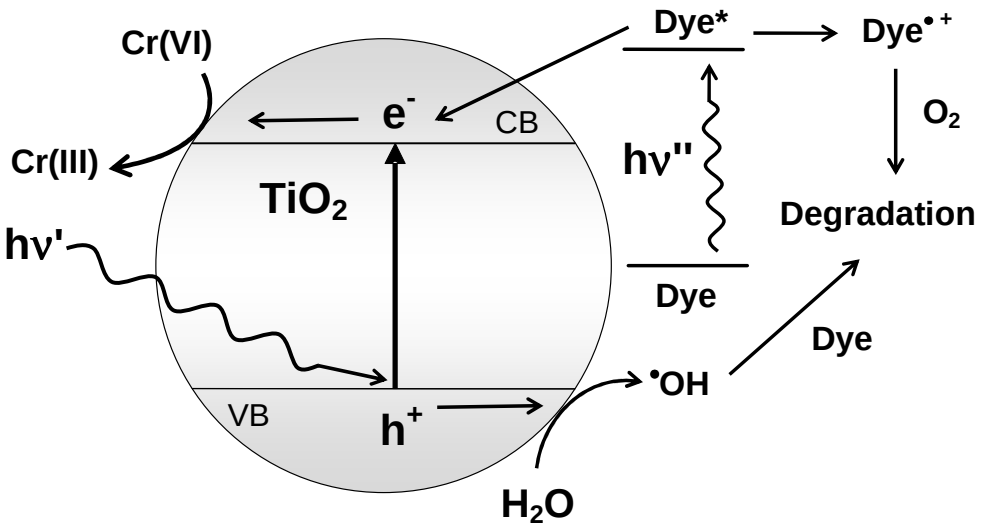

Scheme 6.3 Dye-sensitized and band gap absorption-initiated paths of simultaneous Cr(VI) reduction and AO8 oxidation.

In contrast, present photocatalytic activity results, clearly dependent on the surface area of the employed photocatalyst, seem to exclude that the enhanced Cr(VI) photoinduced reduction observed in the presence of AO8 occurred through direct electron transfer from AO8 to Cr(VI) in a AO8-Cr(VI) complex in the aqueous phase, as suggested to occur in the case of the azo dye Acid Orange 7.[20] In fact, both Cr(VI)

and AO8 were found to be perfectly photostable in aqueous solutions containing no TiO_2, even after prolonged irradiation under the conditions employed in the present study. Similar Cr(VI) complexes were shown to play a role in the photocatalytic Cr(VI) reduction in the presence of, *e.g.*, salicylic and citric acids.[20,22,50]

On the other hand, evidence was recently obtained of the formation of a charge transfer complex between Cr(VI) and TiO_2 that could be excited by visible light.[51] The efficiency of Cr(VI) reduction attained by selectivity exciting this complex was found to be higher than that produced by exciting the semiconductor itself. An electron transfer path initiated by this way cannot be excluded to be at work under the here adopted irradiation conditions.

6.3.4 Effect of formic acid on Cr(VI) photocatalytic reduction

Aiming at excluding the possibility of any dye-sensitized photocatalytic reaction path, we investigated the effect of the presence of formic acid in the photocatalytic reduction of Cr(VI). This acidic organic substrate does not absorb light in competition with TiO_2 and, as already mentioned in Chapter 5, it is known to undergo photocatalytic oxidation mainly through direct interaction with photoproduced valence band holes,[43,46,52] without forming any stable mineralization intermediate.

The effect of FA addition on the rate of Cr(VI) photocatalytic reduction is also shown in Fig. 6.3 and can be easily compared with that of AO8 addition in the irradiated suspensions. The rate of Cr(VI) photoreduction was clearly higher in the presence of both organic species, with respect to the rate measured in the absence of any organics. However, the photoactivity trend within the investigated photocatalyst series obtained after FA addition was completely different with respect to that observed after AO8 addition. In fact, a remarkable rate increase was obtained upon FA addition when employing P25 TiO_2, whereas FA addition had much smaller effects on Cr(VI) reduction rate in the case of the two high surface area pure anatase photocatalysts, the photoactivity of which markedly increased upon AO8 addition. Thus Cr(VI) reduction in the presence of a direct hole scavenger, such as FA, appears to be still limited by the electron-hole separation intrinsic properties of the semiconductors, rather than by effects related to their surface area and substrate adsorption capability.

Simultaneous to Cr(VI) photocatalytic reduction, FA underwent photocatalytic mineralization at constant rate, *i.e.* according to a zero-order rate law, as already

reported in Chapter 5, in line with previous studies.[32,46,52] Fig. 6.7 shows that pure anatase A118 was the best performing photocatalyst in FA mineralization in the absence of Cr(VI). Comparable results were obtained under UV irradiation.[30] However, the rate of FA mineralization dramatically dropped when Cr(VI) was added to the irradiated suspensions, down to a rather low value, almost independent of the employed TiO_2 photocatalyst (Fig. 6.7). Very low FA conversion (below 10%) was attained in this case at the end of the runs. This effect could not be attributed to Cr(VI)-FA interactions in the aqueous phase, because aqueous solutions containing both Cr(VI) and FA at pH 3.7 were found to be perfectly stable both in the absence and in the presence of irradiation, in contrast to previous studies carried out under intense UV irradiation.[53]

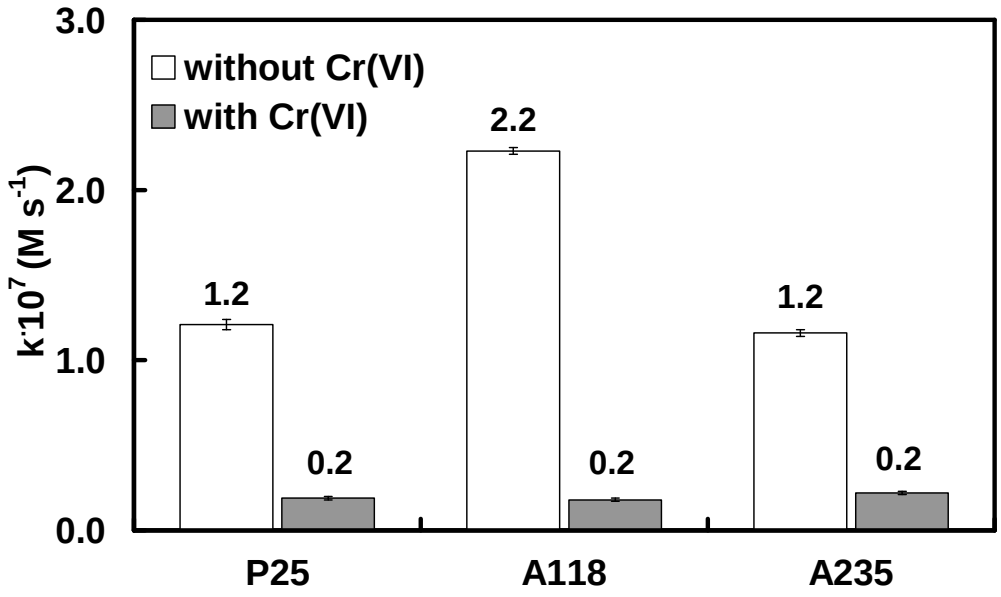

Figure 6.7 Zero-order rate constants of FA photocatalytic oxidation in the absence and in the presence of Cr(VI).

It is worth noting, however, that the initial FA concentration in our suspensions was more than one order of magnitude higher than the initial Cr(VI) concentration and that the rate of FA oxidation, coinciding with the zero-order rate constants values of Fig. 6.7, was similar to the rate of Cr(VI) photocatalytic reduction in the presence of FA, calculated as $r = k$ [Cr(VI)], k being the first order rate constants reported in Fig. 6.3 for Cr(VI) reduction in the presence of FA. Thus the photocatalytic oxidation and reduction processes proceeded at almost the same rate on the photocatalysts surface. This rate was lower than the rate of FA oxidation in the absence of Cr(VI), indicating that chromium species adsorbed on the photocatalyst surface inhibit FA photocatalytic

oxidation. Indeed, previous studies on Cr(VI) photocatalytic reduction in the presence of carboxylic acids evidenced an inhibition in TOC degradation[50] or even an increase of TOC amount[22] during the photocatalytic runs, which were attributed to deactivation of the photocatalyst surface due to Cr(III) adsorption or to desorption of organic species from the photocatalyst surface under irradiation, respectively. This chromium-induced inhibition in the photocatalytic mineralization of organics should deserve attention, because it may cause problems in the photocatalytic treatment of waste waters.

6.3.5 Effect of gold nanoparticles deposition on TiO_2

The effects induced on the rate of Cr(VI) reduction by the presence of gold nanoparticles photodeposited on the surface of P25 TiO_2 can be appreciated in Fig. 6.8, where the first order rate constants obtained with the Au/TiO_2 photocatalysts series are reported as normalized values with respect to the rate constant value k_{P25} obtained with unmodified P25 TiO_2. Also with the Au/TiO_2 photocatalysts, Cr(VI) photoreduction became faster upon FA addition to the irradiated suspensions, with an average 4-fold increase of the rate constants of Cr(VI) reduction (data not shown).

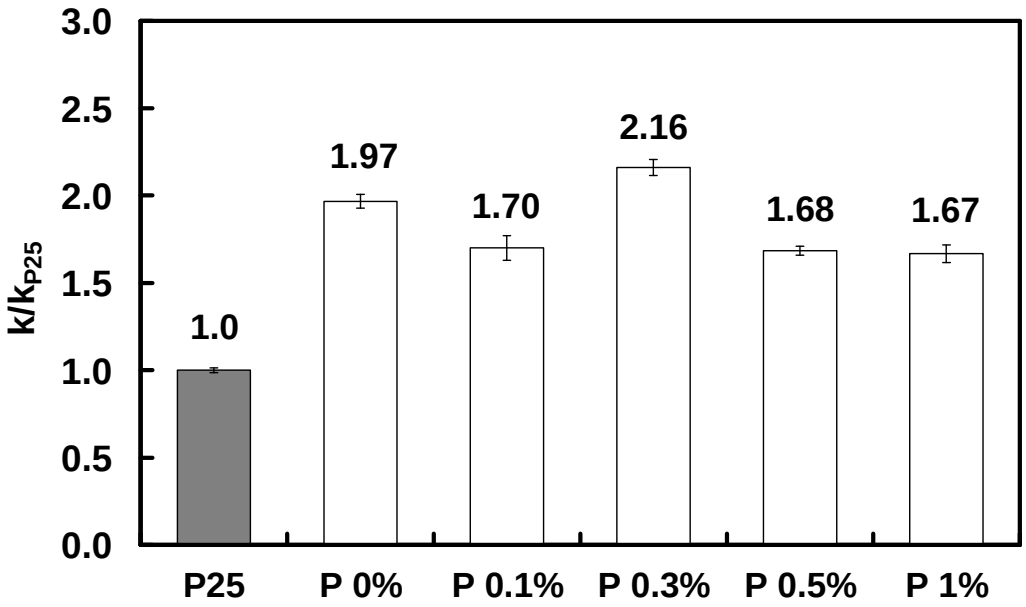

Figure 6.8 Effect of gold nanoparticles photodeposited on TiO_2 on the photocatalytic reduction of Cr(VI): ratio between the first order rate constants k measured in the presence of Au/TiO_2 samples with different gold loading (wt.%) and that obtained with unmodified P25, k_{P25}.

The photocatalytic activity scale of the Au/TiO_2 samples in FA oxidation can be appreciated in Fig. 6.9, showing the ratios between the zero-order rate constants of FA degradation obtained with each photocatalyst and that measured in the presence of unmodified P25. On the other hand, FA oxidation rate dropped to very low values in the presence of Cr(VI), in a way almost identical to that shown in Fig. 6.7 in the case of the unmodified photocatalysts.

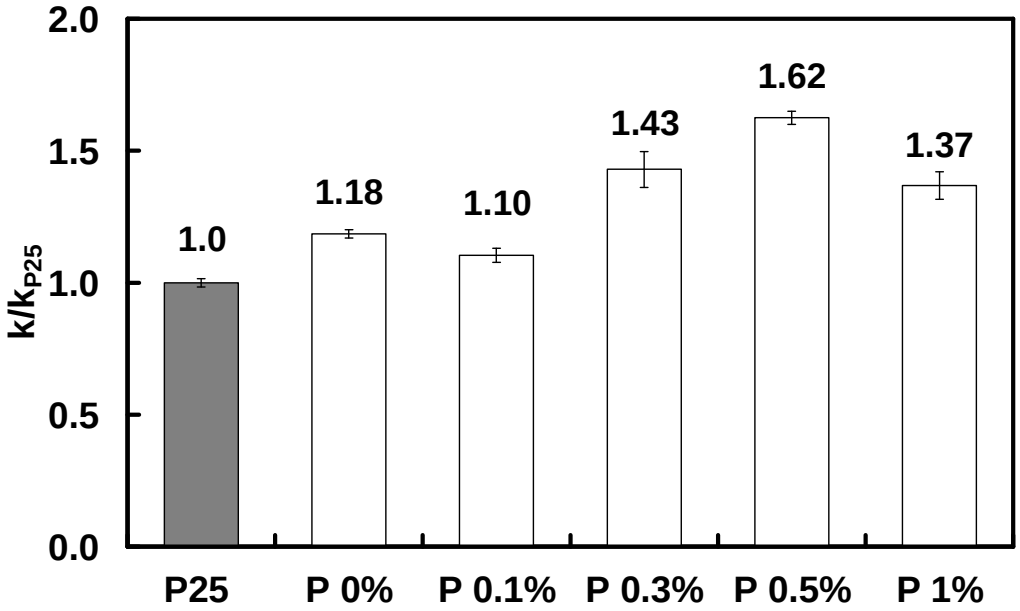

Figure 6.9 Effect of gold nanoparticles photodeposited on TiO_2 on the photocatalytic oxidation of FA: ratio between the zero-order rate constants k measured in the presence of Au/TiO_2 samples with different gold loading (wt.%) and that obtained with unmodified P25, k_{P25}.

As shown in Fig. 6.9 the presence of photodeposited gold nanoparticles had a beneficial role primarily in increasing the rate of FA oxidation and, as already mentioned in Chapter 5, this can be attributed to the formation of the carbon dioxide radical anion upon the one electron oxidation of FA. In fact, such strongly reductant species may contribute in maintaining gold in its photocatalytically active metallic form, avoiding the possible formation of Au^+ by Au(0) interaction with conduction band holes.[32] Furthermore the photoactivity increase in FA oxidation obtained by gold photodeposition on P25 TiO_2 was slightly higher than that obtained with gold-modified TiO_2 prepared according to the deposition-precipitation method (see Chapter 5),[54] as clearly shown in Fig. 6.10, and the photodeposition procedure itself, even in the absence of gold precursor, slightly increased the photoactivity of P25 (see P 0% *vs.* P25 in Fig.s 6.9 and 6.10).

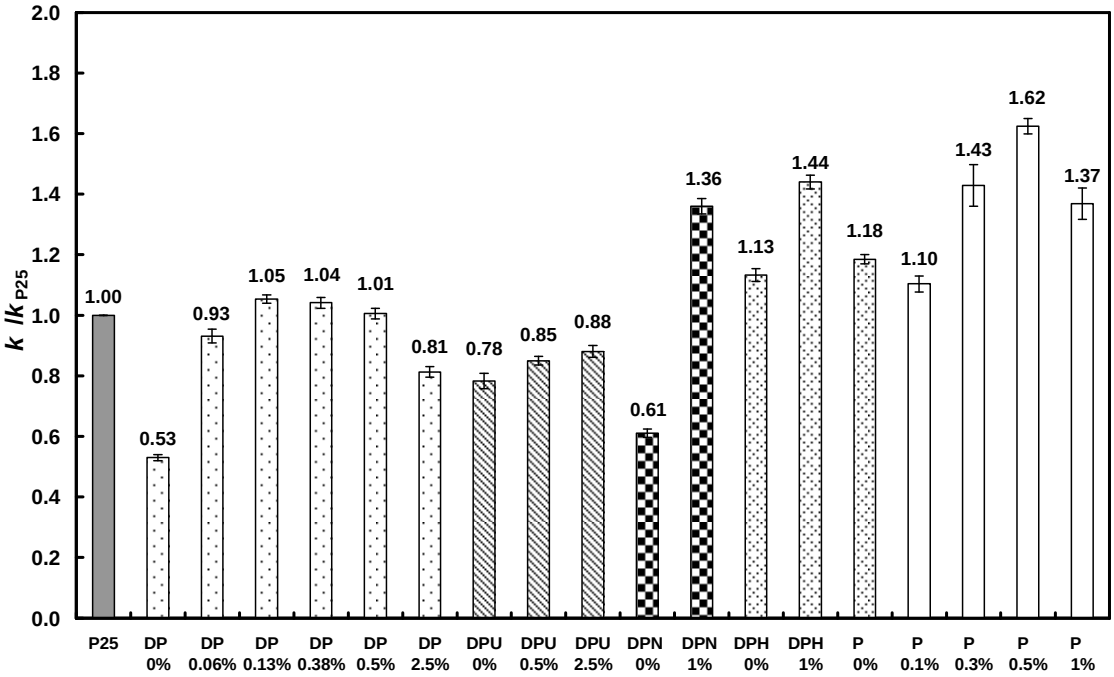

Figure 6.10 Ratio between the zero order rate constants k of formic acid photocatalytic degradation measured with different Au/TiO_2 photocatalysts and that obtained with unmodified P25, k_{P25}. Au/TiO_2 photocatalysts contained the indicated weight percent amounts of gold and were prepared by deposition precipitation (DP), deposition precipitation in the presence of urea (DPU), both followed by thermal gold reduction, and deposition precipitation followed by reduction with $NaBH_4$ (DPN) or hydrogen (DPH); or photodeposition (P).

As suggested by results reported in Fig. 6.10, photodeposition technique, not requiring any kind of high-temperature reduction step, seems thus to be the most promising method for Au nanparticles deposition on TiO_2.

The rate enhancement observed in the case of Cr(VI) photocatalytic reduction upon loading P25 TiO_2 with gold nanoparticles (Fig. 6.8) shows an unclear trend as a function of metal loading. Also in this case the photodeposition procedure produced positive effects on P25 photoactivity, which were even greater than in FA photocatalytic degradation. In fact, the rate constant of Cr(VI) photoreduction almost doubled when P25 TiO_2 was pre-irradiated under anaerobic conditions in the absence of gold precursor (see k/k_{P25} of P 0% in Fig. 6.8), most probably as a consequence of the partial TiO_2 surface reduction, whereas metal loading did not exhibit a definite effect. The improvement of the photocatalytic efficiency of these Au/TiO_2 materials in Cr(VI) reduction should thus be attributed more to partial TiO_2 reduction than to the presence of gold nanoparticles. Indeed, rather small effects of noble metals on the rate of Cr(VI) photocatalytic reduction were reported in the literature, for example in the case of mesoporous titania photocatalysts embedding gold nanoparticles,[55] whereas

platinization of titania was found to produce no improvement in its photoactivity in Cr(VI) reduction.[56]

The rate of both photocatalytic oxidation and reduction reactions were found to slightly vary with metal loading, attaining a maximum value for the P 0.3% photocatalyst in the case of Cr(VI) reduction (Fig. 6.8) and for P 0.5% in the case of FA oxidation (Fig. 6.9), *i.e.* for a 0.5 wt.% gold loading, as in previous studies.[32] These maximum reaction rates were attained for an optimal balance between the detrimental shielding effects of Au surface nanoparticles, decreasing the fraction of light absorbed by TiO_2, and their beneficial role in capturing conduction band electrons, thus reducing the recombination of photoproduced electron-hole couples. Present results demonstrate that, when discussing the modifications in Cr(VI) reduction photoactivity induced by the presence of noble metal nanoparticles on the photocatalyst surface, the effects induced by the deposition procedure should be clearly distinguished from those induced by noble metal nanoparticles themselves.

6.4 References

1. J. A. H. Waterhouse and Br. J. Cancer, **1975**, 32, 262.
2. C. D. Palmer and P. R. Wittbrodt, Environ Health Perspect., **1991**, 92, 25-40.
3. Metal Pollution in Aquatic Environment, 2nd ed., U. Förster, G.T.W. Wittmann, Eds., Springer-Verlag, New York, **1983**.
4. V. Bianchi, A. Zantedeschi and A. Montaldi, J. Majone, Toxicol. Lett., **1984**, 8, 279.
5. S. Music, M. Ristic, M. Tonkovic and Z. Wasser Abwasser Forsch., **1986**, 19, 186.
6. H. Yoneyama, Y. Yamashita and H. Tamura, Nature, **1979**, 281, 817.
7. J. Muñoz and X. Doménech, J. Appl. Electrochem., **1990**, 20, 518.
8. M. R. Prairie, L. R. Evans, B. M. Stange and S. L. Martinez, Environ. Sci. Technol., **1993**, 27, 1776.
9. E. Selli, A. De Giorgi and G. Bidoglio, Environ. Sci. Technol., **1996**, 30, 598.
10. J. Giménez, M. A. Aguado and S. Cervera-March, J. Molec. Catal. A: Chem., **1996**, 105, 67.
11. X. Wang, S. O. Pehkonen and A. K. Ray, Ind. Eng. Chem. Res., **2004**, 43, 1665.
12. M. I. Litter, Appl. Catal. B: Environ., **1999**, 23, 89.
13. X. Chen and S. S. Mao, Chem. Rev., **2007**, 107, 2891.
14. A. Fujishima, X. Zhang and D. A. Tryk, Surf. Sci. Rep., **2008**, 63, 515.
15. H. Fu, G. Lu and S. Li, J. Photochem. Photobiol. A: Chem., **1998**, 114, 81.
16. S. M. Lee, T. W. Lee, B. J. Choi and J. K. Yang, J. Environ. Sci. Health A, **2003**, 38, 2219.
17. L. Wang, N. Wang, L. Zhu, H. Yu and H. Tang, J. Hazard. Mater., **2008**, 152, 93.
18. S. G. Schrank, H. J. José and R. F. P. M. Moreira, J. Photochem. Photobiol. A: Chem., **2002**, 147, 71.
19. T. Papadam, N.P. Xekoukoulotakis, I. Poulios and D. Mantzavinos, J. Photochem. Photobiol. A: Chem., **2007**, 186, 308.
20. H. Kyung, J. Lee and W. Choi, Environ. Sci. Technol., **2005**, 39, 2376.
21. X. R. Xu, H. B. Li and J. D. Gu, Chemosphere, **2006**, 63, 254.
22. G. Colón, M. C. Hidalgo and J. A. Navío, Langmuir, **2001**, 17, 7174.
23. P. V. Kamat, J. Phys. Chem. B, **2002**, 106, 7729.
24. C. M. Wang, A. Heller and H. Gerischer, J. Am. Chem. Soc., **1992**, 114, 5230.
25. A. L. Linsebigler, G. Lu and J. T. Yates Jr., Chem. Rev., **1995**, 95, 735.

26. G. L. Chiarello, E. Selli and L. Forni, Appl. Catal. B: Environ., **2008**, 84, 332.
27. S. L. Lee, J. Scott, K. Chiang and R. Amal, J. Nanopart. Res., **2009**, 11, 209.
28. B. K. Min, J. E. Heo, N. K. Youn, O. S. Joo, H. Lee, J. H. Kim and H. S. Kim, Catal. Commun., **2009**, 10, 712.
29. E. Selli, Phys. Chem. Chem. Phys., **2002**, 4, 6123.
30. C. Bernardini, G. Cappelletti, M. V. Dozzi and E. Selli, J. Photochem. Photobiol. A: Chem., **2010**, 211, 185.
31. Standard Methods for the Examination of Water and Wastewater, 20th ed., L. S. Clesceri, A. E. Greenberg, A. D. Eaton, Eds., American Public Health Association, Washington, DC, **1998**.
32. M .V. Dozzi, L. Prati, P. Canton and E. Selli, Phys. Chem. Chem. Phys., **2009**, 11, 7171.
33. R. Kydd, K. Chiang, J. Scott and R. Amal, Photochem. Photobiol. Sci., **2007**, 6, 829.
34. M. Mrowetz, A. Villa, L. Prati and E. Selli, Gold Bulletin, **2007**, 40, 154.
35. S. Sakthivel, M. V. Shankar, M. Palanichamy, B. Arabindoo, D. W. Bahnemann and V. Murugusan, Water Res., **2004**, 38, 3001.
36. A. Orlov, D. A. Jefferson, N. Macleod and R.M. Lambert, Catal. Lett., **2004**, 92, 41.
37. H. Tran, K. Chiang, J. Scott and R. Amal, Photochem. Photobiol. Sci., **2005**, 4, 565.
38. J. A. Navío, J. J. Testa, P. Djedjeian, J. R. Padrón, D. Rodríguez and M. I. Litter, Appl. Catal. A: General, **1999**, 178, 191.
39. Y. Xu and M. A. A. Schoonen, Am. Mineral., **2000**, 85, 543.
40. Y. Ku and I.-L. Jung, Water Res., **2001**, 35, 135.
41. D. C. Hurum, K. A. Gray, T. Rajh and M. C. Thurnauer, J. Phys. Chem. B, **2005**, 109, 977.
42. A. Di Paola, M. Bellardita, R. Ceccato, L. Palmisano and F. Parrino, J. Phys. Chem. C, **2009**, 113, 15166.
43. J. M. Joseph, H. Destaillats, H. M. Hung and M. R. Hoffmann, J. Phys. Chem. A, **2000**, 194, 301.
44. H. Park and W. Choi, J. Phys. Chem. B, **2004**, 108, 4086.
45. M. Mrowetz, and E. Selli, Phys. Chem. Chem. Phys., **2005**, 7, 1100.
46. M. Mrowetz and E. Selli, New J. Chem., **2006**, 30, 108-114.

47. D. Lawless, D. Meisel and N. Serpone, J. Phys. Chem., **1991**, 95, 5166.
48. J. J. Testa, M. A. Grela and M. I. Litter, Langmuir, **2001**, 17, 3515.
49. J. J. Testa, M. A. Grela and M. I. Litter, Environ. Sci. Technol., **2004**, 38, 1589.
50. J. M. Meichtry, M. Brusa, G. Mailhot, M. A. Grela and M. I. Litter, Appl. Catal. B: Environ., **2007**, 71, 101.
51. Y. Di Iorio, E. San Román, M. I. Litter and M. A. Grela, J. Phys. Chem. C, **2008**, 112, 16532.
52. M. Mrowetz and E. Selli, J. Photochem. Photobiol. A: Chem., **2006**, 180, 15.
53. G. Cappelletti, C. L. Bianchi and S. Ardizzone, Appl. Catal. B: Environ., **2007**, 78, 193.
54. M. V. Dozzi, G. L. Chiarello and E. Selli, J. Adv. Oxid. Technol., **2010**, 13, 305.
55. H. Li, Z. Bian, J. Zhu, Y. Huo, H. Li and Y. Lu, J. Am. Chem. Soc., **2007**, 129, 4538.
56. U. Siemon, D. Bahnemann, J. J. Testa, D. Rodríguez, M. I. Litter and N. Bruno, J. Photochem. Photobiol. A: Chem., **2002**, 148, 247.

Chapter 7

Photocatalytic Activity of S- and F-doped TiO_2 in Formic Acid Mineralisation

7.1 Introduction

As already mentioned, TiO_2 can still be envisaged as the most active and most suitable semiconductor photocatalyst.[1,2] because it is biologically and chemically inert, photostable and cheap, and has a high oxidation ability, its holes being photogenerated at E^0 = 2.9 V *vs.* NHE at pH 0. However, two major factors limit the photocatalytic efficiency of TiO_2: *i)* its band gap is larger than 3 eV, *i.e.* it mainly absorbs light in the UV region and only a small portion (less than 5%) of the sunlight can be exploited for photocatalytic processes; *ii)* as in all photoexcited semiconductors, photogenerated electron-hole pairs undergo fast recombination in competition with charge transfer to adsorbed species yielding redox reactions.

One of the ways which have been successfully pursued to shift the optical response of TiO_2 into the visible spectral range consists in doping with *p*-block elements. However, the insertion of dopant impurities in the oxide structure may favour the recombination of photogenerated charge carriers, whose rate is known to become relatively lower, the higher is the crystallinity degree of the oxide structure.

Whereas the effects of N or C doping on the photocatalytic efficiency of TiO_2 have been widely investigated in recent years,[3-10] much less is known on the use of other dopants, such as sulphur and fluorine. Umebayashi *et al.* first succeeded in synthesising S-doped TiO_2 (S-TiO_2) using the ion implantation method, followed by thermal annealing, and indicated that S is introduced into TiO_2 as an anion to replace lattice oxygen.[11-13] Ohno *et al.* obtained increased photocatalytic activity under visible light with S-TiO_2 prepared from titanium tetra-isopropoxide and thiourea[14,15] and pointed to S^{4+} ions substitution for titanium ions in the lattice. Fluorine-doped titania (F-TiO_2), prepared by hydrolysis of the same titanium precursor in a mixed NH_4F-H_2O solution, was investigated by Yu *et al.*,[16] who observed a small red shift in the band gap transition and a photocatalytic activity exceeding that of P25. F-doped TiO_2 synthesised by spray pyrolysis[17] from an aqueous solution of H_2TiF_6 or prepared by sol-gel[18] with addition of a small amount of trifluoroacetic acid also exhibited increased photoactivity under both ultraviolet and visible light irradiation.

The widely employed sol-gel synthesis method[19,20] is particularly suited to accomplish the incorporation of different dopants in the TiO_2 structure and to investigate systematically the effects of the dopant content and doping conditions on the structural and photocatalytic properties of the material. In fact, the possibility of

altering a great number of variables (*e.g.* pH, Ti precursor, solvent, doping precursor, as well as temperature, reaction time and operational sequence in their synthesis) makes this method very flexible and suitable for systematic studies.

In the present work we investigated the photocatalytic performance under visible light of two series of TiO_2-based doped materials, a sulphur-doped one (S-TiO_2) and a fluorine-doped one (F-TiO_2). Both were prepared by the sol-gel method in the presence of different amounts of dopant sources, followed by calcination at different temperature. Undoped TiO_2 samples prepared by the same synthetic procedure, apart from the addition of the dopant precursor, and calcination conditions were employed as reference materials, to enlighten the effects of dopant concentration and calcination temperature on the structural features of the doped materials, in relation to their photocatalytic activity. The photocatalytic degradation of formic acid (FA) in aqueous suspensions was chosen as test reaction, mainly because it does not absorb in the visible region, thus allowing a straightforward evaluation of the photocatalysts' visible light activity, and undergoes direct photomineralisation without forming any stable intermediate species, which simplifies the interpretation of kinetic results. Furthermore, the effects of surface TiO_2 fluorination on this reaction have been extensively investigated in our research group.[21,22] Of course, different photocatalytic activity scales might be found employing different test compounds.[23,24]

7.2 Experimental section

7.2.1 Photocatalysts preparation and characterisation

The two series of doped titanium dioxide samples, S-TiO_2 and F-TiO_2, were prepared by using the sol-gel method. 100 mL of anhydrous ethanol solution containing 10 mL of dissolved titanium(IV) isopropoxide (Aldrich 97%) was heated at 30°C. Then a water solution containing different amounts of dopant source (thiourea for S-doped TiO_2 and NH_4F for F-doped TiO_2) was added dropwise under vigorous stirring in order to obtain a 1/58 specific molar Ti/H_2O ratio and (S or F)/Ti nominal percent molar ratios equal to 5, 12 and 50 (corresponding to increasing dopant amounts). An immediate exothermic hydrolysis reaction occurred. After stirring and refluxing for one hour, the suspension was concentrated under reduced pressure at 35°C. The so obtained slurry was kept in a furnace at 70°C overnight, to eliminate organic compounds. Precursor powders were then calcined under a 100 mL min^{-1} air flow at different

temperature (500, 600 and 700°C) for 4 h. An initial heating ramp of 5°C min^{-1} was always adopted.

The samples obtained by this way were labelled as X_Y_Z, with X referring to the symbol of the dopant element (X = S or F), Y indicating the dopant/Ti nominal percent molar ratio, and Z the calcination temperature in Celsius. Reference undoped materials were prepared by following exactly the same synthetic route in the absence of dopant precursor, followed by calcination under identical conditions (E_0_Z series photocatalysts). All reagents were purchased from Aldrich and employed as received. Water purified by a Milli-Q water system (Millipore) was used throughout.

The BET specific surface area was measured by N_2 adsorption / desorption at liquid nitrogen temperature in a Micromeritics ASAP 2010 apparatus, after out-gassing *in vacuo* at 300 °C for at least 6 h.

X-ray powder diffraction (XRPD) patterns were recorded on a Philips PW3020 powder diffractometer, by using the Cu K_α radiation (λ = 1.54056 Å). Quantitative phase analysis was made by the Rietveld refinement method,[25] using the "Quanto" software.[26]

UV-vis diffuse reflectance (DR) spectra were recorded by a Perkin-Elmer Lambda 35 apparatus equipped with an integration sphere (Labsphere RSA-PE-20), using a calibrated SRS-99-010 Spectralon Reference Standard, produced by Labsphere, as reference material.

XPS analysis were performed by a PHI-5500-Physical Electronics spectrometer, equipped with a monochromatised source with aluminium anode (K_α = 1486.6 eV), operating at 200 W applied power, 5.85 eV pass energy and 0.05 eV energy step. XPS spectra were collected at take off angles of 45°. The analysis area was around 0.5 mm^2, the depth 10 nm. The charging effect on the analysis was corrected considering the binding energy value of C 1s, due to adventitious carbon, at 284.8 (±0.3) eV. Quantification and spectral line decomposition were obtained using the PC-ACCESS software provided by Physical Electronics. These analyses were performed by Dr. Laura Meda at Eni Donegani, Novara.

HRTEM analysis was carried out with a JEM 3010 (JEOL) electron microscope operating at 300 kV, point-to-point resolution Scherzer defocus of 0.17 nm. Specimens for HRTEM analysis were sonicated in 2-propanol and then transferred as a suspension to a copper grid covered with a holey carbon film.

Electron Paramagnetic Resonance (EPR) spectra were run at the University of Turin by Prof. Giamello's research group, on a X-band CW-EPR Bruker EMX spectrometer equipped with a cylindrical cavity operating at 100 kHz field modulation. EPR spectra were recorded both at room temperature (RT) and at the liquid nitrogen temperature (LNT). Experiments were carried out in static vacuum obtained connecting Suprasil quartz glass tubes to a high vacuum pumping system (residual pressure $P < 10^{-3}$ mbar).

7.2.2 Photocatalysts activity measurements

All photocatalytic FA degradation runs were performed as already detailed in Section 4.1,[27] under atmospheric conditions in a magnetically stirred 60 mL cylindrical quartz reactor, inserted in a home made housing consisting in a black box mounted on optical bench. All irradiated aqueous suspensions contained 0.1 g L^{-1} of photocatalyst and were preliminarily sonicated for 30 min. Then the appropriate volume of formic acid (FA) solution was added, to obtain an initial concentration of FA equal to 1.0×10^{-3} mol L^{-1}. At different time intervals during the runs, 2 mL-samples of the suspension were withdrawn from the reactor, centrifuged and analysed for residual FA content by ion chromatography. All kinetic runs were performed at natural pH, up to *ca.* 70% substrate degradation. During FA degradation the pH increased,[28] as already mentioned in Chapter 5.

7.3 Results and discussion

7.3.1 Photocatalysts characterisation

XRPD analysis evidenced that both types of doping inhibit the anatase into rutile phase transition. In fact, as shown by the traces reported in Fig. 7.1, the undoped material calcined at 500°C contained anatase, exhibiting the (101) reflection at $2\theta = 25.4°$, as the only crystalline phase, with a very small amount (*ca.* 2%) of brookite (small peak at $2\theta = 30.7°$), and underwent a phase tranformation from anatase into rutile when calcined at higher temperature, as revealed by the increase of the rutile (110) reflection at $2\theta = 27.4°$, rutile representing more than 60% of pure TiO_2 calcined at 700°C.

By contrast, all doped materials did not undergo such phase transformation, remaining almost pure anatase, even if calcined at 700°C, as exemplified in Fig. 7.1.

The phase composition of all samples, obtained by Rietveld refinement of XRPD data, are reported in Table 7.1, together with anatase crystallite dimensions, calculated by using the Scherrer equation.[29] These latter clearly increase with increasing the calcination temperature, from 15 to 38 nm in undoped TiO_2, from 7 to 40 nm in the case of S-TiO_2 and from 13 to 50 nm in the case of F-TiO_2. Thus, S-doped TiO_2 exhibit a trend very similar to that of undoped TiO_2, whereas F-doping appears to favour the formation of slightly larger anatase TiO_2 particles.

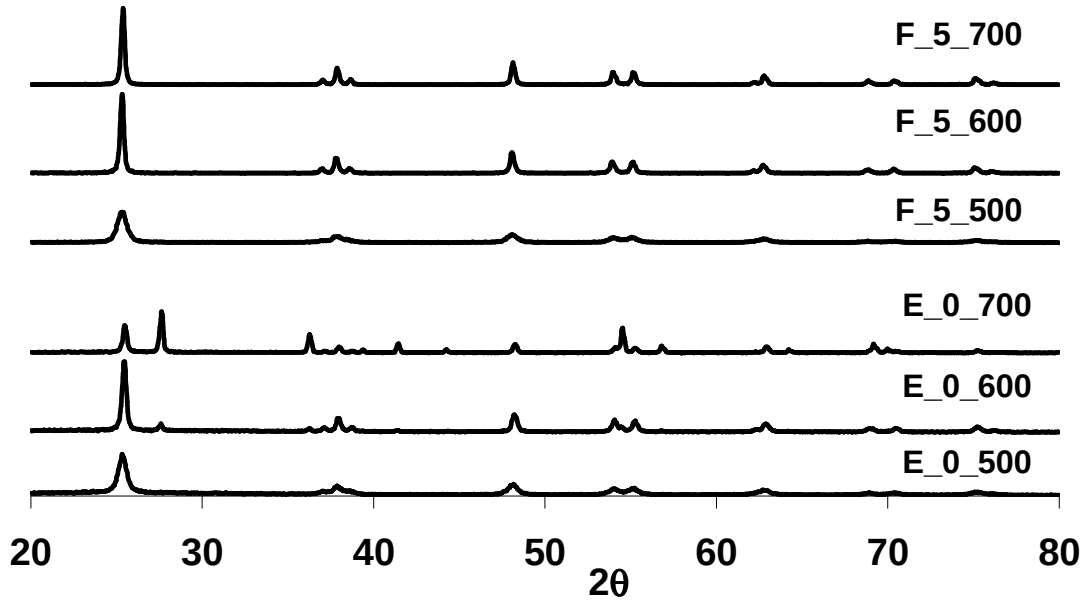

Figure 7.1 XRPD spectra of undoped TiO_2 and of the a series of F-doped TiO_2, calcined at different temperature.

Table 7.1 Phase composition and crystallite dimensions, d_A, obtained from XRD analysis, by assuming the absence of amorphous phase, of the investigated photocatalyst series.

Sample	dopant/Ti molar ratio (%)	anatase (%)	brookite (%)	rutile (%)	d_A/nm
E_0_500	0	99	1	-	15
E_0_600	0	90	-	10	32
E_0_700	0	38	-	62	65
F_5_500	5	98	2	-	13
F_5_600	5	100	-	-	44
F_5_700	5	99	-	1	49
F_12_500	12	100	-	-	19
F_12_600	12	100	-	-	33
F_12_700	12	100	-	-	48
F_50_500	50	100	-	-	30
F_50_600	50	100	-	-	50
F_50_700	50	100	-	-	87
S_5_500	5	98	2	-	8
S_5_600	5	98	2	-	17
S_5_700	5	99	-	1	39
S_12_500	12	100	-	-	7
S_12_600	12	98	2	-	15
S_12_700	12	98	-	-	40
S_50_500	50	99	1	-	7
S_50_600	50	100	-	-	16
S_50_700	50	100	-	-	36

The HRTEM images shown in Fig. 7.2 confirm a somewhat larger dimension of F-doped TiO_2 particles calcined at 700°C, with respect to those of the undoped material calcined at 500°C, and a very high crystallinity degree (Fig. 7.2a).

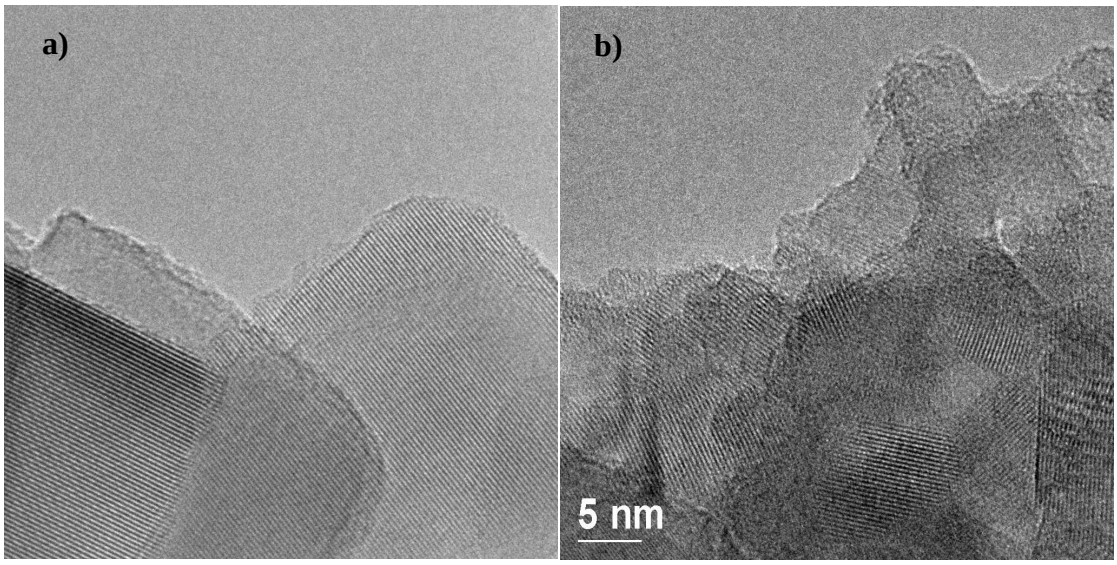

Figure 7.2 HRTEM images of (a) F_5_700 and (b) E_0_500.

BET analysis showed a decrease in surface area of the TiO_2-based photocatalysts with increasing the calcination temperature for the same nominal dopant amount, consequent to particles sintering. The results reported in Fig. 7.3 for different TiO_2 series containing an increasing nominal F amount clearly show that moderate F-doping is beneficial for obtaining materials with larger surface area, especially if calcined at relatively low temperature, which remains higher than that of pure TiO_2, even after calcination at 700°C.

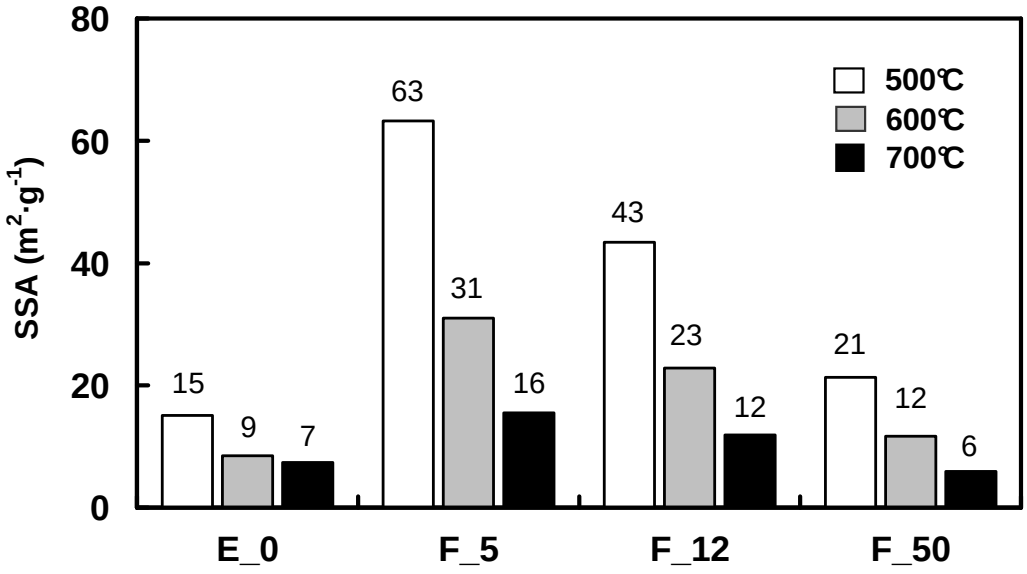

Figure 7.3 Specific surface area of pure TiO_2 and of the F-TiO_2 series of photocatalysts calcined at different temperature.

The absorption features of the investigated TiO_2-based photocatalysts, reported in Fig. 7.4 in the form of $F(R)^{1/2}$ *vs.* energy, evidence that after calcination at 500°C, especially for samples containing a relatively high amount of dopant, doped samples are able to absorb light at wavelengths longer than those typical of the TiO_2 band gap absorption onset. However, when calcined at progressively higher temperature, doped TiO_2 looses this ability.

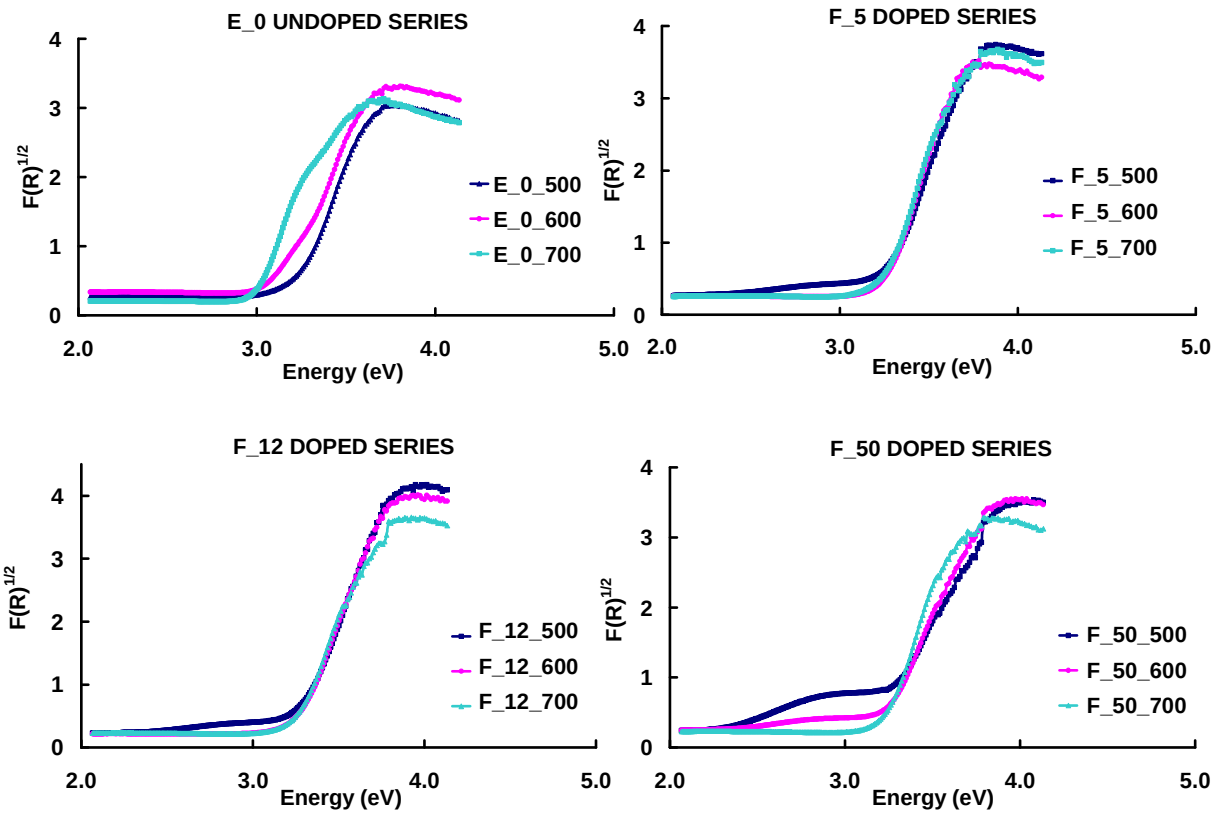

Figure 7.4 Absorption features of undoped TiO_2 and of the F_5, F_12 and F_50 doped TiO_2 series, containing increasing amounts of fluorine in the order, calcined at different temperature.

Table 7.2 reports the results of XPS analysis of the undoped materials and of F- and S-doped TiO_2 with a 5 mol.% nominal F/Ti ratio (X_5_Z series). For all samples the presence of carbon, oxygen and titanium is confirmed on the solid surface, with a O/Ti ratio slightly higher than 2, together with negligible and almost constant surface amounts of nitrogen. The amount of dopant species (F or S) clearly decreased with increasing the calcination temperature and fluorine was below the detection limit in sample F_5_700. Furthermore, F-doped TiO_2 always contained a surface dopant

amount lower than the nominal value (*i.e.* 5%), possibly indicating a higher concentration of dopant species in the bulk favoured by the fact that F^- ions have a ionic radius practically identical to that of O^{2-} ions. In the case of the S-doped series, the surface concentration of dopant was higher than for the F-doped series, though also in this case remaining below the nominal value. Furthermore, the S 2p XPS peak was at 168.7 eV, indicating the presence of S^{4+} and S^{6+} on the photocatalyst surface.[19]

Table 7.2 XPS analysis, in terms of atom per cent, of undoped, F- and S-doped TiO_2.

	Atom %					
	C 1s	**O** 1s	**Ti** 2p	**N** 1s	**F** 1s	**S** 2p
E_0_500	16.6	55.2	26.2	0.4	---	---
E_0_600	17.4	54.8	25.4	0.4	---	---
E_0_700	15.8	56.1	26.2	0.3	---	---
F_5_500	13.9	56.5	26.8	0.3	1.1	---
F_5_600	16.7	55.3	25.8	0.3	0.1	---
F_5_700	15.0	55.8	27.0	0.3	0	---
S_5_500	11.2	59.0	25.6	0.9	---	2.5
S_5_600	13.1	58.6	25.9	0.4	---	1.7
S_5_700	14.2	56.4	27.3	0	---	0.7

7.3.2 Photocatalytic activity

FA oxidative degradation always occurred at constant rate, *i.e.* according to a zero-order rate law, as already mentioned and also found in previous studies.[21,27-29] The photocatalytic activity of the investigated TiO_2 samples can be compared in Fig. 7.5, in terms of zero-order rate constant, k_0. First of all, on the undoped samples the reaction proceeded at a lower rate with respect to that attained on moderately doped oxides. Furthermore, with undoped TiO_2 the reaction rate decreased with increasing the calcination temperature, most probably as a consequence of the anatase into rutile transformation.

Moderate S-doping and particularly F-doping were beneficial in increasing the

photocatalytic activity of the TiO_2 photocatalysts. Furthermore, this effect increased with increasing the calcination temperature, being maximal for moderately F-doped samples F_5_700 and F_12_700. Excessive amounts of dopant (X_50 series) obviously increase the extent of defects in the oxide structure, acting as recombination centres of photogenerated charge carriers, with a consequent decrease of the photocatalytic reaction rate.

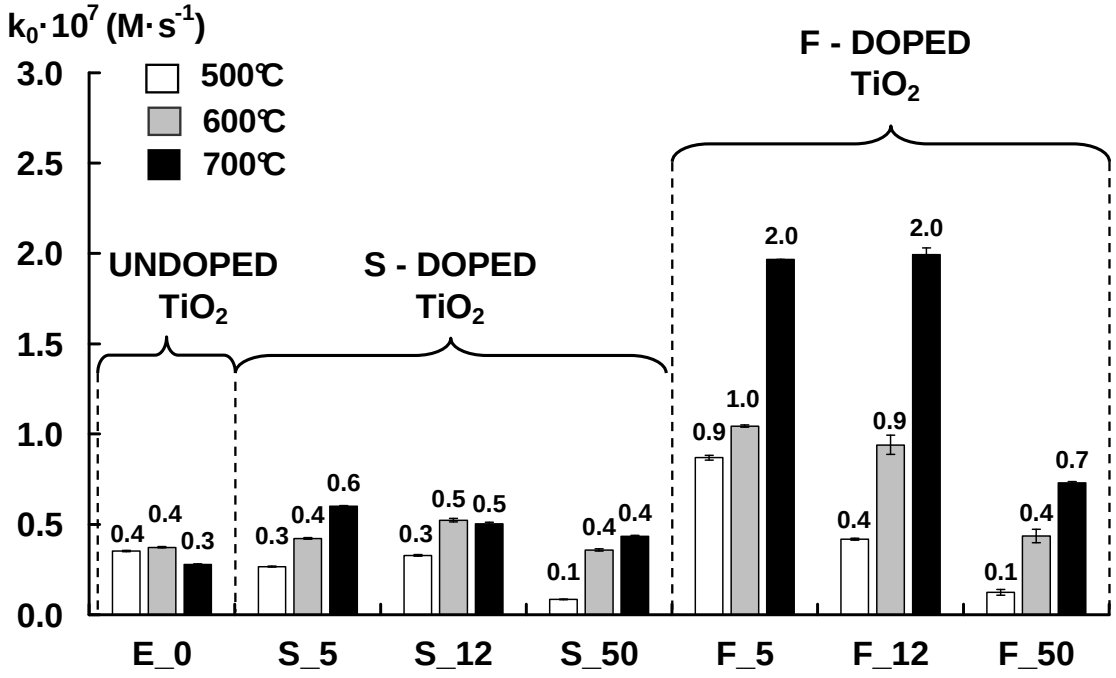

Figure 7.5 Zero-order rate constants of FA photomineralisation on photocatalysts containing different amounts of dopants and calcined at different temperature.

S-doped TiO_2 showed a photocatalytic activity quite similar to that of the undoped materials. In this regard the insertion of S, characterised by a relatively large ionic radius, into the TiO_2 crystalline structure appears rather difficult. Moreover, XPS measurements showed a higher than expected amount of sulphur-containing species on the photocatalyst surface, which might hamper FA adsorption and photocatalytic degradation. However, at difference with respect to the undoped material, the reaction rate was higher in the presence of samples calcined at higher temperature, though being characterised by lower surface area and higher mean particle dimensions. This indicates that sulphur enters indeed into the TiO_2 lattice structure and makes it more crystalline by stabilising the anatase phase up to 700°C.

Low F doping levels and calcination at 700°C were most beneficial in increasing the rate of FA photocatalytic degradation (Fig. 7.5). This may appear surprising, because

the F_5_700 and F_12_700 samples have relatively low surface area (16 and 12 m^2 g^{-1}, respectively). The surface area exposed to the water phase is expected to play a major role in the oxidative degradation of FA, mainly proceeding through direct FA interaction with valence band holes, thus implying direct interaction of the substrate with the photocatalyst surface. Furthermore, TiO_2 surface fluorination was shown to produce the opposite effect, *i.e.* a marked decrease in FA mineralization rate, consequent to the hampered adsorption of FA on the fluorinated TiO_2 surface.[21] Both facts inconvertibly demonstrate that fluorine doping induces bulk modifications of TiO_2 that ensure better charge separation and that such effect is maximum for samples calcined at high temperature.

To better understand the role of fluorine doping in our F-doped TiO_2 samples, a series of photocatalytic runs were carried out employing a 400 nm cut off filter, to ascertain the existence of photoactivity consequent to the formation of intra band gap states possibly involved in light absorption. As shown in Fig. 7.6, under such conditions FA photodegradation occurred at low, but still measurable rate only in the case of F-doped materials calcined at 700°C, with a photoactivity scale identical to that obtained under full lamp emission. This seems to exclude the presence of photoactivity other than that consequent to band gap absorption.

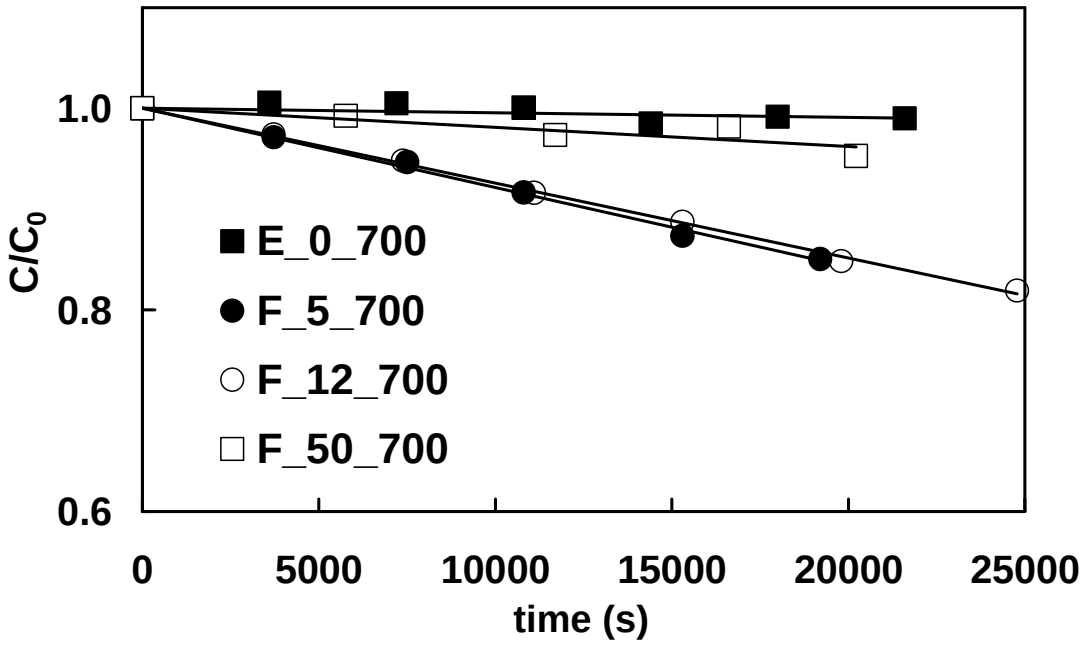

Figure 7.6 Photocatalytic degradation of FA on different photocatalysts, in the presence of a 400 nm cut off-filter.

7.3.3 EPR characterisation

A systematic EPR characterisation of the investigated F- and S-doped TiO_2 photocatalysts was performed in order to ascertain the presence and role of Ti^{3+} centres and of other paramagnetic species in relation to their photocatalytic activity.

Some examples of EPR spectra recorded with doped samples are shown in Fig. 7.7, whereas Table 7.3 resumes the features of all paramagnetic species observed at liquid nitrogen temperature (LNT) in S- and F-doped TiO_2. No other species were detected at room temperature (RT) and for this reason all EPR data will be referred to LNT spectra. Bare TiO_2 does not show any paramagnetic signal, whereas doped systems exhibit different signals whose intensity depends on the calcination temperature (Fig. 7.7). The observed signals can be divided in two categories. The first one involves nitrogen containing species and the second is due to titanium reduced centres (Ti^{3+}). The abundance of these two kinds of species is strictly related to the calcination temperature adopted in preparation.

For F-doped samples the concentration of both paramagnetic species decrease with increasing the calcination temperature. In S-doped samples, paramagnetic nitrogen containing species are much more abundant at low calcination temperature, whereas Ti^{3+} concentration increases at high temperature. Except for F_12_600, the nitric oxide radical (NO) roughly corresponds to the overall EPR spectral intensity in all analysed systems (see for example Fig. 7.7).

Table 7.3 Paramagnetic species observed in S- and F-doped TiO_2 calcined at different temperature.

	E	**F_5**	**F_12**	**F_50**	**S_5**	**S_12**	**S_50**
500 °C	-	NO, $N_b^{\cdot}$, Ti^{3+}	NO, Ti^{3+}	NO, $N_b^{\cdot}$, Ti^{3+}	NO, $N_b^{\cdot}$	NO	NO
600 °C	-	$N_b^{\cdot}$, Ti^{3+}	NO, Ti^{3+}	NO, Ti^{3+}	NO	NO	NO, Ti^{3+}
700 °C	-	NO, Ti^{3+}	NO	NO	Ti^{3+}	NO, Ti^{3+}	NO, Ti^{3+}

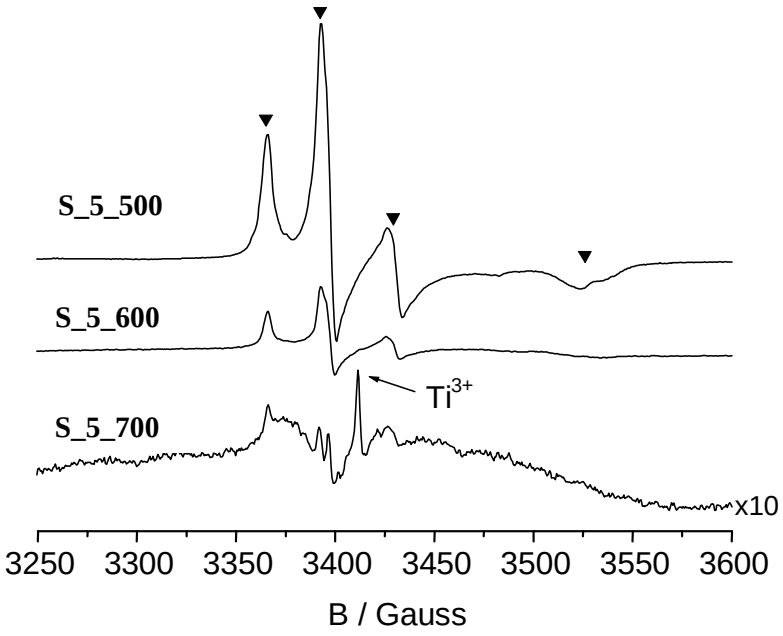

Figure 7.7 Examples of EPR spectra recorded with S-doped samples (containing 5 mol.% of S) calcined at different temperatures. The features typical of NO are marked (▼) in the upper spectrum.

7.3.3.1 F-doped TiO_2

Previous work of Giamello's group in Turin[30-33] put in evidence that when ammonium compounds are employed in the synthesis of non metal doped TiO_2, different nitrogen containing species can be observed. Some of them are diamagnetic and other show paramagnetic character. Among the paramagnetic species, a first type of N based paramagnetic centre is observed at LNT and disappears by raising the recording temperature, but showing up again, reversibly and with unchanged intensity, by cooling the system down to LNT. This species, characterised by a rhombic *g* and *A* tensor, is assigned to the paramagnetic nitric oxide (NO) radical encapsulated in micro-voids (or closed pores) generated during the synthesis process.[32] The temperature effects observed in its signal are due to the fact the EPR spectrum of NO in the gas phase is not observable in the free electron region, but it becomes visible in this region when this species is weakly adsorbed and polarized on a cationic surface centre at relatively low temperature. The second paramagnetic species, also characterised by orthorhombic *g* and *A* tensors, is assigned to a species containing a single nitrogen atom and trapped in the bulk of TiO_2.[33] This species, labelled as $N_b^{\bullet}$, can be observed by EPR both at RT and at LNT. Both species are usually located in the bulk of the doped systems. In the present work, the NO species was observed in almost all samples, its concentration

decreasing upon raising the calcination temperature (see for example Fig. 7.7). By contrast, the $N_b^{\bullet}$ centre, observed mainly for low calcination temperature and always with a very low intensity, are possibly responsible for the visible light absorption observed in samples calcined at 500°C (see Fig. 7.4).

The second signal observed in F-doped samples has no visible hyperfine structure and is characterised by an axial *g* tensor ($g_{\perp}$= 1.991 and $g_{//}$ = 1.951) and narrow line. This signal is unambiguously assigned to Ti^{3+} ions in the lattice. The presence of Ti^{3+} species in the solid is a direct consequence of the inclusion of fluorine. The presence of F in the lattice position usually occupied by oxygen introduces an extra electron in the system, which is localized on Ti ions in the TiO_2 structure.[34-36]

7.3.3.2 S-doped TiO_2

S doped samples show many features in common with the F-doped series. In this case $N_b^{\bullet}$ species was observed in one case only (S_5_500), while the NO radical was observed in all samples except for S_5_700. This series of samples also shows the presence of Ti^{3+} species when they are calcined at high temperature (700°C). The stabilisation of Ti^{3+} species in sulphur-doped TiO_2 was never reported up to date. The presence of such paramagnetic centre, as in the case of fluorine doping, can be ascribed to a charge imbalance effect which needs the presence of an extra electron for compensation.

Concerning sulphur doping of TiO_2, different possibilities are reported in the literature, depending on the sulphur oxidation state. Theoretical and experimental evidences show that S^{2-} substitution in O^{2-} lattice position is possible, but no charge imbalance is expected in this case.[3,37] XPS measurements evidenced high valence sulphur doping in the form of S(IV) or S(VI).[14,38,39] High valence sulphur can be associated either to surface containing species (SO_4^{2-} or SO_3^{2-} like) or to substitutional doping in the Ti^{4+} cation position. In this second case, if a cationic S^{6+} sulphur replaces a lattice titanium, charge imbalance in TiO_2 occurs and two more electrons are needed to warrant the electrical neutrality in the solid. The excess of electrons can be stabilised on the Ti^{4+} ions by generating Ti^{3+} centres, easily detected by the EPR technique, as follows:

$$S_x^{6+}\ Ti^{4+}_{(1-3x)}\ Ti_{2x}^{3+}\ O_2^{2-}$$

7.4 References

1. X. Chen and S. S. Mao, Chem. Rev., **2007**, 107, 2891.
2. A. Fujishima, X. Zhang and D. A. Tryk, Surf. Sci. Rep., **2008**, 63, 515.
3. R. Asahi, T. Morikawa, T. Ohwaki, K. Aoki and Y. Taga, Science, **2001**, 293, 269.
4. S. U. M. Khan, M. Al-Shahry and W. B. William Jr., Science, **2002**, 297, 2243.
5. S. Sakthivel and H. Kisch, Angew. Chem. Int. Ed., **2003**, 42, 4908.
6. M. Mrowetz, W. Balcerski, A. J. Colussi and M. R. Hoffmann, J. Phys. Chem. B, **2004**, 108, 17269.
7. N. Serpone, J. Phys. Chem. B, **2006**, 110, 24287.
8. D. Huang, S. Liao, J. Liu, Z. Dang and L. Petrik, J. Photochem. Photobiol. A: Chem., **2006**, 184, 282.
9. Y. Zhao, X. Qiu and C. Burda, Chem. Mater., **2008**, 20, 2629.
10. D. Gu, Y. Lu, B. Yang and Y. Hu, Chem. Commun., **2008**, 2453.
11. T. Umebayashi, T. Yamaki, H. Itoh and K. Asai, Appl. Phys. Lett., **2002**, 81, 454.
12. T. Umebayashi, T. Yamaki, S. Tanaka and K. Asai, Chem. Lett., **2003**, 32, 330.
13. T. Umebayashi, T. Yamaki, S. Yamamoto, A. Miyashita, S. Tanaka, T. Sumita and K. Asai, J. Appl. Phys., **2003**, 93, 5156.
14. T. Ohno, M. Akiyoshi, T. Umebayashi, K. Asai, T. Mitsui and M. Matsumura, Appl. Catal. A: General, **2004**, 265, 115.
15. T. Ohno, T. Tsubota, M. Toyofuku and R. Inaba, Catal. Lett., **2004**, 98, 255.
16. J. C. Yu, J. Yu, W. Ho, Z. Jiang and L. Zhang, Chem. Mater., **2002**, 14, 3808.
17. D. Li, H. Haneda, S. Hishita, N. Ohashi and N. K. Labhsetwar, J. Fluorine Chem., **2005**, 126, 69.
18. A. Hattori and H. Tada, J. Sol-Gel Sci. Technol., **2001**, 22, 47.
19. P. Periyat, S C. Pillai, D. E. McCormack, J. Colreavy and S. J. Hinder, J. Phys. Chem. C, **2008**, 112, 7644.
20. Y. Wang, J. Li, P. Peng, T. Lu and L. Wang, Appl. Surf. Sci., **2008**, 254, 5276.
21. M. Mrowetz and E. Selli, New J. Chem., **2006**, 30, 108.
22. M. Mrowetz and E. Selli, Phys. Chem. Chem. Phys, **2005**, 7, 1100.
23. H. Kominami, S. Murakami, J. Kato, Y. Kera and B. Ohtani, J. Phys. Chem. B, **2002**, 106, 10501.
24. S. Enriquez, A. G. Agrios and P. Pichat, Catal. Today, **2007**, 120, 196.
25. H. M. Rietveld, J. Appl. Cryst., **1969**, 2, 65.

26. A. Altomare, M. C. Burla, C. Giacovazzo, A. Guagliardi, A. G. G. Moliterni, G. Polidori and R. Rizzi, J. Appl. Cryst., **2001**, 34, 392.
27. M. V. Dozzi, L. Prati, P. Canton and E. Selli, Phys. Chem. Chem. Phys., **2009**, 11, 7171.
28. M. Mrowetz and E. Selli, J. Photochem. Photobiol. A: Chem., **2006**, 180, 15.
29. C. Bernardini, M. V. Dozzi, G. Cappelletti and E. Selli, J. Photochem. Photobiol. A: Chem., **2010**, 211, 185.
30. S. Livraghi, A. Votta, M. C. Paganini and E. Giamello, Chem. Commun., **2005**, 498.
31. S. Livraghi, M. C. Paganini, M. Chiesa and E. Giamello, Res. Chem. Intermed., **2007**, 33, 739.
32. S. Livraghi, M. R. Chierotti, E. Giamello, G. Magnacca, M. C. Paganini, G. Cappelletti and C. L. Bianchi, J. Phys. Chem. C, **2008**, 112, 17244.
33. S. Livraghi, A. M. Czoska, M. C. Paganini and E. Giamello, J. Solid State Chem., **2009**, 182, 160.
34. A. M. Czoska, S. Livraghi, M. Chiesa, E. Giamello, E. Finazzi, C. Di Valentin, G. Pacchioni, S. Agnoli and G. Granozzi, J. Phys. Chem. C, **2008**, 112, 8951.
35. C. Di Valentin, E. Finazzi, G. Pacchioni, A. Selloni, S. Livraghi, A. M. Czoska, M. C. Paganini and E. Giamello, Chem. Mater., **2008**, 20, 3706.
36. S. Livraghi, K. Elghniji, A. M. Czoska, M. C. Paganini, E. Giamello and M. Ksibi, J. Photochem. Photobiol. A: Chem., **2009**, 205, 93.
37. W. Ho, J. C. Yu and S. Lee, J. Solid State Chem., **2006**, 179, 1171.
38. J. C. Yu, W. Ho, J. Yu, H. Yip, P. K. Wong and J. Zhao, Environ. Sci. Technol., **2005**, 39, 1175.
39. P. Periyat, D. E. McCormack, S. J. Hinder and S. C. Pillai, J. Phys. Chem. C, **2009**, 113, 3246.

Chapter 8

Absorption and Action Spectra Analysis of Ammonium Fluoride-doped Titania Photocatalysts

8.1 Introduction

As already mentioned in the previous Chapter, many efforts have been made in the past decade[1,2] in order to overcome one of the major drawbacks of the use of TiO_2 as a photocatalyst, *i.e.* its relatively large energy band gap (3.2 eV for the anatase phase), which hampers the exploitation of solar light in photocatalytic reactions. Anion doping with *p*-block elements has been successfully pursued to sensitize TiO_2 towards visible light,[3,4] either by introducing newly created mid-gap energy states or by narrowing the band gap itself. The effectiveness, but also the still not completely understood nature of doping titanium dioxide with main group elements, such as N,[3,5-12] C,[4,13-16] B,[17-19] S,[12,14,20-24] P,[25,26] I,[27,28] and F,[29-38] has been ascertained in a great number of studies, which also demonstrated that the insertion of dopant impurities into the oxide structure may increase the rate of the undesired recombination of photocatalytically generated charge carriers. In contrast, the recombination rate is known to become lower, the higher is the crystallinity degree of the oxide structure.

Conflicting results regarding the effects of fluorine (F) as dopant element for TiO_2 have been reported,[29-38] likely due to the different routes employed to prepare the doped materials and also to difficulties in the interpretation of photocatalytic results obtained with photocatalysts containing more than one dopant element, because of possible synergistic effects.[33,38] In most cases, F-doping apparently did not cause any appreciable shift of the fundamental band gap absorption edge of TiO_2.[29,34,36] This is consistent with theoretical band calculations,[3,31] indicating that when TiO_2 is doped with fluorine, localized high-density energy levels, composed of F 2p states, reside below the valence band of TiO_2. However, despite this, F-doped materials exhibit visible-light-driven photocatalytic activity, the origin of which is still very uncertain. In fact, F atoms included in the semiconductor structure, owing to their high electronegativity, could stabilize the electron release upon oxygen depletion during the calcination treatment.[34,35] In this case, visible light photocatalytic excitation by extrinsic absorption bands of so-generated oxygen vacancies can generate free charge carriers that can take part in surface chemical reactions. The photocatalytic activity of F-doped materials might also be related to the peculiar formation of Ti^{3+} centres, obtained by charge compensation effects consequent to the insertion of F^- ions in the O^{2-} sites of the TiO_2 lattice. Accumulation of photoexcited electrons on Ti^{3+} surface states, followed by their transfer to oxygen adsorbed on the photocatalyst surface, with

a consequent decrease of the electron-hole recombination rate, was originally proposed[29] to account for the enhanced photoactivity of F-doped TiO_2. However, the Ti^{3+} defect centres were recently located *ca.* 0.6 eV below the bottom of the conduction band[36] and may be unable to react with adsorbed oxygen, if they are not on the external layers of the material.

The systematic investigation described in the previous chapter concerning the photocatalytic activity under visible light of a series of doped TiO_2 photocatalysts synthesized by the sol-gel method in the presence of different amounts of NH_4F and calcined at different temperature (500–700°C)[39] evidenced that the photoactivity of such materials in the degradation of formic acid in aqueous suspensions was higher than that of undoped materials prepared by the same synthetic route. Of course, aiming at verifying the effective visible light activation of doped materials, the choice of an appropriate photocatalytic test reaction is crucial and the use of substrates that are able to absorb visible light and inject electrons into the semiconductor from their electronically excited state should be avoided.[40] Furthermore, the ranking of the photocatalytic activity of TiO_2 samples is known to depend on the test molecule.[41,42]

The photocatalytic behaviour of an extended series of NH_4F-doped TiO_2 photocatalysts was explored in two other reactions, *i.e.* the decomposition of acetic acid in aqueous suspensions and the gas phase mineralization of acetaldehyde. Neither of these substrates absorbs visible light. In order to obtain an insight into the origin of the enhanced photoactivity of such materials under visible light, the photocatalytic oxidation of acetic acid was also investigated systematically as a function of irradiation wavelength, by collecting so-called action spectra. This type of analysis, representing the most powerful photocatalytic characterization tool to determine the effective wavelength-dependent response and activity of a photocatalyst,[40,43] had never been applied to similarly doped materials. By comparing the shapes of the action spectra with those of the absorption spectra of the investigated photocatalysts a model is proposed, which allows a clear distinction between light absorption and effective photoactivity as a function of irradiation wavelength.

8.2 Experimental Section

8.2.1 Doped-TiO_2 preparation and characterisation

The series of doped titania (D-TiO_2) photocatalysts was prepared by the sol-gel method already described in Chapter 7,[39] in the presence of different amounts of NH_4F, used as a dopant source, and calcined at different temperature (500–700°C). The nominal dopant/Ti percent molar ratios were 3, 5, 12 and 25 in this case. NH_4F-doped TiO_2 samples were labelled as D_X_Y, with X referring to the nominal dopant/Ti percent molar ratio and Y referring to the calcination temperature in Celsius. Reference undoped materials, prepared by exactly the same synthetic route in the absence of NH_4F, are referred to as the D_0_Y photocatalysts series. All reagents were purchased from Aldrich and employed as received.

XPS analysis was performed by using a JEOL JPS-9010MC spectrometer with Mg K_α radiation, 10 eV pass energy and 0.1 eV energy step. The analysis area of the sample pellets was about 6 mm^2, the depth about 1–2 mm. The charging effect on the analysis was corrected by considering the binding energy value of C 1s at 284.7 eV, due to adventitious carbon. Quantification was obtained using the SPEC-SURF software provided by Jeol.

Diffuse reflectance (DR) spectra of the photocatalyst powders were recorded on a Jasco V-670 spectrophotometer equipped with a PIN-757 integrating sphere, using barium sulphate as a reference, and then converted into absorption (A) spectra ($A = 1 - R$).

Gas phase acetaldehyde decomposition under polychromatic irradiation was performed as detailed in Section 4.2.1. Acetic acid decomposition was investigated under polychromatic irradiation as detailed in Section 4.2.2, whereas the action spectra analysis of this reaction is fully detailed in Section 4.2.3.

8.3 Results and Discussion

8.3.1 Photocatalysts structure

The main structural features, determined by XRD, BET and XPS analyses, of the investigated series of undoped and doped TiO_2 photocatalysts are collected in Table 8.1. The phase composition of all samples, obtained by Rietveld refinement of XRD data, clearly confirms that doping inhibits the anatase into rutile transformation that occurs when pure TiO_2 is calcined at a temperature above 500°C.[39] This phase transformation is inhibited by the addition of Ti^{4+} complexing ions (*e.g.* sulphates, phosphates, fluorides), reducing the condensation of spiral chains of rutile TiO_6 octahedra.[34] A similar argument was used to account for the full anatase composition of sulphur-doped anatase.[24]

The anatase crystallite dimensions d_A, calculated using the Scherrer equation,[44] clearly increased with increasing the calcination temperature for the same nominal dopant amount. This trend was accompanied by a decrease in specific surface area (SSA), as revealed by BET analysis. Doping appears to be beneficial for obtaining materials with larger surface area, especially if calcined at a relatively low temperature. The SSA of doped materials usually remained higher than that of pure TiO_2, even after calcination at 700°C.

XPS analysis confirmed the presence of carbon, oxygen and titanium on the surface of all samples,[39] with an O/Ti ratio slightly higher than 2, together with roughly constant surface amounts of nitrogen, on both undoped and doped samples (see Table 8.1). The XPS signal in the F 1s binding energy region consisted of only one band, peaking around 684 eV, due to surface fluoride ions.[29,37] No XPS signal at 688 eV, assigned to substitutional ions in the F-TiO_2 lattice, was detected, possibly always being below the detection limit of the XPS technique.

The effective dopant/Ti molar ratio determined by quantitative XPS analysis, also shown in Table 8.1, was usually lower than the nominal value according to the synthesis of the different doped TiO_2 series. Furthermore, the amount of fluoride ions physically adsorbed on the TiO_2 surface usually decreased with increasing the calcination temperature.

Table 8.1 Phase composition and crystallite dimensions, d_A, obtained from XRD analysis, by assuming the absence of amorphous phase; specific surface area (SSA), obtained from BET analysis; and surface F/Ti and N/Ti molar ratios, obtained from XPS analysis of the investigated photocatalysts series.

Sample	dopant/Ti molar ratio (%)	anatase (%)	brookite (%)	rutile (%)	d_A/nm	SSA/m^2 g^{-1}	surface molar F/Ti (%)	surface molar N/Ti (%)
P25		80	-	20	25	50		
A45		100	-	-	35	45		
JRC-TiO-8		100	-	-	4	338		
D_0_500	0	99	1	-	15	15	-	2.8
D_0_600	0	90	-	10	32	9	-	2.8
D_0_700	0	38	-	62	65	7	-	3.0
D_3_500	3	98	2	-	16	65	n.d.	n.d.
D_3_600	3	97	-	3	32	32	n.d.	n.d.
D_3_700	3	93	-	7	40	22	n.d.	n.d.
D_5_500	5	98	2	-	13	63	6.0	2.9
D_5_600	5	100	-	-	44	31	4.3	2.6
D_5_700	5	99	-	1	49	16	3.7	2.9
D_12_500	12	100	-	-	19	43	7.1	2.9
D_12_600	12	100	-	-	33	23	5.0	3.0
D_12_700	12	99.5	-	0.5	48	12	4.4	4.2
D_25_500	25	100	-	-	19	39	9.6	3.4
D_25_600	25	100	-	-	47	15	6.5	3.3
D_25_700	25	100	-	-	110	8	11.5	2.6

n.d. = not determined

8.3.2 Photocatalytic activity tests under polychromatic irradiation

8.3.2.1 Liquid phase acetic acid photocatalytic oxidation under UV light

The photocatalytic activity of doped TiO_2 photocatalysts was first evaluated in the oxidative decomposition of acetic acid in aqueous suspensions. The use of this substrate as a photocatalytic degradation test molecule presents two advantages, apart from the main pre-requisite that it does not absorb visible light: 1) the reaction is relatively simple, yielding CO_2 with few intermediates and 2) because of the acidity of the suspension, CO_2 is promptly removed from the liquid into the gas phase, where it can be easily determined.

The photocatalytic evolution of CO_2 from suspensions containing acetic acid and either pure or doped TiO_2 samples always occurred at constant rate, *i.e.* the rate obeyed a zero-order rate law. Thus, the activity of the investigated photocatalysts can be compared in terms of the zero-order rate constants of acetic acid photocatalytic oxidation reported in Fig. 8.1.

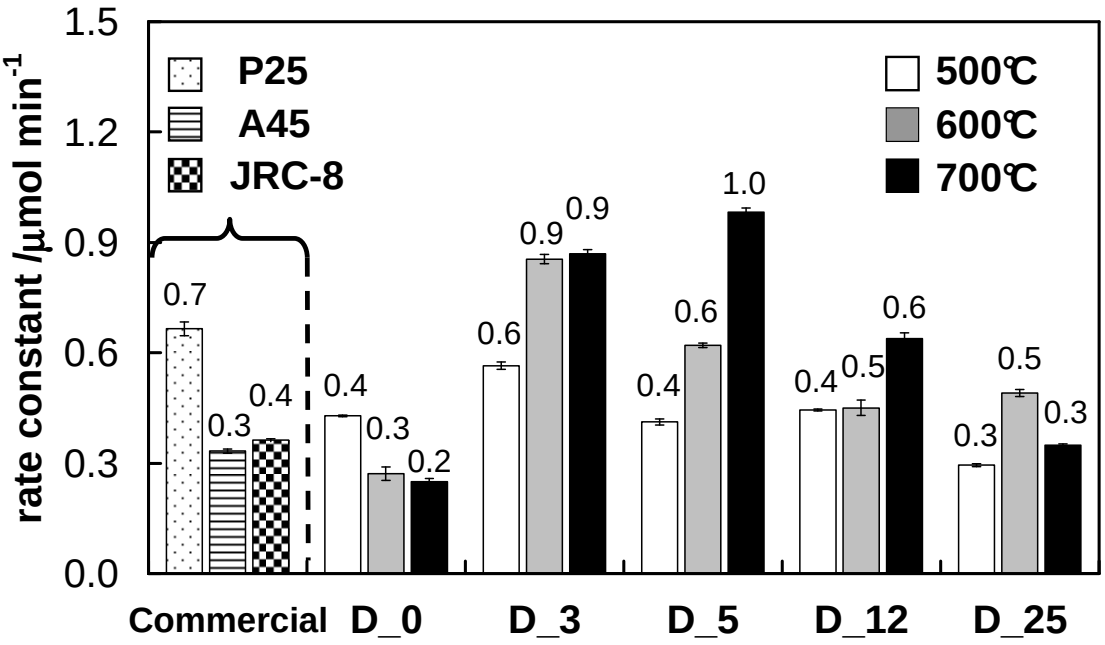

Figure 8.1 Zero-order rate constants of CO_2 photocatalytic evolution during acetic acid decomposition under polychromatic irradiation on commercial TiO_2 photocatalysts and on doped TiO_2 photocatalysts containing different dopant amounts and calcined at different temperature.

One can notice, first of all, that the reaction in the presence of undoped TiO_2 proceeded at a lower rate than that attained in the presence of moderately doped TiO_2. Moreover, with undoped TiO_2 (D_0 series) the reaction rate decreased with increasing the calcination temperature, probably as a consequence of the already mentioned anatase into rutile transformation (Table 8.1).

Moderate doping increased the photocatalytic activity of TiO_2 and this effect increased with increasing the calcination temperature of the photocatalyst, attaining a maximum value for moderately doped D_5_700 calcined at 700°C, in good agreement with the results, discussed in the previous chapter, of formic acid photodecomposition tests.[39] This may appear unusual, since the highest photoactivity was achieved with a photocatalyst characterized by a relatively small surface area and large mean particle

size (see Table 8.1). In any case, doping seems to induce modifications of TiO_2 that increase its photocatalytic activity and such an effect is maximum for samples calcined at high temperature. Although surface fluorination of TiO_2 is expected to retard the photocatalytic oxidation of carboxylic acids, as verified in the case of formic acid,[45] this effect cannot be attributed exclusively to surface effects, *i.e.* to the slightly smaller amount of surface fluorine detected on the surface of D–TiO_2 samples calcined at a higher temperature (Table 8.1). On the other hand, an excessive amount of dopant (D_25 series) could increase the extent of defects in the oxide structure, acting as recombination centres of photogenerated charge carriers, with a consequent decrease in the photocatalytic reaction rate.

The photoactivity data presented in Fig. 8.1 evidence that the best performing doped materials were more active than two pure anatase phase materials, labelled JRC-TiO-8 and A45, possessing very different specific surface areas (see Table 8.1), and also more active than commercial P25 TiO_2.

8.3.2.2 Gas phase photocatalytic decomposition of acetaldehyde under Xe lamp irradiation

The photocatalytic degradation of acetaldehyde proceeded according to a first-order rate law. A comparison of first-order rate constants for CH_3CHO degradation on doped and commercial photocatalysts is shown in Fig. 8.2. They were obtained from the gas phase CH_3CHO concentration *vs.* time profiles, neglecting the amount of substrate adsorbed on the photocatalyst surface. This kinetic behaviour is compatible with a diffusion-limited reaction, with CH_3CHO surface concentration always being close to zero, because substrate molecules undergo oxidation as soon as they come into contact with the irradiated photocatalyst surface. Under such conditions the diffusion rate, and consequently the overall reaction rate, is proportional to the substrate concentration in the gas phase.[46] Furthermore, the diffusion rate of the substrate is expected to increase with increasing the photocatalyst surface area. In fact, if the thickness of the diffusion layer is negligibly small, the diffusion cross section almost coincides with the surface area and a correlation between the photocatalytic reaction rate and the specific surface area of the photocatalyst is usually expected.[46]

However, by considering the first-order rate constant values shown in Fig. 8.2, one can notice, rather surprisingly, that this kind of relation does not apply in the case of

these doped TiO_2 photocatalysts. In fact, the general trend of reaction rate increasing with increasing the calcination temperature obtained for doped TiO_2 in both formic and acetic acid photocatalytic decomposition in liquid phase was also found in this gas-phase test reaction, with the highest photocatalytic activity being achieved with samples characterized by small surface area, and moderately doped D_5_700 being confirmed as the best performing photocatalyst. Opposite results would have been expected for this gas-solid phase test reaction, the rate of which was demonstrated to be positively affected by photocatalysts' large surface areas, ensuring fast diffusion of acetaldehyde and O_2 reactants.[46]

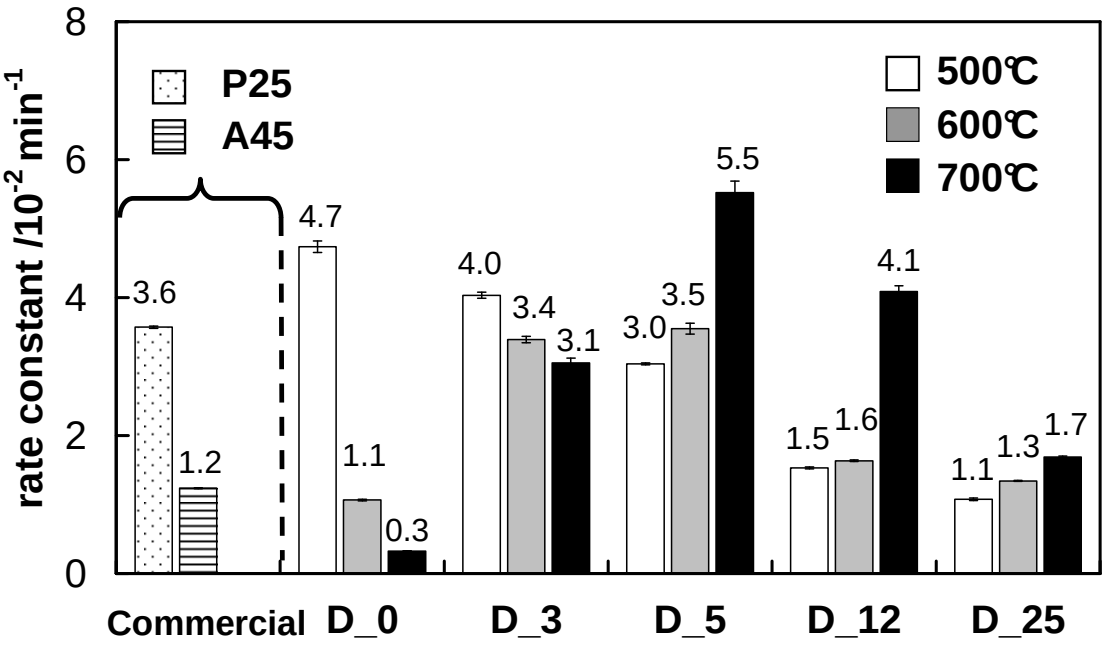

Figure 8.2 First-order rate constants of CH_3CHO photodegradation under xenon lamp irradiation on photocatalysts containing different dopant amounts and calcined at different temperature.

Only doped TiO_2 photocatalysts of the D_3 series showed in acetaldehyde decomposition (Fig. 8.2) an opposite photoactivity trend *vs.* calcination temperature from that shown in acetic acid photooxidation (Fig. 8.1). In fact, within this series the rate of acetaldehyde decomposition slightly decreased with increasing the photocatalyst calcination temperature, probably as a consequence of the anatase into rutile transformation. Both the very low rutile content of D_3_600 and D_3_700 and the decrease in SSA with increasing the calcination temperature of these samples (Table 8.1) contributed to the reduction of their overall photoefficiency. Anatase crystallites

were shown to be highly photoactive in both the present reactions under aerated conditions, whereas a negative contribution of the rutile phase was demonstrated just in the case of gas-phase acetaldehyde decomposition.[46]

8.3.3 Action spectra analysis

8.3.3.1 Action spectra of acetic acid decomposition (300–520 nm range)

In order to better elucidate the origin of the enhanced photoactivity of doped materials and verify their possible activation in the visible region, the photocatalytic oxidation of the transparent acetic acid substrate was systematically investigated as a function of irradiation wavelength. The action spectra were first measured for the D_0, D_5 and D_12 series in the 300–520 nm range with a 20-nm wavelength step. A comparison of the action spectra and the absorption spectra of selected photocatalysts, normalized to the highest apparent quantum efficiency Φ_{app} and absorption value, respectively, is shown in Fig. 8.3. For undoped and doped TiO_2 samples calcined at high temperature, the onset wavelength of the action spectra was red-shifted compared with that of the absorption spectra. This is probably due to the relatively large FWHM of the light employed in photocatalytic runs compared to that used for absorption measurements[46] and to the fact that TiO_2 absorbs more at shorter wavelengths than at longer wavelengths in a given wavelengths range.

This effect was not observed in the case of doped TiO_2 calcined at 500°C. In fact, as shown in Fig. 8.3, these full anatase photocatalysts, though exhibiting small absorption at wavelengths longer than those typical of the TiO_2 band gap absorption onset, did not show any appreciable photocatalytic activity under visible light irradiation. On the other hand, as better outlined in the following systematic analysis of action *vs.* absorption spectra, doped samples calcined at 700°C were active also under irradiation at wavelengths longer than that of their band gap absorption onset (see D_5_700 and D_12_700 panels in Fig. 8.3).

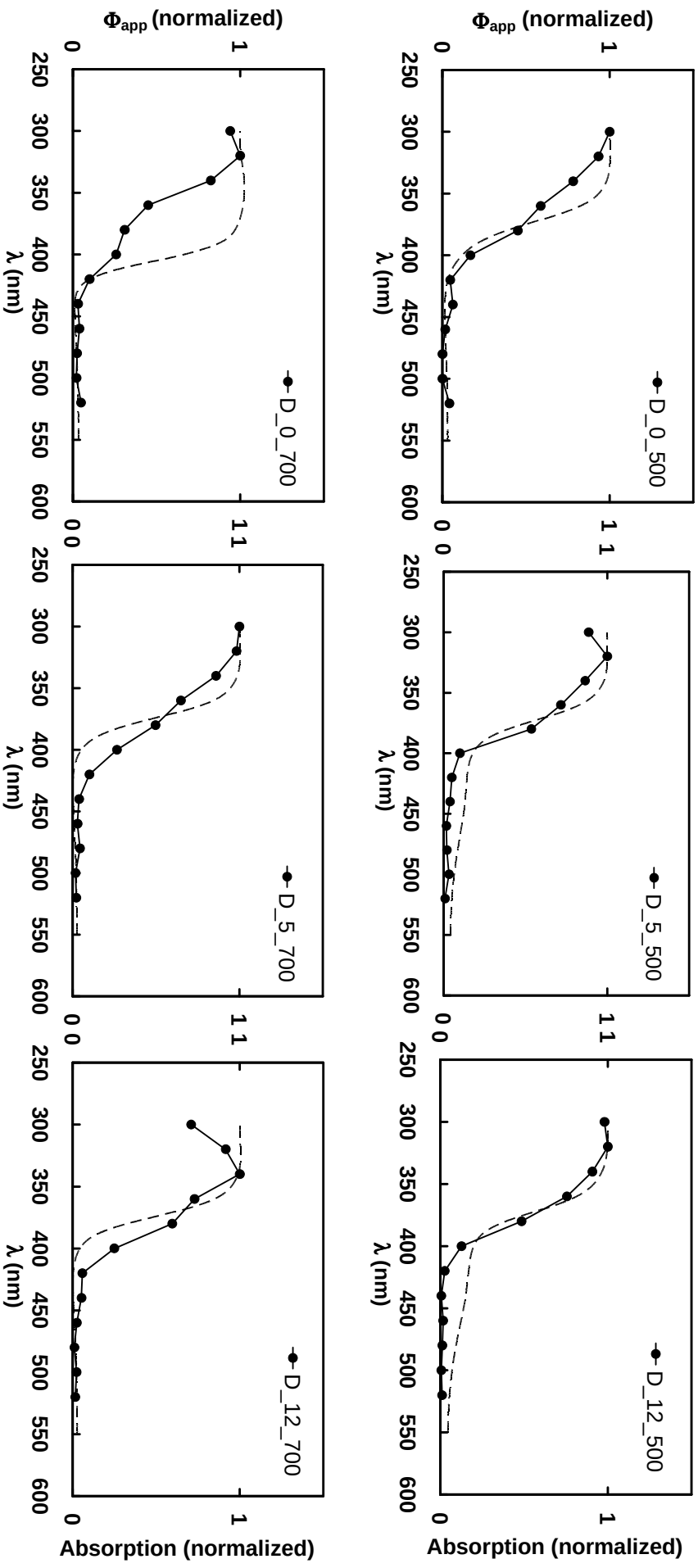

Figure 8.3 Action spectra of acetic acid decomposition (full circles) and absorption spectra (dashed lines) of selected photocatalysts.

The action spectra of acetic acid decomposition obtained in the presence of undoped TiO_2 calcined at different temperature are shown in Fig. 8.4a. The apparent quantum efficiency in the 300–400 nm wavelengths range decreased with increasing the calcination temperature of these undoped materials, whereas their absorption spectra, shown in Fig. 8.4b, exhibit exactly the opposite trend, *i.e.* a red-shifted band gap absorption with increasing the calcination temperature, due to the phase transition from anatase to rutile.

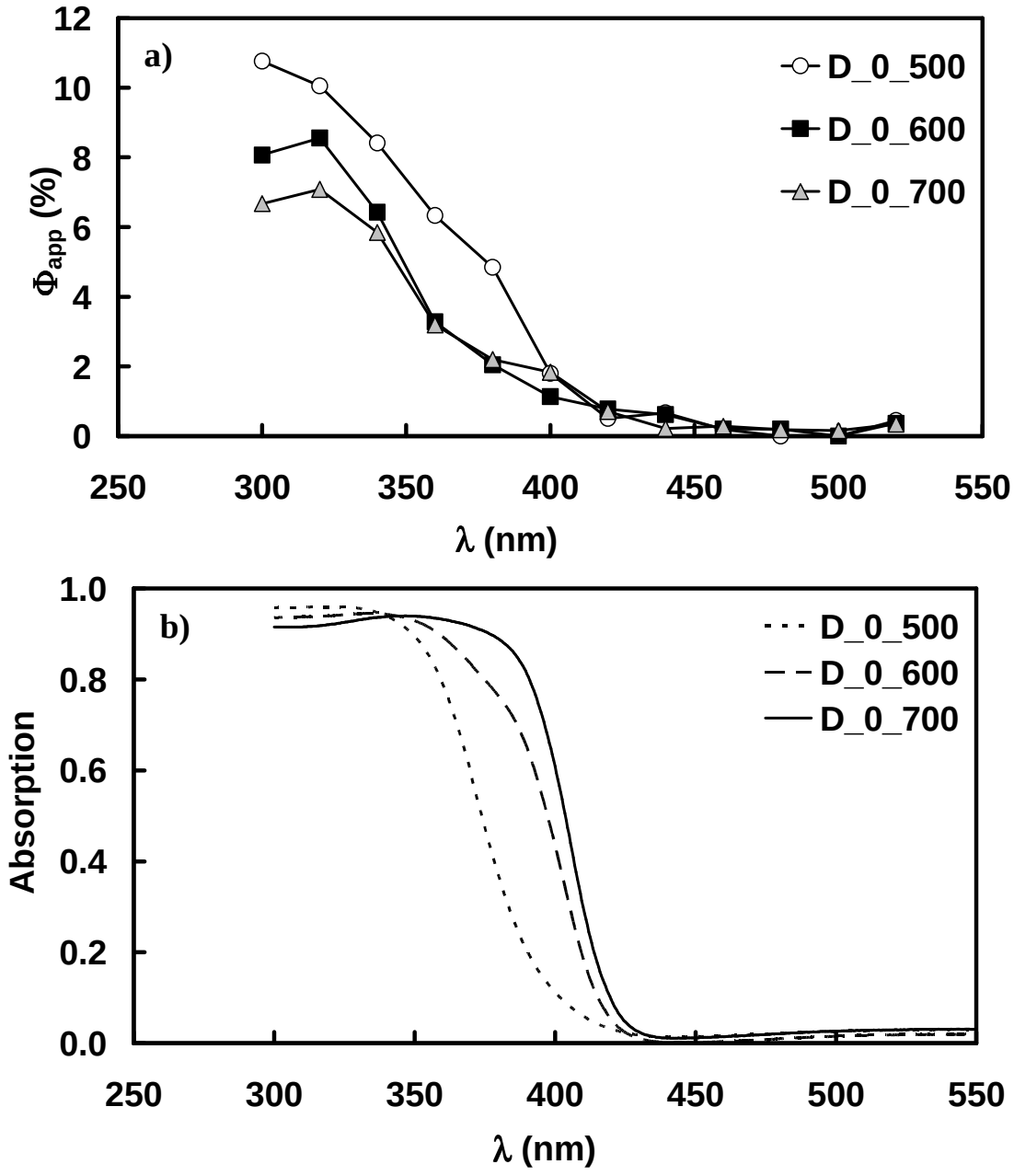

Figure 8.4 a) Action spectra of acetic acid decomposition and b) absorption spectra of undoped TiO_2 calcined at different temperatures.

The results reported in Fig. 8.4 can be explained by assuming that the anatase phase is more photoactive than rutile in acetic acid decomposition.[46] In fact, the flat-band potentials of TiO_2 depend on its crystalline form, being at -0.16 and 0.04 V *vs.* NHE (pH 0) for anatase and rutile TiO_2, respectively. In the case of photocatalytic oxidation reactions, such as acetic acid decomposition, photo-excited electrons are scavenged by molecular oxygen at the TiO_2 surface, where one-electron reduction of O_2 occurs. Considering that the $O_2/HO_2^{\cdot}$ potential is -0.046 V *vs.* NHE, anatase, but not rutile, is expected to efficiently reduce O_2 to $HO_2^{\cdot}$ under band gap excitation, resulting in the higher photocatalytic activity of anatase in acetic acid decomposition. Furthermore, less active rutile in undoped D_0_600 and D_0_700 may also exert a so-called 'inner filter' action, by absorbing a fraction of light that is no longer available for anatase phase photoactivation.[46,47]

For doped samples the wavelength-dependent apparent quantum efficiency in acetic acid decomposition was found to vary with both the dopant content and the calcination temperature of the investigated photocatalysts. The action spectra presented in Fig. 8.5, referring to samples containing different nominal dopant amounts (D_0, D_5 and D_12 series), all calcined at the highest temperature (700°C), showed that the apparent quantum efficiency of doped materials was higher than that of undoped TiO_2. This could be mainly ascribed to the full anatase phase composition of doped materials, whereas D_0_700 also contained rutile, which, as already mentioned, is expected to be less active in the photocatalytic decomposition of acetic acid. However, a larger amount of dopant (D_12 series) led to a lower apparent quantum efficiency, especially under UV irradiation (300–340 nm), probably as a consequence of the already mentioned enhanced recombination of electron-hole couples photoproduced in this region, due to the increased extent of defects in the oxide structure acting as charge recombination centres. The action spectra trend shown in Fig. 8.5 is in line with the photocatalytic activity trend obtained under full lamp emission in both liquid phase and gas phase oxidation reactions investigated in the present work (see Fig.s 8.1 and 8.2, respectively).

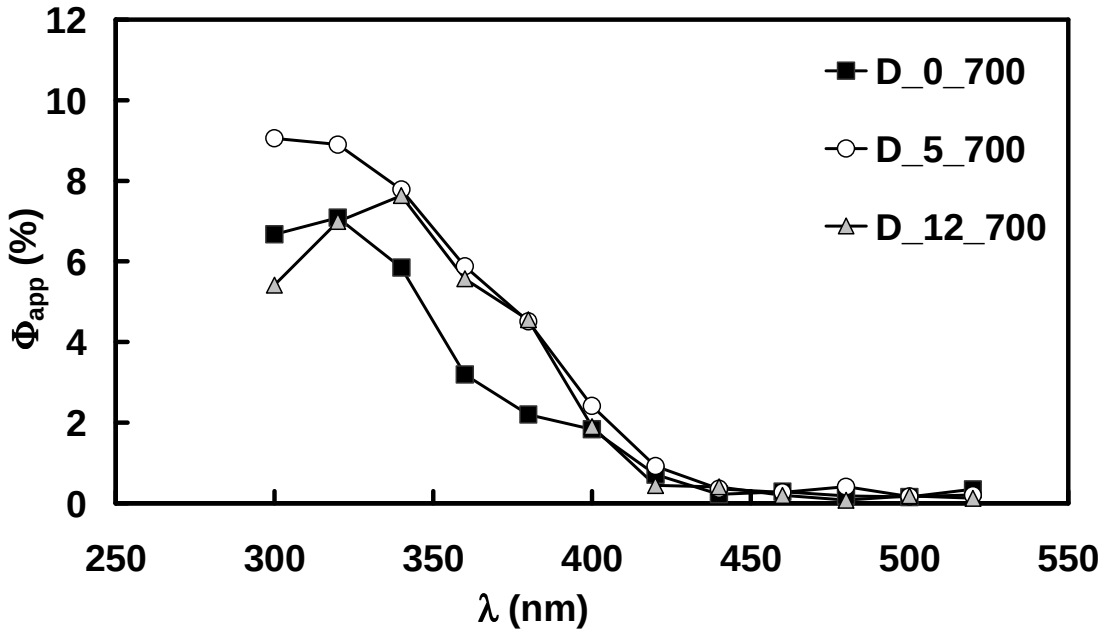

Figure 8.5 Action spectra of acetic acid decomposition obtained in the presence of undoped (D_0) and differently doped samples (D_5 and D_12), all calcined at 700°C.

The effect of calcination temperature on the photoactivity of samples containing the same nominal dopant amount is enlightened by the action spectra of the D_5 series, shown in Fig. 8.6.

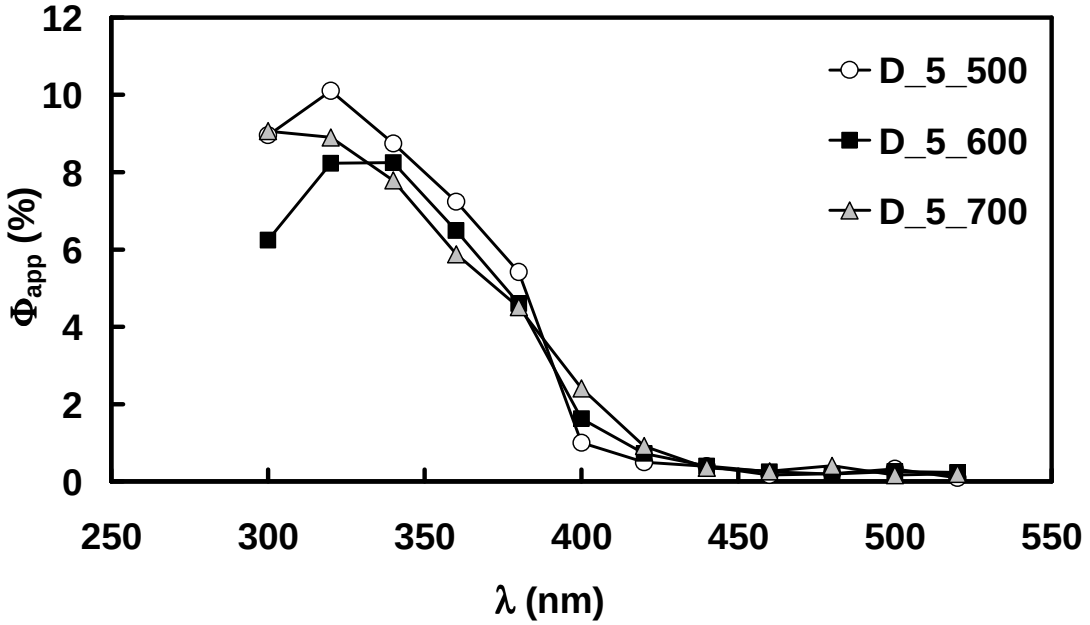

Figure 8.6 Action spectra of acetic acid decomposition obtained in the presence of moderately doped samples (D_5 series) calcined at different temperatures.

Two relative photocatalytic efficiency scales can be found, depending on the irradiation wavelength region. For $\lambda_{irr} < 400$ nm the photoactivity of doped samples slightly decreased with increasing the calcination temperature, whereas for $\lambda_{irr} \geq 400$ nm the opposite trend was observed. The same wavelength-dependent photoactivity trend was also obtained for the action spectra of the D_12 series. This suggests that doping might have beneficial effects on the photoactivity of samples calcined at a relatively high temperature, with a general photocatalytic efficiency trend in this wavelengths region perfectly matching that achieved under full lamp emission.

On the basis of these intriguing results the photoactivity of selected photocatalyst series was investigated more in depth in a smaller wavelengths range, centred in the near UV-Vis region.

8.3.3.2 Action spectra of acetic acid decomposition (370–460 nm range)

The action spectra in the 370–460 nm range obtained with a 10-nm wavelength step for the D_5, D_12 and D_25 doped series, shown in Fig. 8.7, clearly confirm that within each series of doped materials a progressively higher calcination temperature ensured a better apparent quantum efficiency at $\lambda_{irr} < 420$ nm.

The most straightforward demonstration that a certain material is an effective photocatalyst consists in the resemblance of its action spectrum with its absorption spectrum.[40,43] However, no appreciable and obvious similarity can be found by directly comparing the action spectra of doped samples shown in Fig. 8.7 with their absorption spectra shown in Fig. 8.8. In fact, all samples calcined at 500°C, especially those containing a relatively large amount of dopant, absorbed light at wavelengths longer than those typical of the TiO_2 band gap absorption onset. However, this visible light absorption did not induce any appreciable activity in acetic acid photocatalytic decomposition in this irradiation wavelengths range. On the contrary, doped samples calcined at higher temperature (600 and 700°C) did not exhibit any noticeable extra absorption with respect to undoped TiO_2, but they showed increased efficiency in acetic acid photocatalytic oxidation in the 370–410 nm range. By comparing the absorption properties of our materials with their wavelength-dependent photocatalytic activities, a qualitative model was developed, that provides a reasonable interpretation of our apparently controversial results.

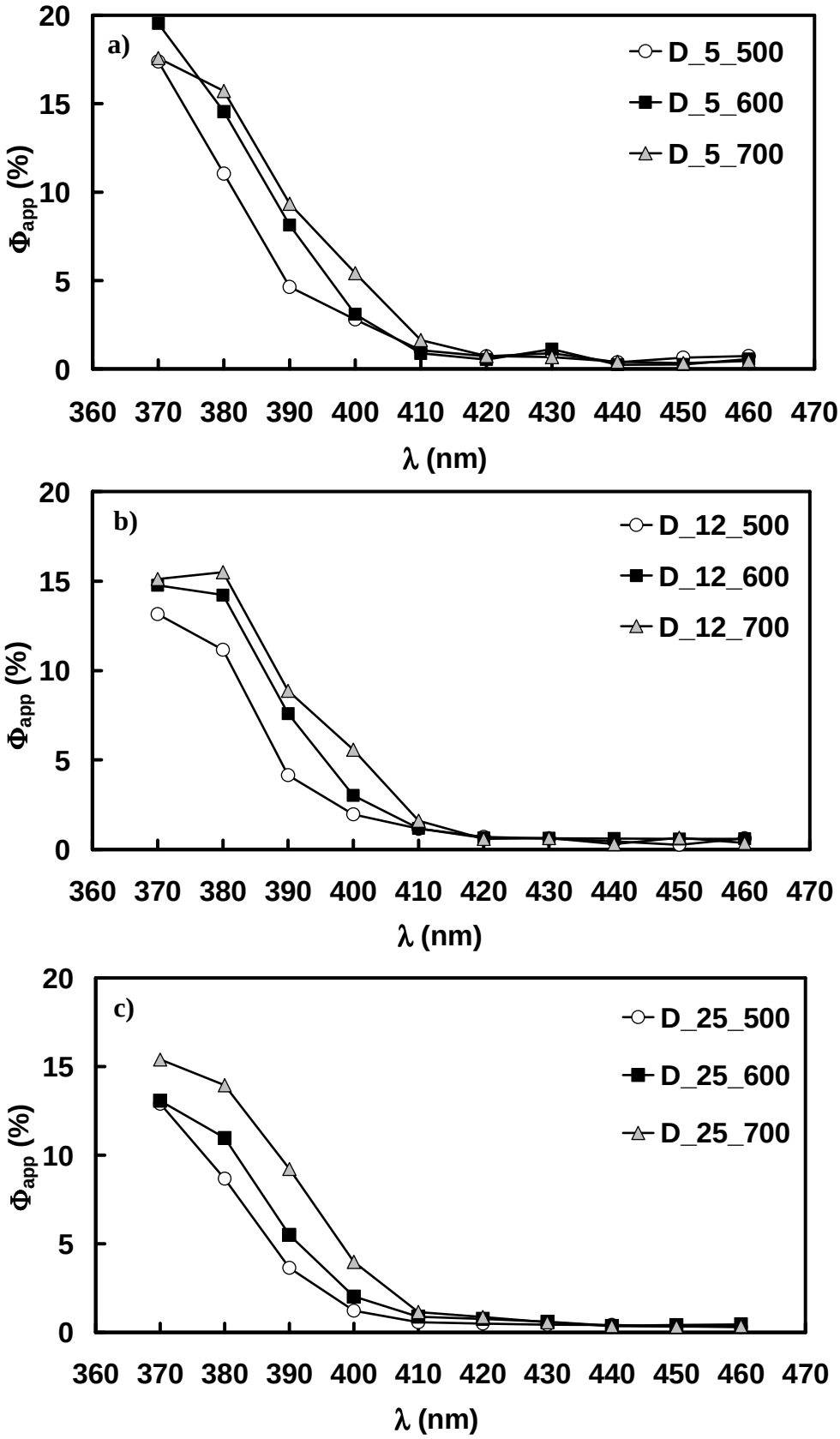

Figure 8.7 Action spectra of acetic acid decomposition in the 370–460 nm wavelengths range of the a) D_5, b) D_12 and c) D_25 doped TiO_2 photocatalysts series.

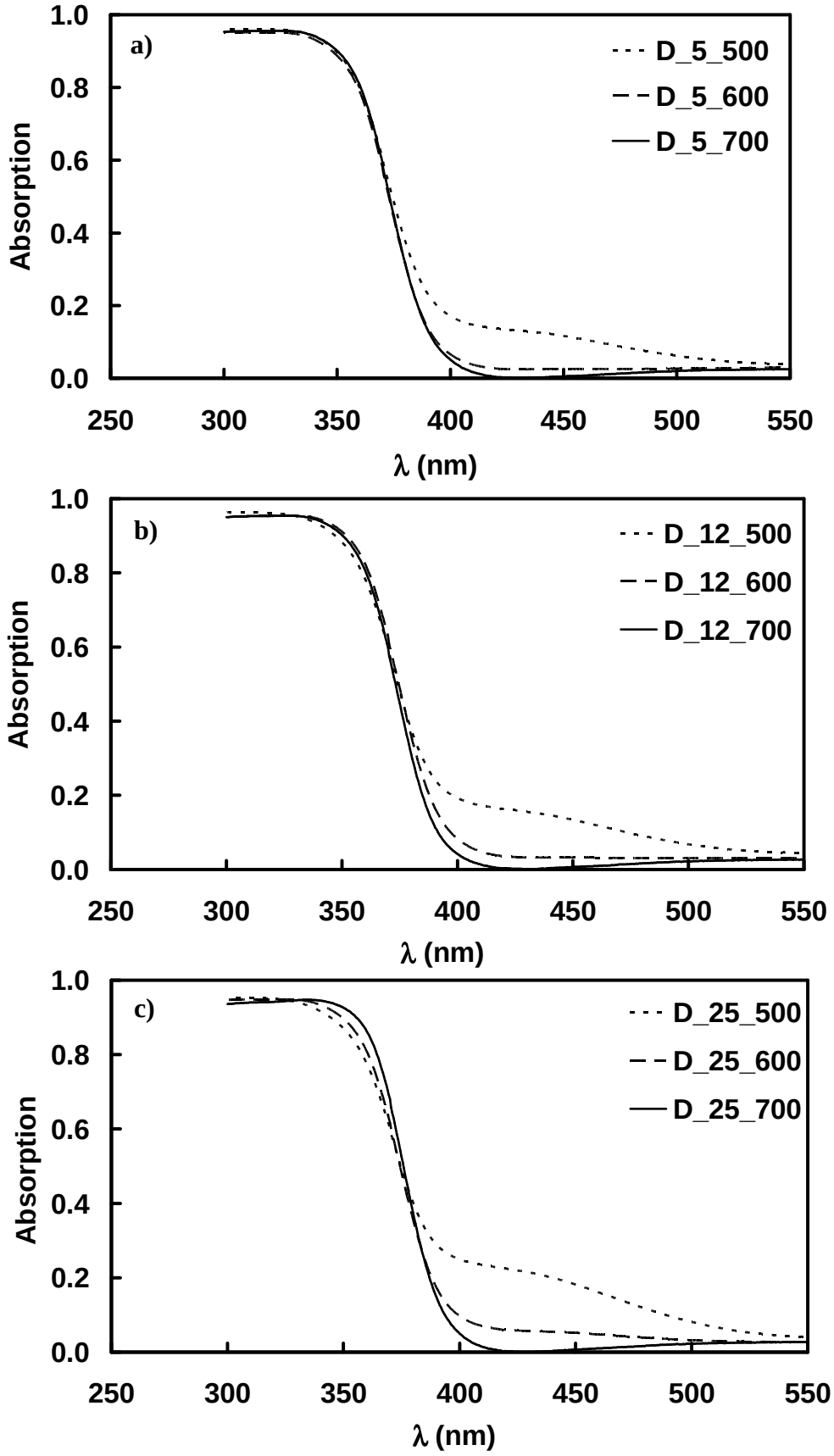

Figure 8.8 Absorption spectra of the a) D_5, b) D_12 and c) D_25 doped TiO_2 series.

8.3.4 Model for absorption and action spectra deconvolution

8.3.4.1 Absorption spectra deconvolution

The absorption spectra of samples belonging to the same series, *i.e.* containing a fixed nominal dopant amount, were compared first, to highlight the effects of calcination temperature and evidence the presence of possible sub-bands, through a procedure of absorption spectra subtraction. As can be seen in the examples shown in Fig. 8.9 referring to the D_25 series, the absorption spectra of samples calcined at a lower temperature were subtracted from those of samples calcined at a higher temperature. As all doped samples, even those calcined at 700°C, consist of pure anatase phase, any artifact in the difference spectra due to rutile phase absorption can be excluded (*vide infra*).

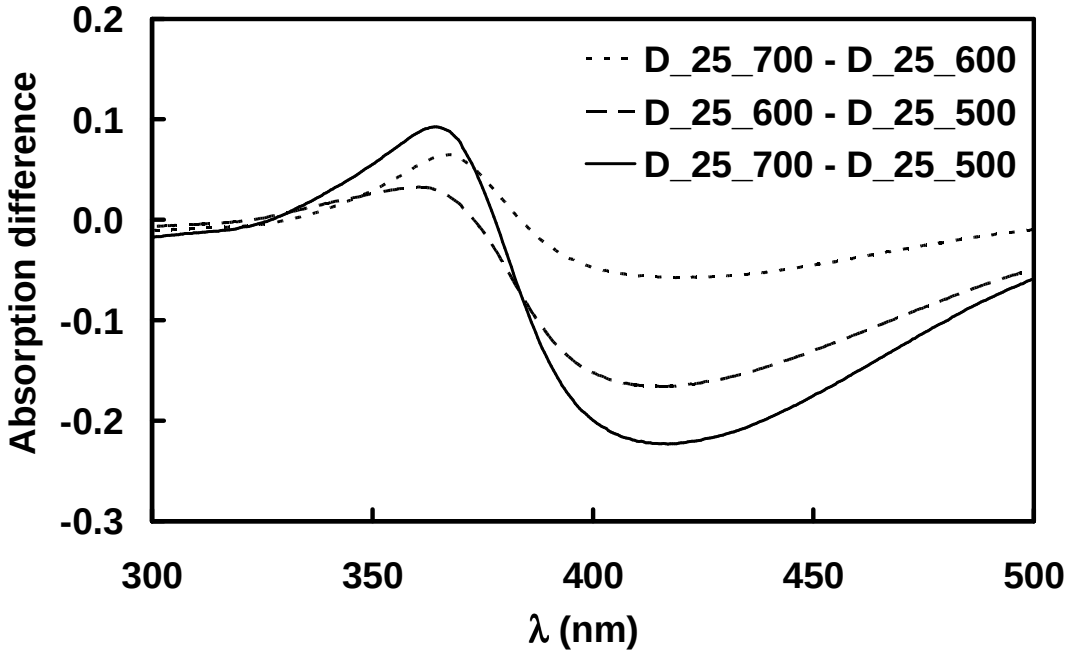

Figure 8.9 Difference absorption spectra calculated for the D_25 series: the absorption spectra of samples calcined at a lower temperature were subtracted from those of samples calcined at a higher temperature.

The so-obtained difference absorption spectra (Fig. 8.9) invariantly consisted of a positive part, labelled peak A, in the near-UV region and a negative part at longer wavelengths in the near-visible region, labelled as peak B.

For each difference spectrum, labelled as curve C in the example shown in Fig. 8.10, a deconvolution of peaks A and B was then performed. Based on the assumption that peak B appearing in the longer wavelengths side is symmetrically shaped, the profile of peak A was obtained after subtracting the so-obtained peak B from curve C. This

procedure was applied to each difference absorption spectrum for each of the D_5, D_12 and D_25 series.

Finally, by assuming that peak A and peak B are absent in the absorption spectrum of doped samples calcined at 500 and 700°C, respectively, within each series the contribution of peaks A and B to the absorption spectrum of each doped sample was finally calculated.

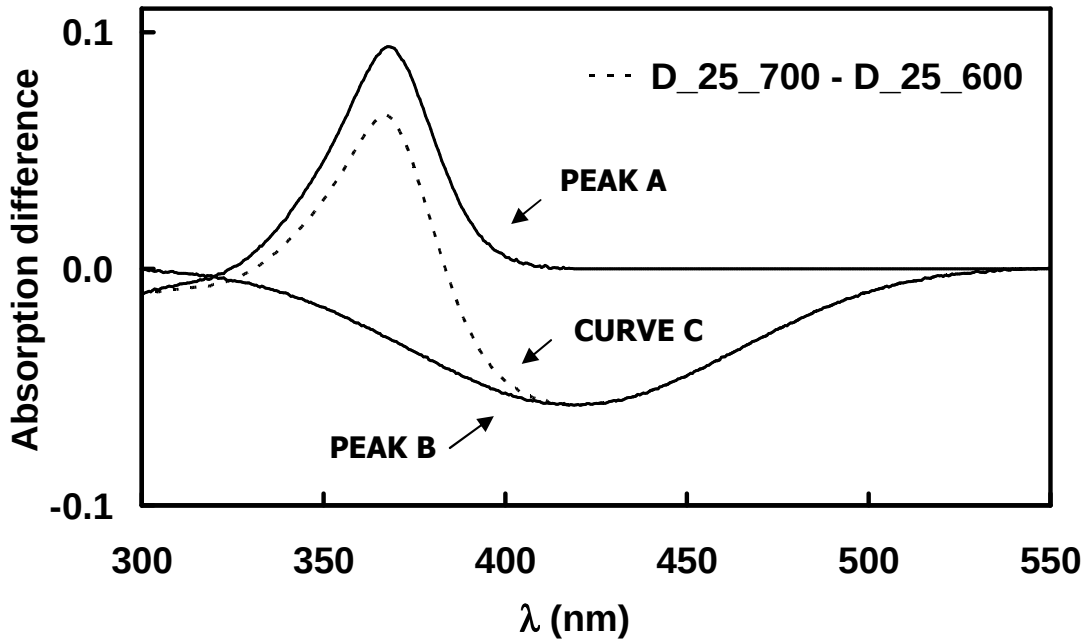

Figure 8.10 Deconvolution of peaks A and B from the difference of the absorption spectra of samples D_25_700 and D_25_600.

The so-obtained results, presented in Fig. 8.11, showed that for each series of doped samples the contribution of peak B (with a maximum around 420 nm) decreased with increasing the calcination temperature, while that of peak A (with a maximum around 365 nm) increased.

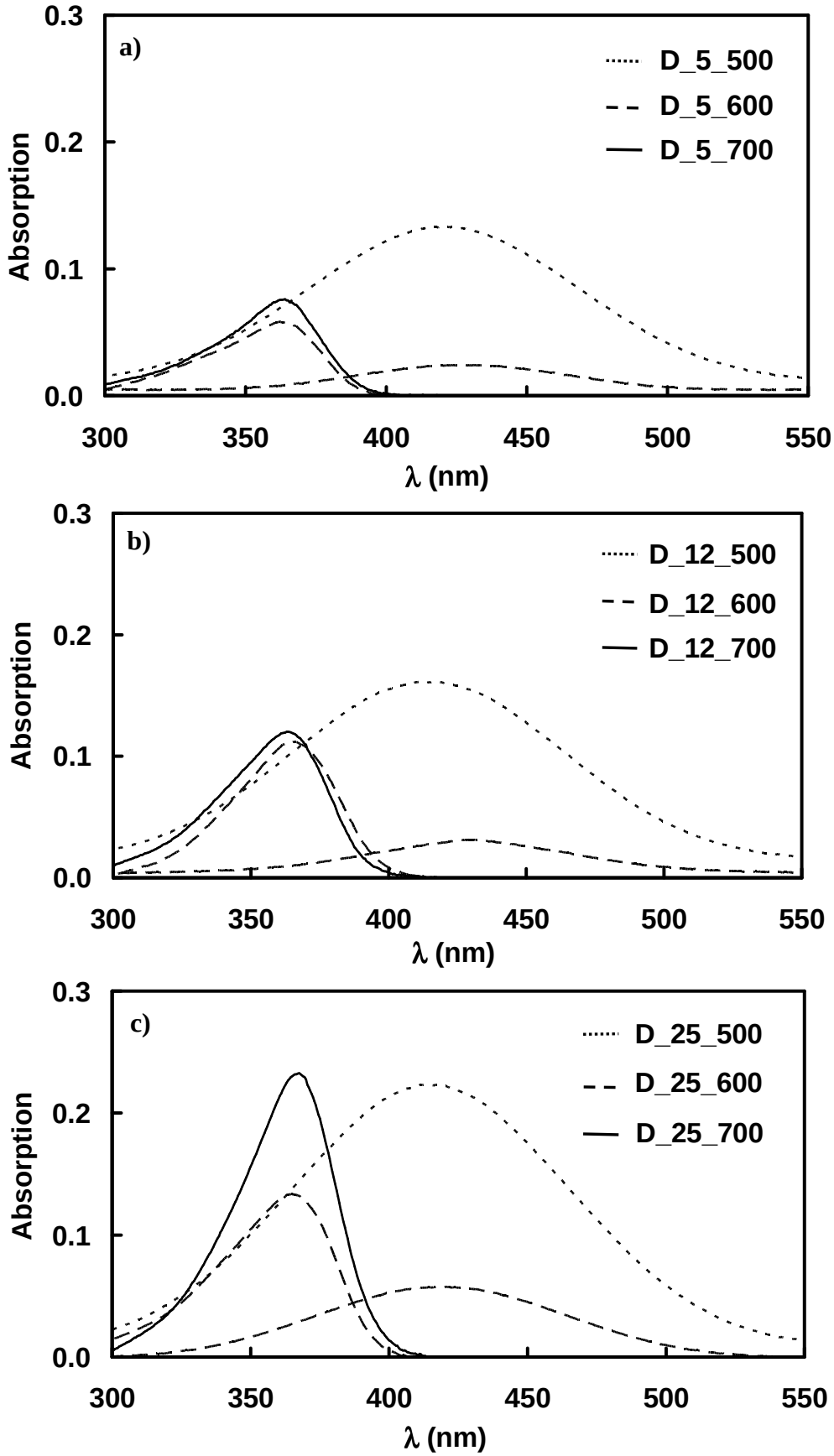

Figure 8.11 Contributions of peaks A and B to the absorption spectra of photocatalysts of the a) D_5, b) D_12 and c) D_25 series calcined at different temperatures.

On the other hand, by comparing the contributions of peaks A and B to the absorption spectra of samples calcined at the same temperature, but containing different nominal dopant amounts, the maximum intensity of both peaks A and B was found to increase with increasing the nominal dopant amount within the D_5, D_12 and D_25 series (see for example Fig. 8.12). The maximum position of both peaks A and B was not affected by either the calcination temperature or the dopant content.

In contrast, different results were obtained when the same kind of spectral subtraction analysis was applied to the absorption spectra of the D_3 series. In this case, sample D_3_700 calcined at 700°C did not consist of pure anatase, but contained *ca.* 7% of rutile phase (Table 8.1). The contribution of the so-obtained peak A for D_3_700 is also included in Fig. 8.12. This extra absorption peak is clearly red-shifted with respect to peaks A of the other D-TiO_2 series and should be ascribed to the typical band gap absorption shift of the rutile phase with respect to the anatase phase. This confirms that peak A with a maximum at about 365 nm obtained for D_5, D_12 and D_25 series is originated by an absorption contribution different from that of the rutile phase.

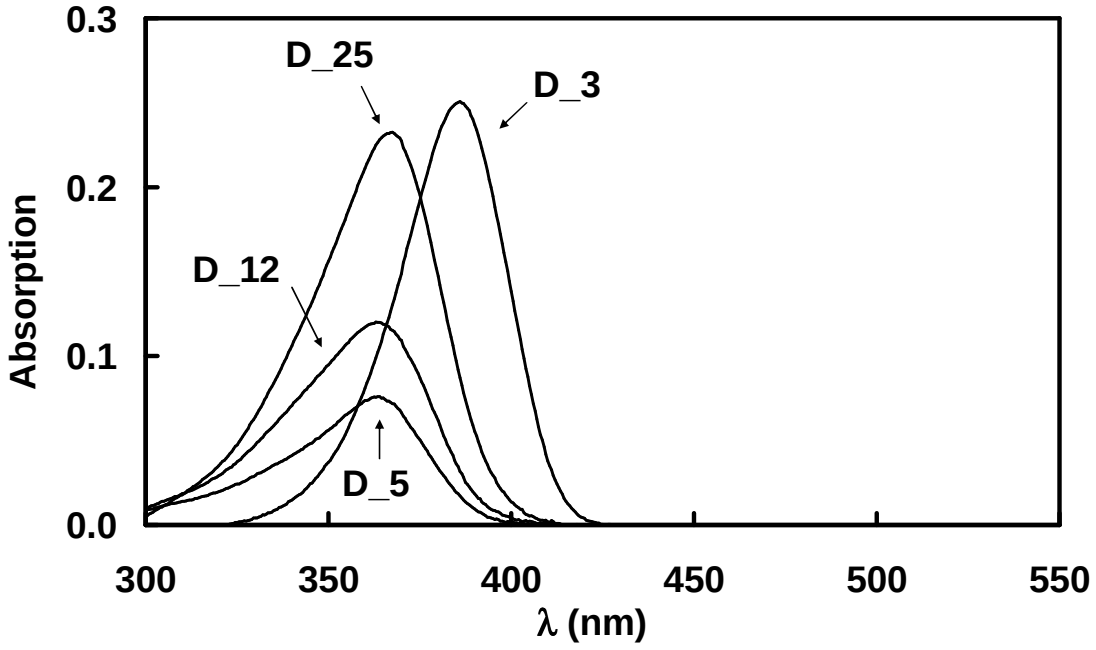

Figure 8.12 Contribution of peak A to the absorption spectra of doped samples calcined at 700°C. Only D_3_700 contains a small amount of rutile phase.

The intensity of the absorption peak B of doped samples was found to linearly increase with increasing the amount of surface fluorine detected by XPS analysis (Table 8.1), with a higher slope for samples calcined at 500°C than for those calcined at 600°C (not shown). An analogous correlation could not be established for the maximum intensity of peak A.

8.3.4.2 Action spectra deconvolution

Aiming at ascertaining whether absorption peaks A and B are active in acetic acid decomposition, a subtraction procedure similar to that performed for the absorption spectra was carried out also for the action spectra recorded in the 370–460 nm range (Fig. 8.7). Thus, for each series of doped materials the action spectra of samples calcined at 500°C were subtracted from those of samples calcined at 600 and 700°C. In this way the difference action spectra shown in Fig. 8.13 were obtained.

In the visible light region ($\lambda > 420$ nm) the action spectra of doped samples calcined at 600 and 700°C do not show any appreciable difference from that of the sample with the same nominal dopant amount calcined at 500°C. This indicates that absorption peak B, which is particularly evident in the absorption spectra of photocatalysts calcined at 500°C, does not produce any photoactivity in acetic acid decomposition to CO_2 under visible light.

On the other hand, doped samples calcined at 600 and 700°C showed an increase of photocatalytic activity in the UVA region with a maximum slightly red-shifted with respect to the maximum of absorption peak A. Such photoactivity enhancement was higher for photocatalysts calcined at the highest temperature (700°C), *i.e.* for photocatalysts exhibiting the most intense absorption peak A, clearly demonstrating that peak A is active in acetic acid decomposition. Of course, this type of analysis was not performed at $\lambda < 370$ nm, because the test reaction in this wavelengths region is mainly promoted by anatase band gap absorption.

By comparing the difference spectra shown in Fig.s 8.11 and 8.13, one may thus conclude that doping TiO_2 with NH_4F, followed by high temperature calcination, extends anatase band gap absorption on the long wavelengths side (peak A) and that this absorption in the UVA region is photoactive in acetic acid decomposition, whereas absorption peak B, appearing at longer wavelengths, is inactive in this reaction.

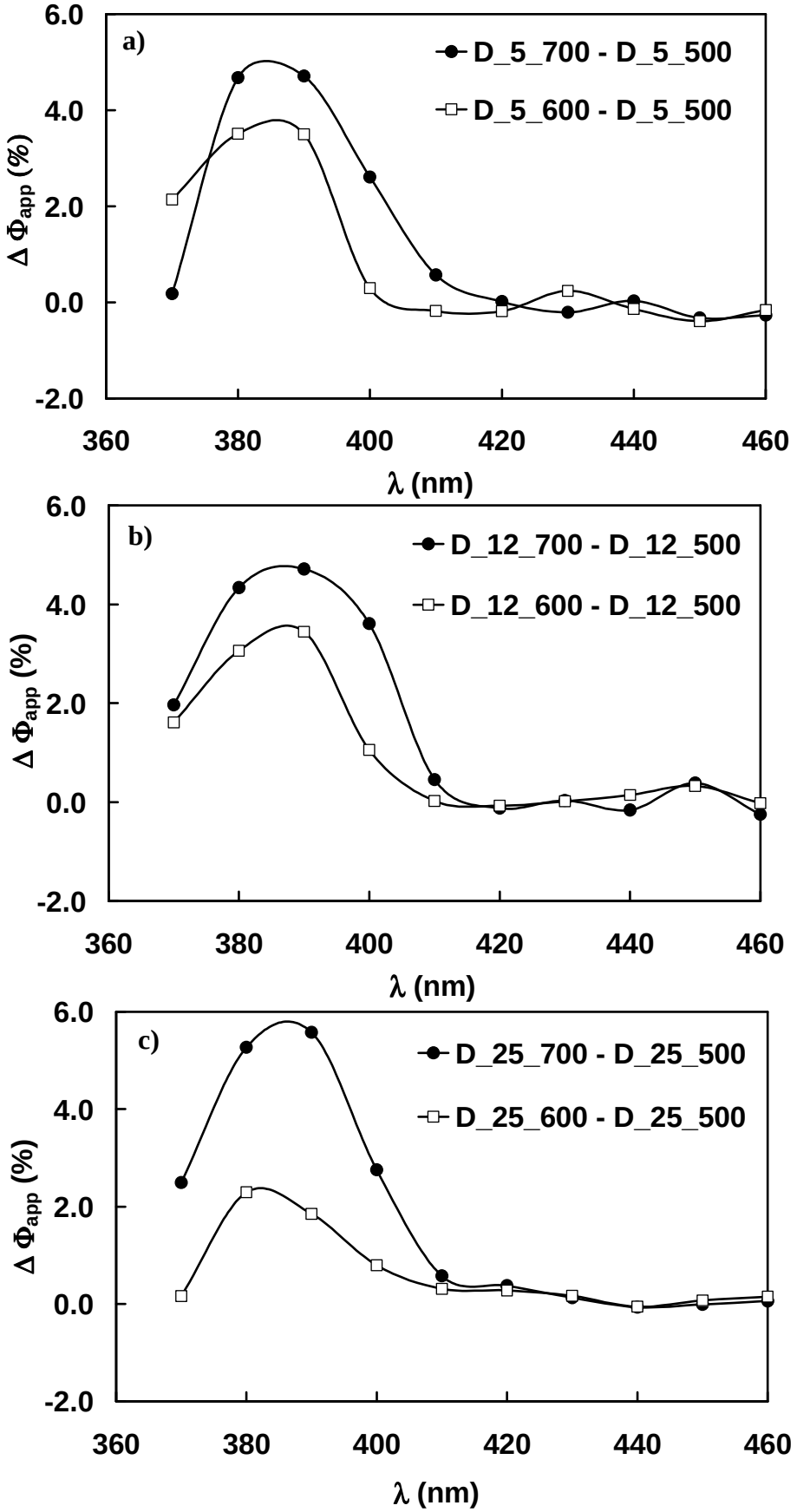

Figure 8.13 Difference action spectra of the a) D_5, b) D_12 and c) D_25 photocatalysts series. The action spectrum of each sample calcined at 500°C was subtracted from those of samples calcined at a higher temperature.

8.3.5 XPS analysis before and after etching

Aiming at correlating absorption peaks A and B to the chemical composition of our doped TiO_2 photocatalysts, a detailed XPS analysis of D_12_500 and D_12_700 was performed before and after etching with Ar ions. High-resolution XPS spectra of D_12_500 in the F 1s and N 1s binding regions are shown in Fig. 8.14 a and b, respectively. The XPS spectrum in the N 1s binding energy region is dominated by a rather broad signal with a maximum around 400 eV, typically assigned to different forms of interstitial nitrogen dopants.[1,48-50] After etching a new component appeared, peaking at 397 eV, usually associated to substitutional nitrogen located on an oxygen lattice site.[3,49,51] On the other hand, the F 1s XPS signal consisted of only one band peaking at *ca.* 684 eV, attributed to F^- ions adsorbed on the photocatalyst surface,[29,34,36] which decreased after etching. No signal located around 688 eV, originating from fluorine substituting oxygen in the TiO_2 crystal lattice,[29.33] appeared either before or after etching (Fig. 8.14a).

Similar results were obtained for the highly photoactive D_12_700 sample calcined at 700°C (Fig. 8.14 c and d). In this case, the F 1s signal at 684 eV was lower than that in the high-resolution XPS spectrum of the D_12_500 sample (Fig. 8.14c *vs.* Fig. 14a), indicating a smaller amount of adsorbed fluorine. This signal almost completely disappeared after etching (Fig. 8.14c), *i.e.* the fluorine content in the bulk was below the detection limit of XPS analysis. Concerning the high-resolution N 1s XPS signal, the component peaking at 397 eV, increasing after etching and attributed to substitutional nitrogen, in Fig. 8.14d, is even more evident than that in Fig. 8.14b, confirming the presence of nitrogen in the photocatalyst bulk, also after calcination at 700°C.

These results exclude the possibility of detecting fluorine in bulk D-TiO_2, especially in samples calcined at high temperature, whereas they confirm the persistence of nitrogen species in the D-TiO_2 structure of photocatalysts calcined at 700°C, even though this does not correspond to any absorption under visible light irradiation. The present results are in line with previous findings obtained by EPR analysis (see Section 7.3.3),[39] revealing the persistence of nitrogen species within the TiO_2 structure even after calcination at 700°C. In fact, the EPR spectra of both D_5 and D_12 series were dominated by the 4-lines signal attributed to the photocatalytically inactive

paramagnetic nitric oxide (NO) radical encapsulated in microvoids, which almost completely masked the possible presence of Ti^{3+} centres.

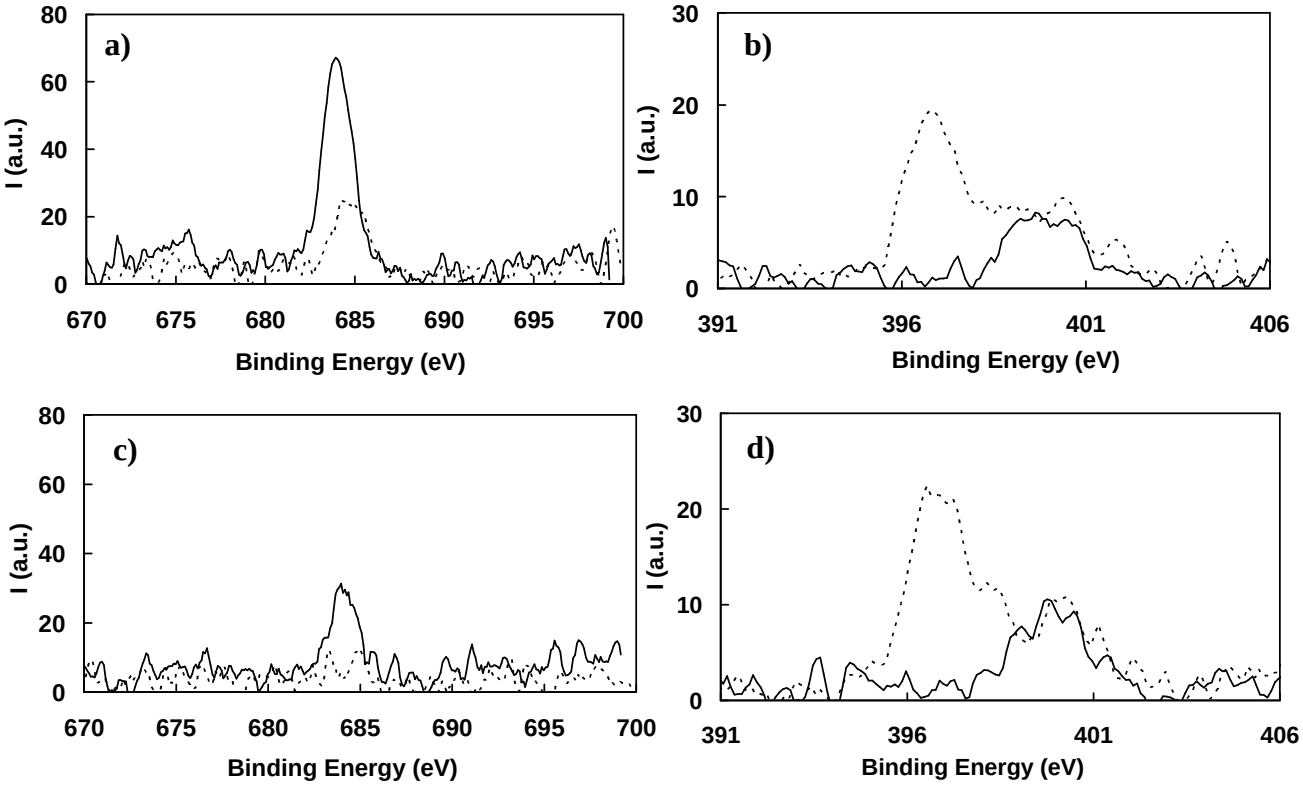

Figure 8.14 High-resolution XPS spectra of the F 1s (a and c) and the N 1s (b and d) binding energy regions of D_12_500 (a and b) and D_12_700 (c and d) before (solid line) and after etching with Ar ions (dotted line).

8.3.6 Origin of absorption peaks A and B

The investigated D-TiO_2 photocatalysts contained both fluorine and nitrogen, according to XPS analysis, and although the nominal N/F molar ratio was fixed to 1 in all samples, their nitrogen content was probably larger than their fluorine content, as already found in similar systems.[52]

According to DFT calculations,[48] N-impurities give rise to localized states above the valence band and greatly favour the formation of oxygen vacancies. Paramagnetic N-containing species, though in concentration three orders of magnitude lower than bulk and surface doping levels,[50] were indicated to be responsible for visible light absorption and for the photoinduced electron transfer to adsorbed electron scavengers, such as molecular oxygen.[48] On the other hand, the main effect of fluorine doping was the retarded anatase into rutile transformation,[29,35] yielding a highly crystalline pure

anatase[39] after calcination at 700°C. Substitutional F dopants induce the formation of Ti^{3+} species in the bulk of polycrystalline anatase,[29] which introduce localized states in the band gap below the conduction band,[36] but no visible light absorption.[33-36] Finally, N–F co-doping produces a charge compensation between *p*-type (N) and *n*-type (F) dopants, that reduces the energy cost to dope the material.[52] Consequently, the number of oxygen defects present in N–F co-doped TiO_2 is expected to be smaller than in N-doped TiO_2.

A strong similarity between the absorption features of D_X_500 samples (Fig. 8.8) and N-doped TiO_2 can be noticed in the visible region. The 'long tail' absorption at $\lambda >$ 400 nm of pale yellow N-doped samples is commonly attributed to nitrogen species of different dopant sources.[1,48,53] The intensity of this visible light absorption increases with increasing the dopant amount and decreases with increasing the calcination temperature, with a trend identical to that observed for N-doped TiO_2.[49,54,55]

Therefore peak B, being most evident in the absorption spectra of doped samples calcined at 500°C and decreasing in intensity with increasing the calcination temperature (see Figs. 8.8 and 8.11), can safely be attributed to nitrogen doping.[33] However, no photoactivity in acetic acid decomposition corresponds to this absorption peak.[56] The holes generated by visible photons absorption in intra-band gap states of N-doped TiO_2 were shown to be ineffective in oxidizing several substrates,[57] formic acid[10] among them, possibly due to their insufficient oxidizing power and/or low mobility. Alternatively, peak B might also be originated by surface states, which, however, would at the same time act as effective charge recombination centres, with the consequent absence of reactivity, a hypothesis which might hardly be proved.

The existence of peak A was evidenced for the first time by the spectral subtraction analysis performed in the present study. Such absorption feature is active in acetic acid decomposition (see Figs. 8.11 and 8.13). However, any attempt to correlate its intensity with the amount of Ti^{3+} species detectable by EPR analysis and with the possibly formed oxygen vacancies failed because the EPR spectra of our NH_4F-doped photocatalysts were dominated by the signal of photocatalytically inactive NO radicals.[39] However, the intensity of peak A, and the consequent activity in acetic acid decomposition, increased with increasing the photocatalyst calcination temperature. Thus, this absorption feature might be attributed to extrinsic absorption originating from surface oxygen vacancies or surface defects,[34,35,58,59] the formation of which is

expected to be favoured by F-doping at high calcination temperature. Indeed, photoluminescence signals attributed to such features have been reported to increase with increasing the calcination temperature of F-doped TiO_2 materials,[34] though the amount of oxygen defects in N–F co-doped TiO_2 is expected to be smaller than that in N-TiO_2.[52] On the other hand, peak A appears as an extra absorption on the longer wavelengths side of the band gap absorption itself. Thus, it may be simply a consequence of the higher crystallinity of D-TiO_2 samples calcined at a high temperature, with respect to those calcined at 500°C, resulting in a higher absorption capability,[56] as originally proposed by Hattori *et al.* in the case of F-doped TiO_2.[60]

A definitive attribution of absorption peaks A and B, together with evidence of possible synergistic effects due to the co-presence of N and F dopants, might be obtained by comparing present results with those obtained with a series of F-doped TiO_2 photocatalysts containing no nitrogen. Such materials were thus synthesised and the results of their photocatalytic activity analysis are discussed in Chapter 9.

8.3.7 Mott-Schottky analysis

In order to investigate more in depth the origin of photoactive absorption peak A and to get information about the electrochemical properties of the materials, such as flat band potential and donor density values, a Mott-Schottky analysis was done by performing EIS (Electrochemical Impedance Spectroscopy) measurements, as described in Section 3.6. Before presenting the main results, some experimental details on the preparation of the thin TiO_2 films on conducting materials and on the conditions adopted in this kind of analysis will be briefly described. All EIS experiments were performed by the Electrochemical group of Prof. Patrizia Mussini in our Department at the Università degli Studi di Milano.

Semiconductor thin films on conductive indium-tin oxide (ITO) glass to be employed as electrodes were prepared following the manual dip-coating procedure described below. 150 mg of photocatalyst powder were suspended within 1.0 mL of ethanol and sonicated for 30 min. A specific glass area (1 cm × 1 cm) of ITO was then immersed for two seconds in the so-obtained suspension and left in air for two seconds. This procedure was constantly repeated ten times for each electrode. The as-prepared electrodes were then dried in oven at 70°C for one day.

The electrochemical setup consisted of three electrodes: the working electrode (TiO_2 thin film), a platinum wire used as counter electrode and a saturated calomel electrode as reference. The experiment was performed in aqueous 0.1 M KCl solution at pH 7 in the absence of light. The potential was systematically varied between -1.00 and +1.00 V with the current frequency range being modulated between 10 Hz to 1000 Hz by using an AUTOLAB PGSTAT20 – Potentiostat Galvanostatic instrument with the specific NOVA software for impedance analysis.

The range of scanning potentials was chosen after applying cyclic voltammetry analysis to the working electrode. In particular, as the flat band potential and the donor density of the analysed semiconductors must be determined when the electrode surface is not modified by the application of any potential, *i.e.* when no redox processes occur, impedance analysis were performed in the so-called capacitive current range, with the electrode working as a capacitor, causing a charge carriers redistribution between the electrolyte and the electrode.

Examples of Mott-Schottky plots (see Section 3.6.1) obtained at 1000 Hz with D_5 doped series samples are shown in Fig. 8.15.

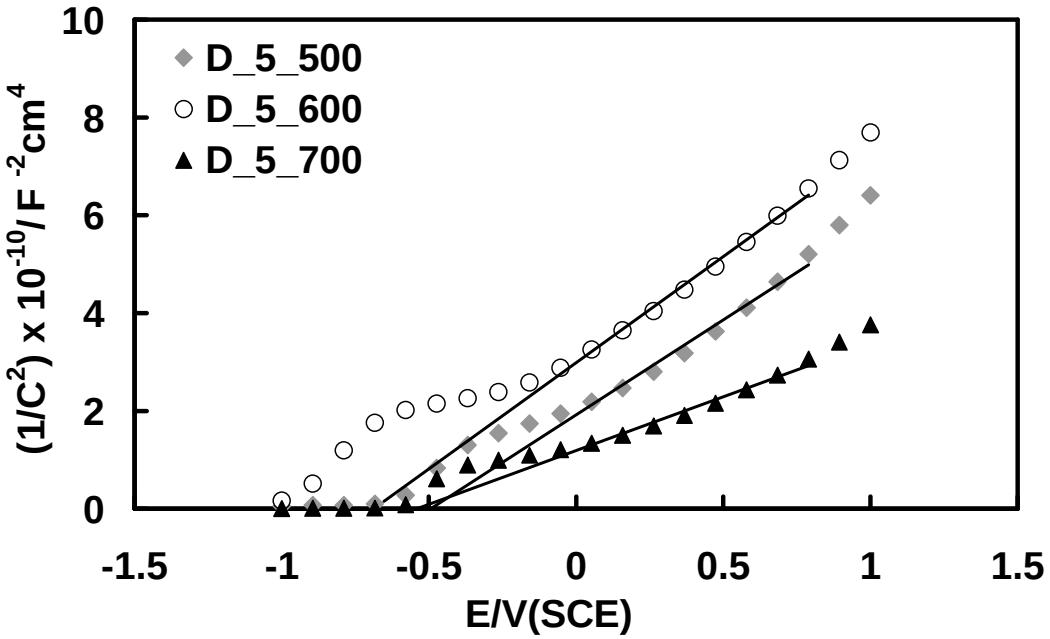

Figure 8.15 Mott-Schottky plots obtained at 1000 Hz for D_5 doped samples.

The calculated values of donor density (N_d) and flat band potential (E_{fb}) of the investigated photocatalysts in film form are presented in Table 8.2.

As TiO_2 is an n-type semiconductor, the flat band potential value can be considered at approximately the same energy level as the conduction band; thus, from E_{fb} values the photocatalytic reducing power of semiconductor materials can be estimated.

As shown in Table 8.2, all flat band potentials obtained from Mott-Schottky plots are negative, as expected, without any significant and systematic variation among them. This may result from two main factors: i) as already mentioned, the thin film electrodes were prepared by dip-coating; this deposition procedure was not so well-optimized and the homogeinity of the films, necessary to perform good measurements, depended on the dispersion extent of the photocatalyst in ethanol within the suspension; ii) according to the definition of flat band potential, only the phenomena occurring in the space charge region are considered, without taking into account the Helmoltz plane and the diffusive layer, where potential abatement also occurs; this approximation results in low precision potential values.[61-63]

The attention was thus mainly focused on a possible correlation between the photocatalytic/absorption properties of doped materials and the corresponding donor density parameter (N_d), determined from the slope of Mott-Schottky plots (see Table 8.2).

Table 8.2 Flat band potential (E_{fb}) and charge carrier concentration (N_d) values of home-made photocatalysts obtained by using the Mott-Schottky analysis.

Sample	E_{fb} (V)	$N_d/10^{20}$ cm^{-3}
D_0_500	-0.381	1.04
D_0_600	-0.353	0.93
D_0_700	-0.430	0.58
D_5_500	-0.310	0.26
D_5_600	-0.535	0.27
D_5_700	-0.283	0.48
D_12_500	-0.184	0.49
D_12_600	-0.363	0.42
D_12_700	-0.459	0.64
D_25_500	-0.335	0.47
D_25_600	-0.366	0.61
D_25_700	-0.334	0.99

Bahnemann *et al.* found that TiO_2 films which exhibit a more negative flatband potential E_{fb} have higher N_d values and also higher photon efficiency values in the reduction of methylviologen under UV(A) irradiation. Hence, a direct correlation between E_{fb}, N_d, and the photocatalytic reduction capability could be postulated. However, a similar correlation between the photonic efficiency of methylene blue oxidation and E_{fb} and N_d properties was not found.[64]

In our case, the donor density values (N_d) obtained for all series of NH_4F-doped TiO_2 photocatalysts can be compared in Fig. 8.16.

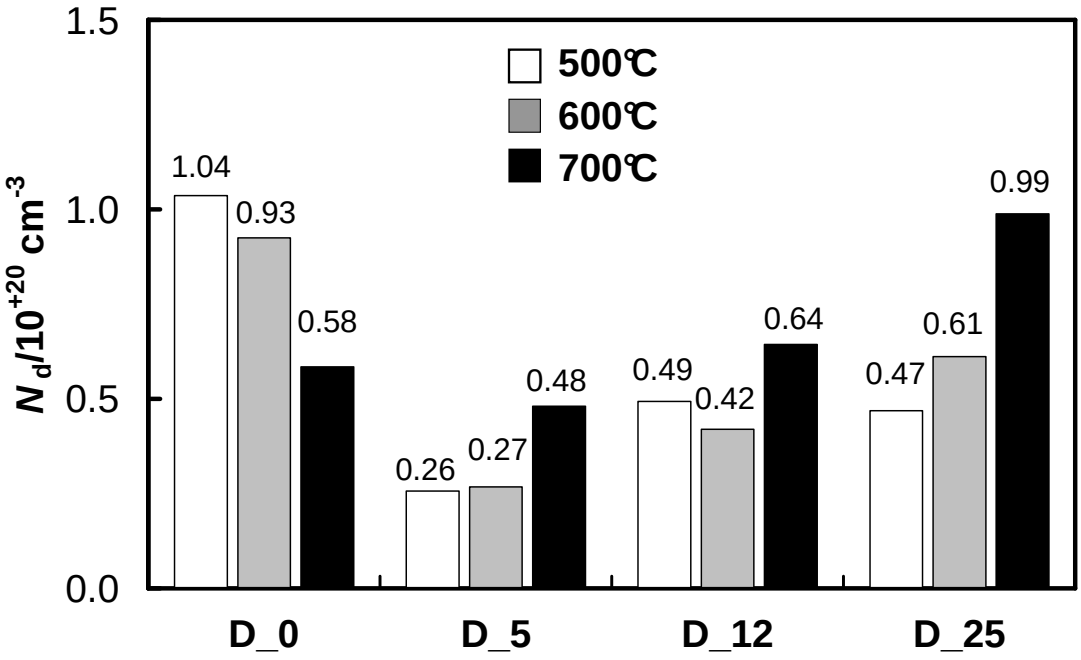

Figure 8.16 Donor density values obtained for doped TiO_2 photocatalysts containing different dopant amounts and calcined at different temperatures.

First of all, for each series of doped materials, containing the same nominal dopant amount but calcined at different temperatures, the trend of N_d values appears in good agreement with that of the corresponding activity in the photocatalytic oxidation of three different organic substrates (acetic acid, formic acid and acetaldehyde). The N_d value was invariantly higher in samples calcined at higher temperature in each series of photocatalysts containing the same nominal dopant amount. In contrast, for the undoped materials (D_0 series), the N_d value decreased with increasing the calcination temperature. In this regard the presence of a dopant, mainly, but not exclusively, fluorine, seems to favour and stabilize the formation of point defects at high calcination

temperature, which in the case of titanium dioxide films can correspond to oxygen-ion vacancies to be related to the donor density parameter (N_d).[65-69]

Therefore by considering the general trend of N_d parameter and photocatalytic activity for each series of doped materials, the formation of oxygen vacancies (and or surface defects) seems to produce beneficial effects on the overall photoefficiency of the materials calcined at high temperature (700°C), which are also expected to be characterised by a higher crystallinity degree.

At the same time, samples calcined at fixed temperature and containing an increasing nominal dopant amount were characterised by progressively higher N_d values, whereas in this case their photocatalytic activity decreased with increasing the dopant content (Figs. 7.5, 8.1 and 8.2). It's worth noting that for NH_4F-doped samples calcined at 600 and 700°C a good correlation can be found between the maximum intensity of photoactive absorption peak A (located at 365 nm) and the corresponding N_d value (Fig 8.17). Doped samples calcined at 500°C are not taken into account in this correlation because, according to the model described in Section 8.3.4 peak A does not contribute to their absorption spectra.

In order to give a possible explanation of these results, it's worth underlining that N_d values have been determined in the absence of irradiation, *i.e.* they give information on the structure of the material under dark conditions. Band gap excitation by light absorption produces electron-hole couples in the semiconductor. Point defects, the amount of which might be thought to increase with increasing the N_d value, may contribute in light absorption (peak A) and activation of the photocatalyst. However, an optimum photocatalytic activity results from the balance of two opposite effects, *i.e.* the possible increased amount of active species produced on the photocatalyst surface upon increased light absorption, which might contribute in increasing interface electron transfer reactions, and the detrimental effect of point defects acting as recombination centres of photoproduced charge carriers, which increases with increasing their amount, *i.e.* with increasing the dopant content. This optimum balance is obtained for doped materials containing *ca*. 5 mol.% of NH_4F, exhibiting the highest photocatalytic activity in the three photocatalytic oxidation reactions (Figs. 7.5, 8.1 and 8.2).

The presence of an optimum content of point defects (and of the N_d parameter) in order to attain the best photocatalytic efficiency was also pointed out by Baram *et al*. In particular their study, based on open circuit potential decay measurements, evidenced

that in TiO_2 films characterized by high charge carrier concentration, the charge transfer rate to the solution can be slower than expected.[70]

On the basis of the results reported in this paragraph, one can outline that impedance measurements can indirectly provide information on the defective structure of doped semiconductors but cannot be used as a unique prediction tool of their photonic efficiency especially in photocatalytic oxidation reactions.

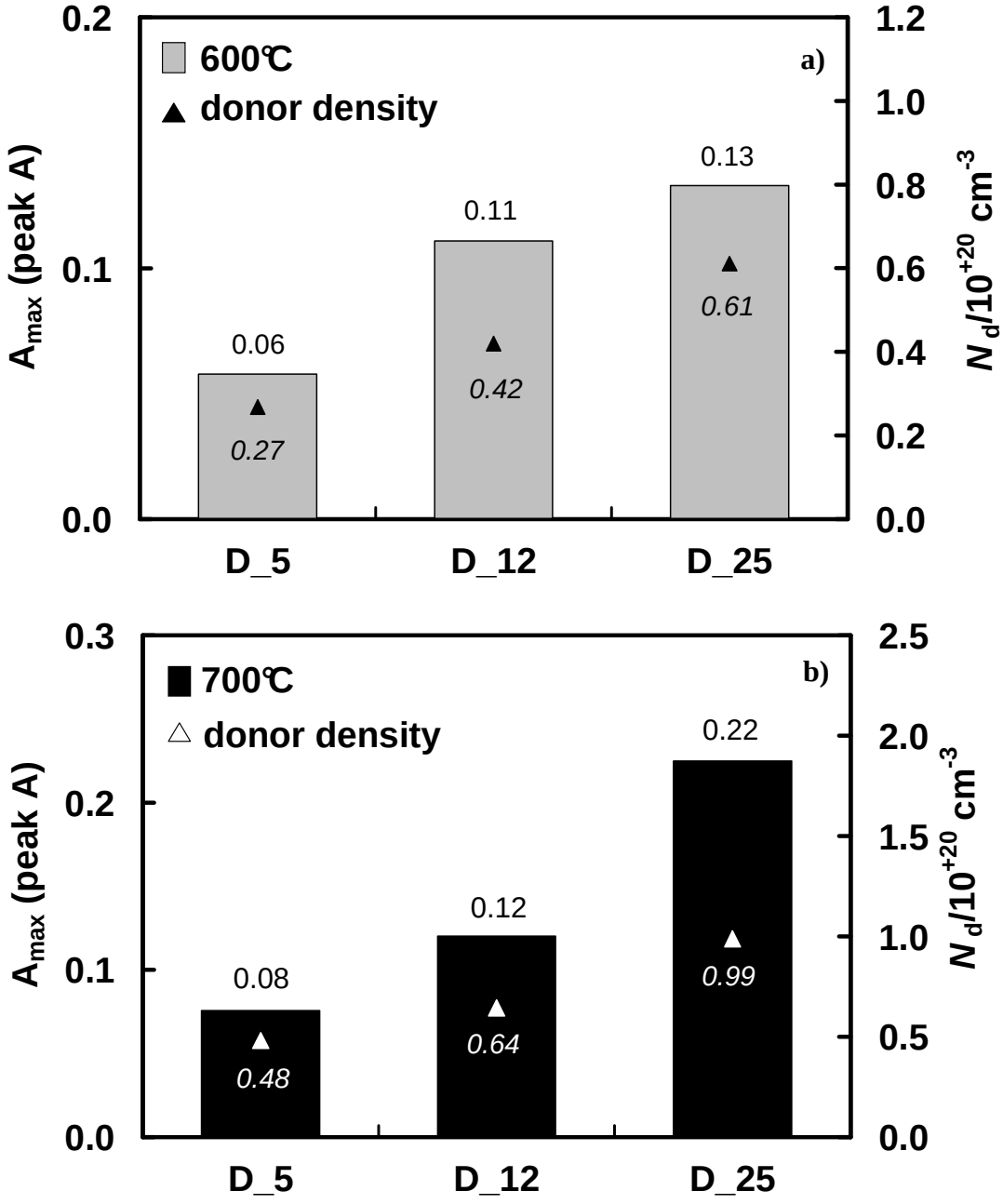

Figure 8.17 Comparison between the maximum absorption intensity of peak A (measured at 365 nm) and the corresponding value of N_d for doped samples calcined at a) 600°C and b) 700°C.

8.4 References

1. A. Fujishima, X. Zhang and D. A. Tryk, Surf. Sci. Rep., **2008**, 63, 515.
2. X. Chen and S. S. Mao, Chem. Rev., **2007**, 107, 2891.
3. R. Asahi, T. Morikawa, T. Ohwaki, K. Aoki and Y. Taga, Science, **2001**, 293, 269.
4. S. U. M. Khan, M. Al-Shahry and W. B. Ingler, Jr., Science, **2002**, 297, 2243.
5. H. Irie, Y. Watanabe and K. Hashimoto, J. Phys. Chem. B, **2003**, 107, 5483.
6. S. Sakthivel, M. Janczarek and H. Kisch, J. Phys. Chem. B, **2004**, 108, 19384.
7. J. L. Gole, J. D. Stout, C. Burda, Y. Lou and X. Chen, J. Phys. Chem. B, **2004**, 108, 1230.
8. X. Chen and C. Burda, J. Phys. Chem. B, **2004**, 108, 15446.
9. G. R. Torres, T. Lindgren, J. Lu, C.-G. Granqvist and S.-E. Lindquist, J. Phys. Chem. B, **2004**, 108, 5995.
10. M. Mrowetz, W. Balcerski, A. J. Colussi and M. R. Hoffmann, J. Phys. Chem. B, **2004**, 108, 17269.
11. C. Di Valentin, G. Pacchioni, A. Selloni, S. Livraghi and E. Giamello, J. Phys. Chem. B, **2005**, 109, 11414.
12. K. Nishijima, B. Ohtani, X. Yan, T. Kamai, T. Chiyoya, T. Tsubota, N. Murakami and T. Ohno, Chem. Phys., **2007**, 339, 64.
13. S. Sakthivel and H. Kisch, Angew. Chem., Int. Ed., **2003**, 42, 4908.
14. T. Tachikawa, S. Tojo, K. Kawai, M. Endo, M. Fujitsuka, T. Ohno, K. Nishijima, Z. Miyamoto and T. Majima, J. Phys. Chem. B, **2004**, 108, 19299.
15. B. Neumann, P. Bogdanoff, H. Tributsch, S. Sakthivel and H. Kisch, J. Phys. Chem. B, **2005**, 109, 16579.
16. J. H. Park, S. Kim and A. J. Bard, Nano Lett., **2006**, 6, 24.
17. W. Zhao, W. Ma, C. Chen, J. Zhao and Z. Shuai, J. Am. Chem. Soc., **2004**, 126, 4782.
18. H. Geng, S. Yin, X. Yang, Z. Shuai and B. Liu, J. Phys.: Condens. Matter, **2006**, 18, 87.
19. D. Chen, D. Yang, Q. Wang and Q, Z. Jiang, Ind. Eng. Chem. Res., **2006**, 45, 4110.
20. T. Umebayashi, T. Yamaki, H. Itoh and K. Asai, Appl. Phys. Lett., **2002**, 81, 454.
21. T. Umebayashi, T. Yamaki, S. Yamamoto, A. Miyashita, S. Tanaka, T. Sumita and K. Asai, J. Appl. Phys., **2003**, 93, 5156.

22. T. Ohno, M. Akiyoshi, T. Umebayashi, K. Asai, T. Mitsui and M. Matsumura, Appl. Catal., A, **2004**, 265, 115.
23. J. C. Yu, W. Ho, J. Yu, J. H. Yip, P. K. Wong and J. Zhao, Environ. Sci. Technol., **2005**, 39, 1175.
24. P. Periyat, S. C. Pillai, D. E. McCormack, J. Colreavy and S. J. Hinder, J. Phys. Chem. C, **2008**, 112, 7644.
25. J. C. Yu, L. Zhang, Z. Zheng and J. Zhao, Chem. Mater., **2003**, 15, 2280.
26. L. Lin, W. Lin, Y. Zhu, B. Zhao and Y. Xie, Chem. Lett., **2005**, 34, 284.
27. X. Hong, Z. Wang, W. Cai, F. Lu, J. Zhang, Y. Yang, N. Ma and Y. Liu, Chem. Mater., **2005**, 17, 1548.
28. G. Liu, Z. Chen, C. Dong, Y. Zhao, F. Li, G. Q. Lu and H.-M. Cheng, J. Phys. Chem. B, **2006**, 110, 20823.
29. J. C. Yu, J. Yu, W. Ho, Z. Jiang and L. Zhang, Chem. Mater., **2002**, 14, 3808.
30. K. Nukumizu, J. Nunoshige, T. Takata, J. N. Kondo, M. Hara, H. Kobayashi and K. Domen, Chem. Lett., **2003**, 32, 196.
31. T. Yamaki, T. Umebayashi, T. Sumita, S. Yamamoto, M. Maekawa, A. Kawasuso and H. Itoh, Nucl. Instr. Meth. Phys. Res. B, **2003**, 206, 254.
32. D. Li, H. Haneda, S. Hishita and N. Ohashi, Chem. Mater., **2005**, 17, 2588; D. Li, H. K. Haneda, S. Hishita and N. Ohashi, Chem. Mater., **2005**, 17, 2596.
33. D. Li, N. Ohashi, S. Hishita, T. Kolodiazhnyi and H. Haneda, J. Solid State Chem., **2005**, 178, 3293.
34. D. Li, H. Haneda, N. K. Labhsetwar, S. Hishita and N. Ohashi, Chem. Phys. Lett., **2005**, 401, 579.
35. W. Ho, J. C. Yu and S. Lee, Chem. Commun., **2006**, 10, 1115.
36. A. M. Czoska, S. Livraghi, M. Chiesa, E. Giamello, S. Agnoli, G. Granozzi, E. Finazzi, C. Di Valentin and G. Pacchioni, J. Phys. Chem. C, **2008**, 112, 8951.
37. G. Wu, J. Wang, D. F. Thomas and A. Chen, Langmuir, **2008**, 24, 3503.
38. S. Livraghi, K. Elghniji, A. M. Czoska, M. C. Paganini, E. Giamello and M. Ksibi, J. Photochem. Photobiol., A, **2009**, 205, 93.
39. M. V. Dozzi, S. Livraghi, E. Giamello and E. Selli, Photochem. Photobiol. Sci., **2011**, 10, 343.
40. B. Ohtani, Chem. Lett., **2008**, 37, 217.
41. R. Enríquez, A. G. Agrios and P. Pichat, Catal. Today, **2007**, 120, 196.

42. T. Hathway and W. S. Jenks, J. Photochem. Photobiol. A: Chem., **2008**, 200, 216.
43. E. Kowalska, O. O. Prieto-Mahaney, R. Abe and B. Ohtani, Phys. Chem. Chem. Phys., **2010**, 12, 2344.
44. C. Bernardini, M. V. Dozzi, G. Cappelletti and E. Selli, J. Photochem. Photobiol. A: Chem., **2010**, 211, 185.
45. M. Mrowetz and E. Selli, New J. Chem., **2006**, 30, 108.
46. O. O. Prieto-Mahaney, N. Murakami, R. Abe and B. Ohtani, Chem. Lett., **2009**, 38, 238.
47. T. Torimoto, N. Nakamura, S. Ikeda and B. Ohtani, Phys. Chem. Chem. Phys., **2002**, 4, 5910.
48. C. Di Valentin, E. Finazzi, G. Pacchioni, A. Selloni, S. Livraghi, M. C. Paganini and E. Giamello, Chem. Phys., **2007**, 339, 44.
49. X. Zhang, K. Udagawa, Z. Liu, S. Nishimoto, C. Xu, Y. Liu, H. Sakai, M. Abe, T. Murakami and A. Fujishima, J. Photochem. Photobiol. A: Chem., **2009**, 202, 39.
50. F. E. Oropeza, J. Harmer, R. G. Egdell and R. G. Palgrave, Phys. Chem. Chem. Phys., **2010**, 12, 960.
51. F. Amano, R. Abe and B. Ohtani, Trans. Mater. Res. Soc. Jpn., **2008**, 33, 173.
52. C. Di Valentin, E. Finazzi, G. Pacchioni, A. Selloni, S. Livraghi, A. M. Czoska, M. C. Paganini and E. Giamello, Chem. Mater., **2008**, 20, 3706.
53. S.-K. Joung, T. Amemiya, M. Murabayashi and K. Itoh, Appl. Catal. A: General, **2006**, 312, 20.
54. S. In, A. Orlov, F. García, M. Tikhov, D. S. Wright and R. M. Lambert, Chem. Commun., **2006**, 4236.
55. Q. Wang, C. Chen, W. Ma, H. Zhu and J. Zhao, Chem. Eur. J., **2009**, 15, 4765.
56. M. V. Dozzi, B. Ohtani, E. Selli, Phys. Chem. Chem. Phys., **2011**, 13, 18217.
57. R. Nakamura, T. Tanaka and Y. Nakato, J. Phys. Chem. B, **2004**, 108, 10617.
58. H. Yang and X. Zhang, J. Mater. Chem., **2009**, 19, 6907.
59. V.N. Kuznetsov and N. Serpone, J. Phys. Chem. B, **2006**, 110, 25203.
60. A. Hattori, K. Shimoda, H. Tada and S. Ito, Langmuir, **1999**, 15, 5422.
61. Y. V. Pleskov and Y. Y. Gurevich; Semiconductor photoelectrochemistry, Consultants Bureau, New York, **1986**.
62. R. De Gryse, W. P. Gomes, F. Cardon and J. Vennik, J. Electrochem. Soc., **1975**, 122, 5, 711.

63. K. Uosaki and H. Kita, J. Electrochem. Soc., **1983**, 130, 4, 895.

64. C. Baumanis and D. W. Bahnemann, J. Phys. Chem. C **2008**, 112, 19097.

65. S. Palmas, A. M. Polcaro, J. Rodriguez Ruiz, A. Da Pozzo, M. Mascia and A. Vacca, Int. J. Hydrogen Energ, **2010**, 35, 6561.

66. K. S. Raja, M. Misra and K. Paramguru, Electrochim Acta, **2005**, 62, 154.

67. D. S. Kong, S. H. Chen, C. Wang and W. Yang, Corros Sci, **2003**, 45, 747.

68. N. E. Hakiki, M. Da Curha Belo, A. M. P. Simoes and M. G. S. Ferreira, J. Electrochem. Soc., **1998**, 145, 3821.

69. S. M. Wilhelm, K. S. Yun, L. W Ballenger and N. Hackerman, J. Electrochem. Soc., **1979**, 126, 419.

70. N. Baram and Y. Ein-Eli, J. Phys. Chem. C, **2010**, 114, 9781.

Chapter 9

Action Spectra Analysis of TiO_2 Singly Doped or Co-Doped with Fluorine and Boron

9.1 Introduction

In the previous Chapter the photocatalytic behaviour of an extended series of NH_4F-doped TiO_2 photocatalysts has been thoroughly investigated in both liquid and gas phase reactions. In particular the attention has been focused on the possible activation of doped materials in the visible range by studying the photooxidation of acetic acid as a function of the irradiation wavelength, thus collecting so-called action spectra. By comparing the shapes of the action spectra with those of the absorption spectra of the investigated photocatalysts a model was proposed, based on spectral features deconvolution, which allows a clear distinction between inactive light absorption and effective photoactivity, possibly consequent to extrinsic absorption originating from surface oxygen vacancies or surface defects. XPS and EPR analysis of NH_4F-doped materials, even if calcined at 700°C, revealed the presence of residual nitrogen-containing species, that might be responsible for the spectral features and/or photoactivity of NH_4F-doped TiO_2, which should thus be more correctly envisaged as N and F co-doped TiO_2.

In order to better clarify the role of fluorine and/or nitrogen dopants in TiO_2, another series of doped photocatalysts was prepared according to the same synthetic procedure employing HF instead of NH_4F as dopant source, thus avoiding the co-presence of nitrogen impurities in the material. At the same time, aiming at elucidating the effects of F-doping and co-doping of TiO_2, an investigation was started on the effects of the co-presence of *p*-block elements boron and fluorine in titania. In the literature there is little information about the photoactivity of B-F co-doped TiO_2 systems; moreover, these materials have been mainly investigated in the photocatalytic degradation of organic dyes,[1,2] which are not appropriate target molecules for photocatalytic test reactions aiming at verifying the effective visible light activation of doped materials.[3]

All photocatalysts were prepared by the sol-gel method in the presence of different amounts of dopant source (HF for HF-doped TiO_2 and H_3BO_3 for B-doped TiO_2), followed by calcination at different temperatures (as already described in Chapter 8). The photoactivity of TiO_2 samples singly doped or also co-doped with fluorine and boron (BF-doped TiO_2) has been investigated in the photooxidation of transparent formic acid and acetic acid in aqueous suspensions.

Finally, in order to compare the photoactivity of these systems with that of samples prepared in the presence of NH_4F as dopant source (Chapter 8), the photooxidation of

the transparent acetic acid substrate was also systematically investigated as a function of irradiation wavelength for the three main new series of doped TiO_2 samples.

The prepared photocatalysts were characterized by BET, XRD, UV-vis absorption and TEM analysis, in order to enlighten the effects of dopant concentration and calcination temperature on the structural features of the doped materials, in relation to their photocatalytic activity.

9.2 Experimental Section

9.2.1 Doped-TiO_2 preparation and characterisation

All photocatalysts were prepared by the sol-gel method starting from an anhydrous ethanol solution containing a fixed concentration of titanium isopropoxide and different amounts of dopant source (HF for HF-doped TiO_2 and H_3BO_3 for B-doped TiO_2), in order to obtain dopant/Ti percent nominal molar ratios equal to 3, 5, 12 and 25, by following the general procedure already described in the Section 7.2.1.

The effect of calcination temperature (at 500, 600 and 700°C) was investigated also for these materials, which were also labelled as X_Y_Z, with X referring to the dopant element symbol, Y to the nominal dopant/Ti percent molar ratio and Z to the calcination temperature in °C. Moreover co-doped materials were prepared in the presence of the two dopant sources HF and H_3BO_3, so as to obtain dopant/Ti percent nominal molar ratios equal to 3, 5 and 12 (BF-doped TiO_2), with the HF/H_3BO_3 ratio always fixed at 1. Reference undoped materials, prepared by exactly the same synthetic route in the absence of dopant source, are referred to as the X_0_Z photocatalysts series. All reagents were purchased from Aldrich and employed as received.

The BET specific surface area was measured by N_2 adsorption / desorption at liquid nitrogen temperature in a Micromeritics Tristar II 3020 V1.03 apparatus, after out-gassing at 300°C for 1 h under N_2 stream. X-ray powder diffraction (XRPD) patterns were recorded on a Philips PW3020 powder diffractometer, by using the Cu Kα radiation (λ = 1.54056 Å). Quantitative phase analysis was made by the Rietveld refinement method,25 using the "Quanto" software.[4] Diffuse reflectance (DR) spectra of the photocatalyst powders were recorded on a Jasco V-670 spectrophotometer equipped with a PIN-757 integrating sphere, using barium sulphate as a reference, and then converted into absorption (A) spectra (A = 1 – R).

All photocatalytic FA degradation runs were performed as already detailed in Section 4.1 under atmospheric conditions in a magnetically stirred 60 mL cylindrical quartz reactor, inserted in a home made housing consisting in a black box mounted on optical bench. All irradiated aqueous suspensions contained 0.1 g L^{-1} of photocatalyst and were preliminarily sonicated for 30 min. Then the appropriate volume of formic acid (FA) solution was added, to obtain an initial concentration of FA equal to 1.0×10^{-3} mol L^{-1}. Acetic acid decomposition under polychromatic irradiation was performed as detailed in Section 4.2.2, whereas the action spectra analysis of this reaction was performed as described in Section 4.2.3.

9.3 Results and Discussion

9.3.1 Photocatalysts structure

The main structural features, determined by XRD and BET analyses, of the investigated series of undoped and doped TiO_2 photocatalysts are collected in Tables 9.1 a-d.

Table 9.1 a-d: Phase composition and anatase crystallites dimensions, d_A of the investigated photocatalysts series, obtained from XRD analysis using the Scherrer equation, by assuming the absence of amorphous phase.

a) Undoped TiO_2

Sample	dopant/Ti molar ratio (%)	anatase (%)	brookite (%)	rutile (%)	d_A/nm	SSA/m^2 g^{-1}
HF_0_500	0	99	1	-	15	15
HF_0_600	0	90	-	10	32	9
HF_0_700	0	38	-	62	65	7

b) HF-doped TiO_2

Sample	dopant/Ti molar ratio (%)	anatase (%)	brookite (%)	rutile (%)	d_A/nm	SSA/m^2 g^{-1}
HF_3_500	3	100	-	-	23	44
HF_3_600	3	100	-	-	41	25
HF_3_700	3	100	-	-	56	20
HF_5_500	5	100	-	-	22	45
HF_5_600	5	100	-	-	40	28
HF_5_700	5	100	-	-	55	22
HF_12_500	12	100	-	-	20	34
HF_12_600	12	100	-	-	50	16
HF_12_700	12	100	-	-	57	18
HF_25_500	25	100	-	-	20	21
HF_25_600	25	100	-	-	49	11
HF_25_700	25	100	-	-	85	8

c) B-doped TiO_2

Sample	dopant/Ti molar ratio (%)	anatase (%)	brookite (%)	rutile (%)	d_A/nm	SSA/m^2 g^{-1}
B_5_500	5	97	3	-	10	103
B_5_600	5	100	-	-	16	45
B_5_700	5	64	-	36	43	9
B_12_500	12	96	4	-	8	132
B_12_600	12	100	-	-	13	52
B_12_700	12	97	-	3	40	9
B_25_500	25	78	13	-	6	133
B_25_600	25	100	-	-	19	25
B_25_700	25	100	-	-	61	8

d) BF-doped TiO_2

Sample	dopant/Ti molar ratio (%)	anatase (%)	brookite (%)	rutile (%)	d_A/nm	SSA/m^2 g^{-1}
BF_3_500	3	100	-	-	12	66
BF_3_600	3	100	-	-	19	46
BF_3_700	3	98	-	2	36	21
BF_5_500	5	100	-	-	12	58
BF_5_600	5	100	-	-	18	41
BF_5_700	5	95	-	5	29	21
BF_12_500	12	100	-	-	11	51
BF_12_600	12	100	-	-	17	37
BF_12_700	12	98	-	2	14	21

XRPD analysis showed that HF doping inhibits the anatase into rutile phase transition even when the starting HF concentration was really low (HF_3 series). In fact, all doped samples, even if calcined at 700°C, contained more than 99% of the anatase phase.

In the case of doping with H_3BO_3 different results were obtained. Firstly, a selective formation of brookite phase occurred for B-doped samples calcined at 500°C, especially with relatively high nominal dopant amounts (B_25_500). Secondly, full anatase material can be obtained after calcination at 700°C only by employing a relatively large nominal amount of H_3BO_3 (B_25 series).

In the case of the BF-doped systems, full anatase materials were generally obtained, but traces of rutile phase (about 2–5 %) appeared after calcination at 700°C. The dimensions of anatase crystallites, calculated according to the Scherrer equation, did not sensibly depend on the nominal amount of fluorine in the HF series, whereas B- and BF-doping appeared to favour the formation of slightly smaller anatase TiO_2 particles. The unusual trend of anatase crystallite dimensions decrease by increasing the nominal dopant amount, in particular in samples calcined at 700°C, was clearly obtained for BF co-doped photocatalysts.

XRPD analysis of singly boron- or boron and fluorine- doped systems did not show any extra signal possibly associated to B_2O_3 phase formation, thus suggesting the possible homogeneous inclusion of the dopant element into the TiO_2 structure. In the literature, the separation of boron from the TiO_2 crystal, generally followed by the formation of a layer of diboron trioxide phase on the surface of TiO_2 nanoparticles was related not only to the calcination temperature but also to the nominal dopant amount.[5] In particular, at high B concentration (generally higher than 20 mol.%), boron ions can be expelled from the TiO_2 structure during calcination, forming nanoclusters and subsequently a film of B_2O_3, which retards the crystal growth, stabilizing the anatase phase. Conversely at low B concentration (lower than 5 mol.%), the formation of oxygen vacancies, induced by the dopant,[6] might favour the anatase to rutile transformation.[5]

BET analysis showed a decrease in surface area of the TiO_2-based photocatalysts with increasing the calcination temperature for the same nominal dopant amount, consequent to particles sintering. SSA obtained for TiO_2 samples containing fluorine (HF and BF series) were not so different respect to those measured for NH_4F-doped materials, already reported in Section 8.3.1. At the same time H_3BO_3-doping seems to be the most beneficial for obtaining materials with larger surface area, especially if calcined at relatively low temperature (500°C). This is in agreement with previous results showing that the presence of boron in the bulk of TiO_2 material resulted in lower crystallite dimensions and, consequently, in a higher surface area of the system.[7]

By considering the great number of doped materials prepared in this thesis work, it's essential to compare the most significant absorption spectra of the differently doped series. Thus, the absorption spectra of the HF series should be compared with those of the NH_4F-doped samples (D-TiO_2), in order to ascertain the origin of the absorption peak B appearing in the near-visible region for these latter, which was demonstrated to be inactive in acetic acid decomposition (Chapter 8).

The differences between the absorption spectra of NH_4F-doped samples (D_5 and D_25 series) and the corresponding ones of the HF-doped series are reported in Fig. 9.1. By considering that all doped samples, even those calcined at 700°C, consist of pure anatase phase, any artifact in the difference spectra due to rutile phase absorption can be excluded, as already mentioned.

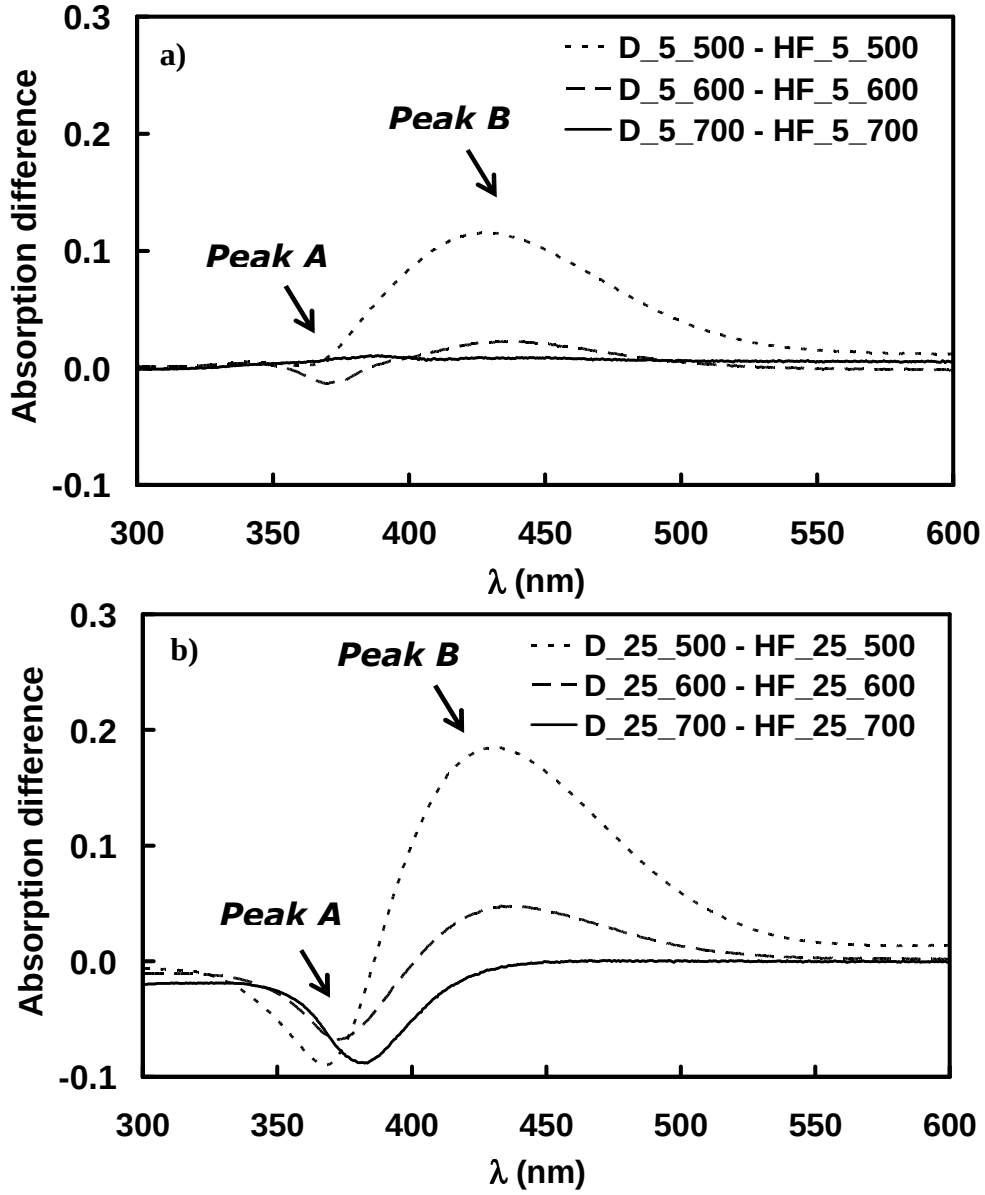

Figure 9.1 Difference of absorption spectra of NH_4F-doped (labelled as D) samples and the corresponding HF-doped samples (containing no nitrogen dopant).

The contribution of peak B (with a maximum around 420 nm) is evident for samples prepared starting from NH_4F as dopant source and calcined at 500°C. At the same time, HF-doped samples calcined at 700°C appear to absorb more in the near UV-region where peak A is located. Thus, the difference spectra reported in Fig. 9.1 seem to confirm the attribution of inactive peak B mainly to nitrogen doping and active peak A to structure effects related to the presence of the fluorine dopant.

The absorption spectra of the B_5 and BF_5 series do not show any significant extra absorption contribution in the visible region similar to those observed for NH_4F-doped TiO_2 calcined at 500°C (Fig. 8.8). For both of these doped series, samples calcined at

700°C exhibit a slightly red-shifted absorption edge due to the presence of the rutile phase, which is more marked in case of B_5_700 (Fig. 9.2a), in agreement with XRPD analysis (see Table 9.1). The addition of fluorine, even if co-present with another *p*-block element such as nitrogen or boron, seems thus to play an essential role in inhibiting the anatase into rutile phase transition.

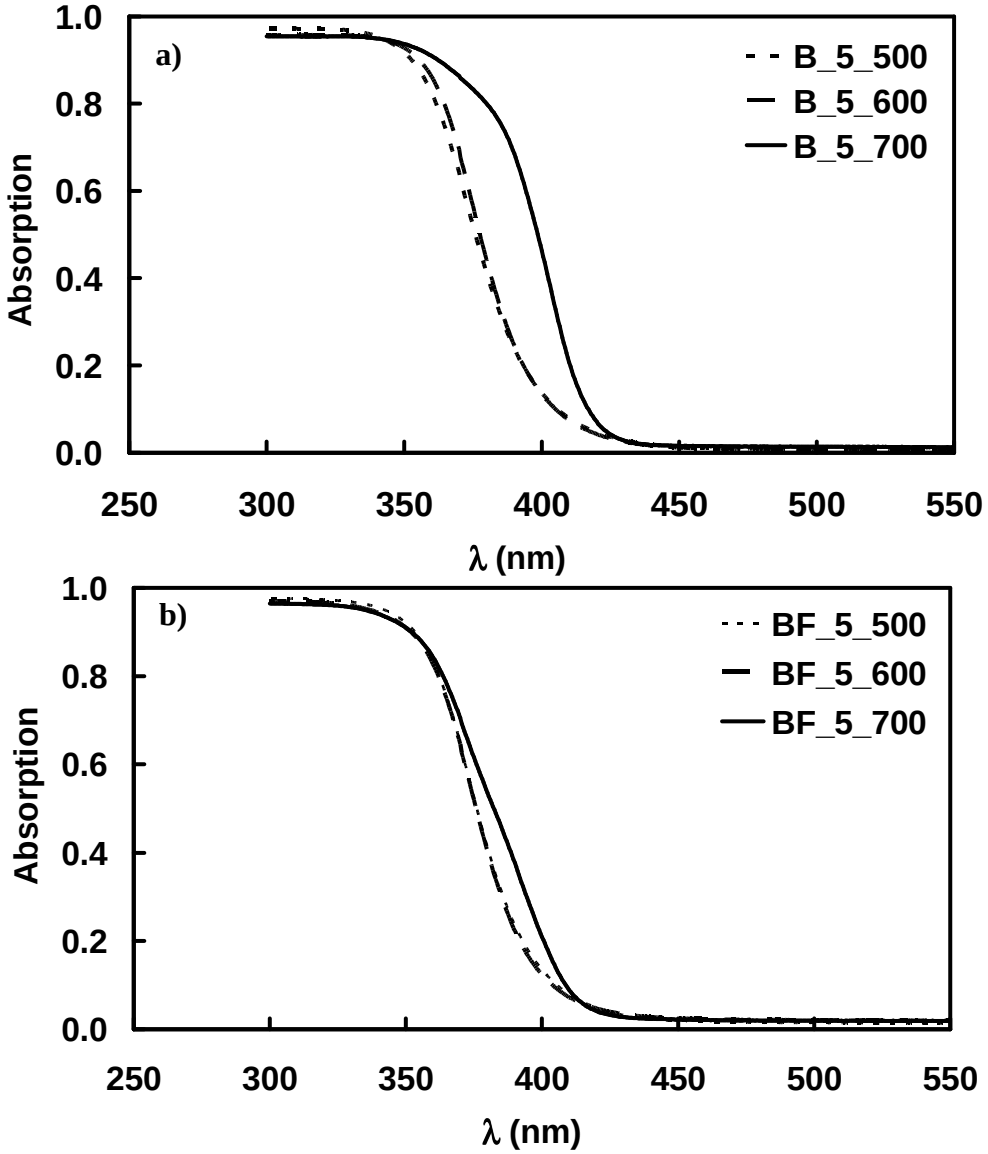

Figure 9.2 Absorption spectra of a) B_5 and b) BF_5 doped TiO_2 calcined at different temperatures.

9.3.2 Photocatalytic tests

9.3.2.1 Formic and acetic acid photocatalytic oxidation under polychromatic irradiation

The photocatalytic activity of these new series of doped TiO_2 samples in the oxidative decomposition of formic and acetic acid in aqueous suspension can be compared in Fig.

9.3 and 9.4, respectively, in terms of zero order rate constants.

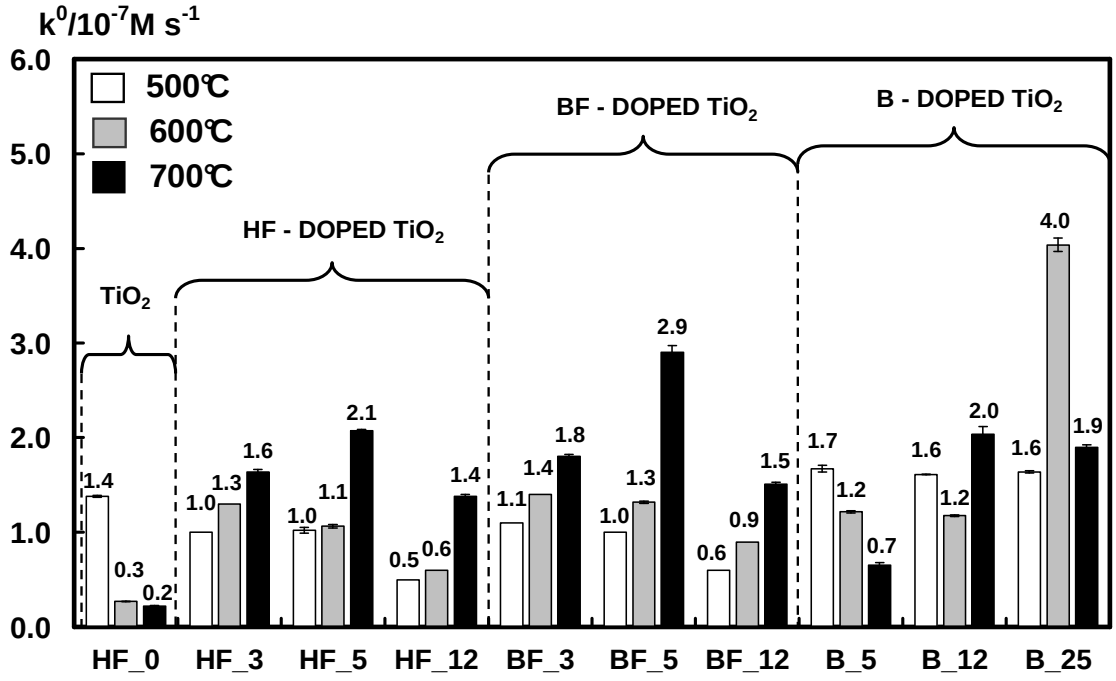

Figure 9.3 Zero-order rate constants of formic acid photo-mineralisation on photocatalysts containing different amount/type of dopants and calcined at different temperatures.

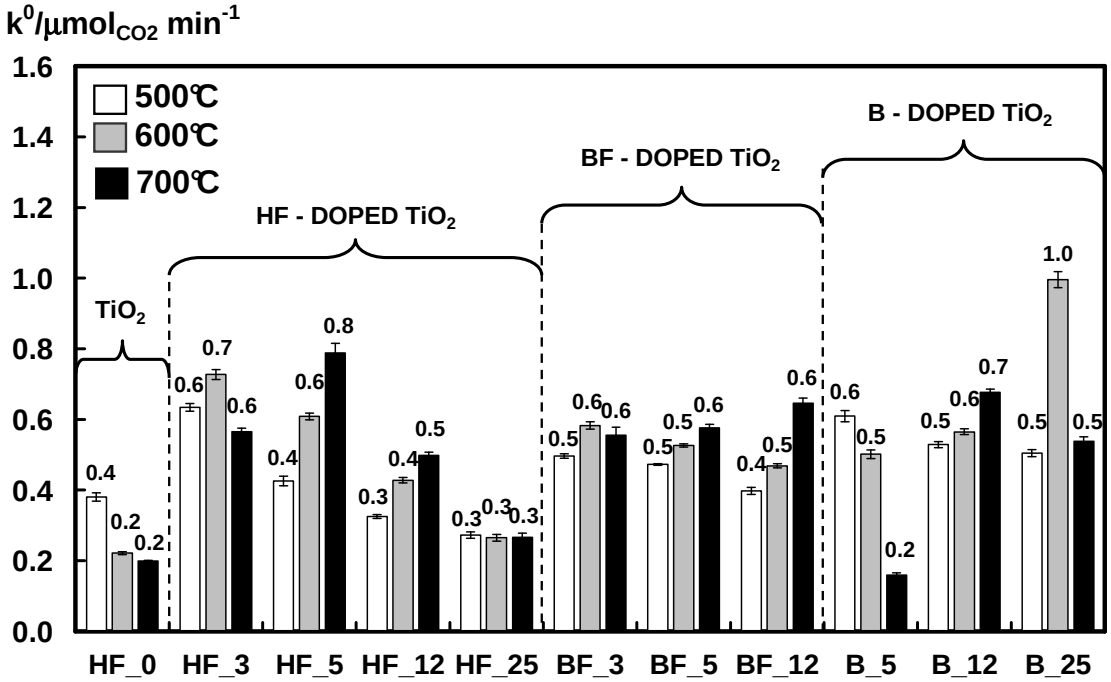

Figure 9.4 Zero-order rate constants of CO_2 photo-evolution during acetic acid decomposition on photocatalysts containing different amount/type of dopants and calcined at different temperatures.

First of all, on the undoped samples both reactions were confirmed to proceed at a lower rate with respect to that attained on moderately doped TiO_2. Moreover, with the undoped (HF_0) and B_5 series the reaction rate decreased with increasing the calcination temperature, most probably as a consequence of the anatase into rutile transformation, as already mentioned. The general trend of reaction rate increase with increasing the calcination temperature of doped materials, especially in case of the HF series, is in perfect agreement with the results previously obtained for NH_4F doped samples (D series) reported in Chapters 7 and 8 (see Fig.s 7.5 and 8.1).

This marked similarity suggests that the beneficial effect obtained for doped samples calcined at higher temperature can be mainly related to the (structural) modifications induced by fluorine rather than by the presence of nitrogen as a dopant.

This fact is outlined in Fig. 9.5, where the effects of a fixed nominal amount (5 mol.%) of each single dopant source in the liquid phase oxidative decomposition of acetic acid is compared for samples calcined at 500 or 700°C. In the case of samples calcined at 700°C the best photoactivity results were clearly obtained for TiO_2 samples fluorine-doped (HF series) or fluorine co-doped with another *p*-block element (N or B).

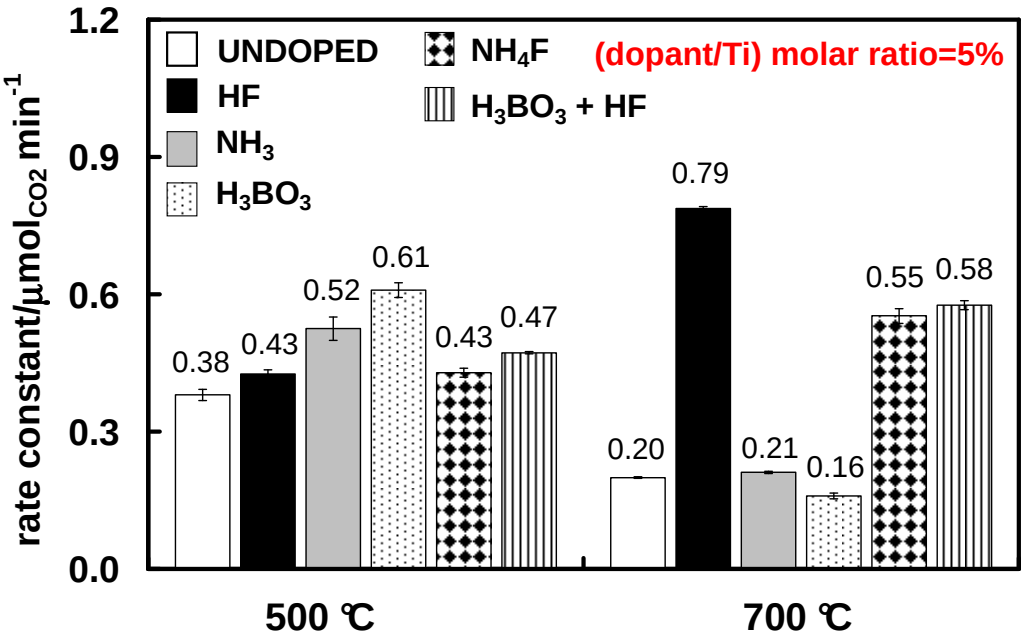

Figure 9.5 Zero-order rate constants of CO_2 photo-evolution obtained during acetic acid decomposition on photocatalysts containing 5 mol.% of different dopants.

It's worth underlining that nitrogen doping of TiO_2, starting from NH_3 as dopant source, cannot inhibit the anatase into rutile phase transition up to 700°C. In fact a TiO_2 sample prepared under identical conditions in the presence of 5 mol.% of NH_3 and

calcined at 700°C was found to contain only 19% of anatase and 81% of rutile phase, with a specific surface area of 7 m^2 g^{-1}. The corresponding nitrogen-doped sample calcined at 500°C was a full anatase material with SSA of 72 $m^2 \cdot g^{-1}$.

Among the new photocatalytic materials discussed in this Chapter the highly boron-doped sample B_25_600 was found to be the best performing one in both liquid phase reactions (Fig.s 9.3 and 9.4). The origin of this marked enhancement of photoactivity still remains unclear. Unfortunately, we could not perform a detailed XPS investigation of the B-doped materials, that should give essential information about the oxidation state and the chemical environment surrounding the boron dopant. In fact, the dopant element can exist in a separate surface B_2O_3 phase, not detected by XRPD analysis, or can be incorporated in the TiO_2 structure both in substitutional to oxygen form or into a tetrahedral interstitial site.[8,9]

Improvement of photoactivity for B-doped TiO_2 systems has already been reported, even if controversial results can be found in the literature. In fact while Chen *et al.* observed a band-gap increase due to B-doping and attributed it to quantum-size effects,[5] Zhao *et al.* detected a red shift in the absorption spectrum of B-doped TiO_2.[8] This apparent contradiction can be explained considering the different geometry and electronic structure of B-doped TiO_2, as recently shown by Geng *et al.*[10] In fact, boron atoms can substitute oxygen atoms, sit in interstitial positions, or also substitute Ti atoms. DFT calculations indicate that the latter case is the least favourable, while the remaining two have comparable energy, suggesting that both cases can occur in real materials.[10] Notably, only O-substitution will lead to band-gap narrowing, while the occupation of an interstitial site will produce a blue-shift of the absorption properties of the doped materials.[8,10]

The absorption spectra of the here investigated B-doped samples, especially in the case of the most photoactive B_25_600 sample, do not show any extra 'tail' contribution in the visible region. This is clearly shown in Fig.s 9.6 and 9.7, reporting the absorption spectra of samples containing different nominal dopant amounts, but all calcined at 600°C, and those of the B_25 series, respectively. Thus, the here adopted preparation methodology seems to lead to interstitial rather than to substitutional B-doped TiO_2. The slight red-shifted absorption observed for B_25_500 could be ascribed to the presence of the brookite phase.

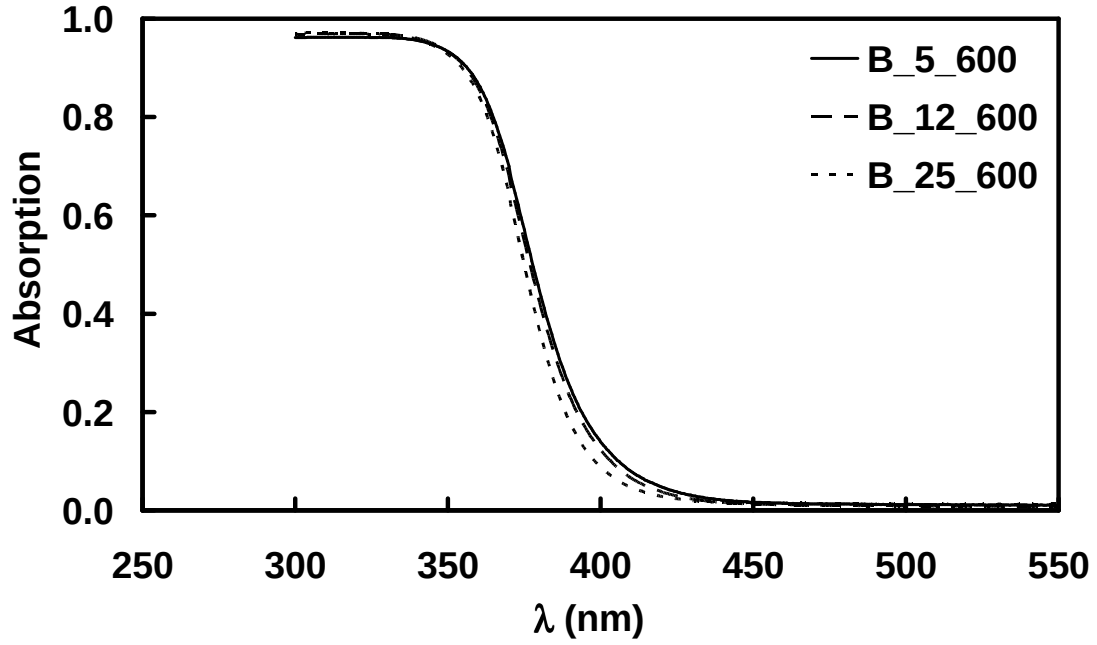

Figure 9.6 Absortpion spectra of B-doped samples containing different nominal dopant amount but calcined at the fixed temperature of 600°C.

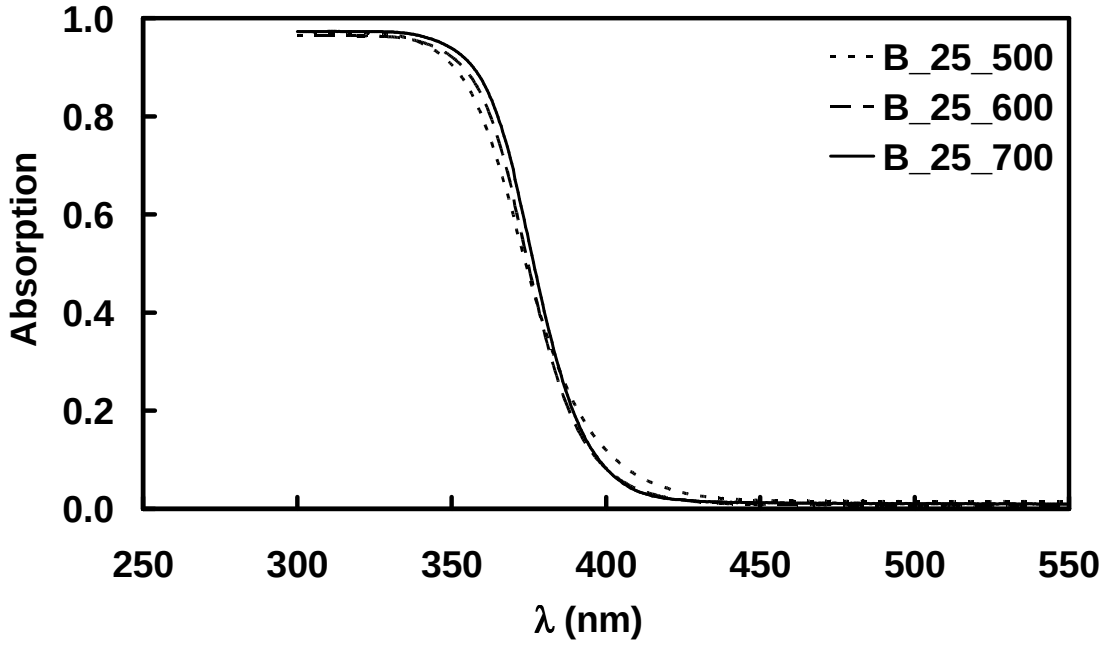

Figure 9.7 Absortpion spectra of B_25 doped TiO_2 series.

Furthermore TiO_2-doping with boron was found to enhance the hydration ability of the photocatalyst;[11] this may produce a beneficial effect on the photoactivity of B_25_600, which, even if characterized by a relative low SSA (25 $m^2 \cdot g^{-1}$), exhibits a very good photocatalytic performance in liquid suspensions (Fig.s 9.3 and 9.4). Also, the possible formation of a new B_2O_3 phase, that XPS analysis could detect, may also

be tentatively invoked to account for the relatively high photoefficiency of B-doped materials (especially of B_25_600), because the interface between the two different phases may act as a separation site for the photogenerated electrons and holes.

Finally, co-doped BF_5_700 was more active than HF_5_700 in formic acid photodecomposition, but not in acetic acid oxidation. This could be related to the different experimental conditions employed in the two test reactions. In fact, while acetic acid photooxidation was performed under UV light irradiation, the photodecomposition of formic acid was studied using a lamp mainly emitting visible light. Under such conditions a higher photoefficiency in the visible region might be evidenced. Therefore, in order to better elucidate the origin of the enhanced photoactivity of doped samples (especially of BF_5_700) and verify their possible activation in the visible region, the photooxidation of transparent acetic acid was systematically investigated with the three main HF_5, BF_5 and B_25 series as a function of irradiation wavelength in the 370-460 nm range, with a 10-nm step.

9.3.2.2 Action spectra of acetic acid decomposition (370-460 nm range)

The action spectra in the 370–460 nm range obtained with a 10 nm wavelength step for the HF_5, BF_5 and B_25 doped TiO_2 series are shown in Figure 9.8.

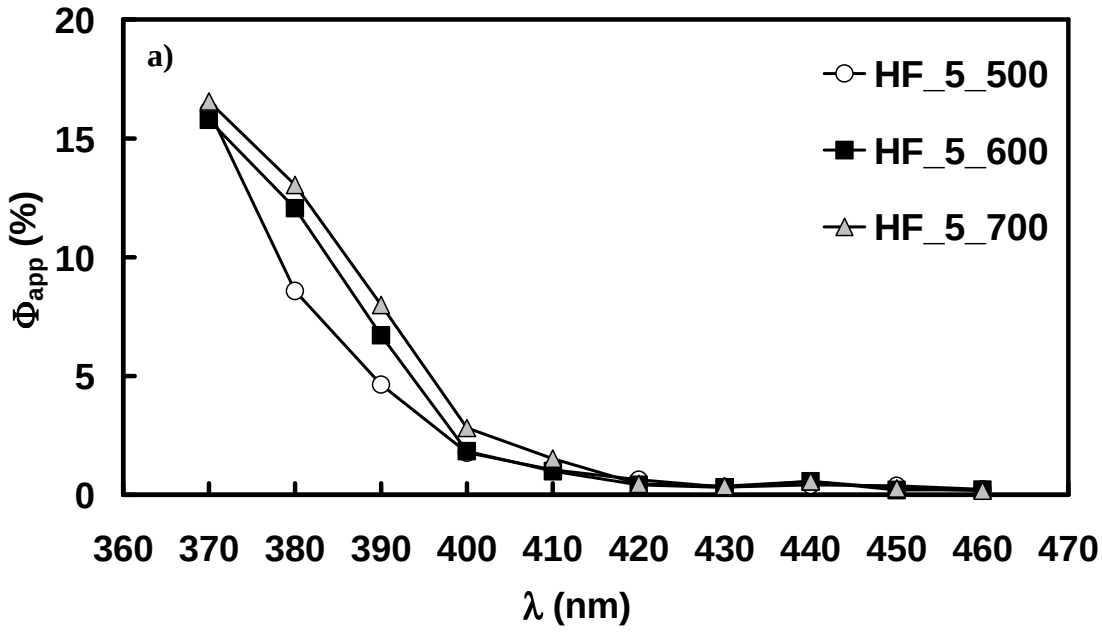

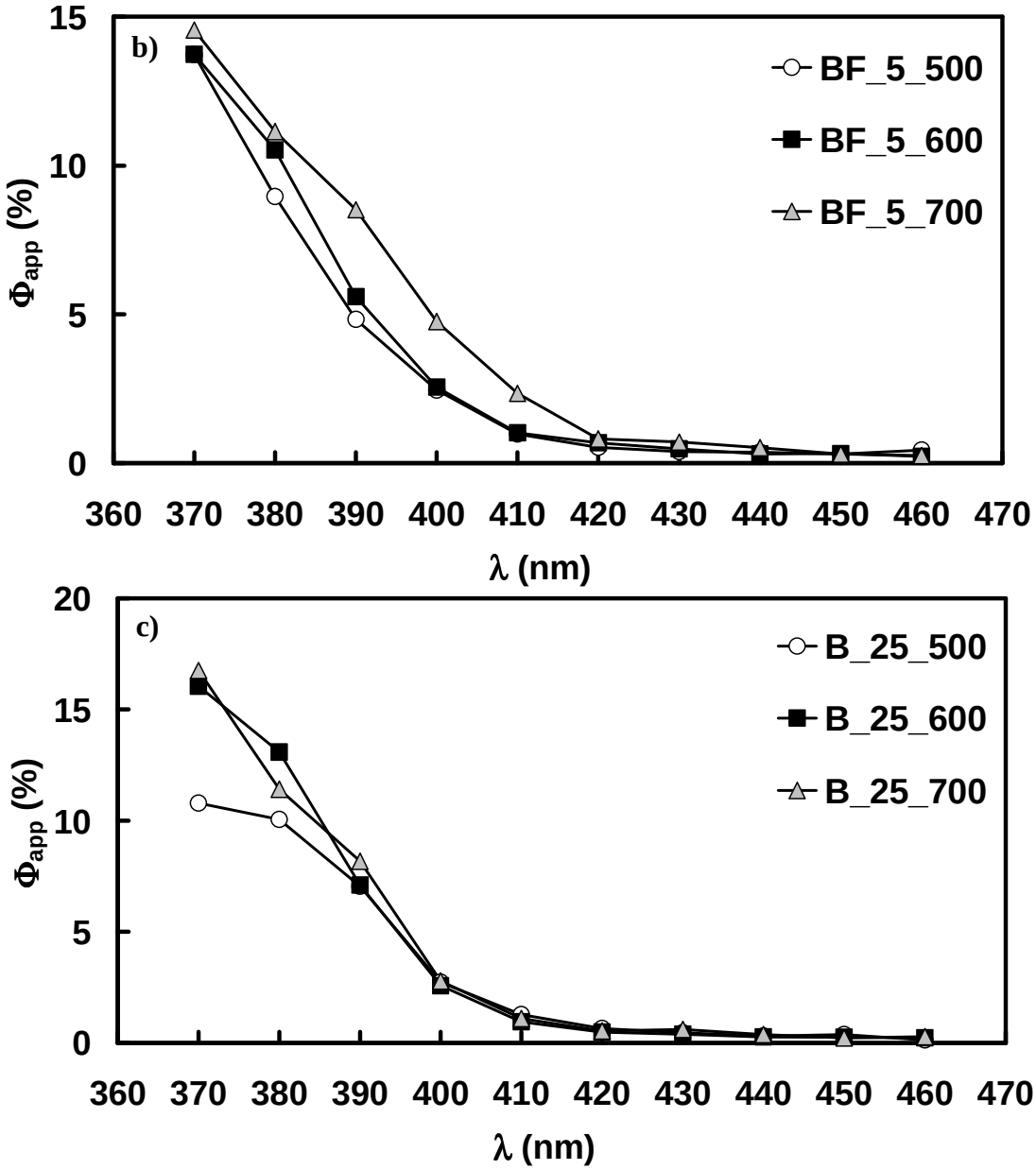

Figure 9.8 Action spectra of acetic acid decomposition in the 370-460 nm wavelength range of the a) HF_5, b) BF_5 and c) B_25 doped TiO_2 photocatalysts series.

First of all only for the HF_5 and BF_5 series a progressively higher calcination temperature ensured a better apparent quantum efficiency in the whole wavelengths region, whereas boron doping (Fig. 9.8 c) did not produce this kind of effect. This effect was also observed with the NH_4F-doped series (D_5 series) in Fig. 8.7 and attributed to the presence of active extra absorption peak A (Chapter 8). A similar explanation may be applied in the case of the full anatase HF_5 series. In fact the action spectra substraction procedure, described in Section 8.3.4.2 and systematically applied for NH_4F doped materials, was applied also to the HF_5 series, *i.e.* the action spectra of

samples calcined at 500°C were subtracted from those of samples calcined at 600 and 700°C (Fig. 9.9). Also for HF-doped samples calcined at 600 and 700°C an increase of photocatalytic activity in the UVA region was ascertained, with a maximum and relative intensity in good agreement with those obtained for the corresponding D_5 series (see Section 8.3.4.2).

This provides an unequivocal confirmation of the hypothesis made in Chapter 8, *i.e.* fluorine (and not nitrogen) as the main responsible for the observed photoactivity increase in the UVA region of doped samples, probably due to an extension of the anatase band gap absorption on the long wavelengths side (peak A) after calcination at high temperature.[12]

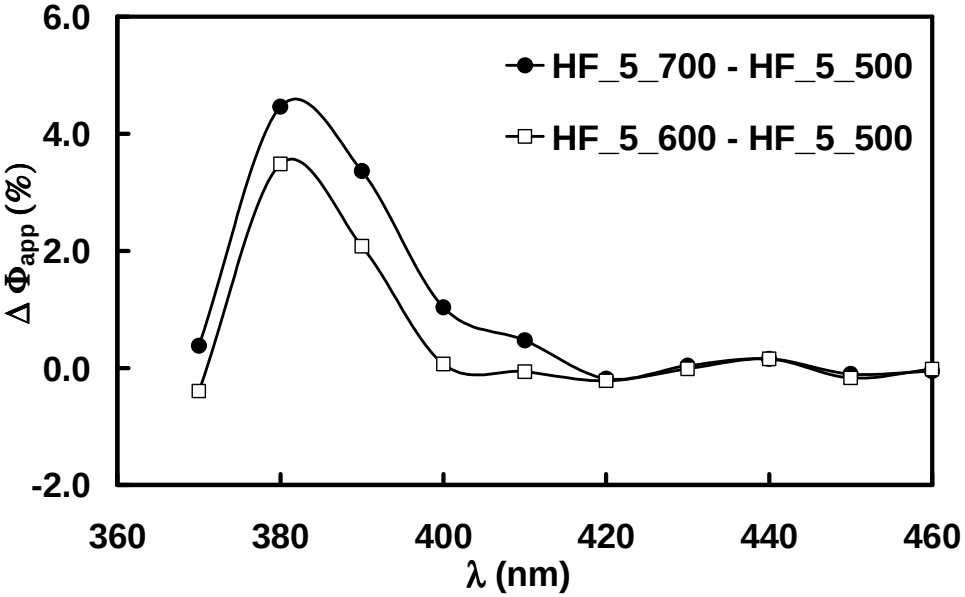

Figure 9.9 Difference action spectra of the HF_5 photocatalysts series. The action spectrum of the sample calcined at 500°C was subtracted from those of samples calcined at higher temperatures.

At the same time the difference absorption spectra obtained for the BF_5 series (Fig. 9.10) should be interpreted differently. In fact, while the photoactivity increase in the UVA region obtained with BF_5_600 could be still related to the effect of fluorine doping, in the case of BF_5_700 a red shift in the maximum position of the photoefficiency increase is observed. However, among the BF_5 series only BF_5_700 contains 5% of rutile, having a band gap absorption onset red shifted with respect to that of the anatase phase. So aiming at ascertaining whether light absorption by rutile could be responsible for the observed photoefficiency increase, a substraction procedure similar to that performed for the action spectra was carried out for the

absorption spectra of the BF_5 series (Fig. 9.11). A satisfactory matching between the maximum positions of both apparent quantum efficiency increase and extra light absorption of mixed phase BF_5_700 (around 390 nm) was found. Thus, the enhanced photoefficiency observed for BF_5_700 sample could be related to the unexpected positive effect produced by the rutile phase rather than to other extra absorption peaks possibly due to co-doping.

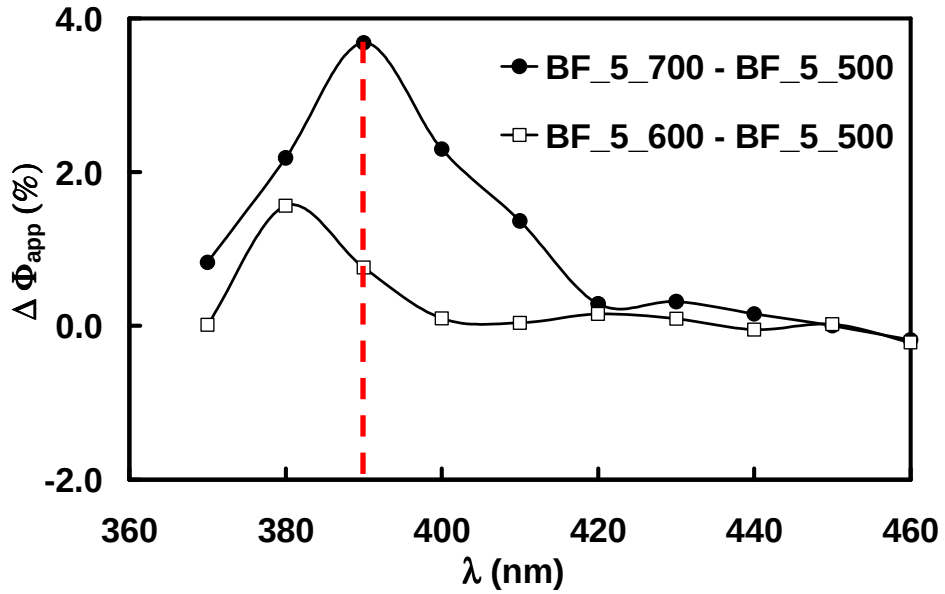

Figure 9.10 Difference action spectra of the BF_5 photocatalysts series. The action spectrum of the sample calcined at 500°C was subtracted from those of samples calcined at higher temperatures.

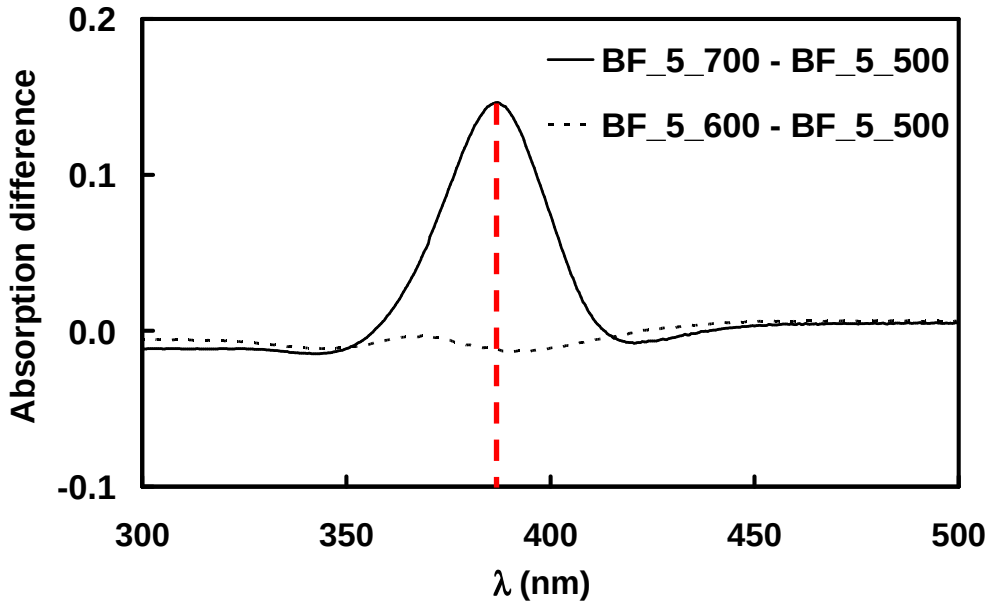

Figure 9.11 Difference absorption spectra of the BF_5 photocatalysts series. The absortpion spectrum of sample calcined at 500 °C was subtracted from those of samples calcined at higher temperatures.

Anyway we can try to check if the extra absorption peak of BF_5_700 can be completely ascribed to rutile phase by comparing the absorption difference profile reported in Fig. 9.11 with that obtained by subtracting the absorption spectrum of full anatase undoped sample calcined at 500°C (HF_0_500) from that of the mixed phase undoped HF_0_700 sample calcined at 700°C. This kind of comparison is reported in Fig. 9.12.

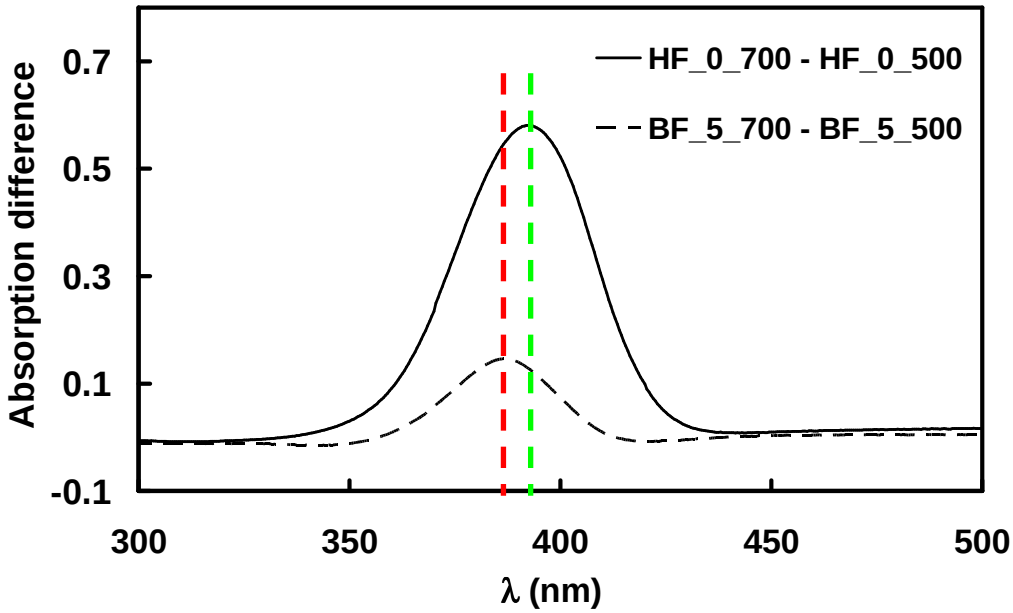

Figure 9.12 Difference absorption spectra of the BF_5 and HF_0 photocatalysts series. The dashed line was obtained by subtracting the absortpion spectrum of full anatase sample calcined at 500°C from that of the mixed phase sample BF_5_700 calcined at 700°C.

The maximum positions of the extra absorption contribution of the rutile phase obtained for undoped and BF codoped samples do not strictly coincide. The position of this maximum may be affected by the presence of the dopant boron element. This fact is further evidenced in Fig. 9.13 where the profiles of Fig. 9.12 are compared to the difference calculated between the absorption spectrum of mixed phase B-doped sample calcined at 700°C (B_5_700) and that of full anatase B-doped sample calcined at 500°C (B_5_500): the maximum positions of rutile phase absorption calculated for B_5_700 and BF_5_700 series almost coincide.

The action spectrum of a BF co-doped sample calcined at a temperature intermediate between 600°C and 700°C and composed of pure anatase phase might allow to discriminate the effect produced by the rutile phase only or by the co-presence of

dopant elements at high calcination temperature in the acetic acid photooxidation reaction.

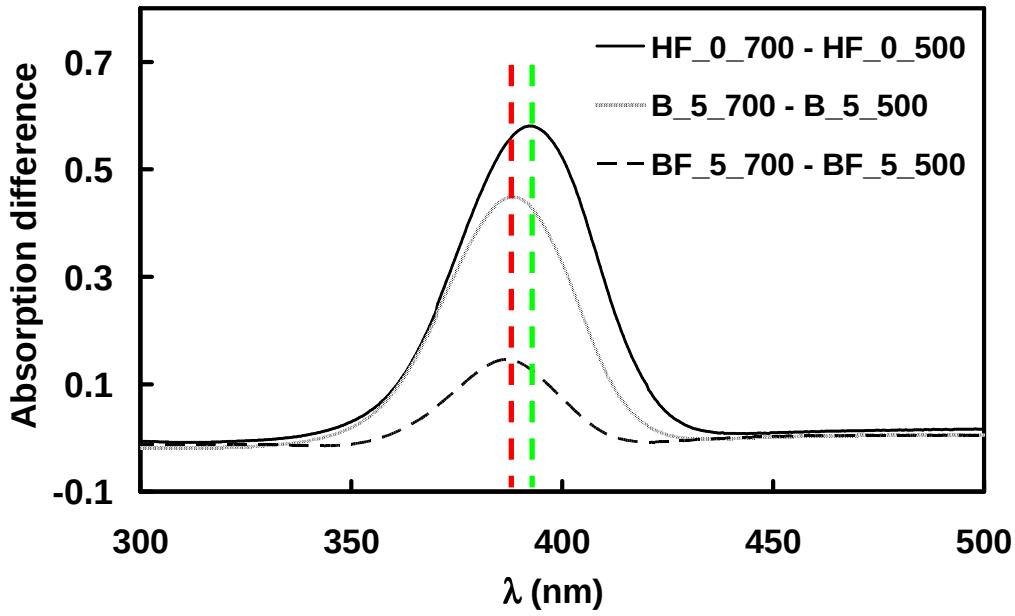

Figure 9.13 Difference absorption spectra of the BF_5, B_5 and HF_0 photocatalysts series. The absorption spectrum of full anatase sample calcined at 500°C was subtracted from that of mixed phase sample calcined at 700°C.

Finally in order to investigate the effect produced by BF co-doping respect to HF doping, the action spectra obtained for the HF_5 and BF_5 series were systematically compared (Fig. 9.14).

At λ < 390 nm, the HF doped samples were invariantly more active that the corresponding BF codoped materials for each calcination temperature. On the contrary, for λ > 390 nm the photoactivity of BF co-doped samples slightly increased with respect to that of the corresponding HF doped materials with increasing the calcination temperature. This means that boron addition can produce positive effects on the photoefficiency in acetic acid decomposition in the near UV region with increasing the calcination temperature of codoped materials. However, it's important to recall that also in this case BF_5_700 contained 5% of rutile, whereas HF_5_700 was a full anatase sample. So the enhanced photoefficiency observed for BF_5_700 could be still related to the unexpected positive effect produced by the rutile phase, rather than to other types of extra absorption peaks to be possibly ascribed to codoping.

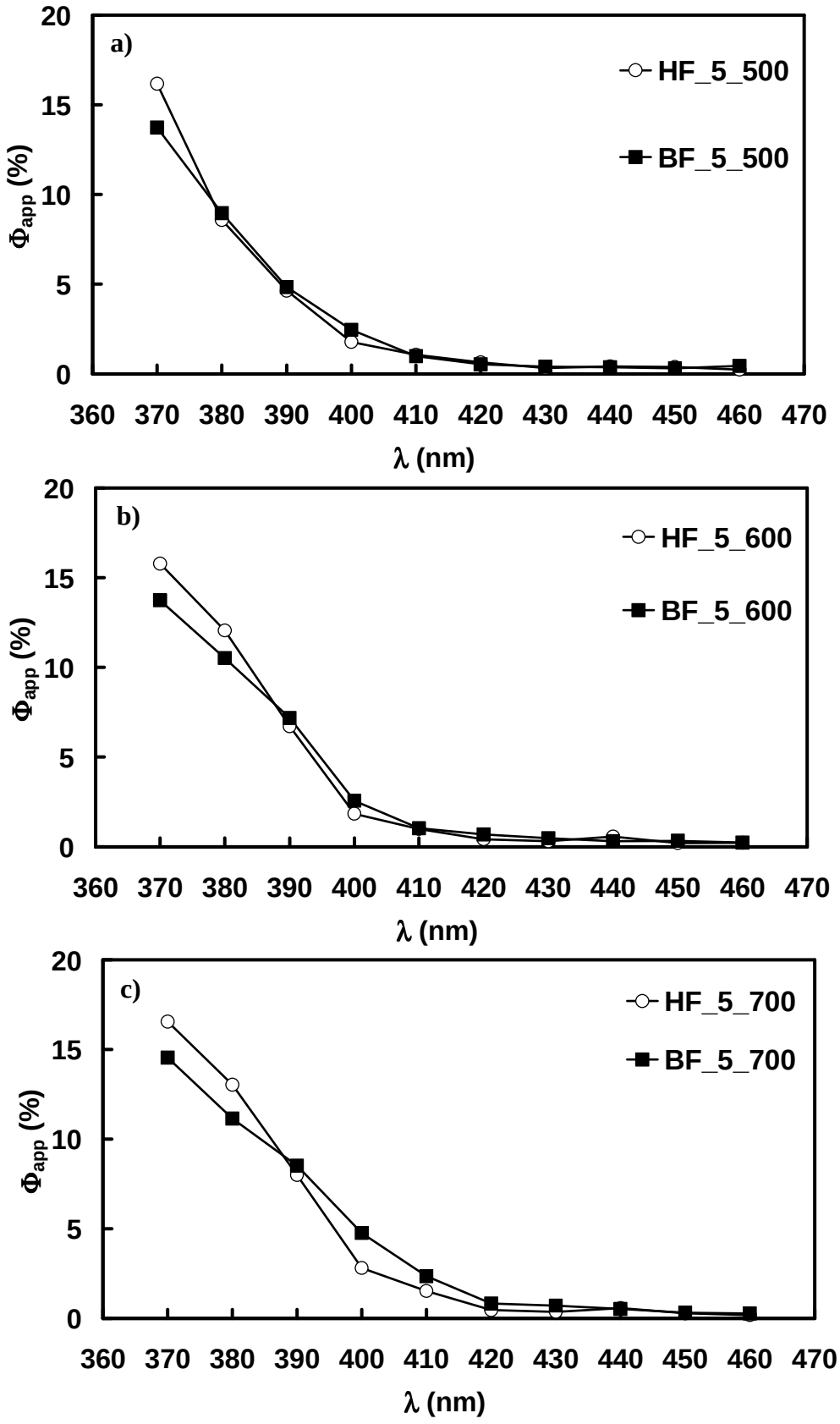

Figure 9.14 Comparison between the action spectra of acetic acid decomposition in the 370–460 nm wavelengths range obtained for the HF_5 and BF_5 series calcined at a) 500°C, b) 600°C and c) 700°C.

9.4 References

1. E. A. Reyes-Garcia, Y. Sun and D. Raftery, J. Phys. Chem. C, **2007**, 111, 17146.
2. M. Fittipaldi, V. Gombac, A. Gasparotto, C. Deiana, G. Adami, D. Barreca, T. Montini, G. Martra, D. Gatteschi and P. Fornasiero, ChemPhysChem, **2011**, 12, 2221.
3. B. Ohtani, Chem. Lett., **2008**, 37, 217.
4. A. Altomare, M. C. Burla, C. Giacovazzo, A. Guagliardi, A. G. G. Moliterni, G. Polidori and R. Rizzi, J. Appl. Cryst., **2001**, 34, 392.
5. D. Chen, D. Yang, Q. Wang and Z. Jiang, Ind. Eng. Chem. Res., **2006**, 45, 4110.
6. O. Carp, C. L. Huisman, A. Reller, Prog. Solid State Ch., **2004**, 32, 33.
7. V. Gombac, L. De Rogatis, A. Gasparotto, G. Vicario, T. Montini, D. Barreca, G. Balducci, P. Fornasiero, E. Tondello and M. Graziani, Chem. Phys., **2007**, 339, 111.
8. W. Zhao, W. Ma, C. Chen, J. Zhao and Z. Shuai, J. Am. Chem. Soc., **2004**, 126, 4782.
9. E. Finazzi, C. Di Valentin and G. Pacchioni, J. Phys. Chem. C, **2009**, 113, 220.
10. H. Geng, S. W. Yin, X. Yang, Z. G. Shuai and B. G. Liu, J. Phys-Condens. Mat., **2005**, 18, 87.
11. S.C. Moon, H. Mametsuka, S. Tabata and E. Suzuki, Catal. Today, **2000**, 58, 125.
12. M.V. Dozzi, B. Ohtani and E. Selli, Phys. Chem. Chem. Phys., **2011**, 13, 18217.

Chapter 10

Photocatalytic Activity of Ammonium Fluoride-doped TiO_2 Modified by Noble Metal Nanoparticles Deposition

10.1 Introduction

The deposition of gold nanoparticles, especially if carried out by photoreduction, can improve the photocatalytic activity of commercial TiO_2 powder (Degussa P25) by increasing the rate of formic acid oxidation (Chapter 6). At the same time home-made NH_4F-doped TiO_2 materials, characterized by a relatively high cristallinity degree, exhibit excellent ability to photo-oxidise different organic substrates (Chapters 7-8). The idea of combining both these positive effects (bulk and surface modifications of TiO_2 materials) was the aim of the work reported in this chapter.

The effect of noble metal nanoparticles (Pt and Au) photodeposition on the series of differently NH_4F-doped TiO_2 photocatalysts calcined at 700°C (previously showing the best photocatalytic performances) was thus investigated in both energetically down-hill and up-hill reactions, *i.e.* in both formic and acetic acid degradation in aqueous suspension and in hydrogen production from methanol/water vapour mixtures, also aiming at getting a better insight into the role played by noble metal nanoparticles on both reduction and oxidation photocatalytic processes. Thermodynamically down-hill oxidation reactions have been employed so far to test the activity of the photocatalytic TiO_2-based materials investigated in the present thesis. The low temperature production of hydrogen through photocatalytic steam reforming of organics on metal oxide semiconductors is an up-hill reaction, which provides a way to convert solar energy into chemical energy with a small CO_2 impact compared to the use of fossil fuels. In fact, contrarily to traditional steam reforming, the photo-assisted process occurs at room temperature and atmospheric pressure and no feed stock needs to be burnt because the required energy is totally supplied by photons.

Organic compounds also deriving from renewable sources, *i.e.* biomasses, acting as hole scavengers, can play an essential role in increasing the overall rate of photocatalytic hydrogen evolution. For instance, methanol is widely used as a sacrificial agent in the liquid–phase photocatalytic production of hydrogen[1-4] and has already been employed by our research group as a volatile organic electron donor in a model reaction for photocatalytic hydrogen formation from renewable sources.[5-7]

The prepared photocatalysts were characterized by BET, XRD, UV-vis absorption, EXAFS and HRTEM analyses and the modifications induced on the photocatalytic activity by the noble method photodeposition treatment were also taken into account. All the photocatalytic activity results have been compared to the photocatalytic

efficiency of commercial P25 (Degussa), also modified according to the same photodeposition procedure.

To the best of my knowledge, there is no report in the literature on NH_4F doping of TiO_2 coupled with noble metal nanoparticles deposition to improve the photocatalytic activity of titania in the UV-vis region.

10.2 Experimental Section

10.2.1 Doped-TiO_2 preparation and their surface modification

A series of doped titania (D-TiO_2) photocatalysts was prepared by the sol-gel method in the presence of different amounts of NH_4F, used as a dopant source, and calcined, in this case, at a fixed temperature of 700°C. The nominal dopant/Ti percent molar ratios were 5, 7 and 12. Doped materials were labelled as D_X, with X referring to the nominal dopant/Ti percent molar ratio. Reference undoped material, prepared by exactly the same synthetic route in the absence of NH_4F, is defined as the D_0 sample. More details on the preparation of the materials and on their characterisation analyses can be found in Chapter 8.

The TiO_2 samples modified by noble metal nanoparticles photodeposition were prepared starting from 6 vol.% of methanol/water suspensions, containing 3 g L^{-1} of D_X sample and the amount of noble metal precursor necessary to obtain a fixed nominal metal loading of 0.5 wt.%, which was already shown to be the optimal content for improving formic acid (FA) photooxidation (Chapter 6). $HAuCl_4$ was employed as noble metal precursor in the case of gold nanoparticles deposition, H_2PtCl_6 was used for platinum deposition.

Au(III) and Pt(IV) photoreduction to metallic nanoparticles deposited on TiO_2 was achieved by irradiating the suspensions for 2 h under nitrogen atmosphere. The immersion fluorescent, low pressure mercury arc lamp (Jelosil), already described in Section 6.2.1, was employed as the irradiation source (see Scheme 6.2b). Noble metal-modified D_X powders were recovered after at least three centrifugation and washing cycles, up to the complete removal of residual ions and organic precursors. They were then dried at 70°C for 1 day and stored in the absence of light and humidity. These samples were labelled as M/D_X, where M refers to the noble metal (Au or Pt) deposited on the previously described home-made NH_4F doped-TiO_2 materials.

Reference samples were prepared by following the same procedure, except for the addition of the noble metal precursor, and labelled as R/D_X with R standing for 'reference'.

The same method of noble metal nanoparticles photodeposition was also employed to modify commercial mixed phase Degussa P25 titanium dioxide.[8] All reagents were purchased from Aldrich and employed as received.

10.2.2 Photocatalysts characterisation

UV-Vis diffuse reflectance (DR) spectra were recorded with a Lambda 19, Perkin Elmer spectrophotometer equipped with an integrating sphere an then converted into absorption (A) spectra (A = 1 – R). HRTEM images were obtained with a JEM 3010 (JEOL) electron microscope operating at 300 kV.

Structural features of the gold and platinum nanoparticles in the as-prepared photocatalyst were characterized by XAFS, including X-ray absorption near-edge structure (XANES) and extended X-ray absorption fine structure (EXAFS). The XAFS spectra for the Au and Pt L_3-edge were recorded on the ANKA-XAS beamline using a Si(111) double-crystal monochromator detuned to *ca.* 60% of the maximum intensity. Incident and transmitted X-ray intensity were measured by ion chambers (Oxford). The experiments were performed at the ANKA Synchrotron Strahlungsquelle of Karlsruhe Institute of Technology by Dr. Gian Luca Chiarello. Standard PtO_2, Pt and Au foils were used to extract experimental EXAFS parameters for Pt-O, Pt-Pt and Au-Au bond lengths, respectively.

10.2.3 Photocatalytic tests

10.2.3.1 Formic acid and acetic acid degradation

All photocatalytic FA degradation runs were performed as already described (Section 4.1) under atmospheric conditions in a magnetically stirred 60 mL cylindrical quartz reactor. All irradiated aqueous suspensions contained 0.1 g L^{-1} of photocatalyst; the initial concentration of FA was equal to 1.0×10^{-3} mol L^{-1}. Acetic acid decomposition under polychromatic irradiation was investigated as described in Section 4.2.2.

10.2.3.2 Hydrogen production from methanol photo-steam reforming

The photocatalytic activity in hydrogen production by methanol photo-steam reforming:

$$CH_3OH + H_2O \rightarrow CO_2 + 3\ H_2 \quad (10.1)$$

was tested in the expressly set up, closed recirculation laboratory scale apparatus sketched in Fig. 10.1, already employed in previous studies.[5,7,9]

The photocatalyst powder was deposited on 20–40 mesh (0.85–0.42 mm) quartz beads by mixing 14 mg of it with 3 g of quartz beads and 1.2 mL of distilled water, followed by drying in oven at 70°C for 6 h. The so-obtained photocatalyst bed was inserted in the photoreactor consisting in a flat cylindrical Plexiglas cell, having a central 2 mm thick and 50 mm in diameter round hollow, frontally closed by a Pyrex glass optical window (irradiation surface *ca*. 20 cm^2). The photoreactor was connected to a closed stainless steel system (see Fig. 10.1a), where the gas phase was recirculated at a constant rate by means of a metal bellow pump. The system was preliminarily purged with nitrogen in order to remove any oxygen trace. During the photocatalytic tests, the photocatalyst bed was continuously fed with a stream of 40 mL min^{-1} of N_2 saturated with the vapour of a 20 vol.% methanol–water solution thermostatted at 30°C, corresponding to a methanol molar fraction *x* of 0.10 in the liquid phase.

The reactor temperature during irradiation was 55 ± 5 °C, as monitored by a thermocouple placed inside the cell. The absolute pressure was 1.2 bar at the beginning of the runs and slightly increased during irradiation, as a consequence of the accumulation of products in the gas phase. During the runs, typically lasting 6 h, the recirculating gas was analysed on-line by sampling it every 20 min by means of a pneumatic sampling valve placed at the exit of the photoreactor. Gas samples were automatically injected into an Agilent 6890 N gas-chromatograph, equipped with two columns (HP-PlotU and Molesive 5A), two detectors (thermoconductivity and flame ionisation) and a Ni-catalyst kit for CO and CO_2 methanation. N_2 was used as carrier gas. The GC response was calibrated by injecting known volumes of H_2, CO and CO_2 into the recirculation system through the loop of a six ways sampling valve. When testing noble metal nanoparticles modified photocatalysts, purging by nitrogen in the dark was required every 2 h, due to the high products accumulation in the recirculating gas phase.

The irradiation source was Xenon lamp (LSH302 of LOT Oriel, 300 W), see Fig. 10.1b, placed at 13 cm from the reactor, emitting in the 350–450 nm wavelength range with a full irradiation intensity of $6 \cdot 10^{-8}$ einstein s^{-1} cm^{-2} on the reactor, determined by ferrioxalate actinometry.[10] Its constancy was checked daily by means of a UVA lux-meter.

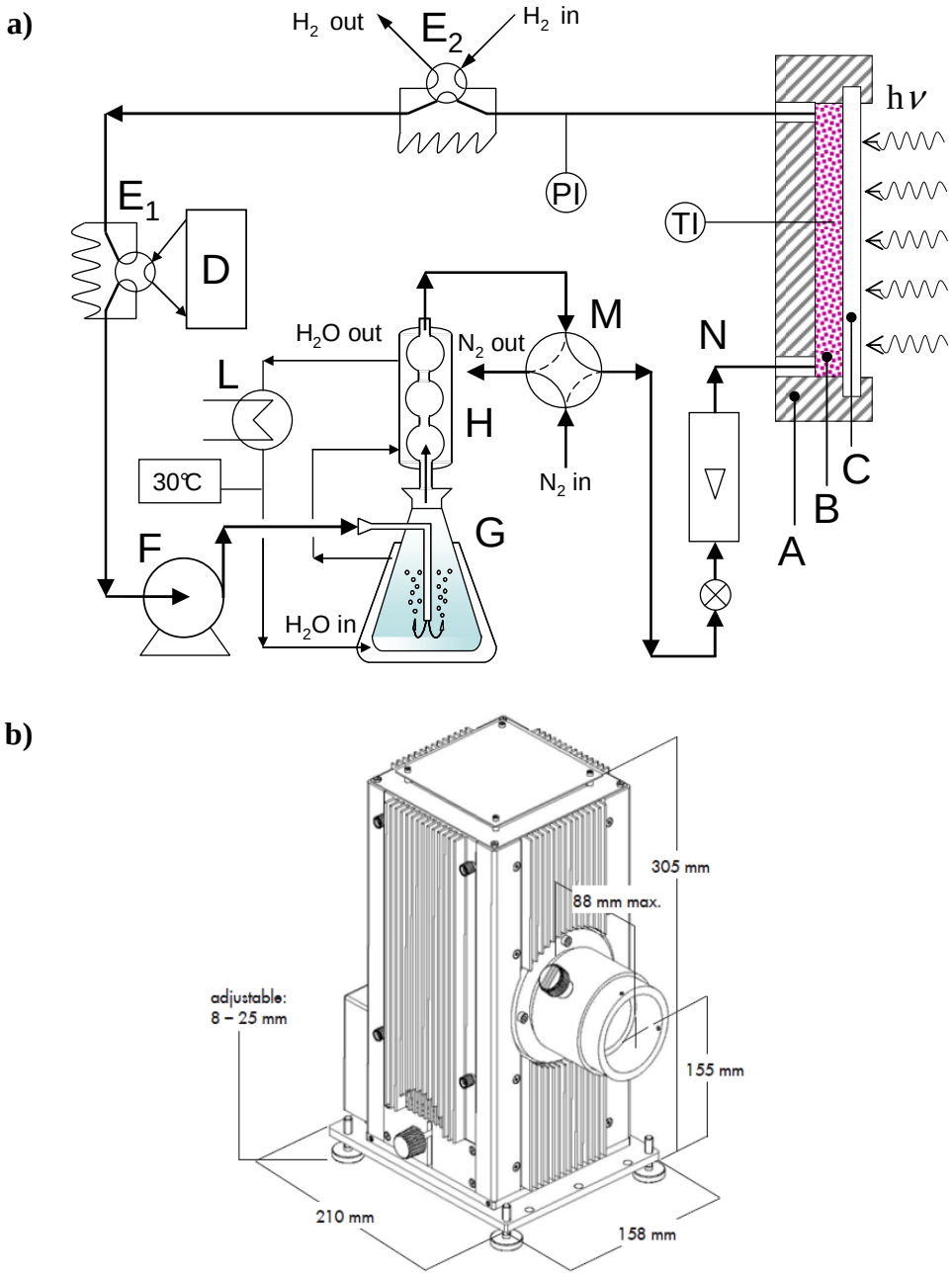

Figure 10.1 a) Sketch of the experimental setup for photocatalytic activity tests: (A) cross section of the Plexiglas photoreactor; (B) photocatalyst bed; (C) Pyrex glass window; (D) detectors (GC with TCD and FID); (E_1, E_2) six ways sampling valves; (F) bellow pump; (G) bubbler containing CH_3OH/H_2O solutions; (H) refrigerator-condenser; (L) thermostat; (M) four ways ball valve; (N) gas flow meter; (TI) temperature indicator; (PI) pressure indicator. b) Sketch of the adopted light source.

10.3 Results and discussion

10.3.1 Photocatalysts characterisation

10.3.1.1 XRD and BET analyses

The main structural features of the investigated naked TiO_2 samples, determined by XRD and BET analyses, are summarized in Table 10.1.

Table 10.1 Phase composition and crystallite dimensions, d_A, obtained from XRD analysis, by assuming the absence of amorphous phase; specific surface area (SSA), obtained from BET analysis of the investigated photocatalysts series.

Sample	dopant/Ti molar ratio (%)	anatase (%)	brookite (%)	rutile (%)	dA/nm	SSA/m^2 g^{-1}
P25		80	-	20	25	48
D_0	0	38	-	62	65	7
D_5	5	99	-	1	49	16
D_7	7	99.5	-	0.5	44	14
D_12	12	99.5	-	0.5	48	12

The phase composition of NH_4F-doped samples, obtained by Rietveld refinement of XRD data, clearly shows that doping inhibits the anatase into rutile phase transition, which is typically observed after annealing undoped titania at 700°C (see Chapter 7). Moreover the SSA of doped materials is slightly larger with respect to that of the corresponding undoped TiO_2.

XRD patterns obtained for the samples modified by noble metal nanoparticles deposition (not shown for the sake of brevity) were practically identical to those of the corresponding unmodified samples. Also the specific surface area of TiO_2 did not vary upon noble metal nanoparticles deposition. This is in agreement with analogous results obtain for gold modified samples discussed in Chapter 7.

10.3.1.2 UV-Vis DR spectra

The deposition of gold nanoparticles on TiO_2 was confirmed by the colour change of the modified oxide powder, turning from white into purple, originated from the surface plasmon resonance of nanocrystalline Au^0 particles.

As shown in Fig. 10.2 gold containing samples display the typical plasmon resonance absorption band, with a maximum around 550 nm, *i.e*. red shifted compared to the pure gold plasmonic peak (520 nm), indicating interaction between gold and titania support. Sample Au/D_0 exhibit a red-shift of the absorption edge because of the relative high content of rutile phase. Au modified samples obtained starting from an intermediate amount of dopant source (D_5 and D_7) exhibit a plasmon resonance band which is slightly shifted to shorted wavelengths with respect to the other samples, indicating smaller Au nanoparticles dimensions,[11] and is characterized by a relatively higher maximum absorption intensity.

Pt/TiO_2 samples, appearing as grey powders, exhibit a broad absorption in the visible region (higher respect to the corresponding unmodified TiO_2 samples), without any specific plasmonic band (Fig. 10.3).

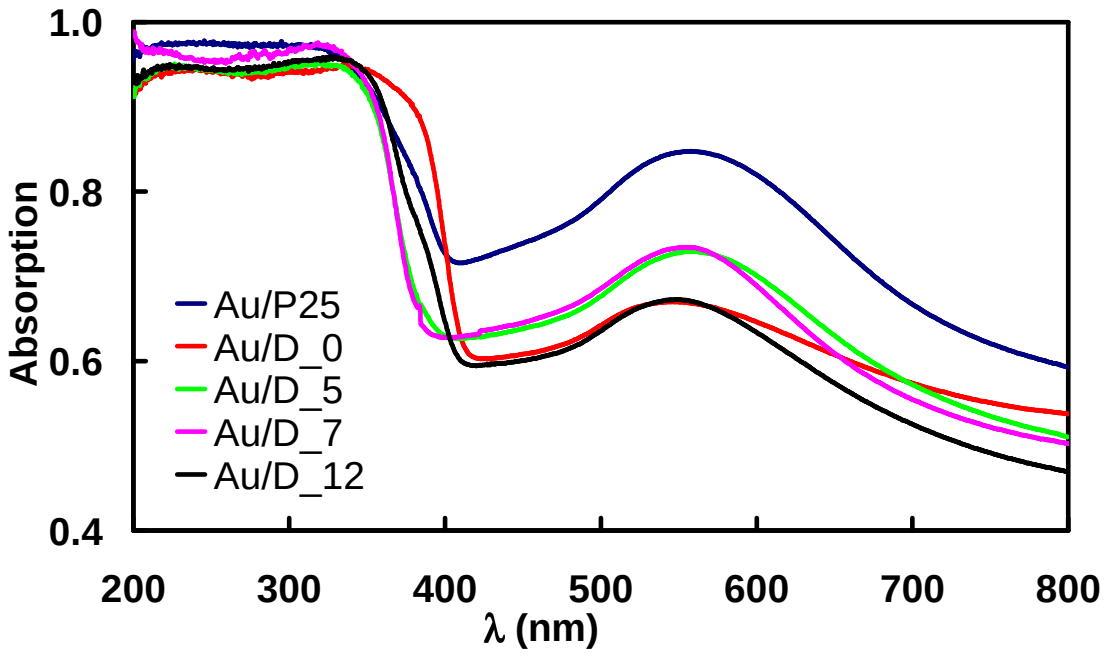

Figure 10.2 Absorption spectra of P25 TiO_2 and NH_4F doped photocatalysts series modified by gold nanoparticles (0.5 wt.%) photodeposition.

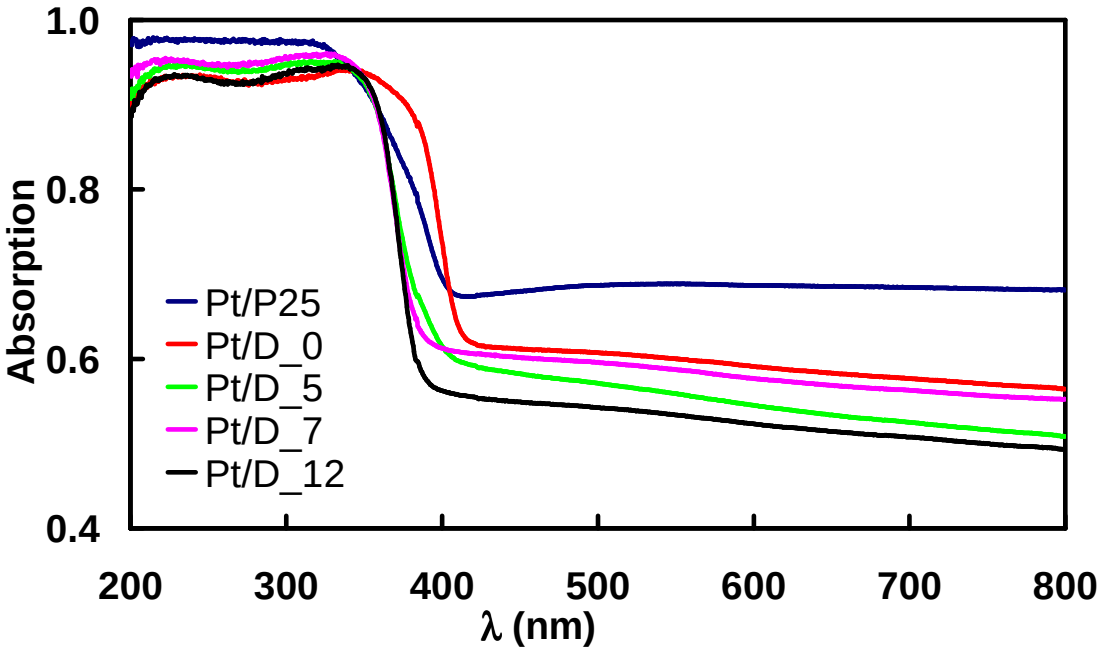

Figure 10.3 Absorption spectra of P25 TiO_2 and NH_4F doped photocatalysts series modified by platinum nanoparticles (0.5 wt.%) photodeposition.

10.3.1.3 EXAFS analysis

10.3.1.3.1 Pt modified TiO_2 samples

The Pt L_3-edge XANES spectra for metallic Pt, PtO_2 and home-made Pt/TiO_2 photocatalysts are shown in Figure 10.4.

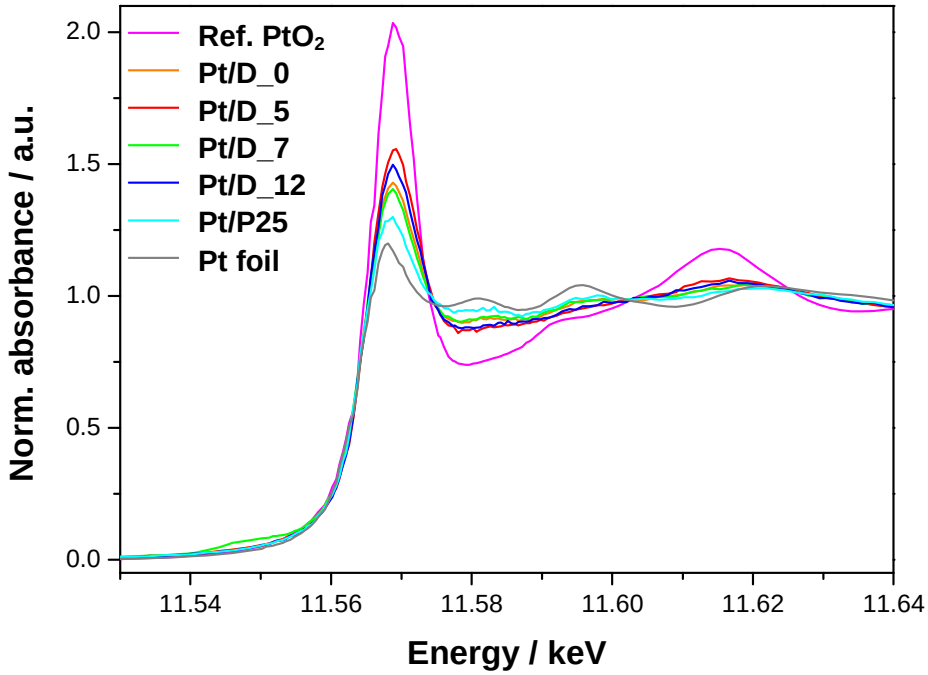

Figure 10.4 Pt L_3-edge (11564 eV) XANES spectra of Pt, PtO_2 and home-made NH_4F-doped photocatalysts series modified by platinum nanoparticles (0.5 wt.%) photodeposition.

The XANES spectra of Pt/TiO_2 photocatalysts are intermediate between those of the two reference samples (Pt foil and PtO_2), suggesting that Pt nanoparticles deposited by photoreduction method on the TiO_2 surfaces are not present with a unique oxidation state. This fact is clearly outlined in Fig. 10.5 where the Fourier transforms (FTs) of $\chi^2(k)$ EXAFS signals for the standard and of the investigated samples are shown without phase shift correction.

The main structural parameters (bond length, R, and coordination number, CN) obtained for Pt/TiO_2 samples by using a proper simulation program are summarized in Table 10.2. All spectra exhibit, with a different relative intensity, both the peak associated to Pt-Pt bond for metallic Pt and the typical signals related to Pt-Pt and Pt-O (first shell of coordination) bonds for oxidized Pt state (PtO_2).

The signal associated to the second shell of Pt-O coordination for PtO_2 is absent in all spectra, suggesting a relative small size of photodeposited Pt nanoparticles. Moreover the absence of the Pt-Pt shell at 3.103 Å typical of PtO_2 demonstrates that the samples possess passivated metal Pt nanoparticles.

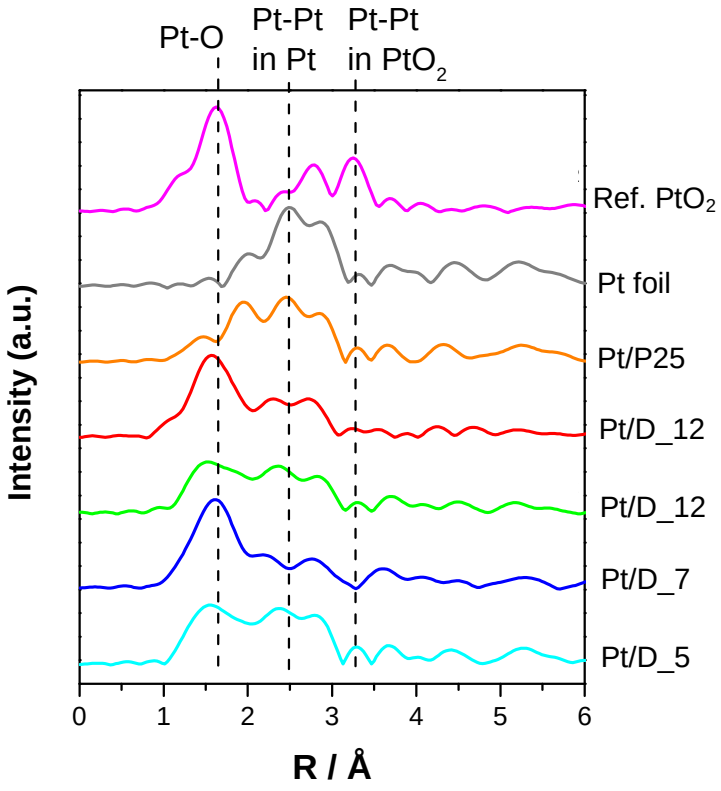

Figure 10.5 Fourier transform (FTs) of the $\chi^2(k)$ EXAFS signals for Pt, PtO_2 and home-made Pt/TiO_2 photocatalysts.

Table 10.2 Main structural parameters (interatomic distances, R, and coordination number, CN) obtained from EXAFS analysis for Pt/TiO_2 samples.

Sample	Shell	CN	R (Å)
Pt foil	Pt-Pt	12.0 ± 0.6	2.765 ± 0.002
Ref. PtO_2	Pt-O_{-1}	5.7 ± 0.5	2.016 ± 0.007
	Pt-Pt*	6.6 ± 1.6	3.103 ± 0.005
	Pt-O_{-2}	11.5 ± 4.7	3.677 ± 0.029
Pt/P25	Pt-O_{-1}	1.4 ± 1.2	2.038 ± 0.046
	Pt-Pt	7.6 ± 1.5	2.747 ± 0.011
Pt/D_0	Pt-O_{-1}	1.7 ± 0.6	1.960 ± 0.026
	Pt-Pt	7.0 ± 1.9	2.730 ± 0.016
Pt/D_5	Pt-O_1	2.8 ± 0.6	1.975 ± 0.021
	Pt-Pt	4.9 ± 2.5	2.743 ± 0.025
Pt/D_7	Pt-O_{-1}	1.5 ± 0.5	1.966 ± 0.026
	Pt-Pt	6.4 ± 1.8	2.731 ± 0.017
Pt/D_12	Pt-O_{-1}	2.5 ± 0.5	1.972 ± 0.019
	Pt-Pt	3.5 ± 1.4	2.723 ± 0.015

By considering the presence of platinum not only in the metallic form, an iterative fitting algorithm was used in order to calculate the relative amount of Pt^{4+} and Pt^0 in each sample. This kind of mathematical approach is briefly explained for the Pt/D_0 sample in Fig. 10.6. In this simulation, a linear combination of the two reference spectra of Pt^{4+} and Pt^0 (red curve) is refined against the experimental curve (in blue color), in order to minimize the residual. The relative percent contribution of oxidized and metallic platinum states are thus calculated and summarized in Table 10.3.

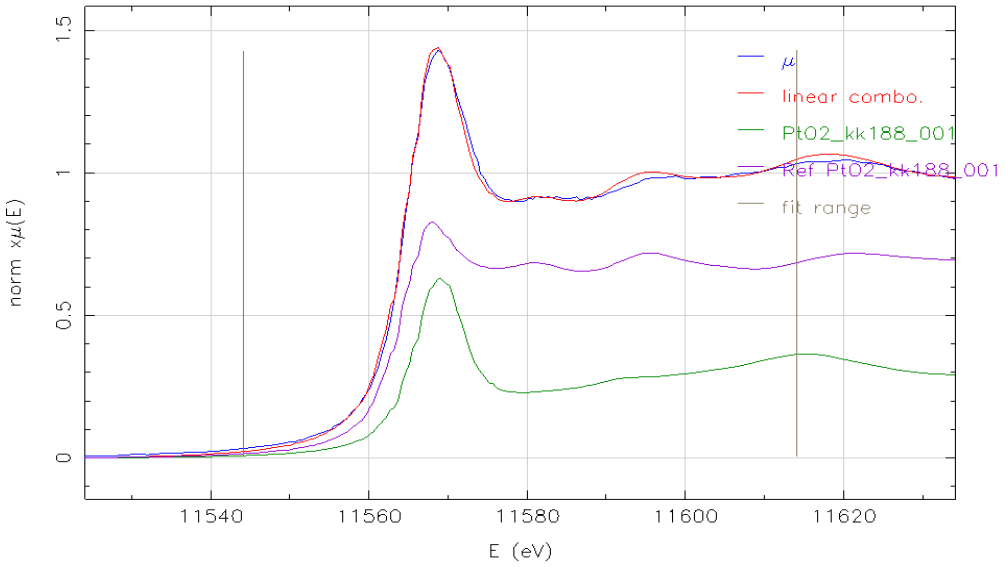

Figure 10.6 Example of iterative fitting algorithm performed in order to calculate the relative amount of Pt^{4+} and Pt^{0} for the Pt/D_0 photocatalyst.

Table 10.3 Relative percent contribution of oxidized and metallic states of platinum nanoparticles, calculated for Pt/TiO_2 samples.

Sample	Pt^0 wt.%	Pt^{4+} wt.%
Pt/P25	85	15
Pt/D_0	69	31
Pt/D_5	54	46
Pt/D_7	73	27
Pt/D_12	61	39

Among all the investigated samples, Pt/D_5 and Pt/P25 materials show the relative highest contribution of Pt^{4+} and Pt^{0} forms respectively. By comparing the results reported in Tables 10.2 and 10.3 an expected correlation between the relative percent of Pt(IV) and the coordination number (CN) associated to the first shell of Pt-O can be found; so the increase of Pt(IV) content is followed by an increase of Pt-O coordination number.

Anyway there seems not to be a direct correlation between the relative percent amount of metallic/oxidized states of deposited platinum nanoparticles and the corresponding nominal NH_4F dopant amount of home-made samples.

10.3.1.3.2 Au modified TiO_2 samples

The Au L_3-edge XANES spectra for metallic Au and home-made Au/TiO_2 photocatalysts are shown in Figure 10.7.

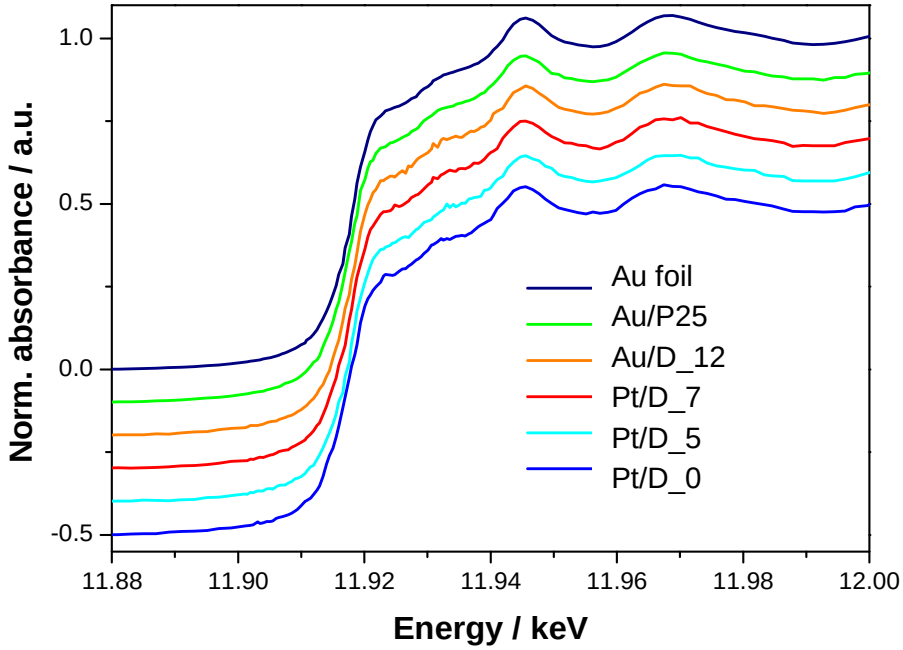

Figure 10.7 Au L_3-edge (11564 eV) XANES spectra of Au and home-made NH_4F-doped photocatalysts series modified by gold nanoparticles (0.5 wt.%) photodeposition.

The XANES spectra of the investigated Au/TiO_2 photocatalysts resemble that of the Au foil reference, indicating that Au nanoparticles, deposited by the photoreduction method on the TiO_2 surfaces, are present in full metallic state. This fact is clearly confirmed in Fig. 10.8, where the Fourier transforms (FTs) of $\chi^2(k)$ EXAFS signals for the standard and the investigated samples are shown without phase shift correction. Main structural parameters (bond length, R, and coordination number, CN) obtained for Au/TiO_2 samples, by using similar simulation programs briefly described for Pt/TiO_2 materials, are summarized in Table 10.4.

Let's focus our attention on the Au coordination number calculated for the investigated samples. Generally a gold atom surrounded only by other gold atoms (in bulk form) has a coordination number (CN) equal to 12. Therefore for a gold atom exposed to the surface a lower coordination number is expected. In particular, the coordination number may decrease for smaller gold nanoparticles, characterized by an average higher amount of gold atoms at the surface with respect to those located into

the bulk. As a result, the coordination number, obtained by EXAFS experiments, could give an indirect information about the relative gold nanoparticles size. On the basis of the data reported in Table 10.4, home-made samples containing an intermediate nominal dopant amount (D_5 and D_7) seem to be characterized by relative smaller gold nanoparticles. No further information about metal nanoparticles size can be obtained for other Au/TiO_2 samples which are characterized by gold coordination number closer to 12.

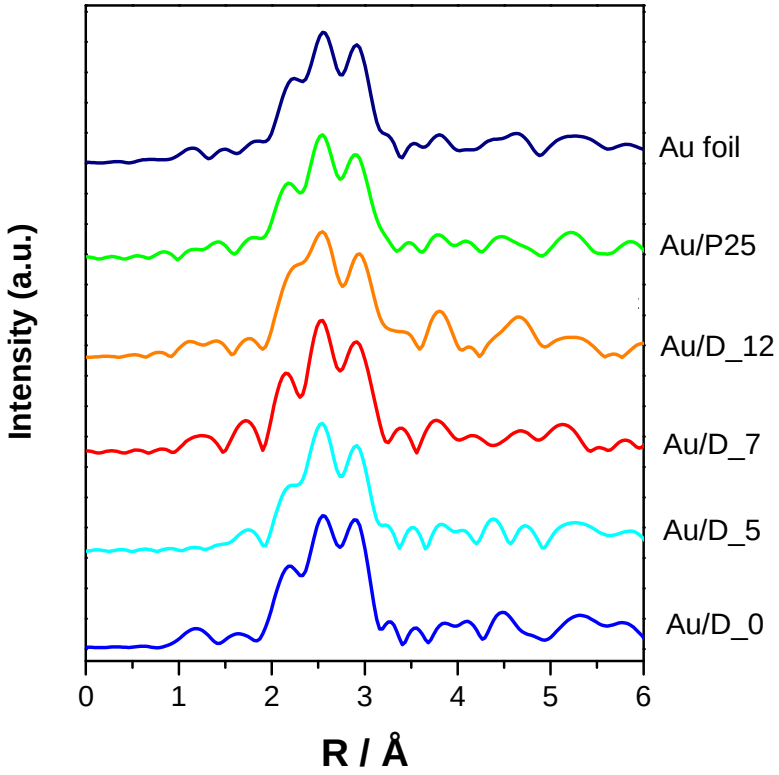

Figure 10.8 Fourier transform (FTs) of the $\chi^2(k)$ EXAFS signals for Au and home-made Au/TiO_2 photocatalysts.

Table 10.4 Main structural parameters (bond length, R, and coordination number, CN) obtained from EXAFS analysis for Au/TiO_2 samples.

Sample	Shell	CN	R (Å)
Au foil	Au-Au	11.9 ± 0.6	2.862 ± 0.003
Au/P25	Au-Au	11.4 ± 0.8	2.856 ± 0.003
Au/D_0	Au-Au	11.1 ± 1.0	2.857 ± 0.004
Au/D_5	Au-Au	9.6 ± 1.5	2.860 ± 0.007
Au/D_7	Au-Au	10.9 ± 1.4	2.851 ± 0.007
Au/D_12	Au-Au	12.0 ± 0.6	2.855 ± 0.004

10.3.1.4 HRTEM analysis

Gold and platinum photodeposition on TiO_2 was also verified by HRTEM analysis, yielding valuable and direct information on the dimension and the distribution of noble metal nanoparticles on the TiO_2 surface (see Fig. 10.9).

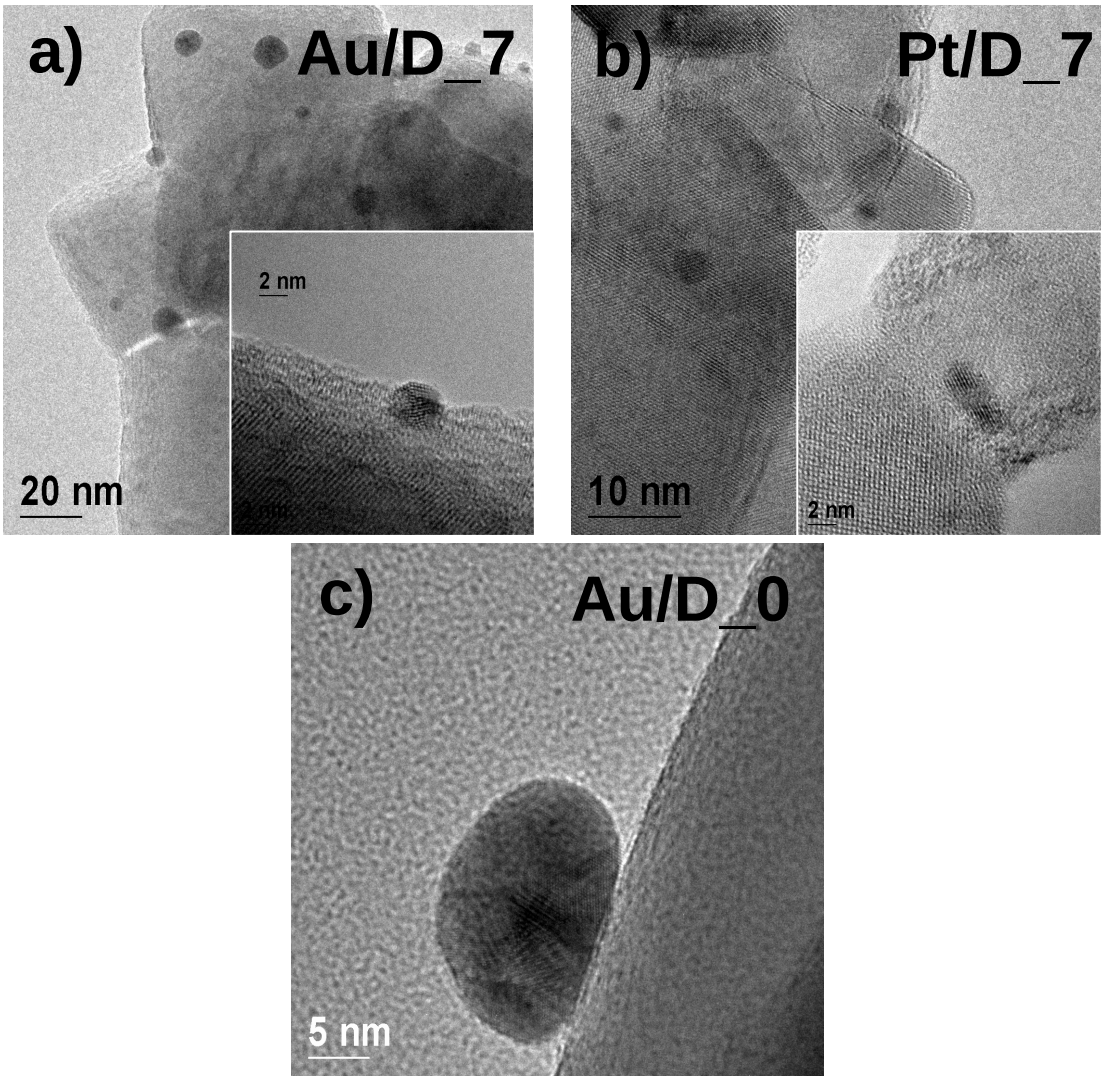

Figure 10.9 HRTEM images of TiO_2 samples modified by noble metal nanoparticles deposition: a) Au/D_7; b) Pt/D_7; c) Au/D_0.

Home-made TiO_2 doped samples consisted of micro-aggregates of single crystal nano-spheres, with average diameter dimensions (40-50 nm) which are consistent with those obtained by XRPD analysis (Table 10.1). In particular, the photodeposition

technique seems to ensure a good dispersion of both gold and platinum nanoparticles on the TiO_2 surface, as shown in Figs. 10.9 a and b.

Moreover in the case of Au/TiO_2 samples, full anatase moderately doped material (D_7) showed smaller gold nanoparticles with respect to those obtained for undoped material (D_0), in agreement with indirect information obtained by EXAFS analysis. It's worth to recall that larger and more spherical gold nanoparticles were also obtained by using the photodeposition method for mixed phase commercial TiO_2 powder (Degussa P25), as shown in Chapter 6.

10.3.2 Photocatalytic tests

10.3.2.1 Liquid phase reactions: formic and acetic acid photocatalytic oxidation

The photocatalytic activity scale of the home-made TiO_2 and the corresponding samples modified by surface Au or Pt nanoparticles photodeposition can be appreciated in Fig. 10.10. The photoactivity scale obtained for the same samples during acetic acid oxidation is shown in Fig. 10.11. In this case the activity is expressed in terms of zero-order rate constant of CO_2 photo-evolution from TiO_2 suspensions containing acetic acid.

For all of the doped TiO_2 series the photodeposition of gold or platinum nanoparticles was beneficial in the degradation of both organic substrates. Moreover in case of FA decomposition (Fig. 10.10) the effects induced by the photodeposition procedure itself can be distinguished from those induced by the presence of noble metal (NM) nanoparticles. Indeed the degradation rates obtained with reference samples (R/TiO_2), prepared by irradiating the bare photocatalysts in a methanol/water solution under nitrogen atmosphere, under identical conditions as those employed for NM nanoparticles deposition, but in the absence of noble metal precursors, were lower that those measured with the corresponding unmodified samples; in particular the rate decrease was larger for blank NH_4F-doped samples than for P25. This negative effect may partly be explained by considering that residual methanol molecules might compete with formic acid molecules for the photogenerated positive holes (h^+). This phenomenon is in line with the results reported in Chapter 5 indicating that any modification of standard P25 TiO_2 (Degussa), consequent to treatments to deposit noble metal nanoparticles on its surface, implied a decrease of photocatalytic activity in

organic substrate degradation; this was particularly evident in the case of the DP (deposition-precipitation) method, which requires thermal treatments.

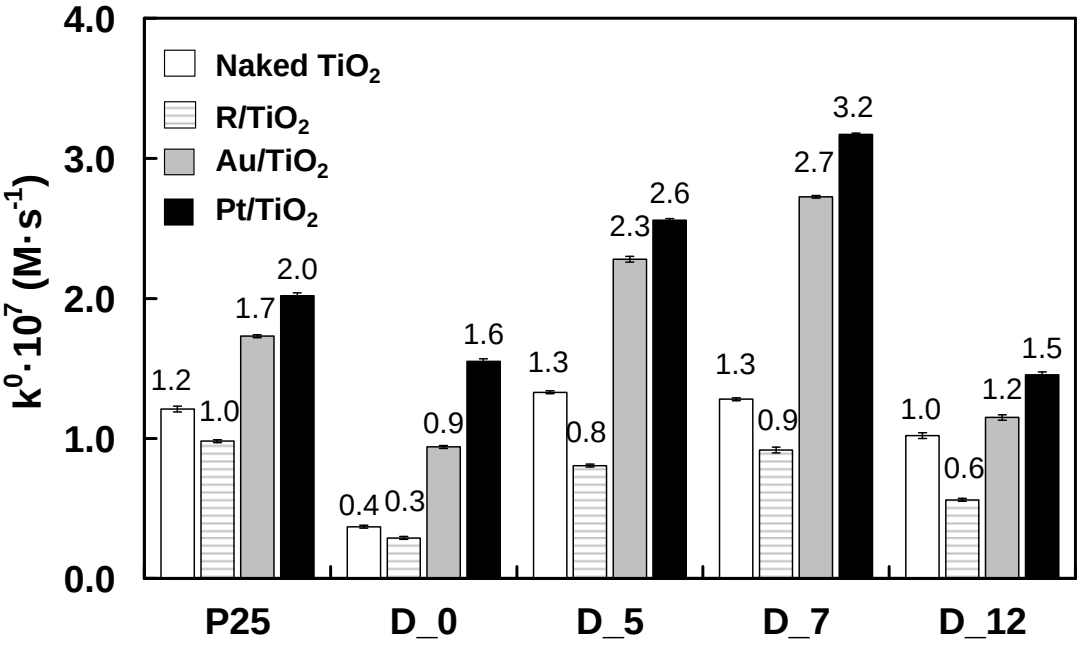

Figure 10.10 Zero-order rate constants of formic acid photo-mineralisation on photocatalysts prepared starting from different amounts of NH_4F dopant (D series) and modified by photodeposition of 0.5 wt.% of Au or Pt nanoparticles. R/TiO_2 refers to blank samples, prepared by following the same photodeposition procedure, except for the addition of the noble metal precursor.

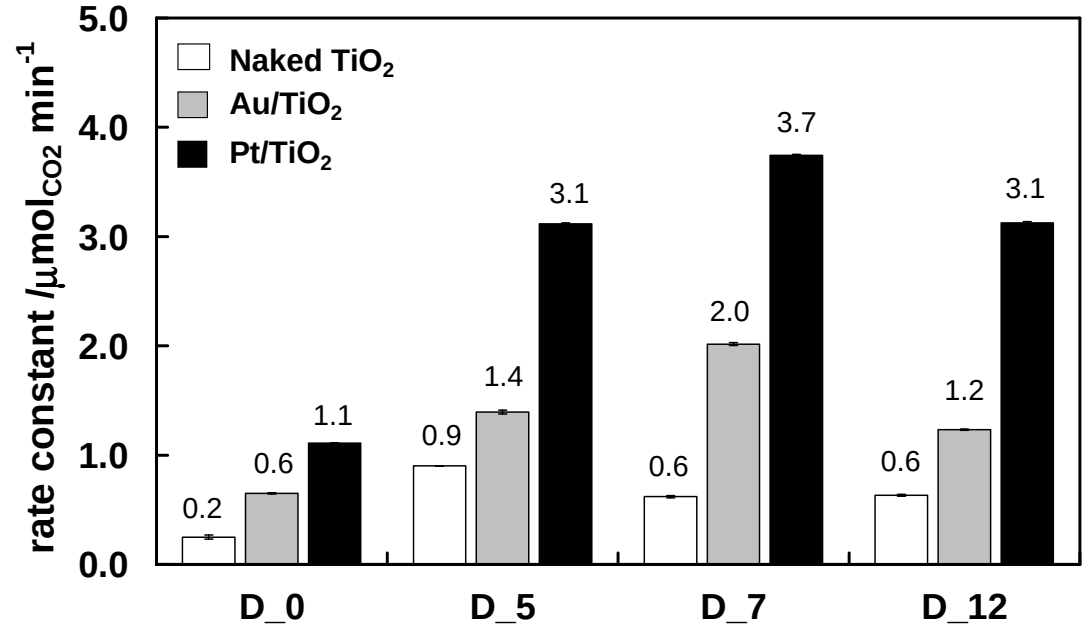

Figure 10.11 Zero-order rate constants of CO_2 photo-evolution during acetic acid decomposition on photocatalysts prepared starting from different amounts of NH_4F dopant (D series) and modified by photodeposition of 0.5 wt.% of Au or Pt nanoparticles.

The rate constant values reported in Fig.s 10.10 and 10.11 clearly confirm that Pt is a better co-catalyst than Au. The difference in the photocatalytic performance of these two metal as co-catalysts can be related to their work function values (Φ), *i.e.* the energy required to promote an electron from the Fermi energy level into vacuum (the higher is Φ , the lower in energy is the Fermi level). In fact, the greater is the difference between the metal work function and that of the TiO_2 support, the higher is the Schottky barrier,[12,13] the electronic potential barrier generated by the band alignment at the metal–semiconductor heterojunction, with consequent increased efficiency of photogenerated electron trapping by the metal and consequent transfer to O_2 molecules adsorbed on the photocatalyst in water. For the 111 crystal plane, Φ = 5.31 eV for Au and Φ = 5.93 eV for Pt,[14] whereas Φ values in the 4.6–4.7 eV range are reported in the literature for TiO_2.[15] Consequently, Pt is a more efficient electron trapper than gold, thus ensuring a more efficient charge separation in line with the higher photoactivity of Pt-modified TiO_2.

Furthermore, the rate constant values in formic acid decomposition presented in Fig. 10.10 evidence that the best performing doped materials modified by surface NM nanoparticles were even more active than P25 TiO_2 from Degussa, modified by following the same photodeposition procedure.

Possible synergistic effects on the photocatalytic activity of the material induced by bulk (NH_4F doping) and surface (NM nanoparticles deposition) TiO_2 modification merit to be outlined. However the term ‘synergetic effect’ has not yet found a unique definition in the field of photocatalysis.

Ohtani in a recent review[16] has tried to explain the concept of ‘synergetic effect’ as follows: when more than two kinds of photocatalysts are used as a mixture, the overall photocatalytic activity exceeds the sum of activities of each photocatalyst. Moreover when a certain component alone is not a photocatalyst, and its mixture with a photocatalyst shows improved activity, that component should be called “co-catalyst” or “enhancer”, and the improvement cannot be attributed to a synergistic effect.

Even if this kind of interpretation does not allow us to talk about a real synergy for our NM modified doped TiO_2 systems, a more detailed comparison about the effects induced by noble metal nanoparticles deposition on different photocatalytic materials (commercial, undoped and differently NH_4F-doped TiO_2 photocatalysts) merits to be undertaken.

In this regard looking at the data reported in Fig. 10.10 the intrinsic positive effect induced by NM nanoparticles deposition (Δ_{Au} or Δ_{Pt}) can be defined as the difference between the zero-order rate constant of formic acid degradation obtained with the Au or Pt/D_0 samples and that obtained with naked D_0. In a similar way the effect produced by only NH_4F doping, Δ_{dop}, can be expressed as the difference between the zero-order rate constant of formic acid degradation obtained with naked D_X samples and that obtained with naked D_0. This contribution of course varies with the amount of dopant source employed in the synthesis of D_X samples. Finally, the overall combined beneficial effect of bulk and surface modification, Δ_{syn}, can be estimated as the difference between the zero-order rate constant of formic acid degradation obtained with Au or Pt/D_X samples and that obtained with naked D_0. This series of calculations can be easily expressed as follows:

$$\Delta_{Au} = k\,(\text{Au/D\_0}) - k\,(\text{D\_0}) \quad (10.2)$$

$$\Delta_{Pt} = k\,(\text{Pt/D\_0}) - k\,(\text{D\_0}) \quad (10.3)$$

$$\Delta_{dop} = k\,(\text{D\_X}) - k\,(\text{D\_0}) \quad (10.4)$$

$$\Delta_{syn} = k\,(\text{Au or Pt/D\_X}) - k\,(\text{D\_0}) \quad (10.5)$$

Therefore, if the value of Δ_{syn} exceeds the sum of each separately calculated contribution (Δ_{dop} + Δ_{Au} or Δ_{Pt}), a synergistic effect of NH_4F doping and surface NM deposition could be recognized. This kind of comparison is depicted in Fig.s 10.12 and 10.13 for formic acid and acetic acid test reaction, respectively.

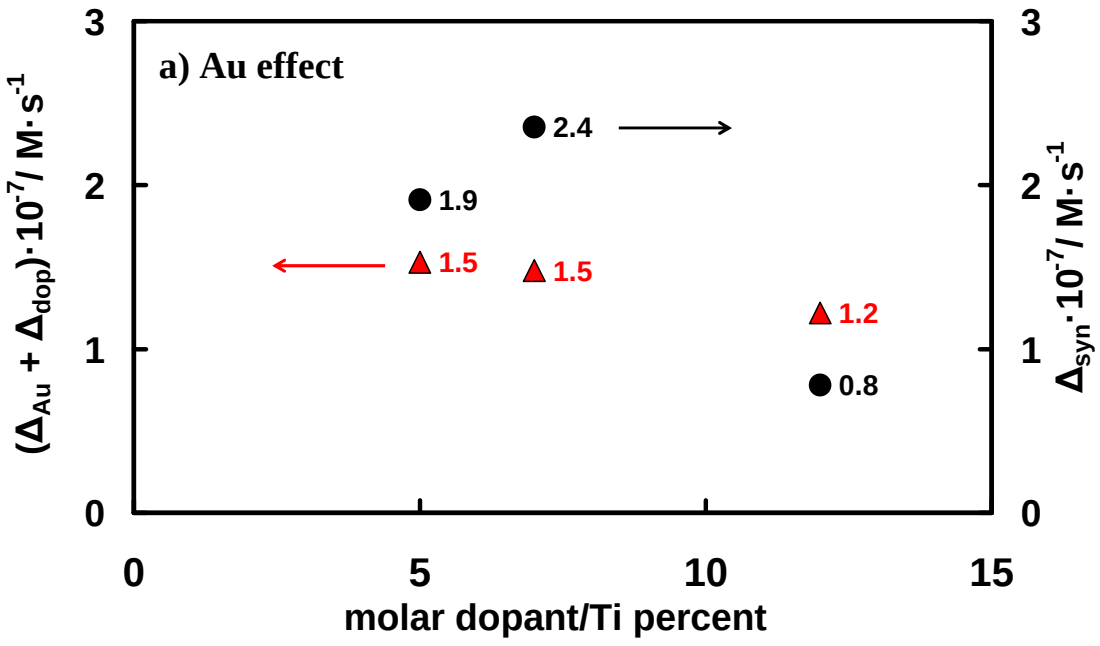

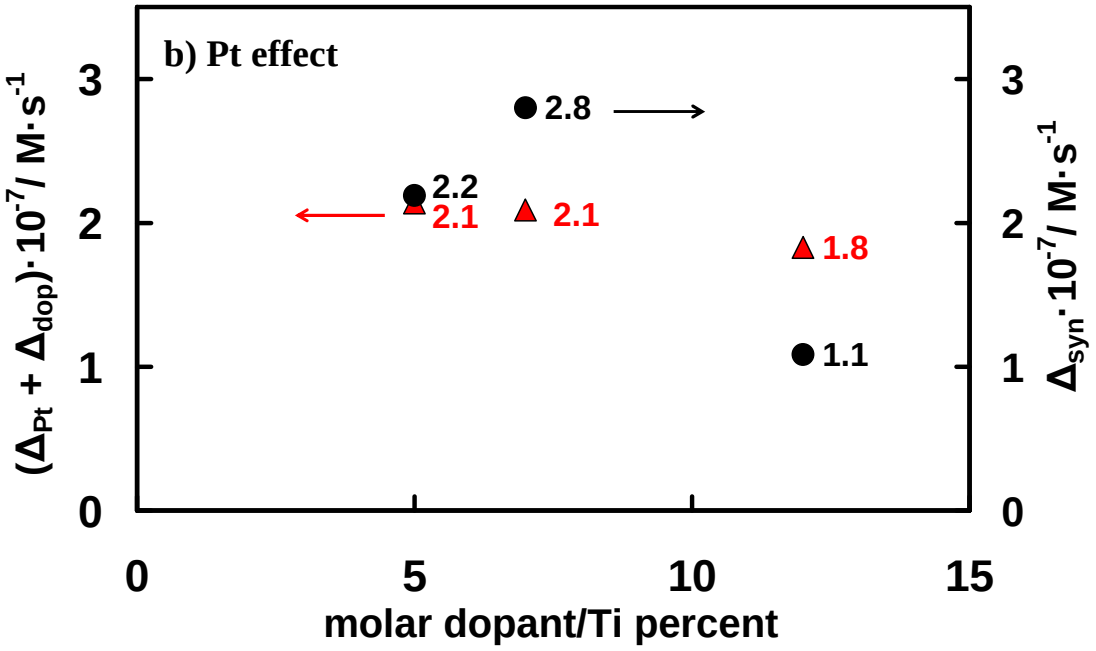

Figure 10.12 Calculation of beneficial effect on the photoactivity in formic acid decomposition, induced by NH_4F doping and a) Au or b) Pt nanoparticles: comparison between the sum of the single contributions (Δ_{dop} + Δ_{Au} or Δ_{Pt}) and the combined effect (Δ_{syn}) of bulk and surface TiO_2 modifications as a function of the percent nominal dopant/Ti ratio.

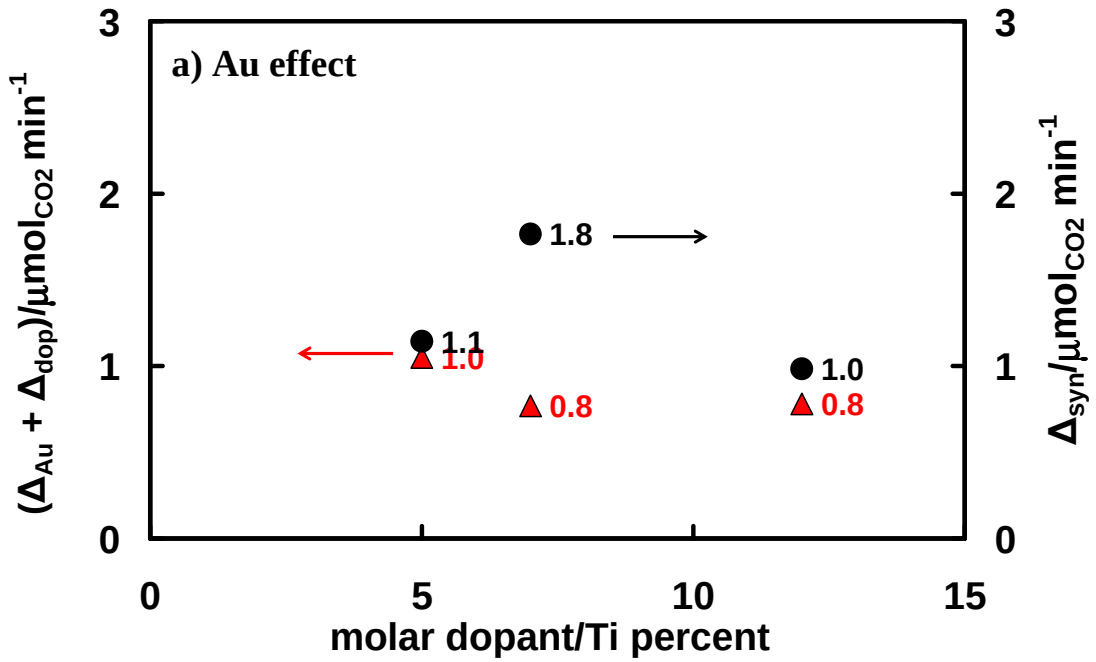

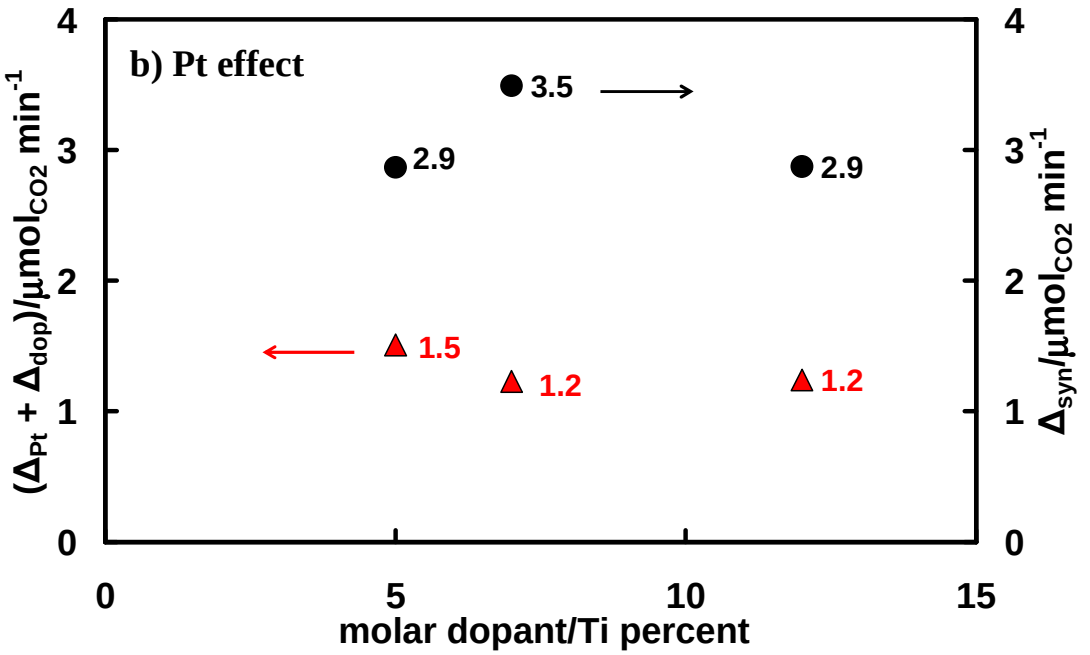

Figure 10.13 Calculation of beneficial effect on TiO_2 photoactivity in acetic acid decomposition, induced by NH_4F doping and a) Au or b) Pt nanoparticles deposition: comparison between the sum of the single contributions ($\Delta_{dop} + \Delta_{Au}$ or Δ_{Pt}) and the combined effect (Δ_{syn}) of bulk and surface TiO_2 modifications as a function of the percent nominal dopant/Ti ratio.

Calculation compared in Figs. 10.12 and 10.13 clearly show that for both liquid phase test reactions (formic and acetic acid photooxidation), Δ_{syn} contributions were always higher than the $\Delta_{dop} + \Delta_{Au}$ or $\Delta_{dop} + \Delta_{Pt}$ sums.

The beneficial synergistic effect of simultaneous bulk and surface TiO_2 modification was particularly evident in the case of acetic acid decomposition performed with Pt modified doped TiO_2 (Fig. 10.13b); the maximum synergistic effect was systematically attained with photocatalysts prepared starting from 7 mol.% of dopant source (D_7 series). On the contrary, no synergistic effect was attained in formic acid photodecomposition with NM-modified and relatively highly doped materials (D_12 series) which, as already observed in Chapter 8, may be characterized by a large extent of defective sites that could act as recombination centres of photogenerated charge carriers, with a consequent decrease in the photocatalytic activity.

10.3.2.2 Photocatalytic production of H_2 by photo-steam reforming of methanol

A recent, systematic investigation on the photocatalytic steam reforming reaction of methanol evidenced that methanol undergoes oxidation up to CO_2 through the formation of formaldehyde and formic acid as intermediate species; carbon monoxide, methane, methyl formate, dimethyl ether and acetaldehyde were also identified as side products.[5]

The products distribution and their selectivity can be tuned by changing the methanol molar fraction x in the liquid solution, thus changing the ratio of the methanol to water partial pressure in the feeding mixture. In particular, H_2 and CO_2 evolution close to the molar ratio expected from overall methanol steam reforming (reaction (10.1)) is achieved only for very low x values ($x < 0.01$) and formaldehyde becomes the main reaction product, for higher x values. Furthermore, the rate of hydrogen production k_{H2} follows a bell-shaped curve when plotted *vs*. x, with a maximum at $x = 0.4$, and the rate of CO_2 production r_{CO2} exhibits a hyperbolic decay curve *vs*. x. Hence, in the present study $x = 0.1$ was adopted as standard reaction condition, because it represents a good compromise between a high r_{H2} value and high selectivity in hydrogen production to CO_2, S_{CO2}, defined as $S_{CO2} = (3\, k_{CO2}/k_{H2}) \times 100$. The selectivity to CO is defined as $S_{CO} = (2\, k_{CO}/k_{H2}) \times 100$.

In all photocatalytic tests H_2, CO_2 and CO evolution occurred at constant rate during irradiation, as in previous studies.[5] The rates of H_2, CO_2 and CO production obtained with the investigated photocatalysts are reported in Table 10.5, together with the S_{CO2} and S_{CO} selectivity values. It is worth recalling that the rate of CO production is very important when considering photocatalytic hydrogen as a feedstock for fuel cells. In fact, CO would certainly be the most undesired by-product, being a well-known poison for Pt-based catalysts in fuel cells.

Among the unmodified oxides, commercial P25 was confirmed to be the most photoactive photocatalysts under UV-Vis irradiation (Table 10.5 and inset of Fig. 10.14). Among the doped oxides, D_5 was by far the most active photocatalyst; however, in contrast with the results obtained during formic or acetic acid photooxidation, undoped mixed phase D_0 sample showed higher photoactivity than full anatase D_7 and D_12 highly doped materials, even if these latter samples were characterized by larger specific surface area (see Table 10.1). By taking into account that anatase phase is characterized by a more negative E_{CB} potential value respect to

that of rutile phase, *i.e.* -0.45 V and -0.37 V *vs.* NHE at pH 7, the electrons photogenerated in anatase conduction bands are thus expected to have a greater ability from promoting hydrogen formation.[6] However, the absorption threshold of anatase is at shorter wavelength with respect to that of rutile, and thus anatase is able to absorb a lower fraction of the emission spectrum of the xenon lamp. This may explain why the D_0 sample exhibits a lower activity with respect to the D_7 and D_12 samples. Furthermore NH_4F over-doping, even if being able to stabilize the most photoactive anatase phase, led to a really marked photoefficiency decrease. This could be ascribed to the possible formation of an excess of structure defects which can play an detrimental role in favouring the undesired electron-hole recombination process.

Table 10.5 Zero order rate constants of H_2, CO_2 and CO production (k) and percent selectivity to CO_2 and CO in hydrogen production on bare and 0.5 wt.% Au or Pt modified doped TiO_2 samples under UV-Vis irradiation. Results obtained with commercial P25 are also reported for comparison.

Sample	k/mmol h^{-1} g_{cat}^{-1}			% Selectivity	
	H_2	CO_2	CO	CO_2	CO
D_0	0.0651	0.0093	0.0042	42.9	12.9
D_5	0.1883	0.0105	0.0111	16.7	11.8
D_7	0.0372	0.0061	0.0029	49.2	15.6
D_12	0.0447	0.0051	0.0014	34.2	6.3
Au/D_0	0.5758	0.0221	0.0064	11.5	2.2
Au/D_5	3.7864	0.1756	0.0778	13.9	4.1
Au/D_7	2.3407	0.1245	0.0643	16.0	5.5
Au/D_12	0.9944	0.0417	0.0184	12.6	3.7
Pt/D_0	3.0012	0.1797	0.0164	18.0	1.1
Pt/D_5	10.4731	0.7670	0.2458	22.0	4.7
Pt/D_7	5.9948	0.3924	0.0964	19.6	3.2
Pt/D_12	2.6848	0.1568	0.0251	17.5	1.9
P25	0.6113	0.0193	0.0466	9.5	15.2
Au/P25	5.8432	0.3297	0.2597	16.9	8.9
Pt/P25	14.4796	1.4224	0.4359	29.5	6.0

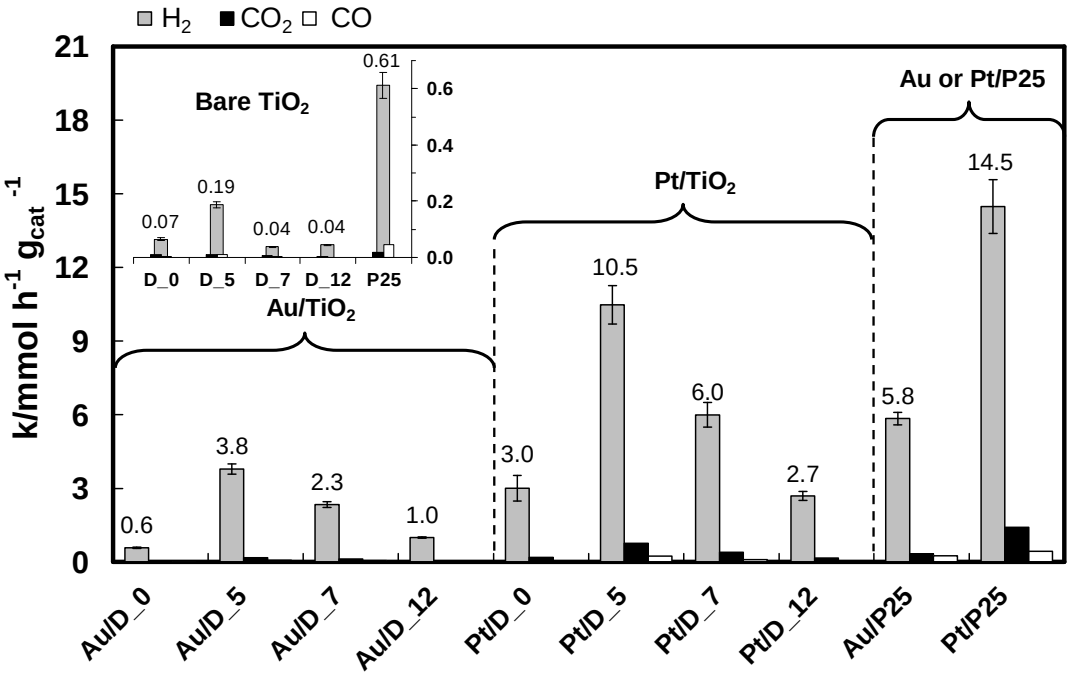

Figure 10.14 Zero order rate constants of H_2, CO_2 and CO production (k) on bare (inset) and 0.5 wt.% Au or Pt modified doped samples under UV-Vis irradiation. Results obtained with commercial P25 are also reported for comparison.

On Au- or Pt-deposited TiO_2 samples the rate of hydrogen production was systematically more than ten-fold higher in comparison to the values obtained with the corresponding bare oxides. Indeed, as already mentioned, noble metal nanoparticles on the semiconductor surface are able to capture photopromoted conduction band electrons, due to the electronic potential barrier generated by the band alignment at the metal/semiconductor heterojunction (Schottky barrier). This phenomenon favours interface electron transfer, thus increasing the efficiency of charge separation of the electron–hole pairs photo-generated on the semiconductor upon light absorption. In this case methanol photo-oxidation occurs at the semiconductor surface, acting as photo-anode, whereas hydrogen evolution takes place on the noble metal surface, acting as photo-cathode.

Moreover, noble metal nanoparticles deposition on TiO_2 samples (especially in case of Pt) generally induced a decrease of the S_{CO} value indicating that the more efficient is the separation between photoproduced charge carriers in the photocatalyst, the more efficient are not only the e_{CB}^- - involving reduction paths, mainly leading to H_2 production, but also the h_{VB}^+ - initiated complete methanol oxidation to CO_2.

An important point that merits to be outlined is the fact that an almost identical bell-shaped photoactivity trend with increasing the dopant content was obtained for the naked, Au- and Pt-modified titania series (see Fig. 10.14), with the 5% NH_4F-doped samples always being the best photocatalysts within each series. This demonstrates the crucial role that the electronic structure of doped materials has in determining the absorption features and the photoproduced charge separation and mobility within the photo-catalyst doped oxide.

Moreover Pt was still confirmed to be a better co-catalyst than Au, in agreement with their work function values (Φ_{Au} = 5.31 eV, Φ_{Pt} = 5.93 eV) as already discussed in Chapter 9. This confirms the main role of the noble metal is limited to an increase efficiency of electron-hole separation by 'capturing' conduction band electrons, Pt always being more efficient than Au in ensuring this. However, the intrinsic charge carrier production and the efficiency in their separation is exclusively determined by the bulk electronic features of the photocatalytic material.

The best photoactivity was reached for Pt-modified samples characterized by smaller noble metal nanoparticles size (2-5 nm), also thanks to their more homogeneous distribution on the oxide surface, as suggested by HRTEM and EXAFS analysis. Recently this general trend of hydrogen production rate increase with decreasing the Pt particle size has also been shown for TiO_2 photocatalysts, prepared by flame spray pyrolysis.[5,17]

However, concerning different methods of noble metal deposition on TiO_2, NM-photodeposition technique seems to guarantee both higher hydrogen production rate and lower selectivity to CO with respect to surfactant-stabilized preformed NM nanoparticles deposition, which was previously investigated in our research group.[5] In fact, in the case of commercial P25 modified by 0.5 wt.% Pt deposited from pre-stabilized preformed Pt nanoparticles,[18] an hydrogen production rate of 7.75 mmol h^{-1} g_{cat}^{-1} and a selectivity to CO of 8.3% were obtained, by adopting the same experimental set-up described in Fig. 10.2 with a more intense light source.

Finally, in order to estimate the relative effect induced by noble metal nanoparticles deposition on commercial, undoped and differently NH_4F-doped TiO_2 photocatalysts, the ratio between the hydrogen production rate obtained with each NM-modified sample and that obtained with the corresponding naked photocatalyst were calculated. These values are reported in Table 10.6.

Table 10.6 Ratio between the zero order rate constants of hydrogen photo-production obtained with each NM modified sample and that attained with the corresponding naked photocatalyst.

H_2 photo-production		
Sample	k_{Au}/k	k_{Pt}/k
P25	9.6	23.7
D_0	8.8	46.1
D_5	20.1	55.6
D_7	62.9	161.2
D_12	22.2	60.1

The increased photoefficiency in methanol photo-steam reforming produced by the presence of Au or Pt nanoparticles on TiO_2 was remarkably higher for the NH_4F-doped systems respect to that of the corresponding undoped or commercial photocatalysts, in good agreement with results previously obtained in acetic acid oxidation. In particular the maximum positive effect was attained for the D_7 sample. By this way NH_4F doping provided a synergistic positive contribution to the already beneficial effect produced by noble metal nanoparticles, in the case of the photo-reduction path leading to H_2 production.

As a conclusion of this chapter, one can thus highlight that very intriguing synergistic effects of simultaneous bulk and surface TiO_2 modification were thus evidenced for both energetically down-hill and up-hill reactions, which can be interpreted in relation to the structural properties of the materials. On one side, doping guarantees that the most active TiO_2 anatase phase is stabilized up to high calcination temperature, ensuring high crystallinity and good photoinduced charge carriers production, whereas noble metal nanoparticles contribute in increasing the separation of photoproduced charge carriers, resulting in enhanced photocatalytic performances of the here investigated photocatalyst systems.

10.4 References

1. G. Wu, T. Chen, W. Su, G. Zhou, X. Zong, Z. Lei and C. Li, Int. J. Hydrogen Energy, **2008**, 33, 1243.
2. O. Rosseler, M.V. Shankar, M. Karkmaz-Le Du, L. Schmidlin, N. Keller and V. Keller, J. Catal., **2010**, 269, 179.
3. N. Strataki, V. Bekiari, D.I. Kondarides and P. Lianos, Appl. Catal. B: Environ., **2007**, 77, 184.
4. J. Greaves, L. Al-Mazroai, A. Nuhu, P. Davies and M. Bowker, Gold Bull., **2006**, 39, 216.
5. G. L. Chiarello, M. H. Aguirre and E. Selli, J. Catal., **2010**, 273, 182.
6. G. L. Chiarello, A. Di Paola, L. Palmisano and E. Selli, Photochem. Photobiol. Sci., **2011**, 10, 355.
7. G. L. Chiarello, D. Ferri and E. Selli, J. Catal., **2011**, 280, 168.
8. C. Bernardini, G. Cappelletti, M. V. Dozzi and E. Selli, J. Photochem. Photobiol. A: Chem., **2010**, 211, 185.
9. G. L. Chiarello, L. Forni and E. Selli, Catal. Today, **2009**, 144, 69.
10. C. G. Hatchard and C. A. Parker, Proc. R. Soc. London, Ser. A, **1956**, 235, 518.
11. S. Link and M. El-Sayed, J. Phys. Chem. B, **1999**, 103, 8410.
12. P. Kamat, J. Phys. Chem. B, **2002**, 106, 7729.
13. A. L. Linsebigler, G. Lu and J.T. Yates, Chem. Rev., **1995**, 95, 735.
14. CRC Handbook of Chemistry and Physics, 87th ed., Taylor & Francis, **2006**, pp. 12–114.
15. C. Young, T. M. Lim, K. Chiang, J. Scott and R. Amal, Appl. Catal. B: Environ., **2008**, 78, 1.
16. B. Ohtani, J. Photochem. Photobiol. C: Photochem. Rev., **2011**, in press, doi: 10.1016/j.jphotochemrev.2011.02.001.
17. G. Wu, T. Chen, W. Su, G. Zhou, X. Zong, Z. Lei and C. Li, Int. J. Hydrogen Energy, **2008**, 33, 1243.
18. J. H. Liu, A. Q. Wang, Y. S. Chi, H. P. Lin and C.Y. Mou, J. Phys. Chem. B, **2005**, 109, 40.

Chapter 11

Conclusions

The present PhD thesis was mainly devoted to explore different routes for improving the photocatalytic activity of TiO_2 for environmental applications, especially in the photodegradation of organic pollutants in aqueous suspensions. The general conclusions achieved by investigating the photocatalytic degradation of different substrates in the presence of TiO_2-based materials modified by non-metal doping and/or by noble metal nanoparticles deposition can be briefly summarized as follows.

Photocatalytic activity of TiO_2 modified by gold nanoparticles deposition: effects of the adopted deposition technique

The first part of the thesis was devoted to a systematic study on the photocatalytic performance of commercial TiO_2 (Degussa P25) bearing gold nanoparticles deposited by deposition-precipitation (DP), with particular attention to the method, either thermal or chemical, employed to reduce Au(III) into metallic gold. Two organic substrates, *i.e.* the azo dye Acid Red 1 (AR1) and formic acid (FA), were employed as substrates in photocatalytic oxidative degradation kinetic tests. Hydrogen peroxide evolution was also monitored during the runs in order to have a better insight into the role played by gold nanoparticles on the reduction path parallel to organics' oxidation.

The presence of gold on TiO_2 was found to facilitate both the electron transfer to O_2 and the mineralization of formic acid, mainly proceeding through direct interaction with photoproduced valence band holes. The so-formed highly reductant $CO_2^{\bullet-}$ intermediate species may contribute in maintaining gold in metallic form. The controversial results obtained in the photocatalytic degradation of the AR1 dye were rationalized by taking into account that with this substrate, mainly undergoing oxidation through a hydroxyl radical mediated path, the photogenerated holes may partly oxidize gold nanoparticles, which consequently act as recombination centres of photoproduced charge carriers.

These investigations also evidenced that the effects due to the presence of gold nanoparticles on the TiO_2 surface should be distinguished from those induced on the TiO_2 surface by the deposition treatment itself. In particular, the DP technique, requiring a high temperature reduction step, produced a decrease in TiO_2 photoactivity, as demonstrated in the case of blank samples produced following the DP procedure in the absence of gold precursor.

For this reason, other Au/TiO_2 photocatalysts were prepared by photodeposition, by irradiating an aqueous suspension containing P25 TiO_2 and chloroauric acid under anoxic conditions. This technique ensures the direct deposition of metallic nanoparticles on the semiconductor, without any need of subsequent heat-treatment. HRTEM analysis showed that photodeposition produced larger and more spherical gold nanoparticles compared to other gold deposition techniques.

Furthermore, the photodeposition procedure itself, even in the absence of gold precursor, produced positive effects on TiO_2 photoactivity, especially in the case of Cr(VI) photoreduction, most probably as a consequence of irradiation under anaerobic conditions, inducing partial TiO_2 surface reduction. The rate of both investigated photocatalytic reactions (formic acid photooxidation and Cr(VI) photoreduction) was found to depend on metal loading, the maximum value being attained for *ca.* 0.5 wt.% Au, representing an optimal balance between the detrimental shielding effects of surface Au nanoparticles, decreasing the fraction of light absorbed by TiO_2, and their beneficial role in capturing photopromoted electrons, thus reducing the electron-hole recombination rate. Photodeposition was thus found to be the best technique for noble metal nanoparticles deposition on TiO_2-based materials.

Photocatalytic activity of non metal doped-TiO_2 materials

In the central part of the thesis the attention was focused on sulphur, fluorine and boron as dopants of TiO_2, the effects of N or C doping on the photocatalytic efficiency of TiO_2 having already been widely investigated in the last decade. The sol-gel method, which is very flexible and suitable for systematic structure *vs.* photoactivity studies, was adopted to incorporate anion dopants in the TiO_2 structure. Two series of TiO_2-based doped samples were first prepared by the sol-gel method in the presence of different amounts of dopant source (thiourea and NH_4F for S-doped and F-doped samples, respectively), followed by calcination at different temperature (500, 600 or 700°C). Reference undoped materials were prepared by following the same synthetic procedure apart from the addition of the dopant precursor.

First of all, XRPD analysis showed that both types of doping inhibit the phase transition from anatase into rutile up to 700°C. Moreover, while the dimension of anatase crystallites seems to be independent of the presence of sulphur, NH_4F doping

appears to produce larger anatase TiO_2 particles. BET analysis showed a surface area decrease with increasing the calcination temperature even if NH_4F doping seemed to limit particles sintering effects, especially in case of samples calcined at 500°C.

While S-doped TiO_2 showed a photocatalytic activity in FA photodegradation quite similar to that of the undoped materials, most probably due to the presence of oxidised sulphur species on their surface, moderate doping with NH_4F was extremely beneficial in increasing the reaction rate, especially for photocatalysts calcined at high temperature, consisting of highly crystalline pure anatase, in which the rate of detrimental charge carriers recombination was reduced.

In particular, the general trend of photocatalytic activity increase with increasing the calcination temperature (attained for each series of doped materials) appeared rather surprising, since the highest photoactivity was reached with photocatalysts characterized by a relatively smaller specific surface area (SSA). In fact SSA is expected to play an essential positive role in FA degradation, mainly proceeding through direct interaction of FA with photoproduced valence band holes. At the same, an excessively high doping level was shown to limit TiO_2 photoactivity, possibly due to the formation of an increasing number of defects in the oxide structure, acting as recombination centres of photogenerated charge carriers.

The same trend of photoactivity improvement was obtained for home made NH_4F-doped TiO_2 in two other reactions, *i.e.* the decomposition of acetic acid in aqueous suspension and the gas phase mineralization of acetaldehyde. This very important achievement demonstrates that the photoactivity scale of materials results from their intrinsic electronic structure, being independent of specific interactions with the substrate and/or the presence of a solvent. Moreover, home made NH_4F-doped samples were even more active than traditional benchmark P25 TiO_2 (Degussa) and other commercial full anatase materials possessing different SSA.

XPS and EPR analysis of NH_4F-doped materials, even if calcined at 700°C, revealed the presence of residual nitrogen containing species. So for these samples it is better to invoke an N and F co-doping.

In order to study the possible activation of these materials in the visible light region the photooxidation of acetic acid was also investigated systematically as a function of the irradiation wavelength, by collecting so-called action spectra. By comparing the shapes of the action spectra with those of the absorption spectra of the investigated

photocatalysts a model was proposed, based on spectral features deconvolution, which allows to make a clear distinction between light absorption by the materials which does not produce any photocatalytic reaction and light absorption leading to effective photoactivity in acetic acid decomposition. In this regard for each doped sample the contribution of two different extra absorption peaks was calculated. The contribution of a photocatalytically inactive absorption peak (called B) located in the near visible region (with a maximum around 420 nm) decreased by increasing the calcination temperature. On the contrary the contribution of a photocatalytically active absorption peak (called A) located in the UVA region (with a maximum around 365 nm), close to the typical band gap absorption onset of anatase TiO_2, increased with increasing the calcination temperature, within each series of doped samples.

While peak B was attributed to nitrogen doping which can produce photoinactive intra band gap states, the origin of active peak A is still under discussion. This absorption feature might be attributed to extrinsic absorption originating from surface oxygen vacancies or surface defects, the formation of which is expected to be favoured by F-doping at high calcination temperature. On the other hand, peak A might be simply a consequence of the higher crystallinity of NH_4F-doped samples calcined at relatively high temperature (700°C).

In order to better clarify the role of fluorine and/or nitrogen dopants of TiO_2, another series of doped photocatalysts was prepared according to the same synthetic sol-gel procedure, employing HF instead of NH_4F as dopant source, in order to avoid the co-presence of nitrogen impurities in the material. At the same time, aiming at elucidating the effects of F-doping and co-doping of TiO_2, an investigation was started on the effects of the co-presence of *p*-block elements boron and fluorine in titania.

A comparison between the photoefficiency of samples singly or co-doped with fluorine was essential in order to confirm fluorine, and not nitrogen, as the main responsible for the observed photoactivity increase in the UVA region for doped samples calcined at high temperature.

Photocatalytic activity of NH_4F-doped TiO_2 modified by noble metal nanoparticles photodeposition

In the last part of the thesis the effect of noble metal (Pt and Au) nanoparticles photodeposition on the series of NH_4F-doped TiO_2 photocatalysts calcined at 700°C was investigated in both energetically down-hill and up-hill reactions, *i.e.* in formic acid and acetic acid degradation in aqueous suspension and in hydrogen production from methanol/water vapour mixtures.

The photoactivity results obtained in formic acid degradation clearly demonstrate that the best performing home made doped materials were even more active than commercial P25 TiO_2 from Degussa, used as a standard photocatalyst, both before and after surface modification by noble metal nanoparticles deposition by the same photodeposition procedure.

Very intriguing synergistic effects of simultaneous bulk and surface TiO_2 modification were evidenced, which can be interpreted in relation to the structural properties of the materials. On one side, doping guarantees that the most active TiO_2 anatase phase is stabilized up to high calcination temperature, ensuring high crystallinity of the photocatalytic material, whereas noble metal nanoparticles contribute to a better separation of photoproduced charge carriers, resulting in a more efficient electron transfer to adsorbed protons, yielding H_2.

Doping of TiO_2 enhanced the hydrogen production rate, with an identical bell-shaped trend with increasing the dopant content for the naked, Au- and Pt-modified titania series, with the 5 mol.% NH_4F-doped sample always being the best photocatalyst within each series. Over-doping led to a photoefficiency decrease, most probably due to an excess of structure defects.

Pt was confirmed to be a better co-catalyst than Au for both organic substrates decomposition and H_2 production, in agreement with their work function values Φ_{Au} = 5.31 eV and Φ_{Pt} = 5.93 eV. In general, the highest photoactivity was reached for Pt-modified samples characterized by smaller noble metal nanoparticles size (2-5 nm), also thanks to their more homogeneous distribution on the oxide surface, as suggested by HRTEM and EXAFS analysis.

Appendix

List of publications, congress contributions and attended schools

List of publications

1. "Effects of gold nanoparticles deposition on the photocatalytic activity of titanium dioxide under visible light".
   M. V. Dozzi, L. Prati, P. Canton and E. Selli, Phys. Chem. Chem. Phys., **2009**, 11, 7171-7180.

2. "Photocatalytic degradation of organic molecules in water: Photoactivity and reaction paths in relation to TiO_2 particles features".
   C. Bernardini, G. Cappelletti, M. V. Dozzi and E. Selli, J. Photochem. Photobiol. A: Chem., **2010**, 211, 185–192.

3. "Effects of Surface Modification on the Photocatalytic Activity of TiO_2".
   M. V. Dozzi, G. L. Chiarello and E. Selli, J. Adv. Oxid. Technol., **2010**, 13, 305–312.

4. "Photocatalytic activity of S- and F-doped TiO_2 in formic acid mineralization".
   M. V. Dozzi, S. Livraghi, E. Giamello and E. Selli, Photochem. & Photobiol. Sci., **2011**, 10, 343–349.

5. "Absorption and Action Spectra Analysis of Ammonium Fluoride-doped Titania Photocatalysts".
   M. V. Dozzi, B. Ohtani and E. Selli, Phys. Chem. Chem. Phys., **2011**, 13, 18217–18227.

6. "Cr(VI) photocatalytic reduction: effects of simultaneous organics oxidation and of gold nanoparticles photodeposition on TiO_2".
   M. V. Dozzi, A. Saccomanni and E. Selli, J. Hazard. Mater., **2011**, doi: 10.1016/j.jhazmat.2011.09.038.

7. "Surface fluorination of titanium dioxide photocatalysts: effects of phase composition on photoactivity".
   M. V. Dozzi and E. Selli, Catal. Today, **2011**, submitted.

Contributions to attended conferences

1. **Maria Vittoria Dozzi**, Elena Selli.
   "Photocatalytic activity of TiO_2 modified by gold nanoparticles deposition". Congresso Nazionale di Fotochimica 2008. Bertinoro (FC), 5-7 June **2008**.
   Oral contribution.

2. **Maria Vittoria Dozzi**, Elena Selli.
   "Cr(VI) photocatalytic reduction on TiO_2: effect of the presence of an azo dye in relation to the photocatalyst structure".
   in-GAP NANOCAT summer school. Trondheim (Norway), 21–26 June **2009**.
   Poster contribution.

3. **Maria Vittoria Dozzi**, Elena Selli.
   "Increased photocatalytic activity of TiO_2 by gold nanoparticles photodeposition". Chemistry and Physics of Materials for Energetics European summer school. Milano, 14–19 September **2009**.
   Poster contribution.

4. **Maria Vittoria Dozzi**, Elena Selli.
   "A comparative study of the effects of sulphur and fluorine doping on the photocatalytic activity of TiO_2 in aqueous suspension".
   FISPHOTON 2009: 2nd France-Italy Symposium on Photosciences. Marseille, 7–10 December **2009**.
   Poster contribution with short oral presentation.

5. **Maria Vittoria Dozzi**, Elena Selli.
   "Photocatalytic reduction of Cr(VI) in TiO_2 water suspensions: synergistic effect of an azo dye".
   International Conference on Photochemical Conversion and Storage of Solar Energy – IPS 18. Seoul (Korea), 25–30 July **2010**.
   Poster contribution.

6. **Maria Vittoria Dozzi**, Bunsho Ohtani, Elena Selli.
   "Effects of fluorine doping on the photocatalytic activity of TiO_2 in liquid and gas phase reactions".
   XXXIX Congresso Nazionale di Chimica Fisica. Stresa, 20–24 September **2010**.
   Poster contribution.

7. Marco Altomare, Gian Luca Chiarello, **Maria Vittoria Dozzi**, Alessia Saccomanni, Elena Selli.
   "Photocatalytic Hydrogen Production from Aqueous Solutions on Noble Metal-Modified and/or Doped TiO_2".
   XXIV Congresso Nazionale della Società Chimica Italiana. Lecce, 11–16 September **2011**. eISBN: 978-88-8305-085-5.
   Poster contribution.

Attended schools

1. V Corso nazionale di introduzione alla fotochimica. Università di Bologna - Dipartimento di Chimica "G. Ciamician". 13–17 September **2010**.

2. Chemistry and Physics of Materials for Energetics European summer school. Milano, 14–19 September **2009**.

3. in-GAP NANOCAT summer school. Trondheim (Norway), 21–26 June **2009**.

Research activity abroad

MARCH – AUGUST 2010 and APRIL – JULY 2011

In order to investigate with additional techniques the photocatalytic performance of doped titania prepared during my PhD project, I worked for ten months at the Catalysis Research Center, Hokkaido University in Sapporo (Japan), under the supervision of Prof. Bunsho Ohtani.

Acknowledgements

I would like to thank my precious supervisor, Professor Elena Selli who supported and encouraged me with ‘NO limits’ of Time and Space.

I am sincerely grateful to B. Ohtani SEN SEI, who at first made me dream with his ‘revolutionary’ papers and then let me work in his unique laboratory. Thank you for all your rigorous teachings and help since our first exchange of e-mails Milano (0°C) – Sapporo (-15°C).

Thanks to my Family, faithfully present in my life, every single day of this long ‘trip’; 300 e-mails, sms and postcards, indelibly marked in my mind. “Everything comes to the end, except for the Parents’ Love”.

Grazie ‘unicum’ Dario.

Thanks to all the people that shared with me this so great and strange experience, both in Milan and in Sapporo. In particular thanks to my big brother Orlando and to all my unforgettable ‘crazy’ international ‘bulk’ 友人, who supported my mood, my work and never stopped to Lovely surprise and deeply help me! 羊蹄山 still in front of me! No words to describe OTO-san and OKA-san idea of hospitality and beautiful time spent together! **温泉一番**, right Mika? ありがとう from the ‘bottom of my heart’!

Finally a special thanks to the so pure Sapporo Snow, which blinded me and will warm my heart forever.